Microscopic Physics of Electrical Double Layers

by

J. Pedro de Souza

Submitted to the Department of Chemical Engineering
in partial fulfillment of the requirements for the degree of

Doctor of Philosophy in Chemical Engineering

at the

MASSACHUSETTS INSTITUTE OF TECHNOLOGY

September 2022

Author . . . . . .
Department of Chemical Engineering
July 21, 2022

Certified by . . . . . .
Martin Z. Bazant
E. G. Roos (1944) Professor of Chemical Engineering
Professor of Mathematics
Thesis Supervisor

Accepted by . . . . . .
Patrick S. Doyle
Robert T. Haslam (1911) Professor of Chemical Engineering
Graduate Officer of Chemical Engineering

Microscopic Physics of Electrical Double Layers

by

J. Pedro de Souza

Submitted to the Department of Chemical Engineering
on July 21, 2022, in partial fulfillment of the
requirements for the degree of
Doctor of Philosophy in Chemical Engineering

Abstract

The electrical double layer exists at the phase boundaries of electrolyte solutions, where counterions from solution preferentially accumulate to screen surface charges. Due to the ubiquity of electrolytes, the electrical double layer plays a central role in many fields in science and engineering, including colloid science, electrochemistry, biology, membrane science, and tribology. Across these fields, mathematical models of the double layer have been used to analyze and predict the behavior of electrochemical interfaces in contact with electrolyte solutions. Even so, the standard continuum approaches and assumptions that are applied usually fail to describe the microscopic arrangement and structuring of ions and solvent in the electrical double layer, limiting their predictive power.

In this thesis, I develop mathematical models to predict the microscopic structure of ionic solutions at charged interfaces, relevant for a wide set of problems including membrane transport, electrochemical capacitors, ionic liquid electrolytes, bioseparations, electrowetting, cement cohesion, and general colloidal stability. The continuum mathematical models I derive for the electrical double layer capture electrostatic correlations in electrolytes containing multivalent ions, the molecular-level layered structures in ionic liquids and concentrated electrolytes, interfacial orientational ordering of common polar liquids such as water, and the effects of electrolyte confinement in pores down to the nanoscale. These effects are not captured in applications of standard continuum theories for dilute electrolyte solutions, but are essential in accurately describing the equilibrium and nonequilibrium properties of electrolytes at charged interfaces. The key feature of the theories explored in this thesis is the inclusion of microscopic physics using formulations of non-local electrostatics, which encode additional microscopic length scales of discrete molecules, ions, and cofinement geometry into the theory.

Thesis Supervisor: Martin Z. Bazant
Title: E. G. Roos (1944) Professor of Chemical Engineering
Professor of Mathematics

Acknowledgments

My PhD has been a long and arduous journey, including rough terrain and also spectacular views. Now, reflecting on my years spent at MIT, I can confidently say that I would not have made it through the years of learning, research, and teaching without my support network of friends, family, mentors, mentees, and collaborators. I spent many years studying the microscopic details of the electrical double layer, but ultimately, the main lessons I take away from my PhD have to do with working with and communicating to *people*. At the end of the day, I feel so grateful to have met an incredible set of people during my time at MIT who helped me have fun, who challenged me to grow, and who enabled me to achieve my professional dreams. I would like to specifically thank:

- My advisor, Prof. Martin Bazant. Martin gave me a lot of freedom to follow my interests in research, and always had useful insights as I navigated through various topics. He has a very critical approach to science, and yet, he has been one of the biggest champions of my scientific and professional accomplishments. Due to Martin's constant excitement and energy, I have always left meetings with Martin reinvigorated and re-convinced of the significance of my work. I also am inspired by Martin's approach to teaching, where he has pushed the frontier of mathematical training in chemical engineering.

- Prof. Alexei Kornyshev. Luckily, I was able to visit Alexei at Imperial College London three times over the course of my PhD, and I ultimately worked closely with Alexei on a majority of the topics in my thesis. Alexei pays attention to the details and challenged me to communicate complex mathematical concepts with clear physical intuition. He has taught me so much about how to conduct and how to communicate scientific work.

- My thesis committee members and mentors: Daniel Blankschtein, Jörn Dunkel, and Maggie Qi. The helpful feedback and advice from the committee really set me on course to complete my PhD, as well as to develop my academic vision for the future.

- My colleagues in the Bazant group. Especially, Michael McEldrew and Amir Levy helped train me as a theoretician when I joined the group without any experience. They were always open to discuss research ideas or to teach me new concepts for our research

that overlapped. I also learned a lot from others in the group, including Mohammad Mirzadeh, Daniel Markiewitz, Emily Krucker Velasquez, Alex Cohen, Debbie Zhuang, Hongbo Zhao, Supratim Das, Dimitrios Fraggedakis, Huanhuan Tian, Mo Alkhadra, Tingtao Zhou, Joey Gu, and others. The community in the group allowed me to have deep scientific discussions and also to find distractions when I needed to take breaks. Further, thank you to my undergraduate research mentee, Nathanael Assefa, who trusted me to design/guide his project on electrokinetic transport and then diligently worked to carry out the research tasks.

- Collaborators in the Center for Enhanced Nanofluidic Transport (CENT): Dr. Alex Noy, Prof. Narayana Aluru, Prof. Zuzanna Siwy, Jake Polster, Dr. Ahn Pham, Fikret Aydin, Cody Ritt, Prof. Mark Reed, Prof. Menachem Elimelech, Rahul Misra, Prof. Daniel Blankschtein, Samuel Faucher, Matthias Kuehne, Volo Koman, Diane Rigos, Zhe Zhang, Joel Martis, Kyle Sendgikoski, Prof. Arun Majumdar, Prof. John Cumings. CENT has been such a blessing for me to work on cool applications of my theoretical analyses and to discuss ideas with intelligent and motivated scientists around the country.

- My collaborators around the world: Aymar de Lichtervelde, Zac Goodwin, Karina Pivnic Gregor Essert, Marko Tesanovic, Amit Shocron, Prof. Alexei Kornyshev, Prof. Michael Urbakh, and Prof. Sonja Berensmeier. It was amazing to be able to travel to England, Germany, and Israel to meet you all and to work on interesting theoretical and applied problems. Also, a thanks to our collaborators at MIT Chun-Man Chow and Prof. Rohit Karnik.

- Barbara Balkwill and Adrienne Bruno, who helped organize the administrative details for our research group. Your encouraging conversations and positive outlook really brightened my day every time I stopped by your offices.

- Fall 2018 and Fall 2020 10.50 classes, and the course teams, including Prof. Bill Deen, Prof. Martin Bazant, Joey Gu, Nathan Corbin, Huanhuan Tian, Chun-Man Chow, and Mo Alkhadra. I loved being involved in teaching my favorite class in chemical engineering, and I learned a ton by teaching both in-person and remote during the pandemic.

- My friends who have helped me enjoy my time in Boston, including joining the ChemE Hockey team, learning how to ski, running in races around town, and more.
- My extended family around the world, including my parents, siblings, cousins, aunts, and uncles who have always been there for me despite how spread out we all are. Within my family, I have so many role models that consistently demonstrate the value of hard work, whether it is in science or engineering, creative work, or other pursuits. You all mean the world to me!
- The Mejia family, who welcomed me into their family as one of their own and graciously hosted me for months in their home during the course of my PhD. Desde el inicio!
- My wife, Karla. Karla has helped me every step of the way during my PhD, through the best and worst of times. I love you!

Contents

List of Figures

Chapter 1

Introduction

The electrical double layer (EDL) spontaneously forms at a solid-liquid interface when ions from an electrolyte solution adsorb to/ desorb from the interface, and, in turn, counterions from the solution accumulate near the interface to neutralize the adsorbed/desorbed charge. The spatial arrangement of the screening counterion charges results from a balance between the electrostatic attraction, which pulls the counterions nearer to the surface, competing against entropy, which pushes the system to do the opposite so as to eliminate concentration gradients [8]. The EDL structure is illustrated in the schematic in Figure 1-1.

The electrical double layer is central to our understanding of various fields of science and engineering where surface phenomena are at play, including electrochemistry, colloid science, biology, tribology, membrane science, and microfluidics. For example, in biology, the double layer is crucial for cellular function, such as directing selective transport through biological ion channels [9] and mediating electrostatic interactions between charged biopolymers in physiological solutions [10]. The electrostatic interactions within electrolyte solutions can be leveraged for important biopharmaceutical separations, including advanced technologies such as ion-exchange chromatograpy for protein separations [11]. Widely applied desalination technologies such as electrodialysis operate via ionic currents through highly charged membranes using accumulation/depletion of ions in the overlapping electric double layers to achieve selectivity [12]. In electrochemical devices, the electrical double layer determines the capacitance of the interface to store charge at the solution-electrode interface [13], influencing the equilibrium and time-dependent re-

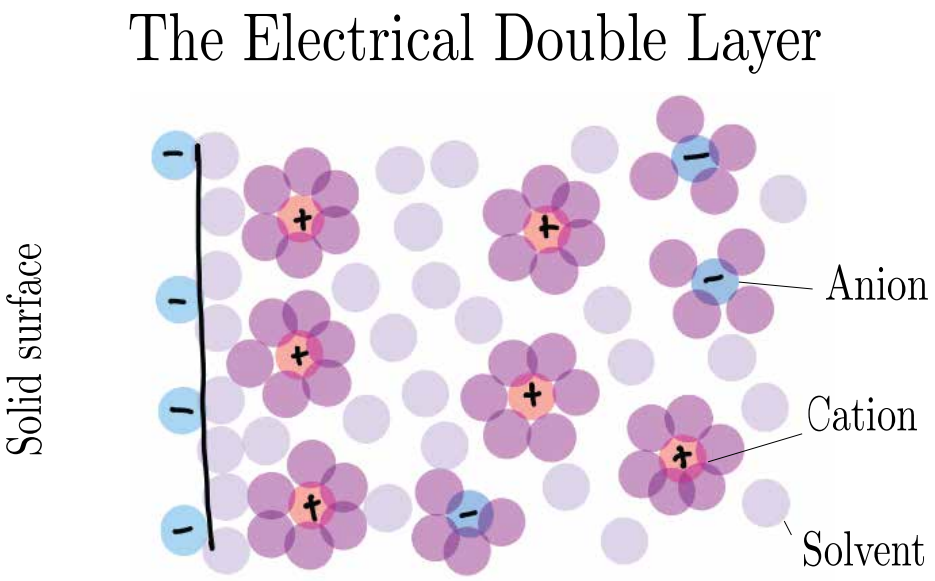

Figure 1-1: The electrical double layer at a solid-liquid interface. When in contact with a liquid, the solid surface acquires a surface charge (in this case a negative charge) due to acid/base equilibria of surface groups or the adsorption/desorption of charged ions from the solution. Counterions from solution are preferentially accumulated near the interface to neutralize the surface charge.

sponse of the device to applied potentials or electronic charges at the electrode interface. Promising microfluidic platforms for biosensing leverage electrokinetic transport driven by the response of charged fluid elements in the double layer via applied electric fields [8].

The ubiquity of the double layer in the fields of science and engineering, has spurred intense research since the end of the nineteenth century, including foundational theoretical analyses performed by Helmholtz, Gouy, Chapman, Stern, Debye, Hückel, Derjaguin, Landau, Verwey, Overbeek, Bikerman, and thousands of other researchers in various fields [14–17]. These theoretical models have converged over time to describe experimental signatures of the ionic structures near interfaces or in the bulk. To briefly summarize, the most commonly applied model, aptly referred to as the Gouy-Chapman-Stern (GCS) model, splits the double layer into two parts. First, the compact Stern layer spans from the adsorbed charge plane (the inner Helmholtz plane) to the plane of the first screening counterions (the outer Helmholtz plane), encompassing surface-oriented water molecules. Second, the diffuse part extends from the outer Helmholtz plane into the bulk, where ion concentrations vary smoothly from their accumulated/depleted concentrations near the interface to their bulk concentration further from the interface. When two surfaces are separated

by distances on the nanometer scale, the diffuse layer can overlap, leading to a screened electrostatic interaction between the surfaces mediated by the EDLs between them.

Experimental probing of the double layer structure has been especially informed by indirect electrochemical methods such as differential capacitance measurements [18]. Electrokinetic methods including electrophoretic mobility, streaming potential, or streaming current measurements provide more evidence of the double layer properties, though interpretation of these methods is very sensitive to assumptions of the no-slip plane and the compact layer contributions to surface conduction [15, 19]. Development of the surface force apparatus [20] and other surface sensitive techniques such as atomic force microscopy has allowed for more direct probing of the double layer properties.

Modern computational advances have allowed for simulations of discrete ions and solvent molecules near interfaces with varying levels of approximation, from classical Molecular Dynamics to ab initio quantum calculations. While these simulations have limitations in accessing large length and time scales, they can serve as a benchmark from which to judge the predictive accuracy of a continuum theory. Compared to experiments, atomistic simulations are especially useful as a "clean" reference system, since all inputs, i.e. force field parameters, are known explicitly. Importantly, the simulations include the structural correlations within the EDL since they explicitly represent discrete atoms or molecules. If a continuum theory can capture or approximate the structural features in an equilibrium molecular simulation, the coarse-grained continuum theory can often then be generalized to problems that the computationally-expensive molecular simulations cannot access.

Over the years, experimental and theoretical analysis has led to a wide consensus on the general principles guiding the formation, structure, and dynamics of the double layer. Nevertheless, continued discoveries and rediscoveries of discrepancies between our standard theoretical understanding and the increasingly sophisticated experimental platforms and/or molecular simulations has led to fresh and more detailed theoretical descriptions of the double layer [17].

Depending on the application, the standard GCS model can capture the essential electrochemical behavior of the interface, often despite the fact that the approximations applied do not rigorously hold. On the other hand, the standard GCS model can miss important fea-

tures of the screening at the interface. Furthermore, certain features from experiments or all atom simulations cannot be captured by the GCS model, often in practically relevant applications. For example, in the analysis of surface force measurements, empirical free energy contributions from hydration or solvation forces are often needed to fit experimental data, though they are not derived self-consistently from the double layer structure [21]. Even more surprisingly, measurements between like-charged surfaces show counter-intuitive signatures of an electrostatic attraction in the presence of multivalent counterions [22, 23]. In induced charge electrokinetics, the standard models double layers for electrokinetic flows are insufficient to describe the magnitude and the sign of flows at high applied voltage [17].

Such observations have motivated evermore sophisticated theoretical descriptions that incorporate some of the molecular nature of the electrolyte solution more directly into the theory. Due to the prominence of the double layer in science and engineering, many theoretical modifications have been proposed over the last century to more accurately capture experimental and/or discrete molecular simulation data. The accuracy of a model often scales proportionally with its complexity, and so these advanced yet highly accurate theories can be difficult to implement or interpret, thus limiting their usability versus the standard GCS approach. Therefore, the most widely used theories are those with some physical transparency and simple mathematical structure, such that they output clear scaling relations between the electrolyte/surface properties and measured variables, or allow for quick numerical implementation and inexpensive computation of such measured variables.

In this same vein, in my thesis research, I have developed theoretical approaches that address some shortcomings of standard continuum theories of the double layer, by including some of the microscopic physics of ions and solvent molecules near the interface. In doing so, I am able to improve the predictive power of the theoretical analysis to capture essential ionic electrosorption, ionic transport, and colloidal interaction mechanisms. Either by mathematical construction or mathematical approximation, I emphasize the key relationships between the microscopic length scales that arise within the EDL to the observed electrochemical behavior.

To set the stage for the presentation of my thesis research, this chapter first reviews the standard theories that are most commonly applied to EDL modeling, including the basic

mathematical models and length scales that arise there. I then highlight the microscopic physical phenomena at play in the EDL which can lead to structural differences compared to standard approaches. While these listed effects are not exhaustive, they are essential to achieving a quantitative understanding of electrochemical interfaces with meaningful physical parameters. Finally, I summarize the main thrusts of my thesis research and the organization of the thesis document.

1.1 Standard EDL Modeling Approaches

The most commonly applied model of the EDL is the Gouy-Chapman-Stern (GCS) model. As mentioned above, the GCS model splits the double layer into two regions, a compact Stern layer and a diffuse layer [16].

The Stern layer exists adjacent to the interface, between the inner Helmholtz plane defined as the plane at which the adsorbed charge is located, and the outer Helmholtz plane, defined as the distance of closest approach for ionic charges. The Stern layer itself is assumed to have no ionic charge, but instead, to include surface water molecules with no net charge. Therefore, within the model, the Stern layer is treated as a parallel plate capacitor with constant capacitance, where the surface charge density of adsorbed charge, q_s, is related to the linear potential drop through the Stern layer, $\Delta\phi_s$, by:

$$q_s = \frac{\varepsilon_s \Delta\phi_s}{L_s} \tag{1.1}$$

where ε_s is the relative permittivity of the Stern layer and L_s is the Stern layer thickness.

In the diffuse part of the double layer in the GCS theory, the mean-field electrostatic interactions of the ions with the smeared potential determine their concentration profiles emerging from the surface. The ions are treated with the Poisson-Boltzmann theory, where the potential, ϕ, satisfies the Poisson equation:

$$-\nabla \cdot (\varepsilon_r \varepsilon_0 \nabla \phi) = \rho_e = \sum_i z_i e c_i, \tag{1.2}$$

and the ions are Boltzmann distributed by the mean field electrostatic potential,

$$c_i = c_{i0} \exp\left(\frac{-z_i e\phi}{k_B T}\right). \tag{1.3}$$

In the above equations, ε_r is the relative permittivity of the solution, ε_0 is the permittivity of free space, ρ_e is the volumetric charge density, e is the elementary charge, k_B is the Boltzmann constant, and T is the absolute temperature. For each ionic species i, z_i is the valency, c_i is the local concentration, and c_{i0} is the bulk concentration of species i that is in equilibrium with the double layer. These assumptions are only valid if the ions are dilute point charges without strong spatial correlations or other non-ideal interactions. Since the “compactness" or spatial arrangement of the diffuse layer is potential-dependent, the capacitance of the diffuse layer is also dependent on the potential drop across the layer. The total capacitance of the double layer is determined by the combination of the Stern layer and the diffuse layer capacitance in series.

Typically, the solvent is only included as a constant dielectric background. In the Stern layer, experiments have pointed to a reduced effective permittivity due to dielectric saturation of the dipoles near the interface. In the diffuse part, the dielectric constant is typically assumed to be constant and equal to the bulk dielectric constant of the fluid.

While lateral patterning can be accommodated for in the theory, the surface charges of density q_s are taken to be smeared out and constant. With this assumption, the three dimensional problem can be simplified to a one dimensional problem in which all variables become uniquely a function of the normal coordinate from the interface.

The GCS model can be extended to cases where the EDLs overlap between two confining walls separated by a distance, L. In fact, the standard approach to determine colloidal stability, the Derjaguin-Landau-Verwey-Overbeek (DLVO) theory [14, 24, 25], is based on a balance between electrostatic repulsion and dispersion attraction forces. The electrostatic forces between like-charged particles are determined by the extent of double layer overlap, which generates a repulsive osmotic pressure resisting the confinement. In these situations, the confining surfaces are often assumed to have zero field, and therefore, the ionic charges are assumed to perfectly balance the surface charge. A critical phenomenon that is often

incorporated within implementations of the DLVO theory is charge regulation, where the local concentration of species is influenced by the extent of confinement, which in turn shifts the surface charge adsorption equilibrium [26].

Based on the above assumptions, the GCS theory predicts a monotonic decay of the potential from an interface. First, in the Stern layer, there is a linear drop in potential accounting for polarization of surface water molecules. Then, in the diffuse layer, the magnitude of the potential gradually decreases, with concavity determined by the local ionic charge density. Analysis of the GCS theory reveals three key length scales that characterize the double layer structure. First, the Debye length, λ_D, defined as:

$$\lambda_D = \sqrt{\frac{\varepsilon_0 \varepsilon_r k_B T}{\sum_i z_i^2 e^2 c_{0i}}} \tag{1.4}$$

determines the decay of potential from the surface into the bulk. The Debye length follows from linearization of the Poisson-Boltzmann equation, as first done by Debye and Hückel in their pioneering study on ionic activity of bulk electrolytes [27]. The linearization is most accurate at small electrostatic potentials, and so the length describes the decay of ionic concentrations towards their bulk concentration in the far-field limit. As a commonly referenced rule of thumb, the Debye length is about 1 nm in water for a concentration of c_0=0.1 M of a 1:1 ionic solution (comparable to physiological conditions) [14]. The Debye length decreases as the concentration increases, and therefore can approach the size of an individual molecule at a concentration of about 1 M or above.

The Debye length not only defines the spatial extent of the double layer, but is also influential when it comes to the interactions between charged surfaces. In the GCS model of the double layer, the overlap of double layers corresponds to an exponentially decaying electrostatic force that decays over a characteristic Debye length. Therefore, the double layer overlap when two collodial particles confine electrolytes between them is determined by a comparison between the Debye length and the distance between the confining surfaces. If the separation distance between surfaces is many times greater than the Debye length, then the surfaces do not “feel" each other, since the ions screen the surface charge independently. If the separation distance is on the order of the Debye length, then the double layers

overlap, and the screening clouds of the two surfaces merge.

At higher surface charge density and thus higher potentials, the nonlinear behavior of the ionic screening becomes important. Here, counterions with the largest valency, z, accumulate preferentially. In this limit, the decay of the counterion charge density is given by the Gouy-Chapman length, ℓ_{GC}, defined as:

$$\ell_{\mathrm{GC}} = \frac{2\varepsilon_r \varepsilon_0 k_B T}{\mid zeq_s \mid}. \tag{1.5}$$

At large potentials, the screening of the surface is dominated by the counterion density, and the Gouy-Chapman length describes the distance at which a point countercharge ineracts with the surface with energy $k_B T$.

Finally, the compact Stern layer introduces another length scale to the GCS model based on its thickness, L_s. In many cases it is useful to frame the Stern layer contribution to the double layer charge storage (i.e. capacitance) in terms of an effective thickness, δ:

$$\delta = \frac{\varepsilon_r}{\varepsilon_s} L_s. \tag{1.6}$$

The Stern layer contribution to the charge storage is dominant when the $\delta \gg \lambda_D$ and $\delta \gg \ell_{\mathrm{GC}}$, corresponding to high ionic concentration or high surface charge density.

Despite its simplicity, the GCS model and its close relatives are capable of rationalizing many data sets in a variety of applications, including electrochemical measurements of surface capacitance, transport measurements through nanopores, and colloidal stability. The model has strong predictive power up to the parameters that must be determined by fitting to experimental data. Nevertheless, the smoothly varying potential and ionic density distributions predicted by the theory may not be accurate if we zoom into the interfacial structure of the electrolyte. In the next section, I highlight the discrepancies between the smeared potential in the GCS theory and the actual potential set by discrete and ordered ions and solvent molecules near the interface or between interfaces.

1.2 Microscopic Physics of Ions and Solvent

The standard dilute-solution theories of the electrical double layer, based on the Poisson-Boltzmann theory embedded within the GCS model, cannot accurately describe the interfacial structure of electrolytes, even for many practically-relevant regimes. This fact is immediately obvious when one compares the GCS solution to predictions of molecular dynamic simulation results that include all the structural details of the electrolyte fluid.

What is missing from the theory? Evidently, the smooth charge distributions, the mean-field potential, and the often applied constant dielectric response assumed in the GCS theory are inadequate when one zooms into the scale of an individual ion or solvent molecule. Microscopic length scales arise that break the most basic assumptions of the theory. Since ions and solvent molecules are spatially correlated in a nonlocal fashion, in many cases, the microscopic interfacial stucturing requires nonlocal electrostatic theoretical approaches.

For my thesis research, I have identified four main areas where improvements to existing theoretical approaches are critical. Specifically, I studied systems that exhibit: (A) strong electrostatic correlations such as those in multivalent electrolytes, (B) highly concentrated electrolytes such as ionic liquids, (C) electrolytes under extreme confinement in pores, and (D) interfacial ordering of the molecular solvent, as sketched in Figure 1-2. I have focused on building models that can capture the unique phenomena that emerge in these regimes, as outlined below.

(A) **Strong Correlations: Multivalent Electrolytes**

While standard continuum approaches assume mean-field electrostatics, the strong electrostatic interactions between multivalent ions lead to significant electrostatic ion-ion correlation effects. These correlation effects are responsible for surprising behavior in solutions containing multivalent ions, including charge-inversion and electrostatic attraction between surfaces of the same charge. The like-charge attraction phenomenon is responsible for the strong cohesive forces in cement, where calcium ions act as a "glue" between cement calcium silicate hydrate particles. Further, the correlation-induced attraction has also been linked to packaging of DNA and the interactions of like-charged biopolymers.

Microscopically, the multivalent ions form ordered structures, eventually arranging into

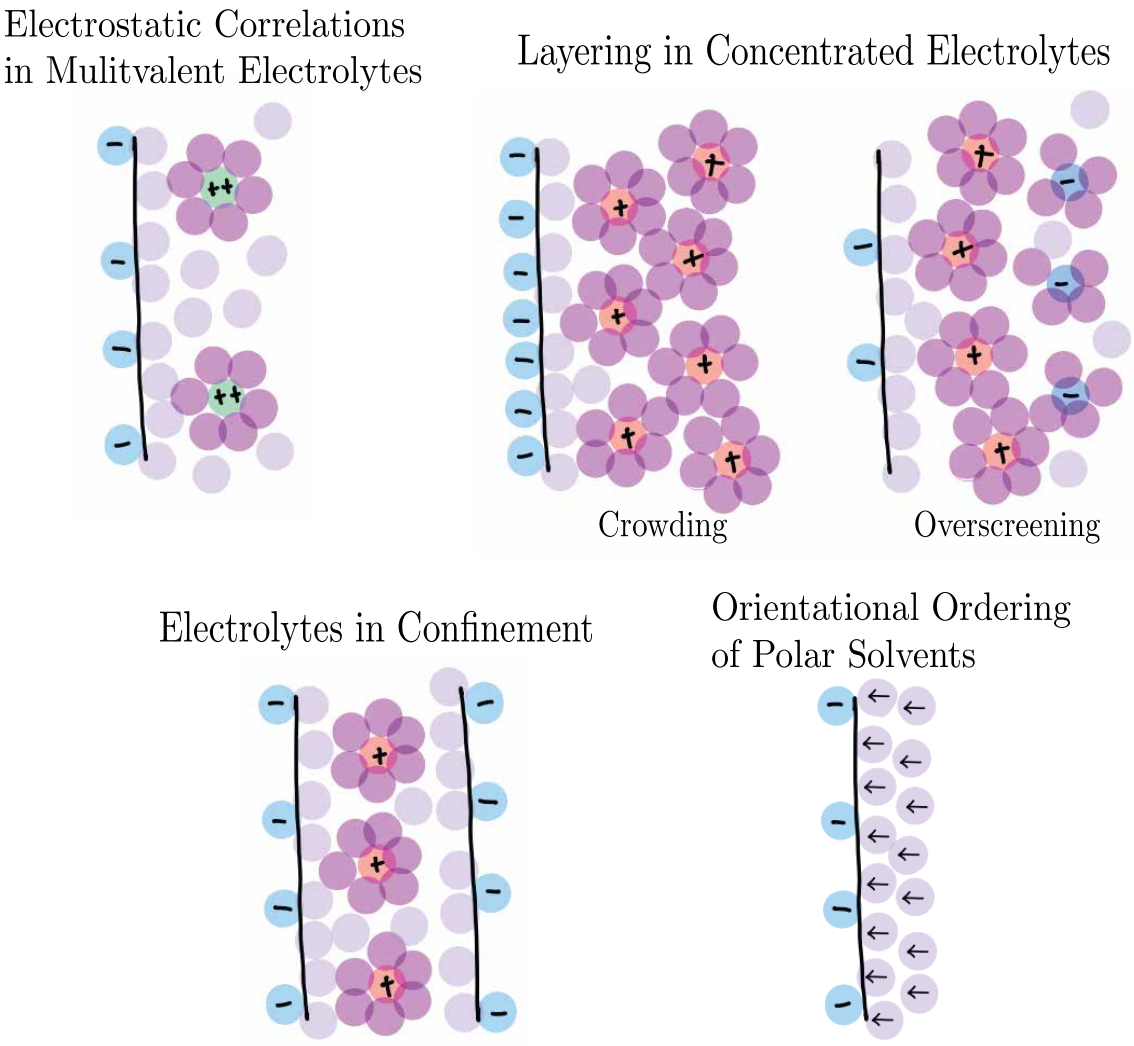

Figure 1-2: Sketches of the different microscopic physics investigated in this thesis. The topics include (A) electrostatic correlations in multivalent electrolytes, where strong electrostatic interactions lead to spatially correlated counterion positions and unique thermodynamic properties (B) layering in concentrated electrolytes, where highly concentrated counterions crowd near the interface at high surface charge density, or overscreening occurs with alternating layers of opposite charge at low surface charge density (C) electrolytes in confinement, where the bounding walls can affect the screening structure and (D) orientational ordering of polar solvent molecules, that form ordered layers at an interface, leading to overscreening in the molecular bound charge density.

a 2D crystal lattice at the contact plane, with a correlation hole size of R_{hole}.

Instead of being influenced by the mean-field potential that is assumed in the GCS theory, the multivalent counterions more strongly “feel" the potential exerted on them by the surface or by the two confining surfaces. The correlation effects can drastically affect the thermodynamics of interfacial electrolytes and ultimately the screening structure.

(B) **Highly Concentrated Electrolytes**

Due to their wide electrochemical stability and low volatility, room temperature ionic liquids and ultraconcentrated water in salt electrolytes could be effective as electrolytes for next-generation batteries and supercapacitors. Concentrated electrolytes exhibit charge layering at interfaces that differs significantly from the GCS prediction. In the highly concentrated regime, the effective Debye length becomes smaller than the ion size, d, and therefore loses its physical significance. In this limit, the phenomena of overscreening (alternating layers of opposite charge) and crowding (dense layers of the same charge) occur near charged interfaces. Such ordering has been shown to be at the ground state of a spin-glass Hamiltonian for nearest neighbor charges [28], a system that is difficult to capture accurately with continuum approaches. Extremely high concentrations result in ion pairing and ionic aggregation that can influence the transport behavior and interfacial structure [29].

(C) **Electrolytes in Extreme Confinement and Electroneutrality Breakdown**

Structuring of the electrolyte at interfaces becomes especially important as the electrolyte is confined between two surfaces or in cylindrical pore, at a length scale $R_{\text{confinement}}$. Both electrolytes with strong electrostatic and steric correlations (including multivalent and/or concentrated electrolytes) have unique properties in confinement, especially as the confinement extent goes towards the molecular scale. These confinement effects determine the interactions between two charged surfaces, or the tangential transport through a nanopore. Therefore, the confinement can be used as a tool for selective ion transport both in biological or synthetic pores.

Typical models of ionic transport in confinement make the assumption of electroneutrality–

that the number of ionic charges within a pore perfectly balances with the charge on the pore walls. The assumption is generally quite accurate for many systems encountered in engineering, but when the pore size is at the molecular scale, this assumption can fail [30]. In this regime, the electric field can escape from the pore through the pore walls, and change the electrolyte screening structure within the pore. Particularly for pores confining an electrolyte to one dimension, the effective screening length becomes exponentially long and can reach macroscopic scales, signifying that the electroneutrality assumption is broken within the pore domain.

(D) **Polar Solvent Structuring**

Virtually all electrolytes are composed of ions dissolved in polar liquid solvent. The standard approximation in continuum modelling is to represent the solvent as a structureless continuum with a fixed dielectric constant. However, near charged interfaces, the polar solvent forms alternating layers in the bound charge density (overscreening). These structures are determined by the interplay between the solvent dielectric constant, ε_r, and the solvent molecular diameter, d_w. Previous simulations have shown that the normal component of the static dielectric tensor has singularities due to the alternating layers of charge [31]. The interfacial dielectric tensor is also highly anisotropic, since the tangential component varies less sharply than the normal component.

The structuring of the liquid can lead to hydration forces that are not captured in standard DLVO theories of colloidal interactions [32]. Instead, they are usually input empirically as a separate interaction contribution. The orientational ordering for water extends about 1 nm from an interface, comparable to the Debye length at 0.1 M concentration, and can therefore be a significant contribution to the interactions between surfaces at physiological ionic concentrations. Furthermore, the preferential surface orientation ordering of water has been linked to the electrochemical behavior of interfaces.

It should be noted that these mechanisms are by no means exhaustive. In fact numerous other phenomena are at play, including but not limited to: image charge effects, polarization effects, quadropolar and higher order effects, ion solvation, electronic effects, surface roughness, and more. Nevertheless, the models reported in this thesis could be extended

to include other important physical mechanisms for the arrangement of solvent and ions at interfaces.

1.3 Thesis Organization

In this thesis, I outline the main progress I have made in including the microscopic physics of the EDL into continuum models of the EDL. Certainly, a large body of literature exists on each of these microscopic mechanisms of EDL interfaces, and I review these works in each chapter as the models are introduced. Specific emphasis is placed on identifying the main length scales that arise within the EDL when the microscopic physics is taken into account.

In Chapter 2, with Prof. Martin Bazant, I investigate the role of electrostatic correlations in multivalent electrolytes on the charge screening structure and colloidal interactions at interfaces [33]. In order to study correlation effects, I built upon the Bazant-Storey-Kornyshev (BSK) theory [34]. The BSK theory is a continuum representation of electrostatic correlations using a nonlocal effective permittivity. It is especially popular due to its simple mathematical form that is quite similar to more standard continuum theories. While the originally proposed theory explained some important qualitative features of ionic screening in concentrated ionic liquids and multivalent electrolytes, the authors only postulated the form of the boundary condition for the theory and the key correlation length parameter. The quantitative predictions of the theory were especially sensitive to the chosen correlation length and boundary condition. I derived the stress tensor for the BSK theory. I used the stress tensor to describe a physical boundary condition for mechanical equilibrium at a surface, and developed approximations for the correlation length via comparisons to previously published simulations, where I found that the correlation length scales most prominently with the correlation hole size:

$$R_{\text{hole}} = \left(\frac{1}{6}\right)^{1/4} \left(\frac{ze}{q_s}\right)^{1/2}. \tag{1.7}$$

By comparison to simulations of primitive model electrolytes, I also propose a correlation

length scaling relation that captures screening structures at higher concentrations.

I showed that the theory could reproduce ionic profiles for infinitely dilute multivalent electrolytes at isolated charged surfaces or between two charged surfaces from weak, intermediate, and strong coupling, where coupling is a measure of correlation effects. I also applied the theory to multivalent ions around charged cylinders. Effectively, this work closed some important unanswered questions for the BSK theory with physical justifications to improve the theory's quantitative predictions. Working with Dr. Rahul Misra and Prof. Daniel Blankschtein, we applied the theory to understand the strong attractive electrostatic correlation forces in cement pastes [23].

In Chapter 3, working with Dr. Zachary Goodwin, Dr. Michael McEldrew, Prof. Alexei Kornyshev, and Prof. Martin Bazant, I developed a model that captured the interfacial layering in the concentrated limit of ionic liquids by representing the ions as charged-shells [7]. The model predicted the fine, discrete layered features that were not given by the BSK model for ionic liquids. We showed that the model could capture the main features of ionic screening in the concentrated limit as well as the capacitance from low to high electrode surface charge. We analytically derived a long wavelength screening length that governs the decay of charge layers of molecular size for the concentrated limit:

$$\lambda_S = \frac{d^2}{12\lambda_D}. \tag{1.8}$$

that actually increases in magnitude with increasing ionic concentration. Along with the charge screening, we found a length that governs the decay in oscillations of the total number density of the liquid, λ_M, which depends on the fluid filling fraction, η:

$$\lambda_M = \frac{d\sqrt{(4-\eta)\eta}}{\sqrt{5}(1-\eta)^2}. \tag{1.9}$$

Further, working with Dr Karina Pivnic, Prof. Michael Urbakh, Prof. Martin Bazant, and Prof. Alexei Kornyshev I have worked on using the model to determine the role of ionic size asymmetry in the structural forces for confined ionic liquids [35].

In Chapter 4, I highlight the role of dimensionality of confinement on the screening

structure for electrolytes in nanopores. My colleague in the Bazant research group, Dr. Amir Levy, discovered the phenomenon of electroneutrality breakdown in 1D confinement [30]. I contributed to our original study on electroneutrality breakdown for single pores, where we showed that the effective screening length in 1D confinement diverges exponentially with increasing concentration:

$$\lambda_S \propto d \exp\left[\left(\frac{\lambda_D}{R_{\text{confinement}}}\right)^2\right], \tag{1.10}$$

such that the argument of the exponential function scales inversely with the ion concentration. When this exponentially long screening length exceeds the axial length of the pore, the ionic charge within the pore does not balance the charge on the pore walls–signifying that the electroneutrality within the pore is broken. The violation of electroneutrality within the pore is counter to most models of ionic conduction for engineered membranes. However, in the literature describing transport through biological pores, the electroneutrality constraint is rarely invoked. Instead, the transport of ions through ion channels is described as ions traversing a free energy landscape specific to each ion. The electroneutrality breakdown phenomenon motivates such models in biological pores that confine the ions in one dimension, since the transport is not beholden to the electroneutrality constraint in these pores. Instead, the occupancy of the pore is determined by specific chemical interactions of ions within the pore.

Then, I outline how closely-spaced, neighboring pores interact in the limit of electroneutrality breakdown [36]. Since electroneutrality breakdown corresponds to electric field escape from the pore, the electric fields between neighboring pores strongly interact and determine the screening within each pore. The pore interactions, are a useful tool to distinguish the electroneutrality breakdown phenomenon compared to other competing phenomena for low concentration electrolytes.

In Chapter 5, working with Prof. Alexei Kornyshev and Prof. Martin Bazant, I describe a model based on the non-local charge distribution in a polar solvent molecule and the properties of the solvent, where I was able to capture the dielectric tensor singularities and anisotropy of the interfacial solvent [35]. Collaborating with Prof. Alexei Kornyshev, I

applied the model to calculations of hydration interactions and capacitance. Additionally, I derived an analytical formula describing the decay of solvent ordering from an interface that depends only on the bulk properties of the solvent:

$$\lambda_h = d\sqrt{\frac{\varepsilon_r - 1}{6}} \tag{1.11}$$

Comparisons to the literature and MD simulations carried out by the Dr. Karina Pivnic with input from Prof. Michael Urbakh suggest that the model can capture the charge ordering in interfacial and confined polar liquids.

In order to make the thesis document more focused, I have primarily included the work specifically describing the structuring of the EDL. In my thesis research, I have also studied various applications of EDL theories, including modeling: pH sensors [37], the thermal signatures of double layer charging in neurons [38], the nonlinear transport of ions through ultrathin membranes such as graphene membranes [39], the ionic associations in ultraconcentrated electrolytes at interfaces [40], the thermodynamics of charge regulation reactions using temperature-resolved nanopore transport, the electrokinetic transport of multicomponent electrolytes through nanopores, and the ionic concentration and voltage dependent wetting of hydrophobic nanopores [41].

The theoretical models I explore in this thesis illustrate the importance of mathematical models of electrolytes that go beyond the standard assumptions of the GCS theory. In order to qualitatively describe the structuring of electrolytes at charged interfaces and within charged pores with mathematical models, one must employ nonlocal models of crowding and electrostatics for ions and solvent,and consider the role of the interfaces on the screening structure in pores.

Chapter 2

Electrostatic Correlations in Multivalent Electrolytes

The following chapter is reproduced from published work describing a model of electrostatic correlations in multivalent electrolytes [33] with Prof. Martin Z. Bazant, and from our collaborative paper [23] with Dr. Rahul Misra and Prof. Daniel Blankschtein building a model to capture unique electrostatic correlation-derived surface forces in multivalent electrolytes.

2.1 Overview

The standard model for diffuse charge phenomena in colloid science, electrokinetics and biology is the Poisson-Boltzmann (PB) mean-field theory, which breaks down for multivalent ions and large surface charge densities due to electrostatic correlations [1]. In this chapter, I formulate a predictive continuum theory of correlated electrolytes based on two extensions of the Bazant-Storey-Kornyshev (BSK) framework: (i) a physical boundary condition enforcing continuity of the Maxwell stress at a charged interface, which upholds the Contact Theorem for dilute primitive-model electrolytes, and (ii) scaling relationships for the correlation length, for a one-component plasma at a charged plane and around a cylinder, as well as a dilute z:1 electrolyte screening a planar surface. In these cases, the theory accurately reproduces Monte Carlo simulation results from weak to strong coupling,

and extensions are possible for more complex models of electrolytes and ionic liquids.

Additionally, aqueous electrolyte solutions containing multivalent ions exhibit various intriguing properties, including attractions between like-charged colloidal particles, which result from strong electrostatic correlations. On the contrary, the classical Derjaguin-Landau-Verwey-Overbeek (DLVO) theory of colloidal stability, based on the PB mean-field theory, always predicts a repulsive electrostatic contribution to the disjoining pressure. In this chapter, I include theoretical predictions of the BSK theory for surface forces, which shows that the contribution to the disjoining pressure resulting from electrostatic correlations is always attractive, and can readily dominate over entropic-induced repulsions for solutions containing multivalent ions, leading to the phenomenon of like-charge attraction. Ion-specific short-range hydration interactions, as well as surface charge regulation, are shown to play an important role at smaller separation distances, but do not fundamentally change these trends. The theory is able to predict the experimentally observed strong cohesive forces reported in cement pastes, which result from strong electrostatic correlations involving the divalent calcium ion.

2.2 Continuum Theory of Electrostatic Correlations

2.2.1 Introduction

Electrostatic correlations can significantly affect the structure and thermodynamic properties of the electrical double layer [42, 43], resulting in qualitative differences from mean-field Poisson-Boltzmann (PB) theory, such as like-charge attraction [22,23] or over-screening of surface charge. Critical applications in biology, colloids, separations, or electrochemistry rely on or operate in the regime where correlation effects are active [42, 43].

Numerous models have been proposed to capture electrostatic correlations, typically with a complicated mathematical structure. Outwaithe derived a modified Poisson Boltzmann models to account for the fluctuation potential of a single ion interacting with a charged wall [44]. The hypernetted chain approximation and mean spherical approximation closure to the Ornstein-Zernike equation require solving integral equations involving

the direct correlation functions of bulk charged spheres [45–48] for the equilibrium structure. Further work based on classical Density Functional Theory determines equilibrium properties based on the minimization of an integro-differential free energy functional. Kierlik and Rosinberg implemented a model (termed the bulk fluid model [49]) which captures correlations based on an perturbative expansion of density with direct correlation functions as an input from the mean spherical approximation [50]. Voudkavinova et al. analyzed the accuracy of two other related density functional theories (reference fluid density [51], functionalized mean spherical approximation [52], and bulk fluid [50, 53]) in comparison to Monte Carlo simulations, finding the reference fluid density approach to be most accurate [49]. These theories implement the accurate Fundamental Measure Theory functional developed by Rosenfeld to describe excluded volume effects [54, 55]. The additional electrostatic interactions beyond mean field are included in the excess free energy separately, without any modification to the mean-field electrostatic part of the free energy.

While these approaches often produce accurate density profiles, they can be involved to implement to a broad range of applications, for different geometries or dynamic problems, especially compared to the classical PB theory. To our knowledge, they also have not yet been shown to recover the correlated behavior of the counterion-only limit for counterions of infinitesimal size. A simpler mathematical structure could help with the application and interpretation of electrostatic correlations to a wider class of problems in physics, including electrokinetics, colloidal interactions, and electrochemical transport/reactions.

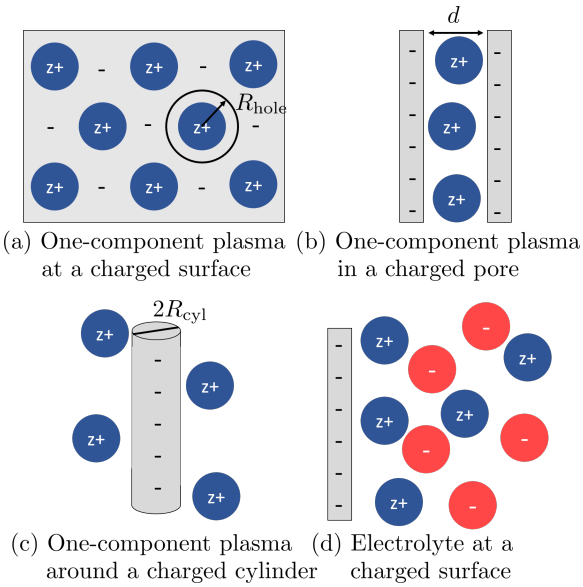

(a) One-component plasma at a charged surface (b) One-component plasma in a charged pore

(c) One-component plasma around a charged cylinder (d) Electrolyte at a charged surface

Figure 2-1: The scenarios considered in the application of the BSK theory.

Bazant, Storey and Kornyshev (BSK) proposed a continuum framework to account for the nonlocal dielectric permittivity of ionic liquids resulting from ion-ion or electrostatic

correlations [34] with a simple mathematical structure, building on intermediate coupling approximations of Santangelo [56] and Hatlo and Lue [57] for the one-component plasma. The model captures correlations based on expansions in terms of *electric field*, rather than ion density, in the free energy functional which leads to a higher-order Poisson equation. In so doing, the electrostatic correlations are included self-consistently in the definition of the electrostatic potential whose gradient determines the electrostatic force on an ion in the diffuse layer. The BSK theory provides a simple framework to predict charge density oscillations and over-screening phenomena in a variety of electrokinetic , electrochemical, biophysical, and colloidal phenomena in electrolytes and ionic liquids. The equations require a similar level of complexity to solve compared to the PB theory, which allows them to be applied to a broad group of applications. The theory was used to describe electrosmotic [58] and electrophoretic mobility [59] reversals in multivalent and concentrated electrolytes, as well as electroconvective instabilities in ionic liquids [60]. It was also applied to the dynamics [61–65] and electrosorption [66–69] at electrochemical interfaces for ionic liquids and concentrated solvent-in-salt electrolytes, including storage [70] and transport [71] in nanoporous media. Electrostatic correlations have a profound effect on colloidal interactions [23, 72, 73], where they can induce like-charge attraction in multivalent electrolytes, also predicted by the BSK theory. The activity and solvation energy of electrolytes at high concentration was also studied including the electrostatic correlation effect [74–78] as well as the extent of ion pairing in confinement [79]. Finally, the electrostatic correlations given by the BSK theory were important in describing the conduction through biological ion channels [9, 80–83]. Despite the numerous applications, fundamental questions remain about the proper boundary conditions and correlation length required to complete the BSK theory.

Here, we show that the appropriate boundary constraint for the higher-order Poisson equation is based on an interfacial stress balance. With corrected boundary conditions, the BSK theory becomes exact in the strong and weak coupling limits for the one-component plasma, and agrees with Monte Carlo (MC) simulations in intermediate coupling. We also suggest scaling relationships for the correlation length without steric constraints in one-component plasma and in multivalent electrolytes, for all the scenarios in Fig. 2-1. We

show how the correlation length can have a simple physical interpretation based on the correlation hole size of counterions at a charged surface. Although generalizations are possible, we restrict the analysis to a restricted primitive electrolyte with hard, spherical ions of equal size in a constant permittivity, ε, medium and smeared out surface charge density, q_s, and neglect all concentrated-solution effects, so as to isolate electrostatic correlations.

2.2.2 Theory of electrostatic correlations

The BSK free energy functional is given by:

$$\begin{aligned} G = \int_V d\mathbf{r} \left\{ g + \rho\phi - \frac{\varepsilon}{2} \left[(\nabla\phi)^2 + \ell_c^2 \left(\nabla^2\phi\right)^2 + \dots \right] \right\} \\ + \oint_S d\mathbf{r_s}\, q_s \phi. \end{aligned} \tag{2.1}$$

Here, $g = (H - TS)/V$ is the enthalpy and entropy density, ρ is the charge density, and ϕ is the electrostatic potential. For simplicity, the free energy is truncated after the first correlation contribution, although higher order terms can be considered [57]. While the original authors performed a gradient expansion to arrive at Eq. 2.1 [34, 58], the mathematical procedure is equivalent to modifying the interaction potential between ions from $U_{\alpha\beta}(r) = z_\alpha z_\beta \ell_B \mid r \mid^{-1}$ to $U_{\alpha\beta}(r) = z_\alpha z_\beta \ell_B \mid r \mid^{-1} (1 - e^{-|r|/\ell_c})$ [56, 63]. The modified interaction potential is solved in the mean-field limit. Thus the BSK theory is a phenomenological correction to PB within the mean-field approximation, by subtracting out interactions with smeared out charges within a correlation length ℓ_c, which should scale as the size of the correlation hole. The modified Poisson equation results by finding the extremal of the functional ($\frac{\delta G}{\delta \phi} = 0$):

$$\varepsilon(\ell_c^2\nabla^2 - 1)\nabla^2\phi = \rho. \tag{2.2}$$

Eq. 2.2 is a statement of Maxwell's equation, $\nabla \cdot \mathbf{D} = \rho$ where the displacement field is $\mathbf{D} = \hat{\varepsilon}\mathbf{E}$ with a non-local permittivity operator $\hat{\varepsilon} = \varepsilon(\ell_c^2\nabla^2 - 1)$ applied on the electric field, $\mathbf{E} = -\nabla\phi$, in a medium of constant permittivity, ε. PB theory is recovered when $\ell_c = 0$. Note that the definition of electrostatic potential itself has changed by adding the higher

order correlation terms, without violating Maxwell's equation. In other words, the potential that determines the energy of an ion in the double layer must satisfy $\nabla \cdot (\hat{\varepsilon}\mathbf{E}) = \rho$ rather than $\nabla \cdot (\varepsilon\mathbf{E}) = \rho$. In this way, the electrostatic correlation contribution to the electrostatic energy for an ion is included self consistently within the electrostatic framework, rather than being added as additional corrections in the excess chemical potential. An advantage of this approach is that the electrostatic force per unit charge of an ion is captured directly with $\mathbf{E}$, meaning that the diffuse electric potential ϕ here could be measured experimentally at an electrode (if also accounting for the potential drop in the Stern layer).

The charge density at equilibrium, $\rho = \sum_i z_i e c_i$, will be determined by the constraint that the electrochemical potential for each ion is a constant at equilibrium. The electrochemical potential can be defined as the variation of the Gibbs free energy with respect to concentration [84], $\mu_i = \frac{\delta G}{\delta c_i}$, or

$$\mu_i = \mu_i^{\theta} + kT\ln(c_i) + z_i e\phi + \mu_i^{\mathrm{ex}} \tag{2.3}$$

where the first term is a reference value, the second term is the ideal entropy contribution, the third term is the electrostatic potential contribution, and the fourth term is the excess electrochemical potential.

The first open question in applying BSK theory is that of additional boundary conditions, beyond Maxwell's equation $\hat{n}\cdot\mathbf{D} = q_s$. Presumably, the boundary condition must take care of the unaccounted short-range part of $U_{\alpha\beta}$. In the original BSK formulation and all subsequent works, the boundary condition of $\hat{n}\cdot\nabla^3\phi = 0$ was applied, with the justification that the correlation term should disappear at the interface at the distance of closest approach of the ions [58, 59, 62–67, 71, 72, 79, 80, 85, 86]. The theory provided reasonable agreement to simulation and experimental results for ionic liquids and multivalent electrolytes. However, the boundary conditions have not yet been proved or validated systematically.

The second open question is the choice of correlation length, which has been arbitrarily set to the Bjerrum length for electrolytes [34,59], and the ion diameter for ionic liquids [34]. The theory is ultimately very sensitive to the choice of boundary conditions and correlation length. Here, we analyze the boundary condition in terms of a stress balance at the interface

and then validate ℓ_c by comparison to MC simulations.

Interfacial balance

Applying the Gibbs-Duhem equation at constant temperature to the electrolyte and screened surface charges, following [17], and neglecting the external electrostatic work done on the system, gives $dP = \sum_i c_i d\mu_i$. Taking the gradient in three-dimensional space and applying the definition of the electrochemical potential:

$$-\mathbf{f} = \nabla P = kT \sum_i \nabla c_i + \rho \nabla \phi + \sum_i c_i \nabla \mu_i^{\text{ex}}, \tag{2.4}$$

where $\mathbf{f}$ is the total thermodynamic force. The first and third terms on the RHS of Eq. 2.4 correspond to the gradient of osmotic pressure, $\nabla\Pi$. For an ideal solution, μ_i^{ex}=0. The gradient of the defined thermodynamic pressure is equivalent to the divergence of the total stress tensor of the electrolyte system, $\mathbf{f} = \nabla \cdot \tau$. The total stress tensor is composed of an osmotic pressure component, Π and a Maxwell stress tensor, τ_e, such that $\tau = -\Pi \mathbf{I} + \tau_e$. The component of interest in this analysis, τ_e, can be defined by:

$$\nabla \cdot \tau_e = \rho \mathbf{E} = \nabla \cdot (\hat{\varepsilon} \mathbf{E}) \mathbf{E} \tag{2.5}$$

in a constant ε medium. Plugging in for the charge density using the BSK Eq. 2.2 and performing integration by parts, one arrives at an expression for the Maxwell stress tensor for a fluid with a non-local permittivity,

$$\begin{aligned} \tau_e = & \varepsilon \mathbf{E}\mathbf{E} - \frac{1}{2}\varepsilon \mathbf{E}^2 \mathbf{I} + \varepsilon {\ell_c}^2 \Big[\left(\mathbf{E} \cdot \nabla^2 \mathbf{E}\right) \mathbf{I} - \mathbf{E} \left(\nabla^2 \mathbf{E}\right) \\ & - \left(\nabla^2 \mathbf{E}\right) \mathbf{E} + \frac{1}{2} \left(\nabla \cdot \mathbf{E}\right)^2 \mathbf{I} \Big], \end{aligned} \tag{2.6}$$

as derived in the Supporing Information. While the above equation was derived for constant ε and ℓ_c, the expression is identical if these parameters vary. For varying ε or ℓ_c, the Korteweg-Helmholtz force density must be included in the electrostatic stress [87],

$$\nabla \cdot \tau_e = \rho \mathbf{E} - \frac{1}{2} \mathbf{E}^2 \nabla \varepsilon + \frac{1}{2} (\nabla \cdot \mathbf{E})^2 \nabla (\varepsilon {\ell_c}^2). \tag{2.7}$$

Within the distance of closest approach of the ions to the surface, correlations cannot affect the value of the Maxwell stress at the surface, $\tau_{e,\text{surf}}$, generated by the surface charge density. The mechanical equilibrium problem therefore requires continuity in the electrostatic stress tensor evaluated in the solution and at the surface,

$$\tau_e - \tau_{e,\text{surf}} = 0. \tag{2.8}$$

At a uniformly-charged, flat surface without a dielectric jump, the Maxwell stress tensor is simply $\tau_{e,\text{surf}} = {q_s}^2/(2\varepsilon)\hat{n}\hat{n}$, while the Maxwell stress tensor in the electrolyte is given by Eq. 2.6. Equating these two expressions, and substituting in $\hat{n}\cdot\mathbf{D} = q_s$ we arrive at a final boundary for a potential varying in one coordinate direction:

$$\hat{n}\cdot\ell_c\nabla^3\phi = \nabla^2\phi\Big|_S \tag{2.9}$$

applied at the distance of closest approach of the ion with the wall.

The method amounts to applying the Contact Theorem to the correlated electrolyte in the absence of correlations, shown below for $\mu_i^{\text{ex}} = 0$ at a flat electrode with constant charge density without a dielectric jump [88, 89]:

$$P = -\frac{q_s^2}{2\varepsilon} + kT\sum_i c_i\Big|_S = -\hat{n}\cdot\tau_e\cdot\hat{n} + kT\sum_i c_i\Big|_S. \tag{2.10}$$

The Contact Theorem is a statement of mechanical equilibrium, where the repulsive osmotic pressure contribution is balanced by the electrostatic attraction from the Maxwell stress. Without the constraint from Eq. 2.8, the BSK theory does not obey this simple relationship which should be valid even for dilute electrolytes in the primitive model [1,90,91]. The procedure of ensuring continuity in the Maxwell stress can be repeated for any higher order $\hat{\varepsilon}$ by equating the τ_e at successive orders of derivatives. The condition in Eq. 2.8 is also applicable to any extended electrolyte mean-field theory with arbitrary models of concentrated solution activity and solvent polarizability, including interactions with a soft wall. The approach may even be extended to media with non-local dielectric constant $\hat{\varepsilon}$ driven by solvent polarization [92, 93].

Correlation length scaling

At a highly charged surfaces, the charge-charge correlations are dominated by the mutual repulsion of counterions at the interface, as demonstrated in the schematic in Fig. 2-1(a). The size of a correlation hole of counterions forming a Wigner crystal is characterized by a length scale R_{hole}:

$$R_{\text{hole}} = \left(\frac{1}{6}\right)^{1/4} \left(\frac{ze}{q_s}\right)^{1/2}, \qquad (2.11)$$

where z is the ion valency and e is an elementary charge. For this work, we assume that the correlation length scales as the size of a correlation hole, determined by the surface charge denisty:

$$\ell_c = \alpha R_{\text{hole}} \qquad (2.12)$$

with one parameter α, which is considered to be a constant. We will demonstrate that the fitted scaling with $\alpha = 0.50$ works well from the limit of zero reservoir concentration (one-component plasma) to more concentrated electrolytes.

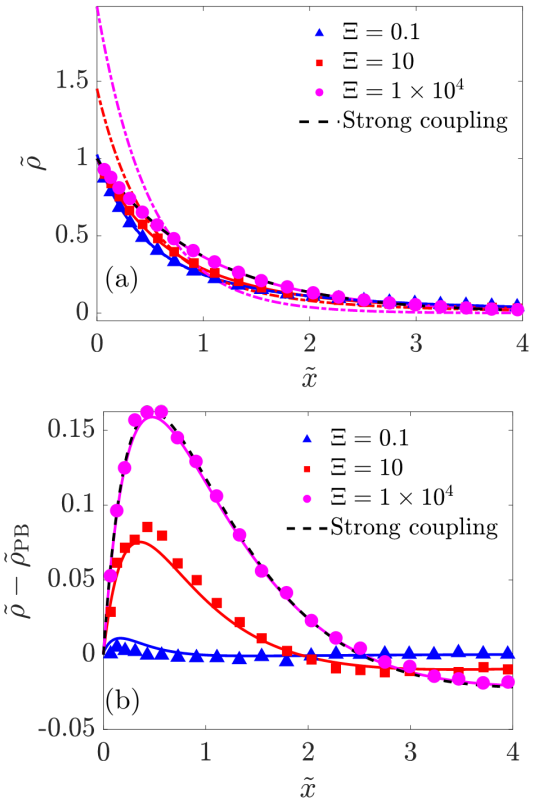

Figure 2-2: Isolated charged plate. BSK theory for one-component plasma compared to MC simulations from [1] with $\alpha = 0.50$ for counterions screening a charged isolated surface. The solid lines are the predictions of the BSK theory with the boundary condition of $\hat{n} \cdot \ell_c \nabla^3 \phi = \nabla^2 \phi \big|_S$, the dashed-dotted lines are the predictions of the BSK theory with the boundary condition of $\hat{n} \cdot \ell_c \nabla^3 \phi = 0$ and the markers are from the MC simulations. Strong coupling limits are plotted as black dashed lines. (a) The charge density is plotted as a function of distance from an isolated surface. (b) The charge density difference relative to the solution to the PB theory as a function of distance from an isolated surface.

At high concentration or at low surface charge densities, this scaling argument breaks down, and the other length scales might dominate in the correlation length. For example, if the surface charge tends to zero, then the charge-charge correlations will be dominated by the Bjerrum length and characteristic mean spacing between ions given by

the bulk concentration. At very large charge densities and for large ion sizes, where R_{hole} becomes comparable to a, the ion diameter, the ion size can dominate in determining the charge-charge correlations due to over-crowding effects. Also, if other length scales are introduced, such as surface curvature, the correlation length between ions can also be affected, as demonstrated with the one-component plasma around a thin charged cylinder.

In the Supporting Information of reference [33], the non-arbitrary scaling of the correlation length is investigated by comparison to Grand Canonical Monte Carlo simulations from ref. [3] for a $z:1$ electrolyte (possessing cation of charge $+ze$ and anion of charge $-e$). Using the Buckingham-Π theorem, we know that the correlation length is related to functions of dimensionless ratios of other length scales of the problem. At small or large values of these dimensionless ratios, the functional dependence becomes a power law relationship by expanding the individual functions, which we assume in this work. Here we choose four length scales from which we can construct three dimensionless groups from: the correlation length, ℓ_c, the Gouy-Chapman length, ℓ_{GC}, the Bjerrum length, $z^2\ell_B$, and the Debye length λ_D, such that the power law relationship can be expressed as:

$$\delta_c = \frac{\ell_c}{\lambda_D} = \alpha_2 \left(\frac{z^2\ell_B}{\ell_{\text{GC}}}\right)^{\alpha_3} \left(\frac{z^2\ell_B}{\lambda_D}\right)^{\alpha_4}, \tag{2.13}$$

where δ_c is the correlation length ℓ_c divided by the Debye length. The definitions and meanings of the different length scales will be included in the Results and Discussion section as they appear in the mathematical framework.

The correlation length scaling that arises from the fitting procedure to the MC data is given by:

$$\ell_c \sim {\ell_B}^{1/4}(q_s/e)^{-1/8}{C_{\text{ref}}}^{-1/6}, \tag{2.14}$$

with a fitted scale of:

$$\delta_c = 0.35 \left(\frac{z^2\ell_B}{\ell_{\text{GC}}}\right)^{-1/8} \left(\frac{z^2\ell_B}{\lambda_D}\right)^{2/3}. \tag{2.15}$$

Note that the fitted exponents are expressed in terms of fractions to emphasize their relationship to the intrinsic length scales in the system.

A detailed investigation of how correlations are affected as a function of surface charge

density, ion valency, concentration, ion size, and surface curvature could motivate a more nuanced scaling of the correlation length, based on direct analysis of the charge-charge correlation function, including variations in the correlation length as a function of the distance from a charged surface. For example, the fitted correlation length relationship in Eq.2.15 does not return the correlation length for the counterion only system in the limit of zero ion concentration. In this work, we isolate the electrostatic correlation effects for a dilute electrolyte at highly charged surfaces. For the purposes of the analysis in the main text, we will assume the correlation length to be $\ell_c = 0.50 R_{\text{hole}}$ for all the scenarios investigated in Fig. 2-1. For the results with the fitted correlation length scaling in 2.15, one can refer to the Supporting Information of reference [33].

2.2.3 Results: One-component plasma

Considering a system of point-like counterions neutralizing a uniformly charged surface, the importance of correlations is governed by a coupling constant,

$$\Xi = 2\pi z^3 {\ell_B}^2 q_s / e, \tag{2.16}$$

which is a measure of the correlation hole size, R_{hole}, compared to the characteristic ion distance from the surface, the Gouy-Chapman length,

$$\ell_{\text{GC}} = e(2\pi z \ell_B q_s)^{-1} \tag{2.17}$$

such that $\Xi \sim {R_{\text{hole}}}^2 / {\ell_{\text{GC}}}^2$. Note that the Bjerrum length, ℓ_B is defined as the distance at which two unit charges experience an electrostatic energy equal to the thermal energy:

$$\ell_B = \frac{e^2}{4\pi\varepsilon k_B T} \tag{2.18}$$

In the weak coupling limit ($\Xi << 1$), PB theory is valid. In the strong coupling limit ($\Xi >> 1$), counterions interact with the electric potential created by the surface since ion-surface interactions dominate [1, 43, 90, 94, 95].

Now we consider applying the mechanical constraint, starting with the one-component plasma of infinitesimally small size with $\mu^{\text{ex}} = 0$. The one-component plasma consists of a single mobile ionic species which neutralizes the charge of a smeared out surface charge density. We can non-dimensionalize lengths with the Gouy-Chapman length, the potential by the thermal voltage for the counterion, $\phi_0 = \frac{kT}{ze}$, and the charge density by $\rho_0 = 2\pi\ell_B q_s^2 e^{-1}$. Here, we assume that the correlation length scales with the size of a correlation hole at the surface, $\delta_c = \ell_c/\ell_{\text{GC}} = \alpha_0\sqrt{\Xi}$ Using $\sim$ to denote non-dimensionalized variables:

$$\alpha_0{}^2\Xi\tilde{\nabla}^4\tilde{\phi} - \tilde{\nabla}^2\tilde{\phi} = 2\tilde{\rho} = 2e^{-\tilde{\phi}} \tag{2.19}$$

with boundary conditions of

$$\begin{aligned} \hat{n}\cdot(\alpha_0{}^2\Xi\tilde{\nabla}^3\tilde{\phi} - \tilde{\nabla}\tilde{\phi}) &= -2 \\ \hat{n}\cdot\alpha_0\sqrt{\Xi}\tilde{\nabla}^3\tilde{\phi} &= \tilde{\nabla}^2\tilde{\phi} \end{aligned} \tag{2.20}$$

at $\tilde{x} = 0$, where $\alpha_0 = 1.36\alpha$ is an order one constant proportional to α. Therefore, the importance of the higher order derivative is governed by the coupling parameter, Ξ.

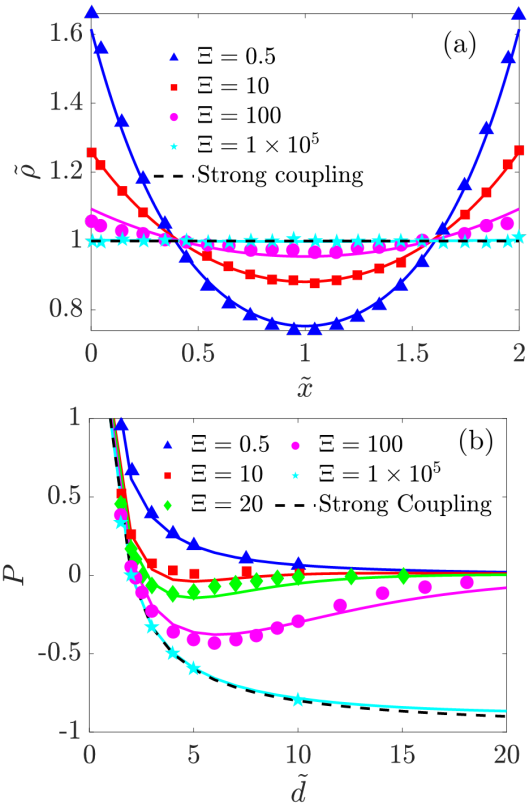

Figure 2-3: Confined geometry. BSK theory for one-component plasma compared to MC simulations of counterions between two like charged surfaces from [1] with $\alpha = 0.50$. The solid lines are the predictions of the BSK theory, and the markers are from the MC simulations. Strong coupling limits are plotted as dashed lines. (a) The charge density is plotted between two surfaces with separation $\tilde{d} = 2$. (b) The pressure is calculated as a function of separation distance between the two plates. As the coupling increases, the pressures between the like-charged surfaces become attractive (negative) rather than repulsive (positive). The dimensionless pressure is $\tilde{P} = Pe^2/(2\pi\ell_B q_s^2)$.

The solution to these equations is compared to the results of MC simulations in Fig. 2-2 for a one-component plasma screening a plane of charge. The BSK theory reproduces the behavior of the one-component plasma from weak coupling, in intermediate coupling, and matches the strong coupling limit with $\alpha = 0.50$. Furthermore, the BSK theory with

the boundary condition of $\hat{n} \cdot \nabla^3 \phi = 0$, represented by the dashed-dotted lines in Fig. 2-2a, does not accurately represent the data at intermediate or strong coupling.

We can also consider the one-component plasma between two charged surfaces of equal charge density with the same sign, confining the counterions in a gap of dimensionless distance $\tilde{d}$, as shown in Fig. 2-3a. In Fig. 2-3b, the pressure is plotted as a function of separation distances between two charged surfaces with different coupling parameters, using Eq. 2.8 and using the same value for α. The BSK theory again provides good agreement with the results of the MC simulations at all the coupling parameters.

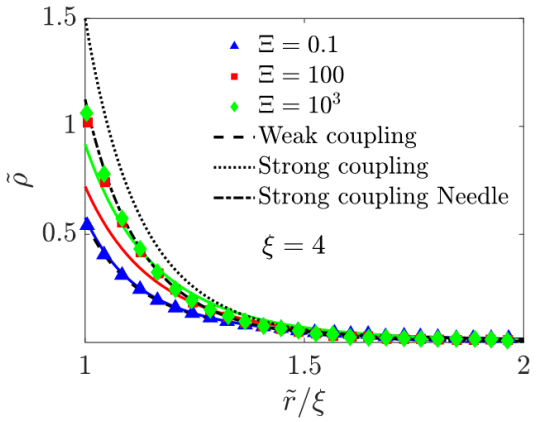

Figure 2-4: Cylindrical geometry. BSK theory for one-component plasma compared to MC simulations from [2] using $\alpha = 0.50$ for the counterion density around a charged cylinder for $\xi = 4$. The solid lines are the results of applying Eq. 2.19 and the markers are the MC simulation results from [2]. The weak coupling, strong coupling, and re-normalized strong coupling needle limits are plotted [2].

Another critical question is the validity of Eq. 2.8 at a curved interface. The simplest model system to test the hypothesis is the one-component plasma surrounding a charged cylinder of radius $\xi = R_{\text{cyl}}/\ell_{\text{GC}}$ at infinite dilution, corresponding to a cylindrical cell with outer radius $R_{\text{out}} \to \infty$. As shown in Fig. 2-4 and Supporting Information Fig. S1 in reference [33], the BSK equation reproduces the results of the weak and strong coupling limits correctly, by applying the boundary condition in Eq. 2.20 at $\tilde{r} = \xi$. However, similar to the strong coupling expansion of [96], the theory does not correctly describe the renormalization of charge arising from Manning condensation in the needle limit, where a fraction $f = 1 - 1/\xi$ of the charge is "condensed" onto cylinder [97]. The charge density must be multiplied by this fraction, f, in order to match the strong coupling expansion taking into account the charge renormalization in the needle limit [2, 98]. The smaller the radius of curvature, the more likely that the configuration of correlated ions is influenced by curvature. In the "needle limit," where $\sqrt{\Xi}/\xi >> 1$, ions are distributed in a nearly linear fashion along the cylindrical backbone with spacing

scaling as $\tilde{a} \sim \Xi/\xi$, which may also be the relevant scaling for the correlation length in this regime rather than $\sqrt{\Xi}$. Supporting Figs. S1 and S2 in reference [33] show the results choosing $\delta_c = \Xi/\xi$, but the counterion condensation transition is still not captured.

2.2.4 Results: Electrolytes

A more useful and relevant application of the BSK theory is to describe the distribution of charges in electrolytes and ionic liquids, as was originally proposed. Here, we focus on the dilute electrolyte limit, to isolate electrostatic correlations directly, without complications from overcrowding.

If the BSK equation for a z:1 electrolyte with salt concentration C_{ref} is non-dimensionalized with the thermal voltage $\tilde{\phi} = (e\phi)/(kT)$ and the Debye length

$$\lambda_D = \sqrt{\frac{\varepsilon kT}{(z^2+z)e^2 C_{\text{ref}}}}, \tag{2.21}$$

$\tilde{\nabla} = \lambda_D \nabla$ and $\delta_c = \ell_c/\lambda_D$ the BSK equation becomes:

$$\delta_c^2 \tilde{\nabla}^4 \tilde{\phi} - \tilde{\nabla}^2 \tilde{\phi} = \tilde{\rho} = \frac{z e^{-z\tilde{\phi}} - z e^{\tilde{\phi}}}{z^2+z}. \tag{2.22}$$

The boundary conditions are similarly modified to:

$$\begin{aligned} \hat{n} \cdot (\delta_c^2 \tilde{\nabla}^3 \tilde{\phi} - \tilde{\nabla} \tilde{\phi}) &= \tilde{q}_s \\ \hat{n} \cdot \delta_c \tilde{\nabla^3} \phi &= \tilde{\nabla}^2 \tilde{\phi}. \end{aligned} \tag{2.23}$$

The agreement of the predicted charge density profiles from Eq. 2.22 with the GCMC data is very good, as exhibited in Fig. 5 for a 0.1 M 2:1 electrolyte. In the Supporting Information of reference [33], the results are expanded to a more complete set of comparisons with simulations. It is seen with $\ell_c = 0.50 R_{\text{hole}}$ or with ℓ_c determined by Eq. 2.15, that the BSK theory can correct the PB charge density profiles, including an overscreening transition. Larger errors from the BSK theory are incurred at large concentration, where the current assumption of $\mu_i^{\text{ex}} = 0$ breaks down.

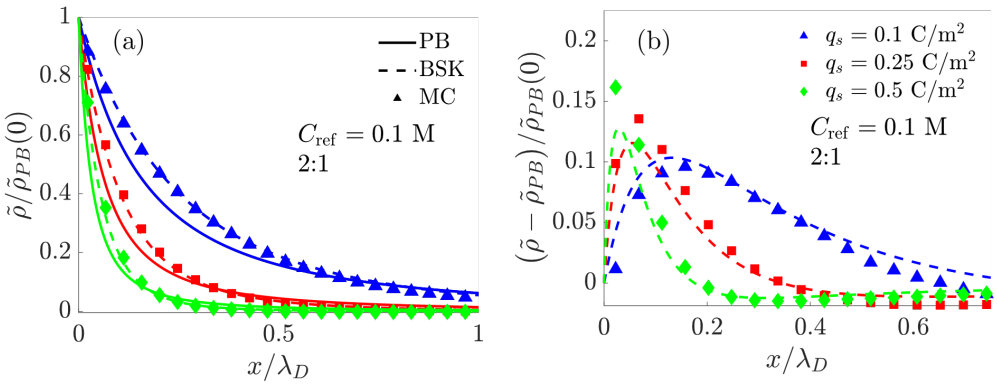

Figure 2-5: Electrolyte at an isolated plate. BSK theory for an electrolyte solution compared to MC simulations [3] of multivalent electrolytes with $\alpha = 0.50$. (a) An example of the charge density profile for a 2:1 electrolyte at 0.1 M concentration compared to the GCMC simulations and PB theory. (b) The difference between the predictions of the BSK theory and the simulations from PB theory predictions.

One implication of the boundary condition is that the differential capacitance for $\ell_c = 0$ is equivalent to the case of $\ell_c \neq 0$ if $\mu_i^{\text{ex}} = 0$. Therefore, the differential capacitance for the correlated, dilute electrolyte is given by the traditional Gouy-Chapman equation:

$$C_D = \frac{\varepsilon}{\lambda_D} \cosh\left(\frac{\tilde{\phi}_D}{2}\right), \tag{2.24}$$

in stark contrast to the original work in the limit of $\mu_i^{ex} = 0$ [34,58]. It would be interesting to explore the implications of the boundary condition on electrokinetic reversals, electrochemical interfaces, biological channels, or colloidal phenomena [58,59,62–67,71,72,79,80,85]. For example, the DLVO theory of colloidal interactions can be modified to include attractive correlation effects [23].

Further extensions of the theory

Charged Dielectric Interfaces: Note that the Maxwell stress condition (Eq. 2.6) has only been stated without a dielectric jump. The stress condition may need further validation at a dielectric interface. A more general statement of matching the Maxwell stress with and without correlations might be given by a jump condition between the two media:

$$\hat{n} \cdot [\tau_{e,1} - \tau_{e,2}] = \hat{n} \cdot [\tau_{e,1} - \tau_{e,2}]_{\ell_c = 0}. \tag{2.25}$$

For a uniformly-charged, flat interface without a dielectric jump, $\tau_{e,2} = 0$, so the RHS of the above equation reduces to $\hat{n} \cdot [\tau_{e,1} - \tau_{e,2}]_{\ell_c=0} = \frac{{q_s}^2}{2\varepsilon_1}\hat{n}$.

Concentrated Electrolytes and Ionic Liquids: The present analysis attempts to isolate the effect of ion correlations in a dilute electrolyte. Ion size effects, particularly for $a/\lambda_D > 1$ will require further validation to properly account for correlations guided by ion size combined with electrostatics, as I will show in the next chapter. A non-local free energy functional might be necessary to capture the size correlations in concentrated solutions [55, 99], in conjunction with electrostatic correlations. Short-range bulk correlations [100] are not captured in this theory. Furthermore, if surface charges are discrete rather than smeared out, the contact condition may change [101], although the boundary condition derived here could be applied to such charge density distributions. For an arbitrary mixture of ions with different valency, the effective correlation length will depend upon correlations between each pair of species, although the correlations at high surface charge density will still be dominated by the most highly charged counterion.

2.2.5 Conclusions

The phenomenological BSK theory describes non-local, discrete correlation effects with a higher-order, local, continuum description of the free energy quite well. The remarkable agreement of the theory with the one-component plasma and primitive model electrolyte suggest that higher-order, continuum equations can properly account for correlation effects, as long as the appropriate constraints are imposed at boundaries. The formalism used here could be extended to the ionic liquid limit, although ion pairing, short-range non-electrostatic correlations, and “spin glass" ordering [28] might preclude a simple continuum description. Further modifications are needed to capture the long range screening exhibited in ionic liquids and concentrated electrolytes [102], as well as density oscillations expected in overcrowded systems [55]. Even so, the BSK theory captures important features of electrostatic correlations, including like-charge attraction and overscreening, driven by electrostatic interactions of spatially correlated counterions. Furthermore, unlike many previous approaches, all the electrostatic forces are contained self-consistently within

the electrostatic potential, ϕ. Detailed analysis of experimental data is needed to determine the competing effects of surface adsorption reactions modifying fixed surface charge [103] or the overscreening/ like-charge attraction effects modeled by the BSK theory [23]. Now, in the next section, we turn to the prediction of surface forces using the BSK theory with the boundary conditions and correlation length scaling found in this section.

2.3 Surface Forces including Electrostatic Correlations

The accurate prediction of forces between charged surfaces in aqueous electrolytes is of paramount importance in diverse scientific disciplines, ranging from colloidal science to biophysics and polymer chemistry [104]. Surface forces ultimately determine whether colloidal particles, and macromolecules, such as DNA, proteins, and polymers, will aggregate or will remain stable in dispersions [105–109]. Typically, two different types of forces operate between charged surfaces in electrolyte solutions: short-range van der Waals forces, which are predominantly attractive, and long-range electrostatic forces, which can be attractive or repulsive depending on the sign and magnitude of the charge on the interacting surfaces [110–112]. The most widely used model of colloidal stability is the classical Derjaguin-Landau-Verwey-Overbeek (DLVO) theory [25, 113], in which the electrostatic contribution to the disjoining pressure (force per unit area acting on the charged surfaces) is described using the Poisson-Boltzmann (PB) mean-field theory, which assumes that the ions residing in the electric double layer (EDL) at the charged surface feel a mean electrostatic potential from the smeared out (volume-averaged) charge density near the charged surface. The PB model also assumes that the dielectric permittivity of the solvent is constant and uniform, considers ions to be point-sized, and neglects any form of electrostatic correlations. The prediction of the disjoining pressure by the DLVO theory utilizing the PB model is in very good agreement [104, 114–127] with experimental data in the so called weak-coupling limit, i.e., the limit corresponding to a low surface charge density, high solvent dielectric permittivity, low valency of counterions (those ions containing charge of sign opposite to that of the surface), or high temperature. As shown in the previous section, in the case of multivalent electrolytes, electrostatic correlations become impor-

tant due to the large valency of the counterions, and the PB model fails to describe the disjoining pressure acting between charged surfaces even qualitatively [1, 128–131]. In particular, mean-field PB theory always predicts a repulsive EDL pressure contribution for like-charged surfaces, irrespective of the magnitude of the surface charge density, the ion concentration, or the valency of the counterions. This is in stark contrast to the experimental results [5, 132–134] and Monte-Carlo simulations [1, 135–137] which have provided ample evidence of the phenomenon of like-charge attraction mediated by multivalent ions. This clear signature of electrostatic correlations is responsible for many important interfacial phenomena, including cement cohesion [5, 138], biopolymer aggregation [139], and colloidal coagulation [131, 140], and nevertheless, it still lacks a simple mathematical description.

Several theoretical approaches have been used in the past to explain like-charge attraction, including the theory by Perel and Shklovskii [141], the hypernetted-chain (HNC) integral equation theory, [135,142] and the dressed-ion theory [143,144]. Although these theoretical approaches have certainly improved our understanding of electrostatic correlations, they lack the mathematical simplicity underlying the PB theory, which allows the disjoining pressure to be directly related to various system parameters, including the salt concentration, the ion valency, the solvent dielectric permittivity, the surface charge density, and the temperature. To this end, as explained in the previous section of this chapter, a simple and general theory of electrostatic correlations based on a Landau Ginzburg-type continuum framework was recently developed by Bazant, Storey, and Kornyshev (BSK) [34], and initially used to explain screening phenomena in solvent-free ionic liquids. Compared to the PB mean-field theory, the BSK free energy functional adds an additional term containing the second derivative of the electrostatic potential to account for electrostatic correlations:

$$\begin{aligned}\mathbb{F} = &\int_V d\mathbf{r} \left\{ \rho\phi - \frac{\varepsilon}{2}\left[|\nabla\phi|^2 + l_c^2 \left(\nabla^2\phi\right)^2 \right] + g\left(c_+, c_-\right) \right\} \\ &+ \oint_S d\mathbf{r}\, q_s \phi\end{aligned} \tag{2.26}$$

where $\rho = e(z_+c_+ - z_-c_-)$ is the mean charge density, $z_\pm$ and $c_\pm$ are the valencies and concentrations of the cations and the anions, respectively, in the electric double layer of volume V, ϕ is the electrostatic potential, q_s is the surface charge density, ε is the dielectric permittivity of the solution, l_c denotes the electrostatic correlation length, and $g(c_+, c_-)$ is the entropic component of the total free energy and corresponds to the entropy density arising from the translational entropy of the ions. Note that $-\frac{\varepsilon}{2}|\nabla\phi|^2$ and $\rho\phi$ represent the self energy of the electric field and the electrostatic potential energy of the ions in this electric field, respectively. The potential gradient term, $-\frac{\varepsilon}{2}l_c^2\left(\nabla^2\phi\right)^2$, is used to model an additional contribution to the self energy resulting from electrostatic correlations between the ions. The terms excluding the entropic contribution, g, arise via a charging process in which ions are added to a system in which they interact with the electrostatic potential, ϕ. Although the higher order equation is still solved in the mean-field of spatially averaged ϕ and ρ, the higher-order third term implies the nonlocal nature of the free energy due to electrostatic correlations. One can interpret this term as a phenomenological correction to the mean-field Poisson-Boltzmann framework that is solved for in the mean field. This simple extension of the PB theory is a useful first approximation of electrostatic correlation effects in ionic liquids [60, 62, 63, 66, 71] and in so-called “water-in-salt" electrolytes [67].

The BSK model has also been applied to electrolytic solutions [58] and shown to capture various ion correlation effects, including electrophoretic mobility reversals of colloidal particles in multivalent electrolytes [59], micelle formation [73],and ion conduction through biological ion channels [81, 83, 145, 146]. The first challenge in applying the BSK theory to different systems is to find a suitable approximation of the electrostatic correlation length, l_c. In the original paper, Bazant et al. [34] suggested using the Bjerrum length, l_b, for dilute electrolytes and the ionic diameter for the opposite limit of room temperature ionic liquids (where it is typically much larger than the Debye length). In the general case of a z:1 primitive-model electrolyte, where z is the valency of the counterion, the correlation length parameter was recently found to scale as [147]:

$$l_c \sim {l_b}^{1/4}(\mid q_s \mid /e)^{-1/8}{c_0}^{-1/6} \tag{2.27}$$

where $l_b = \frac{e^2}{4\pi\epsilon k_B T}$ is the Bjerrum length [104], e is the unit of elementary charge and c_0 is the bulk salt concentration. Note that the Bjerrum length corresponds to the length scale at which the electrostatic interactions between two monovalent ions in the solution is comparable to the thermal energy, $k_B T$, where k_B is the Boltzmann constant and T is the absolute temperature. Physically, the correlation length, l_c, scales with the diameter of a correlation hole in the electrolyte, beyond which the mean-field equations are sufficient to describe the electrostatic interactions between ions, as reflected in the PB model. In this chapter, we describe electrostatic correlations using the BSK model for electrolytes, and study their influence on the disjoining pressure acting between charged surfaces.

The second challenge in applying the BSK model is the choice of an additional boundary condition for the generalized Poisson equation, a fourth order ordinary differential equation (ODE) in our one-dimensional geometries. The second order PB equation requires only one condition on each bounding surface, whereas the BSK equation requires two. Although mixed boundary conditions were first proposed [148], the standard choice, advocated by BSK for ionic liquids, has been to set the third derivative of the potential to zero, effectively cutting off electrostatic correlations at the distance of closest approach. Here, we take advantage of the recent development of more consistent and general boundary conditions, as derived in the previous section, which are obtained by equating the normal Maxwell stress at the charged surface to its form in the absence of electrostatic correlations given by the contact theorem [147].

We should stress here that the phenomenon of like-charge attraction can be modeled using solely the higher order term in the BSK functional Eq. 2.26 (see the Results section for details). However, for an accurate comparison of our theoretically predicted disjoining pressure with experimental data, we also incorporate some additional interactions, to arrive at a more complete generalization of the DLVO theory. In particular, the PB model assumes that ions are point-sized and are distributed throughout the electrolyte according to the Boltzmann distribution. This results in an exponential growth of counterions near the charged surface [148]. In practice, however, the region closest to the charged surface is always hydrated by a condensed layer of water molecules. This layer is inaccessible to the counterions, and is referred to as the Stern layer [25, 149].

Recently, Bohinc et al. [150] formulated the Poisson-Helmholtz-Boltzmann model to describe solvent-mediated, non-electrostatic interactions between ions based on a pair-wise Yukawa potential. In this model, in addition to electrostatic interactions, the ions experience a hydration (h) interaction given by, $U_h/k_BT = e^{-\kappa_h(r-l_h)}/r$, where U_h is the hydration energy, r is the separation distance between the ions, κ_h is the inverse of the length scale corresponding to the decay of ordered water layers around an ion, and l_h is the length scale at which U_h becomes comparable to the thermal energy, k_BT. In this study, we follow the approach of Bohinc et al. [4, 150] to incorporate an additional solvent-mediated hydration interaction into the model in Eq. 2.26. Our approach serves two important purposes. First, we can self-consistently model both the Stern and the Diffuse layer regions of the electric double layer using a single theory. Second, we can study the effect of the Stern layer region on the disjoining pressure acting between charged surfaces. Recall that in the Stern layer region, counterions are repelled from the charged surface due to the short-range hydration interactions while coions, which carry charge of the same sign as that of the charged surface, are repelled due to the unfavorable repulsive electrostatic interactions with the charged surface. We later show that the short-range repulsive hydration forces reported by Israelachvilli and Pashley [151], as well as by LeNeveu and Rand [152], emerge naturally from the incorporation of hydration interactions into our model of the electric double layer.

After incorporating electrostatic correlations and hydration interactions into our EDL model, we implement a final modification by describing the phenomenon of surface charge regulation. This is the electrochemical mechanism by which surfaces in contact with aqueous electrolytes acquire charge from the dissociation of surface species, such as the silanol groups that typically terminate glass or silica surfaces [153]. In this case, the degree of dissociation depends strongly on the pH of the solution. To validate our theoretical predictions on like-charge attraction, we make use of the experimental data of Plassard et al. [5] who measured the disjoining pressure acting between calcium silicate hydrate (CSH) layers in a calcium hydroxide electrolyte solution. We incorporate the mechanism of surface charge regulation into our EDL model by assuming that the charge on the CSH layers results from the dissociation of silanol groups (SiO^-) at the CSH surface [5], which allows us to relate the surface charge density on the CSH surface to the calcium hydroxide concentration in

the solution.

The end result after incorporation of electrostatic correlations, hydration interactions, and surface charge regulation - phenomena which are all currently neglected in the DLVO theory, is a complete, self-consistent theory of the disjoining pressure for multivalent electrolytes. Specifically, we demonstrate that our theory can be used to describe the phenomenon of like-charge attraction, including predicting the disjoining pressure, in reasonably good agreement with the experimental data of Plassard et al. [5] for a broad range of salt concentrations.

2.3.1 Model and Methods

We begin our analysis by considering two similarly-charged surfaces immersed in a z:1 electrolyte solution, where z denotes the valency of the counterion. For reference, we assume that both surfaces are negatively charged, which implies that the cations are the positively charged counterions in this system. Because hydration interactions are short-ranged, we simplify our analysis by assuming that the hydration interactions are only relevant for the cations and negligible for the anions, which are anyways repelled due to the repulsive electrostatic interactions with the negatively charged surface. Therefore, in our model, the cations interact with the negatively charged surface through both electrostatic and hydration interactions, while the anions interact with the negatively charged surface only through electrostatic interactions. Further, as shown in Fig. 2-6, the region closest to the negatively charged surface is accessible only to the water molecules, with these water molecules serving as the source term for the boundary condition for the hydration potential (see below). As discussed by Brown et al. [4], this is similar in spirit to the surface charge density at the charged surface serving as the boundary condition for the electrostatic potential. The negatively charged surfaces electrostatically attract cations from the bulk reservoir, resulting in the formation of an EDL of ions in the region between the charged surfaces. As shown in Fig. 2-6, the formation of the EDL results in the pressure felt by the charged surfaces, referred to as the disjoining pressure, being significantly different than the osmotic pressure in the bulk reservoir.

After incorporation of additional contributions from hydration interactions into Eq. 2.26, we arrive at the following general functional for the total Helmholtz free energy of the system,

$$\begin{aligned}\mathbb{F} = &\int_V d\mathbf{r}\left\{\rho\phi - \frac{\varepsilon}{2}\left[|\nabla\phi|^2 + l_c^2\left(\nabla^2\phi\right)^2\right] + g\left(c_+, c_-\right)\right\} \\ &+ \oint_S d\mathbf{r}\, q_s\phi \\ &+ \int_V d\mathbf{r}\left\{\left[\frac{-\kappa_h^2\psi_h^2 - (\nabla\psi_h)^2}{8\pi l_h e^{\kappa_h l_h}}\right]k_BT + (c_+ - c_0)\,\psi_h k_BT\right\} \\ &+ \oint_S d\mathbf{r}\,\sigma_h\psi_h - \int_V d\mathbf{r}(\mu_+c_+ + \mu_-c_-)\end{aligned} \tag{2.28}$$

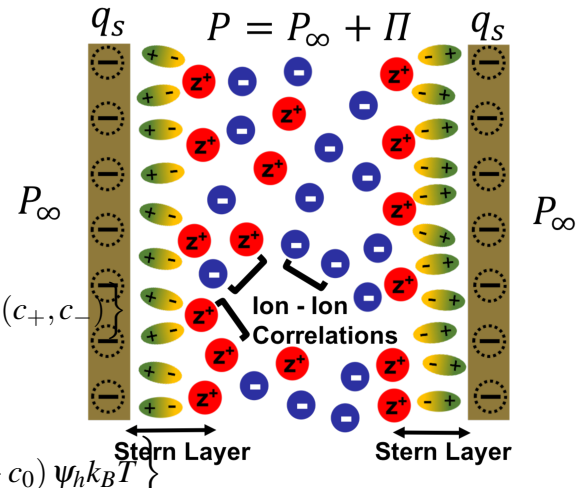

Figure 2-6: Schematic of our model problem: a multivalent $z:1$ electrolyte is confined between two surfaces with surface charge density, q_s. The disjoining pressure, Π, is defined as the difference in the pressure (P) felt between the plates due to the presence of the EDL and the pressure in the bulk reservoir (P_∞). As shown here, the Stern layer which is the region closest to the charged surface is accessible only to the water molecules (depicted as ellipsoids), modeled using the hydration potential while the concentration profiles of the cations (depicted as red spheres) and the anions (depicted as blue spheres) in the EDL are influenced by electrostatic correlations, described in our theory using the BSK model.

where ψ_h is the dimensionless hydration potential, σ_h is the surface density of water molecules at the charged surface which mediate the interaction of cations with the charged surface, and μ_+ and μ_- are the chemical potentials of cations and anions, respectively. The terms in the 1st and 2nd rows in Eq. 2.28 are the same as those of Eq. 2.26, and correspond to the free energy of the system after incorporating electrostatic correlations into the PB model. Further, the terms in the 3rd row and the 1st term in the 4th row in Eq. 2.28 result from the incorporation of hydration effects into our model. Finally, the last term in Eq. 2.28 couples the concentration of ions in the EDL confined by the charged surfaces to that in the bulk reservoir. Although the terms in Eq. 2.28 resulting from electrostatic correlations and hydration interactions have been reported in refs. [34] and [150], respectively, for completeness, a detailed derivation of the Helmholtz

free energy expression in Eq. 2.28 is provided in the Supporting Information (SI) document in reference [23].

We note here that the incorporation of hydration interactions automatically accounts for the finite size of the ions. Therefore, there is no need to incorporate any additional excluded-volume interactions in our model, and we can retain the original expression for the entropy density, $g(c_+, c_-)$, from the PB model given by:

$$g = k_B T \sum_{i=\pm} \left[c_i \left(\ln \left(\frac{c_i}{c_{0i}} \right) - 1 \right) \right] \tag{2.29}$$

where $c_{0i}(i = \pm)$ is the corresponding concentration of cations/anions in the bulk reservoir.

Next, we enforce the conditions of thermodynamic equilibrium in the system by setting $\delta\mathbb{F}/\delta\phi = 0$ for the electrostatic potential and $\delta\mathbb{F}/\delta\psi_h = 0$ for the hydration potential in Eq. 2.28, respectively. For the electrostatic potential, we obtain a fourth order Poisson equation and a boundary condition, respectively, given by:

$$\varepsilon \left(l_c^2 \nabla^2 - 1 \right) \nabla^2 \phi = \rho = (zec_+ - ec_-) \tag{2.30}$$

$$\hat{n} \cdot \varepsilon \left(l_c^2 \nabla^2 - 1 \right) \nabla \phi = q_s \tag{2.31}$$

Similarly, the governing equation for the dimensionless hydration potential, ψ_h, and the corresponding boundary condition are given by:

$$\nabla^2 \psi_h - \kappa_h^2 \psi_h = -4\pi l_h e^{\kappa_h l_h} \Big[c_+ - c_0 \Big] \tag{2.32}$$

$$\hat{n} \cdot \nabla \psi_h = -4\pi l_h e^{\kappa_h l_h} \sigma_h \tag{2.33}$$

We note here that Eq. 2.32 does not contain any term which depends on the concentration of anions, c_-, which is consistent with our assumption that the hydration potential acts only between the cations. As discussed by Brown et al. [4], Eq. 2.33 results from assuming that

each ordered water molecule near the negatively charged solid surface acts like a source term for the hydration interaction of the cations with the charged surface. At thermodynamic equilibrium, $\frac{\delta \mathbb{F}}{\delta c_{\pm}} = 0$, which results in the following expressions for the chemical potential of the counterions and the coions:

$$\frac{\mu_+}{k_B T} = \frac{ze\phi}{k_B T} + \psi_h + \ln\left(\frac{c_+}{c_{+0}}\right); \tag{2.34}$$

$$\frac{\mu_-}{k_B T} = -\frac{e\phi}{k_B T} + \ln\left(\frac{c_-}{c_{-0}}\right) \tag{2.35}$$

where c_{+0} and c_{-0} are the bulk concentration of the counterions and the coions, respectively. To satisfy the condition of electroneutrality in the bulk, $c_{+0} = c_0$ and $c_{-0} = zc_0$ (c_0 is the concentration of the undissociated z:1 salt). Equating Eq. 2.35 at any point in the EDL and in the bulk reservoir results in the following expressions for the dimensionless counterion and the coion densities in the EDL: $\tilde{c}_+ = e^{-z\tilde{\phi}+\psi_h}$, $\tilde{c}_- = e^{\tilde{\phi}}$, where, $\tilde{\phi} = \frac{e\phi}{k_B T}$, $\tilde{c}_+ = \frac{c}{c_0}$ and $\tilde{c}_- = \frac{c}{zc_0}$. For a numerical evaluation of the electrostatic potential in the EDL, it is convenient to convert Eq. 2.30 into a dimensionless form, given by,

$$\left(\delta_c^2 \tilde{\nabla}^2 - 1\right) \tilde{\nabla}^2 \tilde{\phi} = \frac{\tilde{c}_+ - \tilde{c}_-}{1+z}, \tag{2.36}$$

where $\tilde{x} = x/\lambda_D$, λ_D is the Debye-Hückel screening length which for a z:1 electrolyte is given by the expression: ${\lambda_D}^2 = \frac{\varepsilon k_B T}{z(z+1)c_0 e^2}$,$\tilde{\nabla} = \lambda_D \nabla$, and $\delta_c = l_c/\lambda_D$ is the dimensionless correlation length. The dimensionless correlation length for a z:1 electrolyte is given by the following expression in ref. [147]:

$$\delta_c = 0.35 \left(\frac{z^2 l_b}{l_{GC}}\right)^{-1/8} \left(\frac{z^2 l_b}{\lambda_D}\right)^{2/3} \tag{2.37}$$

In Eq. 2.37, the quantity, l_{GC}, denotes the Gouy-Chapman length which is the length scale at which the interaction of a counterion with a uniformly charged surface becomes comparable to the thermal energy, $k_B T$, and is given by:

$$l_{GC} = \frac{e}{2\pi z l_b \mid q_s \mid} \tag{2.38}$$

Similar to the electrostatic potential, the dimensionless governing equation for the hydration potential is given by:

$$\tilde{\nabla}^2\psi_h - \kappa_h^2\lambda_D^2\psi_h = 4\pi l_h e^{\kappa_h l_h} c_0 \lambda_D^2 \left[1 - \tilde{c}_+\right] \tag{2.39}$$

Note that the governing equation for the dimensionless electrostatic potential (Eq. 2.36) is 4^{th} order. Therefore, we need four boundary conditions to solve for the dimensionless electrostatic potential. Assuming that the negatively charged surfaces are located at $-d/2 - l_h$ and $d/2 + l_h$, respectively, where d is the separation distance between the two negatively charged surfaces, corresponding to the region accessible to ions, and l_h is the hydration length parameter, Eq. 2.36 can be solved using the following four boundary conditions:
(i) $\tilde{\phi}'\left(\tilde{x} = -\frac{\tilde{d}}{2} - \tilde{l}_h\right) - {\delta_c}^2\tilde{\phi}'''\left(\tilde{x} = -\frac{\tilde{d}}{2} - \tilde{l}_h\right) = -\frac{q_s e\lambda_D}{\varepsilon k_B T}$,
(ii) $\tilde{\phi}'\left(\tilde{x} = \frac{\tilde{d}}{2} + \tilde{l}_h\right) - {\delta_c}^2\tilde{\phi}'''\left(\tilde{x} = \frac{\tilde{d}}{2} + \tilde{l}_h\right) = \frac{q_s e\lambda_D}{\varepsilon k_B T}$,
(iii) $\delta_c\tilde{\phi}'''\left(\tilde{x} = -\frac{\tilde{d}}{2} - \tilde{l}_h\right) = \tilde{\phi}''\left(\tilde{x} = -\frac{\tilde{d}}{2} - \tilde{l}_h\right)$ and
(iv) $\delta_c\tilde{\phi}'''\left(\tilde{x} = \frac{\tilde{d}}{2} + \tilde{l}_h\right) = -\tilde{\phi}''\left(\tilde{x} = \frac{\tilde{d}}{2} + \tilde{l}_h\right)$.

Note that boundary conditions (i) and (ii) result from equating the electric displacement field at the charged surface, which is similar to the approach used in previous studies to derive the boundary conditions for the PB model. Further, the boundary conditions (iii) and (iv) result from enforcing a force balance at contact, where ionic correlations must vanish [147]. The boundary conditions to solve for the dimensionless hydration potential using Eq. 2.39 are given by [4]: (i) $\psi_h'\left(\tilde{x} = -\frac{\tilde{d}}{2} - \tilde{l}_h\right) = -4\pi l_h\lambda_D e^{\kappa_h l_h}\sigma_h$ and (ii) $\psi_h'\left(\tilde{x} = \frac{\tilde{d}}{2} + \tilde{l}_h\right) = 4\pi l_h\lambda_D e^{\kappa_h l_h}\sigma_h$. Note that for a given d, the actual domain over which the equations are being solved changes depending on whether the hydration potential is included in the model. If hydration potential is included (i.e., $l_h \neq 0$), then the electrolyte domain lies between $x = -d/2 - l_h$ and $x = d/2 + l_h$. If not ($l_h = 0$), then the distance of closest approach must be subtracted, such that the electrolyte domain consists of the region between $x = -d/2$ and $x = d/2$. Such a distinction is important when the predicted disjoining pressure is compared using different models, as shown below in the Results section, where the separation distance between the charged surfaces is denoted using, d, for all the models considered.

In reference [23], we present the full derivation of the disjoining pressure. After applying some mathematical identities and thermodynamic relations, we arrive at the pressure expression for the full theory:

$$\begin{aligned} P(x) = &-\frac{\varepsilon}{2}\phi'^2 - \frac{\varepsilon {l_c}^2}{2}\phi''^2 + \varepsilon {l_c}^2\phi'''\phi' + c_0\psi_h k_B T \\ &+ \Big[\frac{\kappa_h^2\psi_h^2 - \psi_h'^2}{8\pi l_h e^{\kappa_h l_h}}\Big]k_B T - \left\{ g - \sum_{i=\pm} c_i \frac{\partial g}{\partial c_i} \right\} \end{aligned} \tag{2.40}$$

Using the expression for g from Eq. 2.29, and subtracting the pressure in the bulk reservoir obtained by setting the electrostatic potential, the hydration potential, and all the higher-order derivatives of the electrostatic and the hydration potentials to zero in Eq. 2.40, the disjoining pressure, $\Pi = P - P_\infty$, is given by:

$$\begin{aligned} \Pi = &-\frac{\varepsilon}{2}\phi'^2 - \frac{\varepsilon {l_c}^2}{2}\phi''^2 + \varepsilon {l_c}^2\phi'''\phi' + k_B T \sum_{i=\pm}\Big[c_i - c_{i0}\Big] \\ &+ k_B T c_0 \psi_h + k_B T \Big[\frac{\kappa_h^2\psi_h^2 - \psi_h'^2}{8\pi l_h e^{\kappa_h l_h}}\Big] \end{aligned} \tag{2.41}$$

Next, we analyze in more detail each of the terms contributing to the disjoining pressure predicted in Eq. 2.41. Specifically, the 1$^{\text{st}}$ term arises from the self energy of the electrostatic field in the EDL, the 2$^{\text{nd}}$ and 3$^{\text{rd}}$ terms arise from electrostatic correlations, the 4$^{\text{th}}$ term is a contribution due to the translational entropy of the ions, and the 5$^{\text{th}}$ and 6$^{\text{th}}$ terms arise from the incorporation of hydration interactions into the EDL model. If hydration interactions are neglected, i.e., $\psi_h = 0$ and $\psi_h' = 0$, the 1$^{\text{st}}$ four terms in Eq. 2.41 yield the expression of the disjoining pressure in the context of the BSK model, given by:

$$\Pi_{BSK} = -\frac{\varepsilon}{2}\phi'^2 - \frac{\varepsilon {l_c}^2}{2}\phi''^2 + \varepsilon {l_c}^2\phi'''\phi' + k_B T \sum_{i=\pm}\Big[c_i - c_{i0}\Big] \tag{2.42}$$

Further, if electrostatic correlations are also neglected, i.e. if we set $l_c = 0$ in Eq. 2.41, we recover the exact expression of the disjoining pressure for the PB model given by (see

refs. [25, 154]):

$$\Pi_{PB} = -\frac{\varepsilon}{2}\phi'^2 + k_B T \sum_{i=\pm} \left[c_i - c_{i0}\right] \tag{2.43}$$

The disjoining pressure in Eq. 2.41, is uniform throughout the region confined by the two charged surfaces. However, one can obtain additional insights about the nature of the terms contributing to the disjoining pressure by evaluating Eq. 2.41 at the mid-plane between the two charged surfaces. For example, if the two surfaces carry charge of the same sign and magnitude (similarly-charged), the 1st derivative of both the electrostatic and the hydration potentials are zero at the mid-plane between the two charged surfaces due to symmetry conditions. In this case, the predicted disjoining pressure is given by:

$$\begin{aligned}\Pi\Big|_{center} = &-\frac{\varepsilon {l_c}^2}{2}\phi''^2\Big|_{center} + k_B T \sum_{i=\pm}\left[c_i\Big|_{center} - c_{i0}\right] + \\ &k_B T c_0 \psi_h\Big|_{center} + k_B T \frac{\kappa_h^2 {\psi_h}^2\Big|_{center}}{8\pi l_h} e^{-\kappa_h l_h}\end{aligned} \tag{2.44}$$

Eq. 2.44 clearly shows that the contribution from the water-mediated hydration interactions between the cations (last two terms in Eq. 2.44) to the disjoining pressure is always repulsive. The 2nd term in Eq. 2.44, which is the entropic contribution to the disjoining pressure, is also always repulsive. Note that the 2nd term in Eq. 2.44 corresponds to the disjoining pressure according to the PB model. This is the reason why the PB model always predicts a repulsive disjoining pressure between similarly-charged surfaces, irrespective of the surface charge density, the salt concentration, and the valency of the counterions. In contrast, the 1st term in Eq. 2.44, which arises from the electrostatic correlations described by the BSK model, is always negative. Therefore, Eq. 2.44 predicts that there can be an attractive EDL contribution to the disjoining pressure even between similarly-charged surfaces, as long as the attractive contribution due to electrostatic correlations dominates over the contributions due to the repulsive entropic and hydration interactions.

In addition to electrostatic interactions, van der Waals interactions between the two planar surfaces can contribute to the disjoining pressure, although their range is significantly

short-ranged. The van der Waals contribution to the disjoining pressure can simply be added to Eq. 2.44, and is given by [5]:

$$P_{\mathrm{vdW}} = -\frac{A_h}{6\pi(d+2l_h)^3} \tag{2.45}$$

where A_h is the Hamaker constant and determines the magnitude of the van der Waals interaction between the two planar surfaces. It is noteworthy that the attractive disjoining pressure associated with the van der Waals interactions can also result in like-charge attraction, especially if the charged surface is neutralized by the multivalent counterions. However, the magnitude of the attraction resulting from the van der Waals interactions is highly system-specific. Indeed, the attractive contribution to the disjoining pressure resulting from the van der Waals interactions will depend on several factors: (i) the nature of the counterion neutralizing the charged surface, (ii) the thickness of the electric double layer of counterions neutralizing the charged surface, and (iii) the magnitude of the Hamaker constant of the interacting charged surfaces in air. All these effects can be captured in our model by defining an effective Hamaker constant to model the van der Waals interaction between charged surfaces in the presence of a confined electrolyte. Note that unless specifically stated, most of the results in this chapter will not include the contribution in Eq. 2.45, because our study is mainly focused on studying the EDL contribution to the disjoining pressure. However, we will include the van der Waals contribution to the disjoining pressure when comparing the theoretically-predicted disjoining pressure to the experimentally-measured one.

Finally, we also include the contribution due to the phenomenon of surface charge regulation into our EDL model. Although there are several theoretical approaches to model surface charge regulation [155, 156], we have adopted the formulation by Behrens and Grier [153], which is useful to model surface charge regulation in cases where the surface charge is related to the dissociation of silanol groups from the surface. Note that in the case of CSH layers, the surface dissociation of silanol groups is primarily responsible for the negative surface charge on the CSH layers, as reported in the study by Plassard et al. [157]. To model the variation of the surface charge density of CSH layers as a function

of the solution pH [157], we consider reactions of hydroxide ions with silica sites, using the formulation of Behrens and Grier [153]. In basic solutions involving hydroxide ions, the surface reaction proceeds as follows:

$$\mathrm{SiOH} + \mathrm{OH^-} \rightleftharpoons \mathrm{SiO^-} + \mathrm{H_2O} \tag{2.46}$$

The surface is composed of negative (dissociated) and neutral (undissociated) silica sites, determined by the surface reaction equilibrium of the hydroxide ions interacting with the CSH layer. A total site balance on the Si atoms result in the following equation:

$$\Gamma = \Gamma_{\mathrm{SiO^-}} + \Gamma_{\mathrm{SiOH}} \tag{2.47}$$

where Γ is the total surface concentration of Si atoms, $\Gamma_{\mathrm{SiO^-}}$ and Γ_{SiOH}, are the surface concentrations of the negative and the neutral silica sites, respectively. Note that the surface charge density on the CSH layer can be expressed as the product of the number of negative silica sites times their charge, i.e., $q_s = -e\Gamma_{\mathrm{SiO^-}}$. Similar to the study by Behrens and Grier [153], we assume that the distribution of the hydroxide ions near the CSH layer satisfies the Boltzmann distribution given by, $c_{\mathrm{OH^-},s} = c_{\mathrm{OH^-},B}\exp(\tilde{\phi}_s)$, where $\tilde{\phi}_s$ is the dimensionless electrostatic potential at the CSH layer, and $c_{\mathrm{OH^-},B}$ and $c_{\mathrm{OH^-},s}$ are the concentrations of hydroxide ions near the CSH layer and in the bulk, respectively. Further, based on the surface chemical reaction in Eq. 2.46, the following relation is obtained:

$$1/K_b = 10^{pK_b} = \frac{\Gamma_{\mathrm{SiO^-}}}{c_{\mathrm{OH^-},s}\Gamma_{\mathrm{SiOH}}} \tag{2.48}$$

where K_b is the base dissociation equilibrium constant, and pK_b is the logarithmic dissociation constant characteristic of the CSH-water interface. Because the Stern layer is already modeled self-consistently through the incorporation of water-mediated hydration interactions, the surface potential, $\tilde{\phi}_s$ can be set equal to the potential at the surface located at ($x = \pm d/2 \pm l_h$), without the need to account for the Stern capacitance, as done in ref. [153]. Using the relation, $q_s = -e\Gamma_{\mathrm{SiO^-}}$, in conjunction with Eqs. 2.47 and 2.48, the

expression for the surface charge density at the CSH layer is given by:

$$q_s = \frac{-10^{-pK_b} e\Gamma c_{\mathrm{OH}^-,B} \exp(\tilde{\phi}_s)}{1 + 10^{-pK_b} c_{\mathrm{OH}^-,B} \exp(\tilde{\phi}_s)} \tag{2.49}$$

Note that Γ and pK_b are parameters characteristic of the CSH-water interface, and can be obtained through fitting to experimental data. Because the correlation length is itself a function of the surface charge density through its dependence on l_{GC} (see Eqs. 2.37 and 2.38), δ_c must be obtained in an iterative manner. Specifically, the dimensionless electrostatic potential (see Eq. 2.36) is solved using an initial guess for q_S, and subsequently, the deduced value of $\tilde{\phi}_s$ is used to adjust q_S for subsequent iterations using Eq. 2.49. Finally, the converged value of q_S is used to obtain the dimensionless electrostatic potential (see Eq. 2.36), and the disjoining pressure is obtained using Eq. 2.44 for various separation distances between the two similarly-charged surfaces.

2.3.2 Results

Several key predictions of our theory are presented below. First, we consider the role of electrostatic correlations on the disjoining pressure acting between two similarly-charged surfaces, including studying the dependence on the valency of the counterions and coions, the bulk salt concentration, and the surface charge density of the charged surfaces. Second, we study the effect of incorporating hydration interactions and surface charge regulation into our EDL model on the disjoining pressure. Finally, after including the contribution of the van der Waals interactions to the disjoining pressure, we compare the predictions of the disjoining pressure made using our complete model with the experimental data of Plassard et al. [5].

Electrostatic Correlations Cause Like-Charge Attraction

To isolate and properly quantify the effect of electrostatic correlations on the disjoining pressure, as described by the BSK theory, we initially neglect hydration interactions, surface charge regulation, and van der Waals interactions in our EDL model. This is done by setting $\psi_h = 0$ in Eq. 2.41 (thereby neglecting hydration interactions), assuming that

q_s is an independent parameter irrespective of the bulk salt concentration (thereby neglecting surface charge regulation), and setting A_h=0 in Eq. 2.45 (thereby neglecting van der Waals contributions to the disjoining pressure) . In Fig. 2-7 (a), we utilize Eq. 2.42 to plot the disjoining pressure predicted using the BSK model as a function of the separation distance between the two charged surfaces for the case of a 2:1 electrolyte solution. Note that throughout the chapter, the water dielectric permittivity, ε, is expressed as $\varepsilon = \varepsilon_r \varepsilon_0$, where ε_0 is the permittivity of vacuum ($8.85 \cdot 10^{-12}$ F.m^{-1}). In Fig. 2-7 (a), the disjoining pressures predicted using the BSK model (see Eq. 2.42) and the PB model (see Eq. 2.43) are compared. Note that the governing equation for the dimensionless electrostatic potential in the PB model can be obtained simply by setting $\delta_c = 0$ in Eq. 2.36, including using boundary conditions (i) and (ii) in the set of four boundary conditions used to solve Eq. 2.36 in the BSK model. As expected, the PB model always predicts a repulsive (positive) disjoining pressure irrespective of the separation distance between the two charged surfaces. Furthermore, the repulsive disjoining pressure predicted by the PB model decreases monotonically with an increase in the separation distance between the two charged surfaces. However, in stark contrast to the result predicted by the PB model, it is possible to obtain an attractive (negative) disjoining pressure using the BSK model. For example, as shown in Fig. 2-7 (a), the disjoining pressure curve predicted by the BSK model displays an attractive well at a separation distance of ~ 0.8 nm between the two charged surfaces. For separation distances greater than 1 nm, where the disjoining pressure predicted by the BSK model is negative and progressively goes to zero at larger separation distances, the attractive pressure resulting from electrostatic correlations dominates over the pressure arising from the entropic repulsion.

To better understand the above-mentioned competition, in the inset of Fig. 2-7 (a), we plot the contributions to the disjoining pressure due to each of the four terms appearing in Eq. 2.42, all evaluated at the mid-plane between the two charged surfaces. Because we are considering similarly-charged surfaces, the 1$^{\text{st}}$ derivative of the electrostatic potential is always zero at the mid-plane between the two charged surfaces. Therefore, the 1$^{\text{st}}$ and the 3$^{\text{rd}}$ terms in Eq. 2.42 do not contribute to the predicted disjoining pressure. Moreover, as shown in the inset of Fig. 2-7 (a), the pressure resulting from electrostatic correlations

(2^{nd} term in Eq. 2.42) is always attractive (negative) while the entropic pressure (4^{th} term in Eq. 2.42) is always repulsive (positive). For separation distances much smaller than 1 nm, the counterions get compressed between the two charged surfaces, thereby greatly enhancing the entropic contribution, and making the overall disjoining pressure repulsive (positive). On the other hand, for separation distances larger than 1 nm, the disjoining pressure contribution from electrostatic correlations always dominates over the repulsive entropic contribution, which results in an overall attractive disjoining pressure as shown in Fig. 2-7 (a). Interestingly, as Fig 2-7 (b) shows, at a separation distance of 1 nm between the two charged surfaces, the mean charge density ($\rho = zec_+ - ec_-$), and the dimensionless electrostatic potential ($\tilde{\phi}$) profiles obtained using the PB and the BSK models are very similar. The similarity in the two profiles suggests that the form of the Helmholtz free energy, F, and a self-consistent expression of the disjoining pressure, Π, derived from F, are essential in order to obtain a negative disjoining pressure in the context of the BSK model. For example, even if one utilizes Eq. 2.36 to solve for the electrostatic potential using the BSK model, use of Eq. 2.43 which corresponds to the disjoining pressure from the PB model would still result in a repulsive disjoining pressure for all separation distances between the similarly-charged surfaces. Therefore, our study highlights the necessity to self-consistently incorporate terms in the predicted disjoining pressure (see Eq. 2.42) arising from electrostatic correlations to explain the phenomenon of like-charge attraction between similarly-charged surfaces.

It is noteworthy that in previous work, the BSK model was shown to describe overscreening, or charge-inversion, in the case of an EDL of solvent-free ionic liquids placed near a charged electrode [34]. In this case, strong electrostatic correlations give rise to an oscillatory profile for the mean charge density, ρ, where the 1^{st} layer of ions in the EDL overscreens the charge on the electrode, and subsequently, the net charge of the electrode together with the 1^{st} layer of ions is progressively neutralized by additional layers of ions. In this study, we find that although both the phenomena of charge-inversion and like-charge attraction can result from strong electrostatic correlations, there is no direct correlation between them. In other words, it is not necessary for the phenomenon of like-charge attraction to occur concurrently with the phenomenon of charge-inversion.

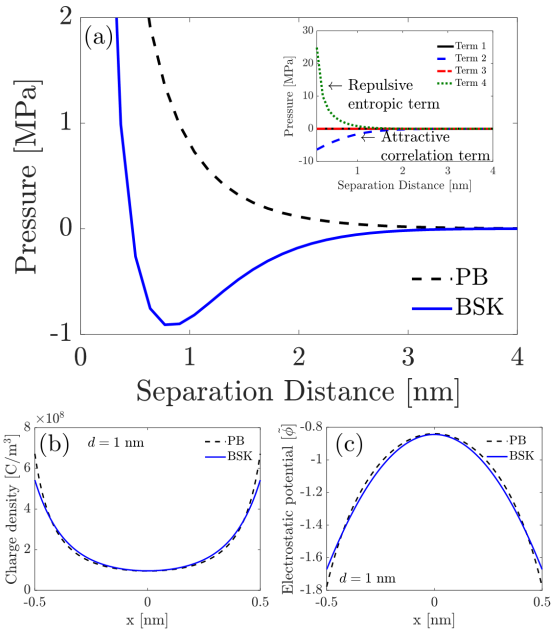

Figure 2-7: Disjoining pressures operating between two similarly-charged surfaces separated by a 2:1 electrolyte solution predicted using the BSK (Eq. 2.42) and the PB (Eq. 2.43) models, for q_s= -0.1 C/m^2, c_0=0.1 M, and $\varepsilon_r = 80$. (a) Variation of the disjoining pressure as a function of the separation distance between the two charged surfaces. The inset shows the contribution of the different terms in Eq. 2.42 based on the BSK model. (b) and (c) Comparison of the charge density and the dimensionless electrostatic potential profiles, respectively, predicted by the BSK model (Eq. 2.36) and the PB model (Eq. 2.36 with δ_c set to zero) when the separation distance between the two charged surfaces is 1 nm, and where x is the spatial coordinate perpendicular to the plane of the charged surface.

Next, we study how the counterion valency affects the disjoining pressure. As the counterion valency increases, the BSK theory predicts a stronger attractive contribution to the disjoining pressure, as shown in Fig. 2-8 (a). The qualitative shape of the pressure profile also changes significantly as the counterion valency increases from 1 to 3, with a deep attractive well developing in the case of a 3:1 electrolyte. Moreover, the position of the minimum in the disjoining pressure shifts towards the left with an increase in the counterion valency, indicating an enhancement in the length scale over which an attractive disjoining pressure is observed due to electrostatic correlations. The predicted attraction is consistent with experimental observations of like-charge attraction and colloidal coagulation in the presence of multivalent salt ions [1, 128–131]. Physically, increasing the counterion valency, z, enhances electrostatic correlations, which is captured in our EDL model by a nonlinear dependence of the dimensionless correlation length on the counterion valency (see Eq. 2.37). Increasing the value of z increases the correlation length parameter, which in turn enhances the attractive electrostatic correlation contribution to the disjoining pressure which scales as the square of the correlation length (see 1st term in Eq. 2.44).

In addition to studying the variation of the predicted disjoining pressure with the counterion valency, it is also interesting to explore the dependence of the predicted disjoining

pressure on the coion valency, i.e., for a 1:z electrolyte solution. To this end, we utilize the same parameter values used to generate Fig. 2-8 (a), except that we change the sign of the surface charge density, q_s, on the two surfaces. This, in turn, is equivalent to studying a 1:z electrolyte solution instead of the z:1 electrolyte solution considered earlier. Further, note that we also set $z = 1$ in Eqs. 2.37 and 2.38. In Fig. 2-8 (b), we show plots of the predicted disjoining pressure for a 1:z electrolyte, where the sign of q_s is positive. Interestingly, the predicted disjoining pressure is not sensitive to the coion valency, where the plots of the disjoining pressure predicted using different coion valencies, $z = 1, 2$, and 3, are all very similar to the predicted disjoining pressure plot for a 1:1 electrolyte solution. This indicates that the phenomenon of like-charge attraction is more strongly controlled by the valency of the counterion than by that of the coion. Our important finding that the coion valency plays an insignificant role in controlling the surface forces between two charged surfaces is well supported by the recent experimental data of Uzelac et al. [158]. These authors measured surface forces between charged silica particles mediated by multivalent coions, and reported that the valency of the counterions, and not the valency of the coions, controls the surface forces operating between the charged silica particles that they considered.

Next, we explore the dependence of the predicted disjoining pressure on the surface charge density and the salt concentration of the bulk reservoir. As shown in Fig. 2-9 (a), increasing the surface charge density of the two charged surfaces for a 2:1 electrolyte solution results in an enhancement of the attractive well for the disjoining pressure as the magnitude of q_s is increased from -0.01 C/m^2 to -0.2 C/m^2. In the case of an electrolyte confined between two charged surfaces, increasing the surface charge density of the two surfaces results in an enhancement of the overlap of the EDLs produced by each surface, because more counterions over an extended region are required to screen the increased charges on the surfaces. This results in an increase in the curvature, or the second derivative, of the electrostatic potential. As a result, the attractive electrostatic correlation contribution to the predicted disjoining pressure (2$^{\text{nd}}$ term in Eq. 2.42), which scales as the square of the 2$^{\text{nd}}$ derivative of the electrostatic potential, increases similarly. Consequently, increasing the surface charge density in the context of the BSK model results in a pronounced enhancement of the attractive well for the predicted disjoining pressure.

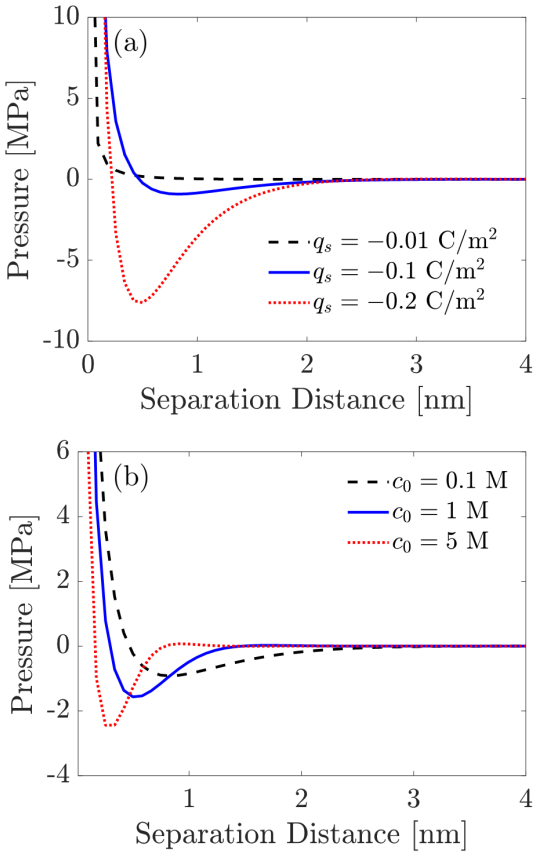

Figure 2-9: Effect of the surface charge density and the salt concentration for a 2:1 electrolyte solution on the predicted disjoining pressure as a function of the separation distance between the two charged surfaces. (a) Predicted disjoining pressures for three surface charge densities, where the following parameter values were use to generate the three plots shown: c_0=0.1 M and $\varepsilon_r = 80$. (b) Predicted disjoining pressures for three salt concentrations in the bulk reservoir, where the following parameter values were used to generate the three plots shown: q_s= -0.1 C/m^2 and $\varepsilon_r = 80$.

Our findings clearly show that the disjoining pressure predicted by the BSK model strongly disagrees with that predicted by the DLVO theory which uses the PB model to predict the EDL contribution to the disjoining pressure acting between two charged surfaces. Notably, increasing the surface charge density in the PB model enhances the overlap of the EDLs originating from the two similarly-charged surfaces, which in turn results in an increased entropic repulsion, and consequently, in an enhancement of the repulsive disjoining pressure acting between the two similarly-charged surfaces. While it is certainly true that like in the PB model, the magnitude of the repulsive entropic term (4^{th} term in Eq. 2.42) also increases with an increase in the surface charge density in the BSK model, the attractive electrostatic correlation term completely dominates over the repulsive entropic term, leading to a deepening of the attractive well for the predicted disjoining pressure in the case of the BSK model. Our result is in good agreement with that obtained by Plassard et al. [5] who experimentally measured the disjoining pressure operating between charged CSH layers in a calcium hydroxide salt solution. Indeed, Plassard et al. [5] reported an enhancement of the attractive well for the experimental disjoining pressure upon increasing the surface charge density on the CSH layers. The fact that the DLVO theory fails to predict the ex-

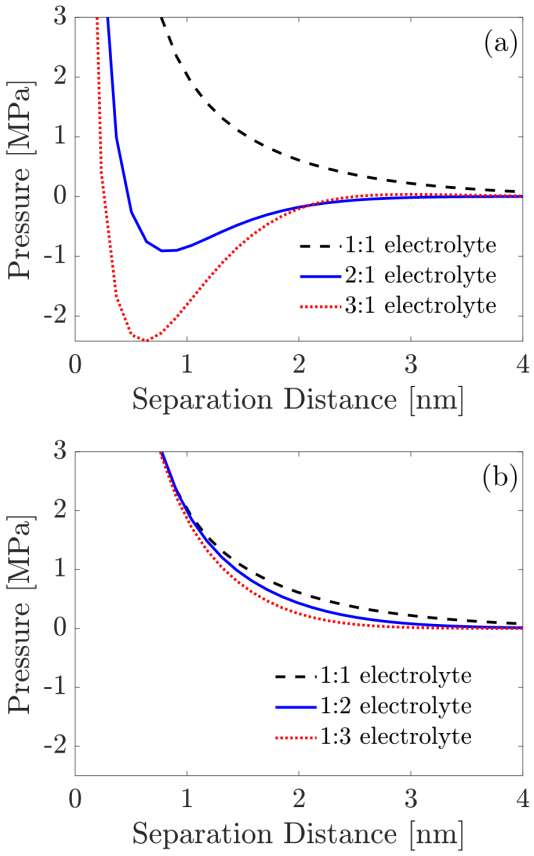

Figure 2-8: Effect of the ion valency on the predicted disjoining pressure acting between two similarly-charged surfaces as a function of the separation distance between the two charged surfaces for z:1 and 1:z electrolytes (z = 1, 2, and 3) solutions using the BSK model (Eq. 2.42). To generate the various plots, we used the following parameter values: $|q_s|$=0.1 C/m^2, c_0=0.1 M, and $\varepsilon_r = 80$. (a) Predicted disjoining pressure of a z:1 electrolyte solution, corresponding to a negative charge on the two surfaces, $q_s = -0.1$ C/m^2. (b) Predicted disjoining pressure of a 1:z electrolyte solution, corresponding to a positive surface charge on the two surfaces, $q_s = +0.1$ C/m^2.

perimentally observed trend, even at a qualitative level, demonstrates the importance and need for the availability of a theory such as the one presented here, capable of accurately modeling electrostatic correlations.

As shown in Fig. 2-9 (b), the predicted disjoining pressure also depends strongly on the salt concentration of the bulk reservoir. Indeed, as the salt concentration increases, the depth of the attractive well increases, reflecting stronger electrostatic correlations. In addition, the position of the disjoining pressure minimum shifts toward the left, reflecting a decrease in the overlap of the EDLs originating from the two similarly-charged surfaces. We have explored a wide parameter space for the dependence of the predicted disjoining pressure on salt concentration and surface charge density, as shown in the two contour plots in the SI document (see Fig. S1).

We note that like-charge attraction can also be obtained in the limit of a counterion-only system (also referred to as the one-component plasma limit), [1] where the surface charge is screened by a fixed number of counterions, with no coions present in the system. In this context, the BSK theory with the appropriate correlation length scale and boundary conditions, has been shown to exactly match the strong and weak coupling limits for the counterion-only system. [147] Further, the BSK theory can also accurately reproduce the intermediate coupling limit, including describing correlation-induced like-charge attraction in the case of counterion-only systems. [147]

Another interesting question is whether the BSK theory can predict like-charge attraction in systems with monovalant counterions, as was shown recently in simulations of charged nanoparticles [159]. In Fig. 2-10, we show the predicted disjoining pressure curves for a 1:1 electrolyte solution with varying surface charge density and varying bulk salt concentration. Fig 2-10 (a) clearly shows that, as the surface charge density increases from -0.1 to -0.4 C/m^2, the disjoining pressure between two similarly-charged surfaces predicted by the BSK theory can become strongly attractive (negative), even in the case of monovalent counterions.

Further, increasing the bulk salt concentration can result in the appearance of an attractive well in the disjoining pressure predicted by the BSK theory, similar to the ones predicted earlier in the case of a 2:1 electrolyte solution. However, very high bulk salt con-

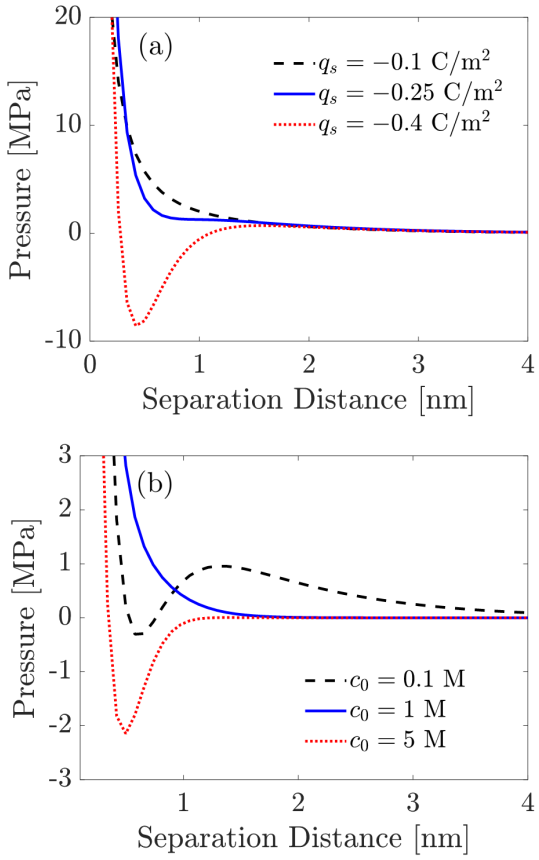

Figure 2-10: The disjoining pressure for a 1:1 electrolyte solution predicted by the BSK theory can be attractive depending on (a) the surface charge density, or (b) the salt concentration. For (a), the bulk salt concentration is fixed at $c_0 = 0.1$ M. For (b), the surface charge density is fixed at $q_s = -0.3$ C/m^2.

centrations or moderate to high surface charge densities, are needed to predict attractive disjoining pressures in the case of a 1:1 electrolyte solution. Our BSK model predictions for the disjoining pressure suggest that attractive interactions between two like-charged surfaces do not result exclusively from the presence of multivalent counterions. However, the presence of multivalent ions can significantly augment the attractive disjoining pressure arising from electrostatic correlations, as shown earlier in Fig. 2-8 (a).

Contributions to the Disjoining Pressure from Hydration Interactions and Surface Charge Regulation

Along with the contributions from electrostatic correlations, it is also interesting to explore the role of short-range water-mediated hydration interactions between the cations on the predicted disjoining pressure. As expected, water-mediated hydration interactions prevent two cations from approaching each other too closely, where the distance of closest approach between any two interacting cations is controlled by the parameter, l_h, which is the effective hydration size of the cation. In Fig 2-11, we plot the predicted disjoining pressure operating between two similarly-charged surfaces for a 2:1 electrolyte solution, where we incorporated hydration interactions into both the PB model and the BSK model. As discussed earlier, incorporation of hydration interactions allows us to model the Stern layer self-consistently in both the BSK and the PB models. However, for an appropriate comparison between the BSK model without hydration and the BSK model with hydration, we need to shift the separation distance values obtained in the case of the BSK model with hydration by $-2l_h$ to be consistent with the distance of closest approach in the two models. Similarly, the separation distance values for the PB model with hydration is also shifted by $-2l_h$.

Fig. 2-11 (a) shows that incorporation of the hydration potential into both the PB and the BSK models results in a strong repulsive (positive) contribution to the predicted disjoining pressure. In the case of the PB model, addition of the hydration potential makes the predicted repulsive disjoining pressure even more repulsive. In the case of the BSK model, addition of the hydration potential results in a disappearance of the attractive (negative) well, with a very weak attractive (negative) disjoining pressure visible at $\sim$ 3 nm separa-

tion distance between the two charged surfaces. Note that the plots shown in Fig. 2-11 (a) were obtained using, $q_s = -0.1$ C/m^2, corresponding to low to moderate surface charge densities typically encountered on the two charged surfaces. However, as shown later in this section, surface charge densities reported in some experimental studies can exceed this value. In such cases, we will be able to recover the attractive well in the disjoining pressure predicted using the BSK model where hydration interactions are included. Note that we selected $q_s = -0.1$ C/m^2 to carry out these calculations to demonstrate the key role of the hydration interactions in modulating the predicted disjoining pressure, especially at low to moderate surface charge densities on the the two charged surfaces. Moreover, if the EDL is decomposed into Stern and Diffuse layer regions, with the Diffuse layer region modeled using a EDL theory such as the PB model, it follows that the contribution of the Stern layer to the predicted disjoining pressure cannot be modeled self-consistently. In this study, we use the hydration potential to model the Stern layer and self-consistently incorporate the repulsive contribution from the hydration potential to the predicted disjoining pressure (see 3$^{\text{rd}}$ and 4$^{\text{th}}$ terms in Eq. 2.44), which are currently neglected in the PB model. Furthermore, the predicted repulsive disjoining pressures resulting from the hydration potential can also qualitatively explain the repulsive pressures reported in the experimental data of Israelachvilli and Pashley [151] and of LeNeveu and Rand [152].

To further elucidate the role of the hydration interactions in modulating the predicted disjoining pressure, in Fig. 2-11 (b) and (c), we compare the counterion profiles predicted using the BSK model without hydration and the BSK model with hydration, when the two charged surfaces are separated by a distance of 1 nm and 2 nm, respectively. Note that the distances of minimum approach for the BSK model and BSK model with hydration are d and $d + 2\ell_h$, respectively. This is the reason why the counterion profiles in the context of the BSK model with hydration extend beyond d in Fig. 2-11 (b) and (c). An analysis of the counterion profiles in Fig. 2-11 (b) and (c), shows that in the case of the BSK model without hydration, the predicted counterion concentrations near the two charged surfaces (at $x = \pm 0.5$ nm and $x = \pm 1$ nm, where x is the spatial coordinate perpendicular to the charged surfaces) are unbounded and several folds higher than those predicted in the case of the BSK model with hydration. As discussed earlier, hydration interactions limit the

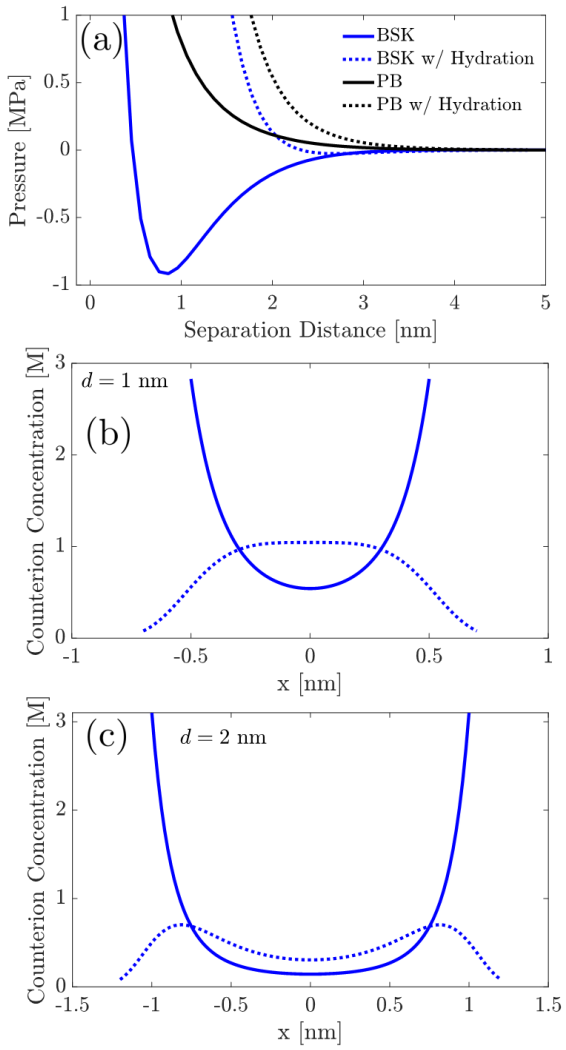

Figure 2-11: (a) Variation of the disjoining pressure with the separation distance between two similarly-charged surfaces for a 2:1 electrolyte solution, predicted by the BSK and the PB models with inclusion/exclusion of the hydration potential. Note that the parameters used to generate these results include: $q_s = -0.1$ C/m^2, $c_0 = 0.1$ M, ε_r=80, $\sigma_h = 5/\text{nm}^2$ (from ref. [4]), $\kappa_h^{-1} = 0.3$ nm (from ref. [4]), and $\ell_h = 0.2$ nm. The parameters for the hydration potential (σ_h, κ_h^{-1} and ℓ_h) can be further fine-tuned to reproduce the experimental data. (b) Comparison of the counterion profiles predicted using the BSK model without hydration and the BSK model with hydration, for d=1 nm, as a function of x, where x is the spatial coordinate perpendicular to the plane of the charged surface. (c) Same as (b), but for a separation distance of 2 nm between the two charged surfaces.

counterion concentrations near the two charged surfaces to replicate a Stern layer region which is devoid of counterions. Consequently, to neutralize the charge on the two surfaces, the concentration of counterions at the mid-plane between the two charged surfaces (located at $d = 0$ in Fig. 2-11 (b) and (c)) is higher in the BSK model with hydration than in the BSK model without hydration. This results in an enhancement of the repulsive entropic contribution to the predicted disjoining pressure (2^{nd} term in Eq. 2.44) in the BSK model with hydration, which together with the new repulsive terms arising from the incorporation of the hydration interactions (3^{rd} and 4^{th} terms in Eq. 2.44), contribute significantly towards making the overall predicted disjoining pressure repulsive, especially at smaller separation distances. As Fig. 2-11 (b) and (c) show, increasing the separation distance between the two charged surfaces from 1 to 2 nm, weakens the contribution from the hydration potential, such that the counterion concentration near the midplane (at $x = 0$) between the two charged surfaces, predicted using the BSK model with hydration (dotted blue curve), approaches that predicted using the BSK model without hydration (solid blue curve).

Finally, to complete our analysis, we consider the effect of surface charge regulation on the predicted disjoining pressure and the predicted surface charge density, where q_s is no longer an independent parameter, but instead depends on the bulk salt concentration. As a representative example, we consider two similarly-charged CSH layers immersed in a calcium hydroxide salt solution. We consider this system because, in the next section, we will compare the disjoining pressure predicted by our theory for this system with the experimental data of Plassard et al. [5]. As discussed in the Model and Methods section, the value of q_s in Eq. 2.49 depends on the bulk concentration of OH^- ions as well as on the dimensionless surface potential. As a result, q_s needs to be obtained in an iterative manner, such that Eqs. 2.36 and 2.32, together with the boundary conditions, and Eq. 2.49 are simultaneously satisfied.

In Fig. 2-12 (a), we plot the disjoining pressure as a function of the surface separation distance, d, predicted by first including hydration interactions into the PB and BSK models, and subsequently, by including surface charge regulation in the BSK and PB models. The disjoining pressure versus the separation distance profiles were predicted for a bulk salt concentration of 19.1 mM, a typical concentration for which the experimental data of

Plassard et al. [5] is available. To predict the disjoining pressure when charge regulation is neglected (e.g., BSK model and BSK model with hydration), we need to assign a value to the surface charge density, q_s, which serves as an independent parameter. To this end, we choose $q_s = -0.63$ C/m^2, obtained by solving Eq. 2.49 using $c_0 = c_{OH^-,B} = 19.1$ mM. Fig. 2-12 (a) shows that choosing a value of q_s which is much larger than the q_s value used to predict the results in Fig. 2-11 (a), we predict large attractive (negative) disjoining pressures using the BSK model. Including hydration interactions in the BSK model results in a large repulsive (positive) pressure contribution to the disjoining pressure. However, for $q_s = -0.63$ C/m^2, the predicted attractive (negative) disjoining pressure contribution resulting from electrostatic correlations dominates over the repulsive (positive) contributions resulting from the entropy of the ions as well as from the hydration interactions (2nd, 3th and 4th terms in Eq. 2.44). This results in an attractive (negative) well at ~ 1 nm separation distance between the two charged surfaces. For comparison, we also plotted the disjoining pressure profiles predicted using the PB model. It is clear that if electrostatic correlations are neglected, it will be impossible to predict an attractive (negative) well for the disjoining pressure using the PB model.

Interestingly, after inclusion of the hydration interactions in the PB and the BSK models, further inclusion of charge regulation in the two models does not affect at all the predicted disjoining pressure profiles. This indicates that for both the BSK and the PB models, the surface charge density is almost insensitive to the separation distance between the two charged surfaces. Indeed, as shown in Fig. 2-12 (b), the surface charge density varies with the separation distance between the two charged surfaces only at very small separation distances, and remains constant beyond a separation distance of 1 nm. In addition, there is not much difference between the predictions made using the PB and the BSK models, indicating that the dependence of the surface charge density on the separation distance between the two charged surfaces is insensitive to the modeling of electrostatic correlations. In fact, the surface charge density shows a very strong dependence on the pH of the solution. Recall that the concentration of OH^- ions present in the calcium hydroxide salt solution in the bulk reservoir can be related to the pH of the solution using the relation, $c_{OH^-,B} = 10^{pH-14}$. Therefore, increasing the pH of the solution results in a larger dissociation of silanol groups

at the CSH layer (see Eq. 2.46), which in turn results in an increase in the surface charge density at the CSH layer. Once again, the striking similarity of the variation of q_s with the pH of the solution, obtained using the PB and BSK models indicates that the variation of the surface charge density with the pH of the solution is insensitive to the modeling of electrostatic correlations. Finally, we also note that the variation of q_s with the solution pH, as predicted in Fig. 2-12 (c), is in good qualitative agreement with that reported experimentally by Plassard et al. [5]. This finding is reassuring in terms of the values of the surface charge regulation parameters, Γ and pK_b, used to model the variation of q_s with the solution pH in Fig. 2-12 (c). For example, Plassard et al. have reported that increasing the solution pH from 10 to 12.5 results in a monotonic enhancement in the surface charge density, q_s, at the CSH surface from -0.08 C/m^2 to -0.69 C/m^2. Similarly, in Fig. 2-12 (c), for a similar variation of the solution pH, we predict a monotonic enhancement of q_s from -0.02 C/m^2 to -0.58 C/m^2, for both the BSK and the PB models.

Comparison of the Disjoining Pressures Predicted from our Complete Theory with the Experimental Data

Plassard et al. [5] used atomic force microscopy to study the surface forces responsible for the strong cohesive strength of cement pastes. These authors observed strong attractive (negative) disjoining pressures operating between the CSH layers in the presence of a $Ca(OH)_2$ electrolyte solution. They attributed the observed behavior to the strong electrostatic correlations between the divalent calcium ions. Plassard et al. noted that because the DLVO theory neglects electrostatic correlations, the disjoining pressure predicted by the DLVO theory is not consistent with their experimental findings even qualitatively. In Fig. 2-13, we compare the disjoining pressure versus the surface separation distance profiles predicted by our complete theory (Eq. 2.44 plus Eq. 2.45) to those measured by Plassard et al. (see Fig. 5 in ref. [5]) for five $Ca(OH)_2$ salt concentrations. Plassard et al. measured the forces operating between the two CSH layers, and we converted their experimental surface force data into disjoining pressure data by dividing the reported surface forces by the surface area of the CSH layers, estimated to be 64 nm^2 in their study [5].

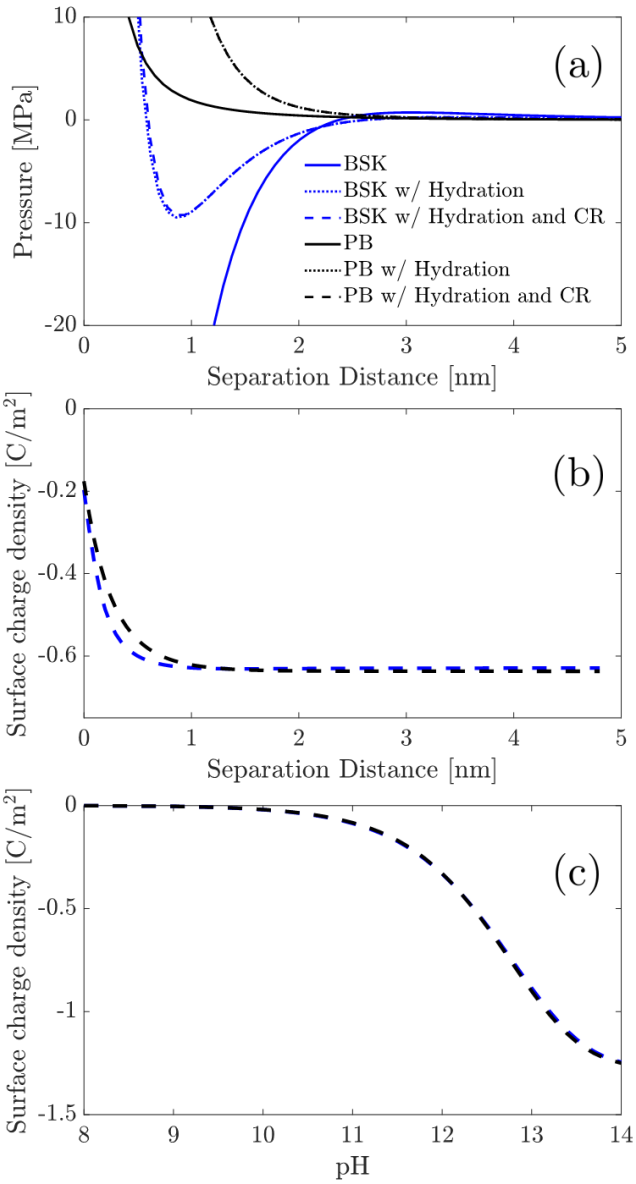

Figure 2-12: (a) Disjoining pressure versus the surface separation distance profiles predicted by the BSK model without hydration, the BSK model with hydration, and the BSK model with hydration and with charge regulation (CR) are compared with those predicted by the PB model without hydration, the PB model with hydration, and the PB model with hydration and with CR. The parameters used to generate the results shown here are: $c_0 = 19.1$ mM, $\varepsilon_r = 80$, $\kappa_h^{-1} = 0.3$ nm, $\sigma_h = 5/\text{nm}^2$, $\ell_h = 0.1$ nm, $\Gamma = 8 \times 10^{18}$ m^{-2} and $pK_b = 4$. Note that when CR is neglected, we used $q_s = -0.63$ C/m^2. (b) Surface charge density versus the surface separation distance profiles predicted using the BSK model with hydration and CR (blue dotted line) and the PB model with hydration and CR (black dotted line). Note that the parameters are the same as those used in (a), and that due to the incorporation of CR, q_s varies with the separation distance between the two charged surfaces. (c) Surface charge density versus the solution pH profiles predicted using the BSK model with hydration and CR (blue dotted line) and the PB model with hydration and CR (black dotted line), for a separation distance of 4 nm between the two equally, negatively charged surfaces. Further, the parameters used to generate the plot are the same as those used in (b).

Note that in the study by Plassard et al., one of the CSH layers was coated over an atomic force microscopy (AFM) tip, while the other CSH layer was coated over a calcite crystal. A key assumption made by Plassard et al. (also implemented here) is that the interaction of the two CSH layers can be approximated as the interaction between two flat surfaces. Note that to solve for the disjoining pressure, we used the following parameters: $l_h = 0.1$ nm, $\kappa_h^{-1} = 0.3$ nm, $\sigma_h = 5/\text{nm}^2$, $\Gamma = 1 \times 10^{18}$ m^{-2}, $pK_b = 4$, and $A_h = 14 \times 10^{-20}$ J. The following parameters were used in our predictions: (i) the Hamaker constant, A_h, used in this study is the same as that determined by Plassard et al. by measuring the surface forces operating between two CSH layers in air, (ii) the values of the hydration parameters, σ_h, and κ_h^{-1}, used here are identical to those reported by Brown et al. [4], (iii) the value of the surface site density, Γ, is identical to that reported by Behrens et al. [153], (iv) the pK_b is the same as that used in Fig. 2-12 (c), where we showed that the combination of the surface charge regulation parameters, Γ and pK_b, is able to predict the variation of q_s with the solution pH in reasonably good agreement with the experimental data of Plassard et al., and (v) the ℓ_h parameter is obtained by fitting to the experimental disjoining pressure data. We note here that the choice of the parameters for the hydration potential, σ_h, κ_h^{-1} and ℓ_h, used to predict the disjoining pressure curves reported in Fig. 2-13, is not unique. While the values of σ_h and κ_h^{-1} are quite reasonable as noted in the study by Brown et al. [4], the value of $\ell_h = 0.1$ nm, used here is smaller than the hydration shell diameter of 0.48 nm reported for the Ca^{2+} ion (see the tabulated hydration shell radius in Table V of ref. [160]). We note here that, in principle, one can choose a larger value of ℓ_h to be closer to the corresponding experimental value of the hydration shell diameter and still obtain similar disjoining pressure curves reported here by also concurrently changing the values of σ_h and κ_h^{-1}. However, we found that following such an approach does not change any of the overall trends of the disjoining pressure curves reported here.

As shown in Fig. 2-13, the disjoining pressures predicted by our complete theory are in good qualitative agreement with the experimental data of Plassard et al. for the five $Ca(OH)_2$ concentrations considered. For a 0.2 mM $Ca(OH)_2$ salt concentration, the predicted disjoining pressure is purely repulsive (positive) for all values of the surface separation distance (see the solid pink line) which agrees very well with the corresponding ex-

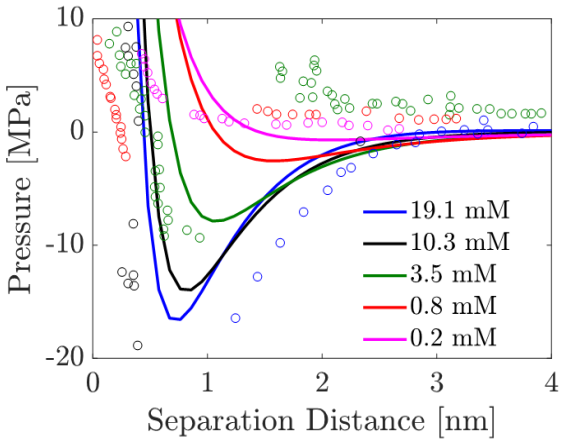

Figure 2-13: Comparison of the disjoining pressure versus the surface separation distance predicted by our complete theory (Eqs. 2.44 and 2.45, solid lines) with the experimental data of Plassard et al. [5] (circles) for the five $Ca(OH)_2$ salt concentrations shown.

perimental data (see pink circles). However, as the $Ca(OH)_2$ salt concentration increases, the experimental disjoining pressures become increasingly attractive (negative; see the red, green, black, and blue circles in Fig. 2-13), a trend which is captured reasonably well by our theory (see the red, green, black, and blue solid lines in Fig. 2-13). Note that the Hamaker constant for CSH reported by Plassard et al. is large when compared to the value for silica ($A_h = 2 \times 10^{-21} J$) reported in the literature. [161, 162] However, in the SI document we show that, even if the Hamaker constant is reduced to $A_h = 2 \times 10^{-21} J$, our theory can still capture the experimental trends with minor modification in the value of σ_h, as shown in Fig. S2.

Finally, it is noteworthy that although our complete theory for the disjoining pressure (Eqs. 2.44 and 2.45) contains several parameters: σ_h, κ_h^{-1}, ℓ_h, Γ and pK_b, these parameters are introduced in order to incorporate new physics into the EDL model, including hydration interactions and surface charge regulation. However, most importantly, no fitting parameter is introduced in our theory to model electrostatic correlations, because the dimensionless correlation length is determined directly based on Eq. 2.37. As Fig. 2-13 clearly shows, accurate modeling of electrostatic correlations is essential to predict the attractive electrostatic contribution to disjoining pressures between similarly-charged surfaces. This is, in fact, the main reason why the DLVO theory, which neglects electrostatic correlations,

fails to model surface forces/disjoining pressures even qualitatively, especially in solutions containing multivalent salt ions.

2.3.3 Conclusions

In our work on surface forces, we formulated a general theory of the disjoining pressure operating between two charged surfaces in a multivalent electrolyte solution. We used the BSK framework to model electrostatic correlations, and derived a closed-form expression for the contribution resulting from electrostatic correlations to the disjoining pressure. In stark contrast to the predictions of the PB mean-field theory, which always predicts a repulsive (positive) disjoining pressure operating between two similarly-charged surfaces, we showed here that the attractive (negative) disjoining pressure resulting from electrostatic correlations can dominate over an entropic repulsion, and thereby cause the overall disjoining pressure to be attractive (negative). Our theory predicts that both the magnitude as well as the sign of the disjoining pressure are strong functions of the counterion valency. Indeed, increasing the valency of the counterion significantly enhances the attractive pressure resulting from electrostatic correlations, thereby promoting attractions between similarly-charged surfaces in aqueous solutions containing divalent and trivalent counterions. On the other hand, we found that the dependence of the disjoining pressure on the valency of the coion is insignificant. We also showed that the disjoining pressure in the case of monovalent ions can still be attractive, provided that the charge densities on the two charged surfaces are sufficiently high to induce significant electrostatic correlations.

Another important limitation of the DLVO theory of colloidal stability and the PB model on which it is based, is that it predicts an enhancement of the repulsive disjoining pressure operating between two similarly-charged surfaces when the surface charge densities of the two surfaces increase. This is in stark contrast with the available experimental data [5], which conclusively show that the disjoining pressure operating between two similarly-charged surfaces becomes attractive upon increasing the surface charge densities of the two surfaces. Our new theory of the disjoining pressure can explain this experimental finding based on the existence of electrostatic correlations, which are neglected in

the DLVO theory.

In addition to modeling electrostatic correlations, we also included water-mediated hydration interactions and surface charge regulation in our theory to allow a direct comparison of the disjoining pressure predicted by our theory with the experimentally available disjoining pressure data. To this end, we showed that modeling the Stern layer self-consistently through water-mediated hydration interactions results in a significant repulsive contribution to the disjoining pressure, although the attractive pressure resulting from electrostatic correlations can still dominate over the repulsive pressures resulting from the entropy of the ions as well as from the hydration interactions. Furthermore, incorporation of surface charge regulation into our model enabled us to relate the surface charge density at the charged surface directly to the salt concentration in the electrolyte solution. Finally, we demonstrated that the disjoining pressure operating between calcium silicate hydrate layers in a calcium hydroxide salt solution, predicted by our theory is in reasonable qualitative agreement with the experimental data of Plassard et al. [5]. Therefore, we believe that the complete theory of surface forces presented here shows promise in overcoming the known limitations of the DLVO theory, especially for multivalent counterions.

In terms of future work, although the BSK model can describe electrostatic correlation effects at an interface, currently, it does not capture Bjerrum pair formation which can decrease the effective ion concentration in the bulk reservoir. [163] Further, the BSK model does not capture long-range oscillations in the charge density at high electrolyte concentrations. [164] This can be corrected by considering weighted concentrations in the expression for the entropy of ions (i.e. the $g\left(c_{+}, c_{-}\right)$ term in Eq. 2.28), as implemented in various theoretical approaches, including the classical density functional theory. [164, 165]

Finally, at separation distances of ~ 1 nm between the two charged surfaces, in addition to an attractive disjoining pressure resulting from electrostatic correlations, short-ranged attractive van der Waals interactions as well as repulsive hydration interactions can play important roles. A better estimation of the parameters used to model the van der Waals interactions, the hydration interactions, as well as of the scaling proposed for the correlation length, may be carried out through a systematic comparison of the disjoining pressure predicted by our theory with that available experimentally, as well as that obtained using

Monte Carlo and Molecular Dynamics simulations.

2.4 Summary of Findings

In this chapter, I demonstrated the role of electrostatic correlations in the screening structure of multivalent electrolytes. First, I presented physical arguments for the key boundary condition and correlation length parameter in the BSK theory via comparison to MC simulations, testing the validity of the theory for the one-component plasma and electrolytes. Then, within a general framework for mathematically predicting surface forces, I showed the impact of electrostatic correlations on surface forces. We find that the contribution of electrostatic correlations to the pressure leads to strong attraction in multivalent electrolytes.

In the next chapter, I will return to the interfacial layered structures at high electrolyte concentration, which are not directly captured by the BSK theory. Further, while we were able to include the contributions of hydration forces to colloidal interactions, we were not able to reproduce the specific structure of the confined solvent in the Stern layers. In Chapter 5, I will present further developments of a theory that predicts the detailed structures of solvent near charged interfaces.

Chapter 3

Interfacial Layering in Concentrated Electrolytes and Ionic Liquids

The following chapter is reproduced from our published paper on the interfacial layering of concentrated electrolytes and ionic liquids [7] with Dr. Zachary Goodwin, Dr. Michael McEldrew, Prof. Alexei Kornyshev, and Prof. Martin Bazant. I also reproduce our published work on the impact of interfacial layering on surface forces [166] for confined size-symmetric and size-asymmetric ionic liquids, in collaboration with Dr. Karina Pivnic, Dr. Martin Bazant, Dr. Michael Urbakh, and Dr. Alexei Kornyshev.

3.1 Overview

Ions in ionic liquids and concentrated electrolytes reside in a crowded, strongly-interacting environment, leading to the formation of discrete layers of charges at interfaces and spin-glass structure in the bulk. In the first section of this chapter, we propose a simple theory that accurately captures the coupling between steric and electrostatic forces in ionic liquids. The theory predicts the formation of discrete layers of charge at charged interfaces. Further from the interface, or at low charges, the model outputs slowly-decaying oscillations in the charge density with a wavelength of a single ion diameter, as shown by analysis of the gradient expansion. The gradient expansion suggests a new structure for partial differential equations describing the electrostatic potential at charged interfaces. We find quantitative

agreement between the theory and molecular simulations in the differential capacitance and concentration profiles.

Generally, ionic liquids (ILs) are composed of size-asymmetric anions and cations. The ordering of charge and density in ILs confined between charged interfaces underlies numerous applications of IL electrolytes. In the second section of this chapter, we analyze the screening behavior and the resulting structural forces of a representative IL confined between two charge-varied plates. Using both molecular dynamics simulations and a continuum theory, we contrast the screening features of a more-realistic asymmetric system and a less-realistic symmetric one. The ionic size asymmetry plays a non-trivial role in charge screening, affecting both the ionic density profiles and the disjoining pressure distance dependence. Ionic systems with size asymmetry are stronger coupled systems, and this manifests itself both in their response to the electrode polarization and spontaneous structure formation at the interface. Analytical expressions for decay lengths of the disjoining pressure are obtained in agreement with the pressure profiles computed from molecular dynamics simulations.

3.2 Charged Shell Model for Symmetric Ionic Liquids

3.2.1 Introduction

The spatial organization of ions in concentrated electrolytes leads to strong density and charge oscillations in the electric double layer (EDL) at charged interfaces [17, 167, 168]. When the concentration is beyond the dilute limit of the established Poisson-Boltzmann (PB) theory, one must account for correlation and packing effects, particularly as the Debye length approaches the size of a single ion [169]. Methods to correct the PB equations include the hypernetted-chain equation [47, 48, 170–173], mean-spherical approximation [174, 175], density functional theory [176–184], and dressed-ion theory [144, 185]. While many methods can accurately predict EDL profiles, they often lack the simplicity and physical transparency of the PB theory which they seek to correct [169].

More recently, with the rediscovery of room temperature ionic liquids (RTILs) [186,

187] and their applications to energy storage devices [167, 188], the task of understanding the interfacial structure in concentrated electrolytes has surged [189]. Describing the EDL of RTILs is particularly difficult because of the competition between strong steric and electrostatic forces [167], as illustrated in Fig. 1, and the fact that the expected Debye screening length is unphysically smaller than the diameter of an ion. In fact, the coupling of density and charge has been described as the ground state for a spin-glass Hamiltonian for ionic nearest neighbors (given their positions) [28], which is extremely difficult to describe with continuum equations. The interplay between ion position and charge order gives rise to the well known crossover from the overscreening regime (where decaying oscillations of charge density occur) to the crowding regime (where dense layers of countercharge accumulate at the interface before an overscreening tail) [190–193].

Perhaps one of the most popular descriptions of the overscreening versus crowding problem [190, 191] in RTILs is the Bazant-Storey-Kornyshev (BSK) theory [192]. There, a higher order gradient term in electrostatic potential was proposed, in addition to the commonly used lattice-gas excluded-volume excess chemical potential [6, 194]. As discussed

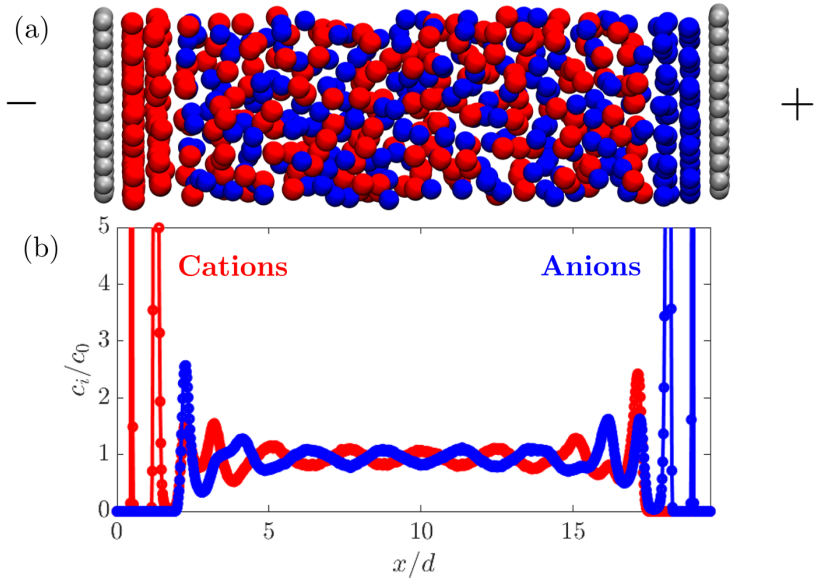

Figure 3-1: (a) Illustration of a concentrated, crowded electrolyte forming structured double layers at high surface charge density. The cations are red, the anions are blue, and the surface atoms are shown in gray, with negative charge on the left surface and positive charge on the right surface. (b) Corresponding concentration profile for a representative room temperature ionic liquid of equal-sized hard spheres ($c_0 = 5$ M, $d = 0.5$ nm, $\varepsilon_r = 10$, $q_s = 120$ μC/cm^2, $T = 300$ K).

in the previous chapter, the BSK theory has been shown to accurately describe electrostatic correlations for dilute electrolytes containing multivalent ions and counter-ion only systems [23, 195]. In the concentrated limit of RTILs, however, the BSK theory has some notable limitations: The screening is always short-ranged; the period of the oscillation is not necessarily the size of an ion; the number and extent of oscillations is significantly underestimated; and the formation of discrete charged layers at the interface is not captured. More recent work has suggested that the overscreening structure is a similar concept to the finite-size [196] and orientation of ionic aggregates [197] near charged interfaces.

In this chapter, we propose a free energy functional to describe the coupling between steric and electrostatic forces, and therefore, capture the “spin-glass" nature of charge-mass correlations in RTILs. The theory predicts discrete layering, extended overscreening with a longer screening length than the size of an ion with an oscillation period of one ion diameter, and quantitative agreement with simulated differential capacitance. Our free energy functional uses the weighted density approximation to describe the finite size of ions in both their electrostatic and steric interactions. Without fitting parameters, the theory has strong predictive capabilities, and it has a similar simplicity to the other modified-Poisson-Boltzmann approaches. While we explore the equilibrium properties at interfaces, the presented formulation could be extended to RTILs out of equilibrium, phase field crystal models, or systems including a structured solvent.

3.2.2 Theory

We modify the electrostatic and hard sphere packing free energies by representing them in terms of weighted densities of local concentrations, similar to weighted-density approximations including fundamental measure theory [54, 55, 198]. We rationalize these choices by treating the ions as hard, conducting, charged spheres of finite size, with point potential:

$$G_i(r) = \begin{cases} \frac{z_i e}{4\pi\varepsilon r} & r \geq R \\ \phi_0 & r < R \end{cases} \tag{3.1}$$

where ϕ_0 is a constant within a given ion, ε is the permittivity surrounding the ion (assumed constant in this work as an average effective background value), $z_i e$ is the charge of the ion, R is the radius of an ion, and r is the distance from the center of an ion. The physical basis for the Ashcroft pseudopotential character [199] of the Green's function is that the electrostatic potential within a finite-sized ion is effectively overwhelmed by the hard sphere potential within the ion. Therefore, the electrostatic potential is an undefined constant within the sphere and can decay as a $1/r$ potential only beyond the ionic radius. The linear integro-differential equation corresponding to this Green's function is:

$$\begin{aligned} \varepsilon\nabla^2\phi &= -\bar{\rho}_e(\mathbf{r}) = -\int d\mathbf{r}'\rho_e(\mathbf{r})w_s(\mathbf{r}-\mathbf{r}') \\ w_s(\mathbf{r}-\mathbf{r}') &= \frac{1}{4\pi R^2}\delta\left(R- \mid \mathbf{r}-\mathbf{r}' \mid\right) \end{aligned} \tag{3.2}$$

which is the key modified mean-field Poisson equation in our work. Here ϕ is the electrostatic potential, $\rho_e = \sum_i z_i e c_i$ is the charge density of ionic centers, c_i is the number density of the centers of species i, $\bar{\rho}_e$ is the weighted charge density (charge density calculated for the smeared charge of an ion over its surface), and w_s is the weighting function. Integrating contributions of the smeared charges results in the "actual" charge density which resides in the Poisson equation. While our weight function for the charge density resembles the choice of charge form factor in Ref. [196] for ionic screening in the bulk, we construct a mean-field equation that gives the ionic density at a flat interface at high charge density. Similar models were previously constructed for ionic intramolecular charge distributions [52, 200–206].

From the above modified Poisson equation, the electrostatic free energy density becomes:

$$\mathscr{F}^{\mathrm{el}}[\bar{\rho}_e,\phi] = \int d\mathbf{r}\Big\{-\frac{\varepsilon}{2}(\nabla\phi)^2 + \bar{\rho}_e\phi\Big\}. \tag{3.3}$$

The chemical part of the free energy contains an ideal entropic contribution: $\mathscr{F}^{\mathrm{id}}[\{c_i(\mathbf{r})\}] = \sum_i k_B T \int d\mathbf{r}\, c_i(\mathbf{r})\big[\ln(\Lambda^3 c_i(\mathbf{r})) - 1\big]$, where $k_B T$ is thermal energy and Λ is the thermal de Broglie wavelength [55]. There is also an excess contribution from crowding of the finite-sized ions. The Carnahan-Starling equation of state accurately describes the properties of hard sphere liquids. Here, we adapt it and assume that the local excess free energy depends

on volumetrically weighted densities, similar to fundamental measure theory [54, 55]:

$$\mathscr{F}^{\text{ex}}[\bar{c}_i(\mathbf{r})] = \frac{k_B T}{v} \int d\mathbf{r} \left[\frac{1}{1-\bar{p}} - 3\bar{p} + \frac{1}{(1-\bar{p})^2} \right] \tag{3.4}$$

where $\bar{p} = \sum_i v\bar{c}_i$ is the weighted volumetric filling fraction and $v = 4\pi R^3/3$ the volume of an ion. The weighted densities are defined by:

$$\begin{aligned} \bar{c}_i(\mathbf{r}) &= \int d\mathbf{r}' c_i(\mathbf{r}) w_v(\mathbf{r}-\mathbf{r}') \\ w_v(\mathbf{r}-\mathbf{r}') &= \frac{1}{v}\Theta\left(R - \mid \mathbf{r}-\mathbf{r}' \mid\right) \end{aligned} \tag{3.5}$$

where the scalar valued weighting function has units of inverse volume, and the function Θ represents a Heaviside step function. Therefore, the densities with which the mean field electrostatic interaction or hard sphere interaction occurs are computed with a quantized volume of one ion. Physically, the free energy is infinite as the volumetric-weighted filling fraction goes to one [1]. For the purposes of this study, the electrostatic weighting function will be homogenized on a surface of an ionic sphere, whereas the volumetric packing fraction will be homogenized over a volume of an ionic sphere.

Minimizing the free energy functional, we arrive at a modified PB equation, Eq. (3.2), where the distribution of ion (center) densities are determined by

$$c_i = c_{i,0} \exp(-z_i \beta e \bar{\phi} - \beta \bar{\mu}_i^{\text{ex}} + \beta \mu_{i,bulk}^{\text{ex}}) \tag{3.6}$$

with β as the inverse thermal energy, $\bar{\phi} = \phi * w_s$ and $\bar{\mu}_i^{\text{ex}} = \mu_i^{\text{ex}} * w_v$, (with $*$ denoting convolution), and excess chemical potential defined as $\beta\mu_i^{\text{ex}} = (8\bar{p} - 9\bar{p}^2 + 3\bar{p}^3)/(1-\bar{p})^3$ [2].

[1] The weighted density is necessary to describe the formation of discrete layers of charge at high surface charge density, which cannot be captured by local-density approximations.

[2] A continuum theory of this kind does not require distinguishing 'free,' 'paired,' or 'clustered' ions [29]. The ionic associations are reflected in oscillating charge density distributions.

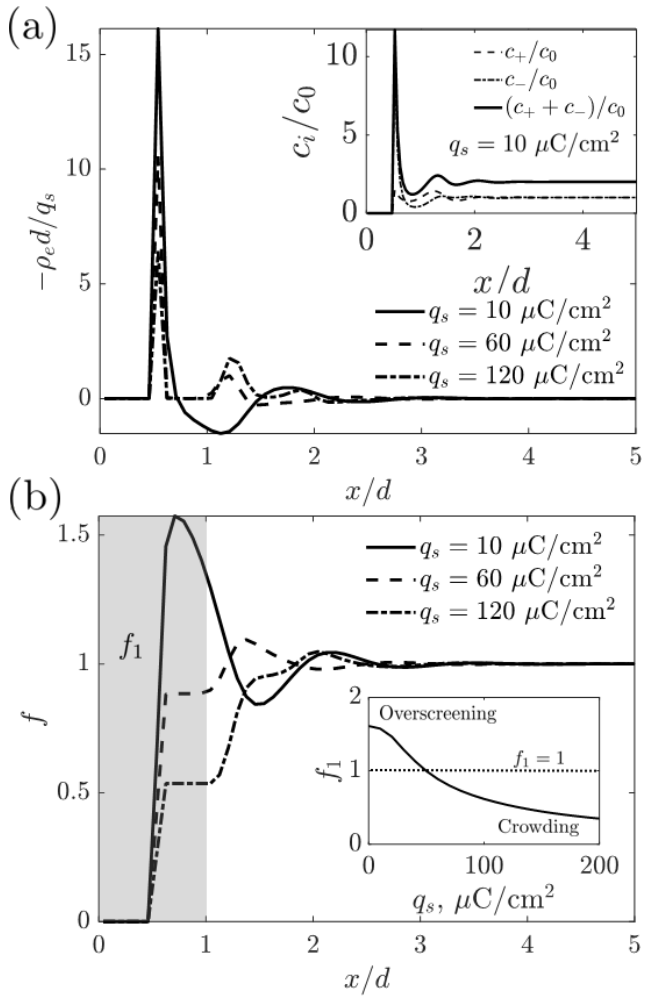

Figure 3-2: Layering of ions in a concentrated electrolyte or ionic liquid. (a) The overscreening 'signature:' the charge density of ions near a positively charged electrode scaled to the surface charge density on the electrode. The inset shows the concentration profile for each ion at $q_s = 10$ μC/cm^2, with oscillations in both the sum of concentrations and in the difference in concentrations. (b) The cumulative charge density as a function of the distance from the interface, with inset showing the extent of screening in the first layer of charge, f_1. Overscreening occurs when the net charge in the first layer is larger than the charge on the electrode.

3.2.3 Results and Discussion

We solve the above coupled integro-differential equations 3.2 and 3.6 at a flat electrode, with surface charge density, q_s, at $x = 0$. In this case, the standard boundary condition for the potential is applied $\hat{\mathbf{n}} \cdot \varepsilon \nabla \phi|_s = -q_s$. The local ionic densities (of centers) c_i and charge density (of ionic centers) ρ_e are assumed to be zero within one radius from the surface, from $x = 0$ to $x = R$, due to hard sphere exclusion. We solve for the area averaged density, and we therefore reduce all equations to be dependent on one coordinate, x. Numerically, we discretize the equations using a simple finite difference approach, similar to how the standard PB equations could be solved. More details on the numerics are provided in the Supplemental Material of [7].

For further intuition, we analyze a simple gradient expansion of the weighting functions that turns them into operators: $w_j = 1 + \ell_j{}^2 \nabla^2$, where ℓ_j is given by $\ell_s = d/\sqrt{24}$ for w_s and $\ell_v = d/\sqrt{40}$ for w_v, as derived in the SM of [7]. The corresponding free energy density is given by:

$$\mathscr{F}^{\mathrm{el}}[\bar{\rho}_e, \phi] = \int d\mathbf{r} \Big\{ -\frac{\varepsilon}{2}(\nabla\phi)^2 + \rho_e \phi - \ell_s{}^2 \nabla \rho_e \cdot \nabla \phi \Big\}. \tag{3.7}$$

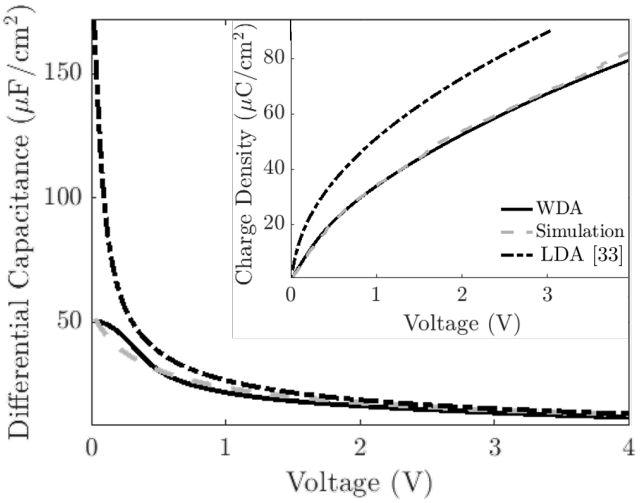

Figure 3-3: Differential capacitance of the EDL as a function of the applied voltage, for the weighted density approximation (WDA) in Eq. (3.2), simulations, and the local density approximation (LDA) formula [6], given in the Supporting MAterial of [7]. *Inset:* The charge density in the double layer as a function of the applied voltage. The parameters are identical to Fig. 3-2.

The leading order term in the expansion corresponds to a dipole density interacting with an electric field, interpretable as ionic pairs of effective volumetric dipole moment $\ell_s{}^2 \nabla \rho_e$, an effective polarization vector formed by gradients in the local charge density ρ_e [197]. Note that since the order of the differential equation increases, we need an additional boundary condition. We assume this to be $\mathbf{n} \cdot \nabla \rho_e|_s = 0$ in order to satisfy electroneutrality in the

differential equation, namely that: $\int d\mathbf{r}\rho_e(\mathbf{r}) = -\int d\mathbf{r_s} q_s(\mathbf{r_s})$.

The above gradient expansion does not reproduce the profile at the initial contact of the ionic liquid with the surface. In particular, the differential form cannot capture the discontinuous contact point at $x = R$, and so the solutions are shifted by one ionic radius. Even so, the gradient expansion is valid farther from the surface and is useful for deriving analytical approximations for the theory. Furthermore, the differential form may be easier to apply to problems in diverse applications such as electrokinetics [58], colloidal interactions [23], or electrochemical storage [61, 67] than the full integro-differential theory [207]. As an example, we will first analyze the gradient expansion of the continuum theory in terms of its limiting linear response behavior, which asymptotically matches the behavior of the full integral equation far from the interface. Further comparisons are included in the SM of ref. [7].

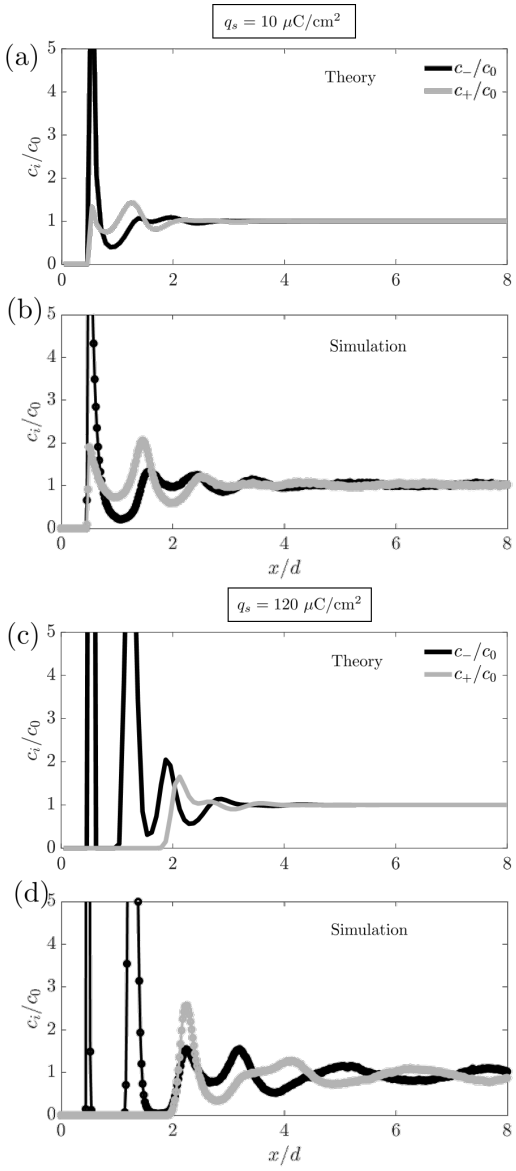

Figure 3-4: Comparison of theory (a,c) and simulation (b,d) concentration profiles for two different charge densities: $q_s = 10\ \mu$C/cm^2 and $q_s = 120\ \mu$C/cm^2. The electrolyte has the same parameters as in Figs. 3-2 and 3-3 .

In linear response, the equation for the potential is:

$$\lambda_D^2 \nabla^2 \phi - (1 + \ell_s^2 \nabla^2)^2 \phi = 0. \qquad (3.8)$$

where λ_D is the Debye length.While the equation is fourth order, similar to the linearized BSK equation, it has different decaying modes due to an additional second order term.

The eigenvalues of the above differential equation, denoted by the inverse decay length $\kappa_s = 1/\lambda_s$, have the form:

$$\kappa_s \lambda_D = \frac{1 \pm \sqrt{1 - 4(\ell_s/\lambda_D)^2}}{2(\ell_s/\lambda_D)^2}. \tag{3.9}$$

Note that the form of Eq. (3.8) bears some resemblance to the Swift-Hohenberg equation [208], commonly used to describe pattern formation and other phase-field crystal models [209]; here electrostatics and finite size drive the pattern formation. When $\ell_s/\lambda_D > 1/2$, oscillations appear in the solution, and in the limit of $\ell_s/\lambda_D \gg 1/2$, the screening length takes the form: $\kappa_s \lambda_D = \lambda_D^2/\ell_s^2 \pm i\lambda_D/\ell_s$. At high concentration, the ions will therefore form charge density layers on the scale of the ionic size, with period of 1.28 d, similar to the result from simulations. In strongly correlated regimes, the real part of the screening length will scale as: $\ln[\mathrm{Re}(\lambda_s/\lambda_D)] = 2\ln(d/\lambda_D) + \mathrm{const}$, increasing with concentration. This result is qualitatively in agreement with surface force experiments [210,211], but they find a scaling factor 3 rather than 2. They also measure monotonic decay, and not decaying oscillations in the overscreening tail as predicted by the theory. Note that the mass density oscillations also have a characteristic decay length, but it is decoupled from the electrostatic potential at linear response for ions of the same size, as discussed in the SM of [7]. The discrepancy in exponents may be due to the symmetric size of ions in the analysis here, which limits the coupling.

Next, we compute the ion concentration and density profiles as a function of charge density for some model parameters ($c_0 = 5$ M, $d = 0.5$ nm, $\varepsilon_r = 10$, $T = 300$ K), shown in Fig. 3-2. Note the parameters shown here are meant to be representative of RTILs, but the simplifying assumptions of similarly-sized cations and anions prevent a direct comparison with experimental results for asymmetric ionic liquids [3]. We also present the cumulative screening charge, defined as $f(x) = -\int_0^x \rho_e(x')dx'/q_s$. At low surface charge density, the first layer of charge has about 57% more counter charge than the surface charge. Subsequent layers of alternating charge are formed. At low surface charge density, the ion

[3]The symmetric size limits the possible parameter space due to maximal packing constraints, leading to a high differential capacitance at zero charge for both the theory and the simulation relative to experiments on real RTILs.

concentrations themselves are affected by overall structuring of the fluid ($c_+ + c_-$) due to packing at the interface. At higher charge density, the inhibitive force of packing at the interface decreases the extent of overscreening in the first layer, f_1. Eventually, as the charge density exceeds the total amount of charge that can be stored in a single layer of ions, a secondary layer is formed. When this occurs, the extent of overscreening becomes determined by the renormalized charge on the interface. The chosen simulation parameters are in the strongly oscillating regime $\ell_s/\lambda_D \approx 2.1$, meaning that the far range screening tail has approximate wavelength of one ionic diameter and long decay length.

It is instructive to compare the predictions of the theory to MD simulations of a Lennard-Jones electrolyte with the same parameters. The differential capacitance, $C = \mid dq_s/d\phi_0 \mid$ is evaluated in Fig. 3-3 as a function of the potential at $x = 0$, ϕ_0. Compared to simulations, the weighted density theory captures the low capacitance at zero charge and the decay of capacitance at large voltages. The theory presented here agrees much better with simulations compared to the local density approximation formula [6, 212]; the improvements in the crowding regime, at large voltages, are due to use of the weighted Carnahan-Starling approximation rather than the simple local density approximation formula, both obeying, however, the $V^{-1/2}$ limiting law [6, 207]. In Fig. 3-4, the layering structure is compared between theory and simulation for low and high charge densities. The theory is able to qualitatively match the structuring in the simulations, with charge density oscillations and eventually layers of the same charge at high charge density. Even so, the wavelength in the charge density oscillations are off by about a factor of 1.3. Such a discrepancy could be captured by changing the form of w_s to extend beyond the size of the ionic radius, but modifications to w_s are not considered in this work [4].

3.2.4 Conclusions

The developed continuum theory captures the key points in the interplay between overscreening and crowding in EDL of ionic liquids, including: 1) Decaying charge density profiles near the electrode and the overscreening effect as a consequence of molecular layering, 2) The onset of crowding through the shift of the overscreening to a third, and then

[4] A different form of w_s implies different physical assumptions for the Green's function in equation 3.1

subsequently further layers, and 3) The emergence of the long range screening tail in ultra-concentrated ionic systems.

In a separate study [213], our collaborators led by Dr. Hao-Kun Li and Prof. Arun Majumdar were able to directly observe the crowded structure of ions near charged interfaces. Using the model of nonlocal crowding and similar simulations to those performed here, we were able to reproduce the main features of the ionic arrangements near the charged surface. The combination of experiment, simulation, and theory demonstrates the importance of including the nonlocal crowding effect to accurately predict the interfacial structure of the highly concentrated electrolyte at the surface.

3.3 Structural Forces in Ionic Liquids: Role of Ionic Size Asymmetry

3.3.1 Introduction

Room-temperature ionic liquids (ILs) are molten salts composed of majorly asymmetrically sized anions and cations. [214, 215] ILs have wide electrochemical stability windows, low vapor pressure, and are thermally stable. [167, 216] Due to their exceptional properties, they are used in energy storage applications including supercapacitors and batteries, [167] as solvents for reactions and for catalysis, [215] and can also be employed as electrotunable lubricants. [217, 218] In these applications, the ILs can be confined in charged nanopores down to the nanometer scale, in which the extent of the nanopore confinement and its polarity determine the interfacial IL structure and charge layering. [219–222]

In order to optimize the interfacial behavior of ILs for their many applications, researchers need to accurately model ILs. This is done either through computationally expensive atomistic simulations or via sophisticated theoretical approaches, which go beyond standard mean-field theories of dilute electrolytes. In such highly concentrated electrolytes as ILs, the dilute solution theory is predestined to fail since ILs form structures determined by dense packing of ions in the *crowding* [6, 17, 194, 223–225] (layering of ions of the same charge at highly charged electrodes) and *overscreening* [190, 226] (alternating layers of op-

posite charge at weakly charged electrodes) regimes. Most egregiously, the dilute solution theoretical description does not take into account the ionic size. [15–17] In order to capture these screening features, multiple continuum theories have been developed to include the finite size of ions in their steric and electrostatic interactions, especially for concentrated systems at high voltages. [7, 67, 181, 192, 227, 228] However, most theoretical models of these systems have been developed, for 'simplicity,' for the case of ions of the same size. This was natural to do as a start, although most ILs exhibit strong size asymmetry. In theories, ion asymmetry has typically been studied within the mean field approach that accounted for crowding, particularly in the explanation of the asymmetry of the double-layer differential capacitance curves in such systems. [6, 167, 229–233] In molecular dynamics (MD) simulations, ion asymmetry has been either specially introduced [226] or naturally included with fully atomistic or coarse grained models of ions [167]. Certain classical Density Functional Theories (DFT) have also been applied to asymmetric ILs, predicting interfacial layering in line with MD simulations. [181,234] These studies of ILs draw from the wide body of theoretical research on primitive model electrolytes either through classical DFT [52, 182, 235–237] or integral equation theories. [46, 171, 238–241] In fact, earlier work from Greberg and Kjellander revealed the role of asymmetry in the contact behavior and decay of bulk correlations in primitive model electrolytes. [242]

Surface Force Apparatus (SFA) and Atomic Force Microscopy (AFM) measurements have emerged as the main experimental tools to investigate the nanoscale structure of interfacial liquids, [243] including ILs. [219, 220, 244, 245] While in SFA experiments the mica surfaces are spontaneously negatively charged, the AFM setup can incorporate a conductive electrode, allowing for the independent control of charges on the surfaces. Both SFA and AFM measurements have been performed in a variety of ILs, and in all cases decaying oscillatory forces were observed, with an oscillation period of the order of an ion pair diameter (usually dominated by the largest ion diameter), indicative of the underlying alternating charge layering structure. [220, 221, 245, 246] At even longer ranges than the oscillatory forces, SFA measurements found an additional monotonically decaying 'tail' of the force, both in concentrated electrolytes and ILs. [210, 211, 246, 247]

Despite of these findings, however, simulations and theoretical descriptions of primi-

tive model electrolytes have not succeeded to recover the existence of such a tail. [235] Long-range electrostatic forces in the dilute limit can be described by analytical formulas derived from Debye-Huckel linearization, but such simple analytical equations are not readily available for the oscillatory structural forces. While the above-mentioned theories presented sophisticated analyses of the role of asymmetry on interfacial ionic behavior, they still did not present simplified, explicit formulas for the oscillatory IL structure and structural forces, nor did they directly validate the role of asymmetry on the structural forces and screening structure by MD simulations of the concentrated IL limit in varying extents of confinement. Instead of directly applying theoretically-derived formulas, the experimental oscillatory forces are typically empirically fitted to an oscillatory decaying function. Therefore, the physical and quantitative interpretation of oscillatory structural forces in experiments could greatly benefit from analytical formulas derived within theories of concentrated, and generally asymmetric ILs.

In the present work, we go further into investigating the double layer structure of asymmetric IL under confinement between equally-charged surfaces using both MD simulations and an advanced continuum theory. The ion density profiles and disjoining pressure curves that we calculate based on our original theory [7] show qualitative and quantitative agreement with the results of simulations for a range of surface charge densities and surface separations. By a comparison of a representative IL with asymmetric ions to an IL composed of size-symmetric ions, we demonstrate that the size asymmetry strongly determines the ionic layering structure between two flat charged interfaces. Even at *zero charge of the electrode* there is an entropy-driven 'preferential adsorption' of smaller ions, which results in *spontaneous layering of positive and negative charges near the electrode*. The order of layering may, in fact, be changed by specific adsorption of any of these ions, which is not included in our simple model, but which could easily be modeled by adding a specific term in the interaction potential between the ions and the surface. In whatever direction that effect could have shifted the result, it would act at the background of the noted effect.

Furthermore, the size asymmetry leads to a strong coupling of charge density and number density oscillations even far from the interface that is absent for the symmetric case. Analytical approximations are shown to reproduce the simulated modes of decaying oscil-

lations in the disjoining pressure at the nanometer scale. However, neither the simulations nor the theory contain any evidence of an abnormally long decay length or long range exponential tails. Nevertheless, the main value of the theory lies in the analytical description of the decaying modes of the structural forces and their dependence on surface charging in terms of the IL physical properties. The numerical predictions of the full nonlinear theory can be generated with relatively small computational cost compared to atomistic simulations.

All-in-all, the presented theory demonstrates that the ion asymmetry in electrostatics and steric interactions are essential in describing the double layer structure for ultraconcentrated, asymmetric ILs. These findings therefore signify an important step in the advancement of our understanding of the screening behavior and the resulting structural forces of ultraconcentrated, asymmetric ILs as well as of solvent-in-salt systems, under nanoconfinements.

3.3.2 Simulations and Theory

An IL is approximated in both MD simulations and a continuum theory, first with asymmetric anion and cation sizes, and then with an equal anion and cation size, as charged Lennard-Jones (LJ) spheres. Such level of simplification has been chosen first of all to investigate the effects not obscured by any chemical complexity of the ions, and secondly because this would be most straightforward comparison between the simulations and the theory that we use here. We highlight the properties and parameters of the MD simulations and the continuum theory before applying them to model the IL and the resulting disjoining pressures. It should be noted that the coordinate system here is rotated compared to the previous section in this chapter such that the normal coordinate is now the z-coordinate instead of the x-coordinate, in order to be consistent with the orientation convention in the simulations.

Simulation Details

Within this minimal model, the ions are represented as a 1:1 mixture of oppositely and singly charged LJ spheres, [226, 248, 249] as shown in Figure 3-5. The concentration of both anions and cations in the simulation box is $c_0 = 4.586$ M and the absolute temperature is $T = 600$ K (as usual elevated temperature is taken when 'experimenting' with charged LJ-spheres, because at room temperature dense plasma of such spheres freezes out). In our model, we account for the electronic polarizability of the ions in an effective manner. For this, we have set the background permittivity to be $\varepsilon = 2\varepsilon_0$, [248, 249] where ε_0 is the permittivity of free space. The ions interact through LJ and coulombic potentials, where the size asymmetry of the ions is controlled by adjusting their diameters through the LJ parameter σ_{ij} for species i interacting with species j, or σ_i when $i = j$. The ion sizes that we consider here for the asymmetric system are $\sigma_- = 0.7$ nm and $\sigma_+ = 0.35$ nm, and the ion size for the symmetric system is $\sigma_- = \sigma_+ = 0.58$ nm, such that the filling fraction is approximately equal in both systems, making $\sum_i \sigma_i^3 c_0$ unchanged. While we choose spherical ions in our model for simplicity, we still include attractive dispersion interactions. This is done to be able to capture a more realistic representation of the IL, as these attractive dispersion interactions are active in real ILs. Therefore, in our simulations, the cutoff distance of the LJ potential is set to be as long as 1.8 nm. Even so, as reaffirmed in the theoretical predictions which do not incorporate dispersion interactions, the main balance guiding the structural forces is the interplay between the ionic charge and ionic finite size.

Two parallel plates in the x-y plane are immersed in a bulk of IL. We consider flat surfaces comprised of LJ spheres in contact with the confined liquid, and a lattice parameter of mica. [248] Performing constant charge simulations, the surface charge on each plate is varied between $q_s =$ -0.12 C/m^2 and $q_s =$ +0.12 C/m^2. In the simulations, the image charge interactions are not taken into account. Simulations of IL nanofilms (1-10 nm thick) showed that the effect of electrode polarizability (image charges) on the vertical and lateral structure of the confined liquids is insignificant at practically feasible applied voltages. [250–252] Since they involve solving for the fields inside the confining surfaces, image charge interactions can lead, in principle, to the depletion of ions in the nanogap for a single layer of ions confined between two uncharged or slightly charged dielectric walls. In

this case, the ions, instead of 'seeing' their counterions nearby, see their own weak images in the side walls (the situation may be different for metallic surfaces [253]). However, for larger separation distances between the surfaces, there is a weak dependence of the IL's structuring on the electrode polarizability which is explained by the screening of image charge interactions by the first layer of ions. [254] Therefore, in our work, we choose not to include image charge interactions, as we are particularly interested in isolating the structural layering of the liquid, which occurs even without the complexity that is added with the introduction of image charge interactions.

In the simulations, for each fixed surface charge the ionic density profiles between the surfaces are computed at fixed separation distance, and the separation distance is varied to generate a pressure curve. Expansion on the simulation details and the used methods can be found further in the Supporting Information (SI) of ref. [166].

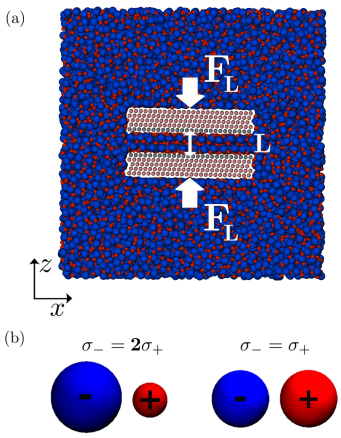

Figure 3-5: MD simulations. (a) Snapshot of the asymmetric IL immersing two charged surfaces in a fully periodic simulations box. The surfaces are pushed together along the z-direction with a normal force F_L to ultimately calculate the pressure as a function of the separation distance, L. (b) The ionic sizes, characterized by the LJ diameter, σ_i, for the (left) asymmetric and (right) symmetric systems.

3.3.3 Theoretical Derivation

The theory is based on an approximation of the Helmholtz free energy of a system of asymmetric, hard-sphere 1:1 electrolyte with a constant background permittivity, ε, the primitive model. [3, 235, 255, 256] The phenomenological basis for the theory is that the electrostatic and hard sphere components of the free energy of the system can be expressed in terms of locally homogenized quantities of the ion densities, the weighted-density approximation (WDA). The distinguishing feature of this model, as opposed to other similar classical DFT approaches, [257] is that the electrostatic contribution to the free energy is directly expressed in terms of

weighted ionic densities. [7, 200, 204] The model is a generalization of the density functional for ILs presented in Ref [7] that was reproduced the previous section of this chapter.

The core ingredients of the theory that allow us to capture the discrete layering in ILs are (i) representing the ions as delocalized shells of charge in their electrostatics and (ii) encoding the hard sphere packing of ions in their excess chemical potential. While these effects introduce some mathematical complexity, they have straightforward physical interpretations and do allow for some analytical progress, especially in the linear response limit.

To start, the free energy of the system can be broken down into three contributions, an ideal part $\mathscr{F}^{\text{id}}$, an excess part $\mathscr{F}^{\text{ex}}$, and an electrostatic part $\mathscr{F}^{\text{el}}$:

$$\mathscr{F} = \mathscr{F}^{\text{id}} + \mathscr{F}^{\text{ex}} + \mathscr{F}^{\text{el}} \tag{3.10}$$

The ideal contribution is related to the entropy of an ideal gas:

$$\mathscr{F}^{\text{id}}[\{c_i(\mathbf{r})\}] = \sum_i k_B T \int d\mathbf{r}\, c_i(\mathbf{r}) \left[\ln(\Lambda_i^3 c_i(\mathbf{r})) - 1 \right] \tag{3.11}$$

where $k_B T$ is thermal energy and Λ_i is the thermal de Broglie wavelength of ion i, and c_i is the number density of ion i. Here, we incorporate a phenomenological, simplified version of Fundamental Measure Theory (FMT) [55] for the hard sphere contribution to the free energy. The advantage of this approach is that more compact expressions can be derived for the ionic excess chemical potential in terms of fewer weighting functions, aiding in the process of deriving simplified analytical approximations to the theory.

The phenomenological excess free energy we define is given by:

$$\mathscr{F}^{\text{ex}}[\bar{c}_i(\mathbf{r})] = \frac{k_B T}{\hat{v}} \int d\mathbf{r} \left[\frac{1}{1-\bar{p}} - 3\bar{p} + \frac{1}{(1-\bar{p})^2} \right], \tag{3.12}$$

where $\bar{p}$ is the weighted volumetric filling fraction,

$$\begin{aligned} \bar{p} &= \sum_i v_i w_{v,i} * c_i \\ w_{v,i}(\mathbf{r}-\mathbf{r}') &= \frac{1}{v_i}\Theta\left(R_i - \mid \mathbf{r}-\mathbf{r}' \mid\right) \end{aligned} \tag{3.13}$$

where R_i is the effective hard-sphere radius of the ion, $v_i = 4\pi R_i^3/3$ is the volume of the ion, $*$ denotes a convolution, $w_{v,i}$ is the volumetric weighting function, Θ represents the Heaviside step function, and the filling-fraction weighted volume $\hat{v}$ is given by:

$$\hat{v} = \frac{\sum_i v_i^2 c_{i,0}}{\sum_i v_i c_{i,0}} = \frac{\sum_i v_i^2 c_{i,0}}{\eta}. \tag{3.14}$$

Here, $c_{i,0}$ is the bulk concentration of species i and η is the bulk filling fraction, $\eta = \sum_i v_i c_{i,0}$. By construction, the key criteria that the simplified form of the hard sphere excess free energy satisfies are: (i) it retains the Carnahan-Starling equation of state [258] for the limit of symmetric ions or where one ionic species becomes vanishingly small while the other is of finite size, and (ii) it maintains the same singularities as the FMT functional. Physically, the model captures the packing of all asymmetric species, and the filling fraction of each species is homogenized over the volume of its effective spherical size.

The electrostatic part of the free energy in a medium with dielectric constant ε is expressed in terms of the electrostatic potential, ϕ, and the homogenized charge density, $\bar{\rho}_e$ [7]:

$$\mathscr{F}^{\mathrm{el}}[\bar{\rho}_e, \phi] = \int d\mathbf{r}\Big\{ -\frac{\varepsilon}{2}(\nabla\phi)^2 + \bar{\rho}_e\phi \Big\}. \tag{3.15}$$

This corresponds to the modified form of the Poisson equation, via minimization of the functional with respect to the electrostatic potential potential, $\delta\mathscr{F}/\delta\phi = 0$:

$$\begin{aligned} \varepsilon\nabla^2\phi &= -\bar{\rho}_e = -\sum_i z_i e c_i * w_{s,i} \\ w_{s,i}(\mathbf{r}-\mathbf{r}') &= \frac{1}{4\pi R_i^2}\delta\left(R_i - \mid \mathbf{r}-\mathbf{r}' \mid\right) \end{aligned} \tag{3.16}$$

where z_i is the valency of ion i, e is the elementary charge, and $\delta()$ denotes the delta function of 1D argument, such that each ionic weighting function $w_{s,i}$ corresponds to homoge-

nizing over the surface of the ionic spheres. The weighted ionic concentrations signify that the ions act as shells of charge that interact with the local electrostatic potential.

Minimizing the free energy functional with respect to concentration, the ion densities at equilibrium satisfy:

$$c_i = c_{i,0} \exp(-z_i \beta e w_{s,i} * \phi - \beta w_{v,i} * \mu_i^{\mathrm{ex}} + \beta \mu_{i,b}^{\mathrm{ex}}) \tag{3.17}$$

with β as the inverse thermal energy and excess chemical potential, μ_i^{ex}, defined as:

$$\beta \mu_i^{\mathrm{ex}} = \frac{v_i}{\hat{v}} \frac{8\bar{p} - 9\bar{p}^2 + 3\bar{p}^3}{(1-\bar{p})^3}, \tag{3.18}$$

taking on a value in the bulk, $\mu_{i,b}^{\mathrm{ex}}$, of:

$$\beta \mu_{i,b}^{\mathrm{ex}} = \frac{v_i}{\hat{v}} \frac{8\eta - 9\eta^2 + 3\eta^3}{(1-\eta)^3}. \tag{3.19}$$

We again note that $v_i = \hat{v}$ for the case where (i) the two ions have the same size or (ii) when one ion is vanishingly small while the other has finite size. These limits give the standard expression for the Carnahan-Starling equation of state. For asymmetric ILs in which the ions both have significant packing effects, the formula effectively interpolates between these two limits.

We solve the above coupled integro-differential equations 3.16 and 3.17 for the ionic densities and electrostatic potential between two flat electrodes, with equal surface charge density, q_s. In this case, the standard boundary condition for the potential is applied $\hat{\mathbf{n}} \cdot \varepsilon \nabla \phi|_s = -q_s$. In the theory, the surface is assumed to be perfectly flat and hard with smeared charge density, so the space corresponding to the surface atoms is subtracted. In the theory, the representative surfaces are defined at $z = \pm L/2 \mp R_s$, where L is the distance between surface atom centers in the simulation and R_s is the surface atom radius. Therefore, the theoretical ionic densities are zero for $z < -L/2 + R_s + R_i$ and $z > L/2 - R_s - R_i$. We solve for the area averaged density, and we therefore reduce all equations to be dependent on one coordinate, z. [7] Numerically, we discretize the equations by finite difference.

To compare the simulations and theory results, we determine a consistent definition of

the ion diameter in the theory, d_i, compared to the σ_{ij} values of the simulation. Since the LJ interaction is not exactly the same as the hard sphere interaction assumed in the theory, the ions in the simulation can overlap slightly with the surface and each other below a center to center separation of σ_i. We assume that the effective ionic diameter in the theory is set by a cutoff criterion, where the LJ potential is $U_{LJ} = 0.3k_BT$, corresponding to $d_i \approx 0.9\sigma_i$. The sensitivity of the results with respect to this criterion is discussed in the SI.

The pressure between the two equally charged surfaces as a function of separation distance is calculated as [259–262]:

$$P = -\frac{\delta(\Omega/A)}{\delta L} \tag{3.20}$$

at constant temperature and reference chemical potential (constant bulk ionic concentrations), where A is the area of the surfaces, and Ω is the grand potential

$$\Omega = \mathscr{F} - \sum_i \int d\mathbf{r}\Big\{\mu_{i,b}c_i\Big\} \tag{3.21}$$

and $\mu_{i,b}$ is the bulk chemical potential. By definition, the pressure corresponds to the change in the grand potential per differential change in the system volume, assuming fixed area of the confining surfaces. The values of Ω/A for a range of separation distances are numerically computed, and we then numerically differentiate this function to calculate the disjoining pressure. The zero value for the disjoining pressures corresponds to the bulk reference value as $L \to \infty$, $P_\infty = 0$.

3.3.4 Results and Discussion

Ionic charge and density profiles

We start by comparing in Figure 3-6 the ionic densities calculated from the simulations (circles, ○) and theory (lines, —) as the ionic layers are squeezed out (columns, panels a-f) at varying surface charge/polarities (rows). Beyond simply plotting the density of ionic centers, c_i, the layering in the charge is plotted with the cumulative charge function

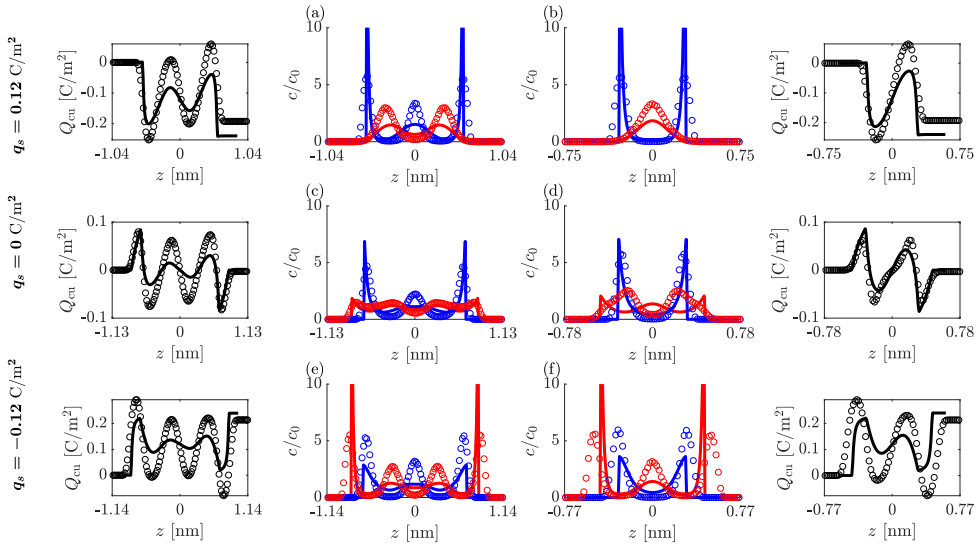

Figure 3-6: Charge and ion density profiles in asymmetric ILs between the charged plates. Rows correspond to the fixed surface charge densities of (a-b) $q_s = 0.12$ C/m^2, (c-d) $q_s = 0$ C/m^2, and (e-f) $q_s = -0.12$ C/m^2. Columns correspond to the squeeze out of a central electroneutral layer between two stable states where (a, c, e) $L \approx 2.2$ nm and (b, d, f) $L \approx 1.5$ nm. Cumulative charge functions are plotted to the left or right of the corresponding concentration profile plot. Markers, (○): simulations; Lines, (—): theory. Color coding: (—) - anions, (—) - cations.

(accompanying plots to the left and right of panels a-f), $Q_{\mathrm{cu}}(z)$, defined as:

$$Q_{\mathrm{cu}}(z) = \int_{-L/2}^{z} \sum_i z_i e c_i(z')\,\mathrm{d}z'. \tag{3.22}$$

Analyzing Figure 3-6, the theory captures the main features of the charge ordering found in the simulations, particularly when plotted in terms of $Q_{\mathrm{cu}}(z)$. However, the theory does not accurately predict the magnitude of the overscreening as the separation distance increases, and underpredicts the decay into the bulk for the widest separations. Interestingly, the theory is more in line with simulations when describing the charge ordering at small separations between the plates, where the bulk correlations of the ions are the least influential. At zero surface charge (panels c and d), both the theory and the simulations show that the smaller ion, the cation in our study (displayed in red color, —), can access the surface more easily. For negatively charged surfaces (panels e and f), the small cation concentration is enhanced drastically near the surfaces, maintaining the same number of layers as in the zero charge case. At positive surface charge (panels a and b), however, the cation is pushed out of the region closest to the surfaces, resulting in fewer layers of ions in this limit. The main discrepancies between the theory and simulations is the sharpness and magnitude of the ionic density peaks, arising because the theory assumes hard-sphere interactions while the simulations assume LJ interactions. Further, whereas the theory obeys electroneutrality within the space between the two charged surfaces ($Q_{\mathrm{cu}}(z = L/2) = -2q_s$), the simulations exhibit some partial charge screening from the IL outside the gap, so that $Q_{\mathrm{cu}}(z = L/2) \neq -2q_s$.

We can then contrast the screening with asymmetric ions to screening with symmetric ions. In Figure 3-7, the ionic density profiles for the symmetric system are shown, for increasing negative surface charge and two separation distances. Since a change in the surface polarity gives identical profiles (up to the identity of the symmetric ions) only negative surface charge values are shown. Again, overall, the theory captures ordering in charge and density between the charged surfaces quite well, with close agreement for the smallest separation distances. At zero surface charge (panels a and b), no local ionic charge density occupies the gap, since neither ion preferentially accesses the surface. The ions

then form overlapping layers, which turn into alternating ones when increasing the surface charge (panels c-f). Overall, the overscreening structure remains similar as the surface charge magnitude increases, since the surface charges tested are not large enough to enter the crowding regime. Additional charge and density profiles with varying surface charges and separation distances for both the asymmetric and symmetric systems are presented in the SI.

Disjoining pressure profiles

Simulations and integro-differential theoretical results: Finally, the role of ionic asymmetry on structural forces is demonstrated in Figure 3-8. Pressure profiles are plotted as a function of the surface separation distance for the asymmetric (panels a-c) and symmetric (panels d-f) systems, where they are confined between negatively (panels a and d), uncharged (panels b and e), and positively charged surfaces (panels c and f). Additional

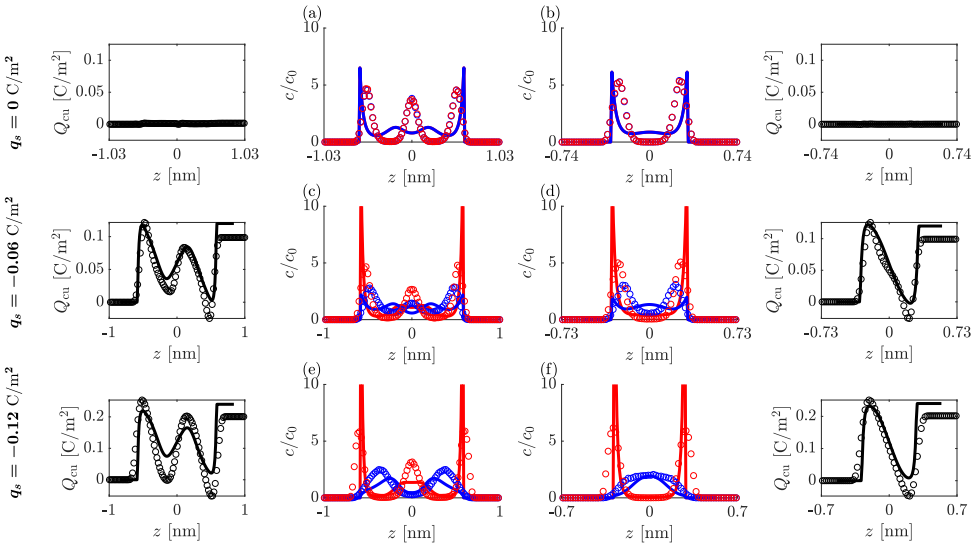

Figure 3-7: Charge and ion density profiles in symmetric IL. Rows correspond to the fixed surface charge of (a-b) $q_s = 0$ C/m^2, (c-d) $q_s = -0.06$ C/m^2, and (e-f) $q_s = -0.12$ C/m^2. Columns correspond to the squeeze out of a central electroneutral layer between two stable states where (a, c, e) $L \approx 2$ nm and (b, d, f) $L \approx 1.4$ nm. Cumulative charge functions are plotted to the left or right of the corresponding concentration profile plot. Markers, (○): simulations; Lines, (—): theory. Color coding: (—) - anions, (—) - cations.

results with varying surface charge magnitudes are presented in the SI. Comparing the theory to the simulations, overall, there is an agreement between the MD simulation pressure profiles (black markers, ○ in Figure 3-8) and the full integro-differential results from the theory (the orange line — represents the asymmetric system and the purple line — represents the symmetric one). This agreement is most pronounced at the smallest separation distances, where the pressure magnitudes are the most significant. The main discrepancy, as similarly noted already for the ionic density profiles, is that the oscillations decay more quickly for the theory than those that are observed in the simulations. While the pressure profiles in Figure 3-8 appear to be similar for both systems, there are still significant differences with respect to surface charge magnitude and sign. Referring specifically to the simulated pressure profiles (black markers, ○ in Figure 3-8), as expected, the amplitude of the pressure oscillations increases as the surface charge magnitude increases for both the asymmetric and the symmetric systems. However, for the asymmetric system, the pressure oscillation amplitudes are larger for the positive surface charge polarity, due to the larger

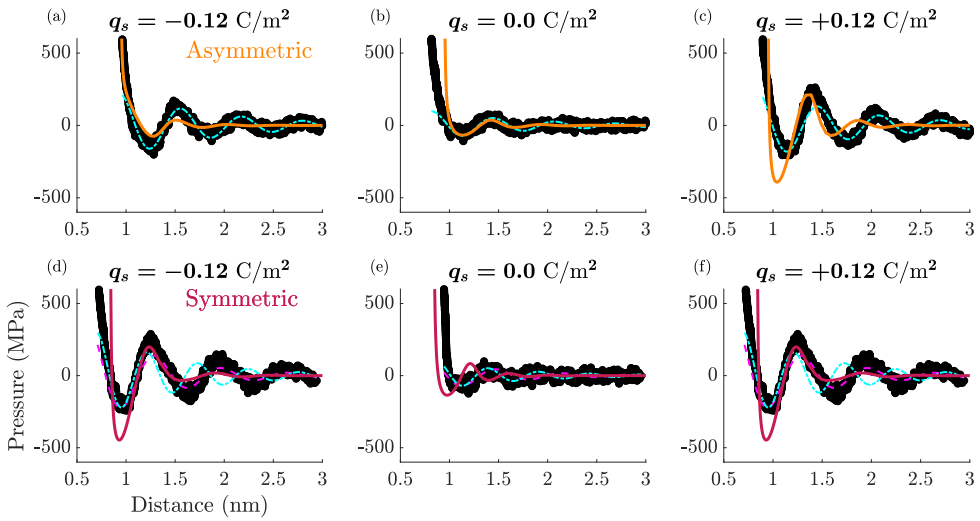

Figure 3-8: Disjoining pressure profiles. (a-c) Asymmetric system and (d-f) symmetric system for (a, d) negative, (b, e) uncharged, and (c, f) positive surfaces. The black markers (○) are the MD simulation data points. The solid lines are the full, nonlinear integro-differential theory, where (——) corresponds to the asymmetric system and (——) corresponds to the symmetric one. The other dashed and dash-dot lines are applications of the approximation in equation 3.23, where the parameters P_0 and z_0 are fit only to the first minimum. Here, the (– – –) lines correspond to the analytical expressions for κ in equations 3.37 and 3.38, while the (– – –) lines plotted in (d-f) correspond to the definitions in equations 3.39 and 3.40.

anions accumulating between the positively charged surfaces. Meanwhile, as expected, the pressure profiles for the symmetric system do not depend on the sign of the surface charge density. In the asymmetric system, the period of oscillation is not affected by the electrode polarity or magnitude. This is because at small potential drops across the double layer, overscreening is always present, and the overscreening period and decay are determined by the diameter of the larger ion. For the symmetric system, the period of the pressure oscillations increases slightly at $q_s = \pm 0.12$ C/m^2, yet it still remains on the scale of an individual ionic diameter. The theory in general also captures these features, particularly the asymmetric pressure response of the asymmetric IL with changing surface polarity, as well as the oscillation period, being on the order of the largest ionic diameter (orange line, —in Figure 3-8).

Linear response analysis

In order to gain further insight into the differences between the pressure profiles of the symmetric and asymmetric systems, we seek an approximate theoretical description in which the pressure profiles are represented by an exponentially decaying oscillating form,

$$P = P_0 e^{-\kappa_1 (z - z_0)} \cos\left(\kappa_2 (z - z_0)\right), \tag{3.23}$$

where κ_1 encodes the decay length of oscillations while κ_2 encodes the period of oscillations. Approximating the theory at linear response, the values for κ_1 and κ_2 are determined from the decay modes in charge density, which is proportional to $c_+ - c_-$, and the total number density $c_+ + c_-$. While the equations presented thus far are generally nonlinear integro-differential equations, in the limit of small, slowly varying perturbations in number density or charge density in linear response, we can derive analytical formulas to approximate the oscillatory decay of the charge and number density as a function of the IL properties. Here, we present the detailed derivation and analysis of the approximations involved for the theory at linear response.

Limit of small perturbations: Equation 3.17 for small perturbations in linear response

can be approximated as:

$$c_i \approx c_{i0}(1 - z_i e\beta w_{si} * \phi - \beta w_{vi} * \mu_i^{\text{ex}} + \beta \mu_{i,bulk}^{\text{ex}}). \tag{3.24}$$

The excess chemical potential can be linearized to give:

$$\beta \mu_i^{\text{ex}} = \frac{v_i}{\hat{v}} \frac{(8\bar{p} - 9\bar{p}^2 + 3\bar{p}^3)}{(1-\bar{p})^3} \approx \beta \mu_{i,bulk}^{\text{ex}} + \frac{v_i}{\hat{v}} \frac{2(4-\eta)}{(1-\eta)^4} (\bar{p} - \eta) \tag{3.25}$$

where we have linearized the weighted filling fraction $\bar{p}$, with reference value given by the bulk filling fraction, η. Therefore, if we assume linear perturbations of the bulk state, where $\delta f = f - f_b$, we have the following coupled equations for the linearized Poisson equation and the ionic concentrations:

$$\delta c_i \approx -z_i c_{i0} e\beta w_{si} * \phi - \frac{v_i c_{i0}}{\hat{v}} \frac{2(4-\eta)}{(1-\eta)^4} w_{vi} * \sum_j v_j w_{vj} * \delta c_j \tag{3.26}$$

$$\varepsilon \nabla^2 \phi = -\sum_i z_i e w_{si} * \delta c_i \tag{3.27}$$

In the proceeding equations, we will analyze the decaying modes for these differential equations for the cases of (i) the symmetric IL system and (ii) the asymmetric IL system. We briefly comment on (iii) systems with only a small degree of size asymmetry. In each of these analyses, we will use the following differential approximation for the convolution integrals, derived by truncating the Fourier transform of the convolution operations for small perturbations, [7] giving:

$$w_{vi} * \delta f \approx \left(1 + \ell_{vi}^2 \nabla^2\right) \delta f \tag{3.28}$$

$$w_{si} * \delta f \approx \left(1 + \ell_{si}^2 \nabla^2\right) \delta f \tag{3.29}$$

where ℓ_{vi} and ℓ_{si} are determined by the ionic size:

$$\ell_{vi} = \frac{d_i}{\sqrt{40}} \tag{3.30}$$

$$\ell_{si} = \frac{d_i}{\sqrt{24}} \tag{3.31}$$

where the numerical values of $\sqrt{40}$ and $\sqrt{24}$ are given directly from the mathematical form of the weighting functions.

The symmetric case: For the symmetric case, $w_{si} = w_s$, $w_{vi} = w_v$, and $v_i = \hat{v}$. The linear response for the symmetric system has been reported before, [7] but we again go through the process in order to draw contrast with the asymmetric case. For a 1:1 IL, we get the following:

$$\delta c_+ \approx -c_0 e\beta w_s * \phi - v c_0 \frac{2(4-\eta)}{(1-\eta)^4} w_v^2 (\delta c_+ + \delta c_-) \tag{3.32}$$

$$\delta c_- \approx c_0 e\beta w_s * \phi - v c_0 \frac{2(4-\eta)}{(1-\eta)^4} w_v^2 (\delta c_+ + \delta c_-) \tag{3.33}$$

$$\varepsilon \nabla^2 \phi = -e w_s * \delta c_- - w_s * \delta c_+ \tag{3.34}$$

If we sum the first two expressions and multiply by v, we get:

$$\delta p = \sum_i v \delta c_i \approx -\frac{2\eta(4-\eta)}{(1-\eta)^4} w_v^2 \delta p \tag{3.35}$$

where again, $p = v\sum_i c_i$ is the local filling fraction. Next, if we subtract the first two expressions and substitute into the third equation, we get:

$$\varepsilon \nabla^2 \phi = 2e^2 \beta c_0 w_s^2 \phi \tag{3.36}$$

Here, we see that the two systems at linear response are decoupled for the symmetric system. For the case where all functions become a function of z only, we can trial the solution $\delta f = A\exp(-\kappa z)$ to find the values for the decaying modes, κ. For the equation governing the filling fraction, $\delta p = A_m \exp(-\kappa_m z)$, (directly proportional to the total number density) the decay has both a real and imaginary part, where

$$\kappa_{1m} = \mathrm{Re}(\kappa_m) = \frac{\sqrt{40}}{d}\sqrt{-\frac{1}{2}+\frac{1}{2}\sqrt{1+\frac{(1-\eta)^4}{2\eta(4-\eta)}}} \tag{3.37}$$

$$\kappa_{2m} = \mathrm{Im}(\kappa_m) = \pm\frac{\sqrt{40}}{d}\sqrt{\frac{1}{2}+\frac{1}{2}\sqrt{1+\frac{(1-\eta)^4}{2\eta(4-\eta)}}} \tag{3.38}$$

Next, for the equation governing the electrostatic potential in the limit of high ionic concentration, with trial solution $\delta\phi = A_c \exp(-\kappa_c z)$, the decaying mode has different real and imaginary components:

$$\kappa_{1c} = \mathrm{Re}(\kappa_c) = \frac{12\lambda_D}{d^2} \tag{3.39}$$

$$\kappa_{2c} = \mathrm{Im}(\kappa_c) = \pm\frac{12\lambda_D}{d^2}\sqrt{\frac{d^2}{6\lambda_D^2}-1}, \tag{3.40}$$

where λ_D is the Debye length.

Even in linear response, we see that the two decaying modes will compete with one another in determining the overall disjoining pressure for the symmetric system. Both have similar nanometric decay ranges in the concentrated limit of ILs. At high charge density, the mode governing the decay of charge will dominate, κ_c. At low charge density, the decay of charge is unimportant in the double layer structure, so the decay in the number density (and packing fraction), κ_m will dominate.

The asymmetric case: For the asymmetric system, it is more difficult to make analytical progress in solving for the decaying modes. First and foremost, the decay in number density (packing fraction) is coupled explicitly to the decay in charge density (potential). This fact arises because of the differences in the excess chemical potential between the different ions, which do not allow for the neat cancellations that were derived for the symmetric system.

Further, even in solving the general problem for the decaying modes in each ionic species and the potential, analytical progress towards simple formulas is burdensome. For that reason, we will perform analysis for the limit of perfect asymmetry $d_- \gg (d_+ \approx 0)$

and high packing fraction, both reasonable approximations for the IL model explored in this work. If these assumptions are the case, then the governing linear response equations can be reframed as:

$$\delta c_+ \approx -c_0 e\beta\phi \tag{3.41}$$

$$\delta c_- \approx c_0 e\beta w_{s-} * \phi - \nu_- c_0 \frac{2(4-\eta)}{(1-\eta)^4} w_{\nu-}^2 \delta c_- \tag{3.42}$$

$$\varepsilon\nabla^2\phi = -e\delta c_+ + w_{s-} * e\delta c_- \tag{3.43}$$

By substitution for ϕ and δc_+ into the equation for the potential, we get a single characteristic equation for the anion concentration decay:

$$\left[1 + \frac{2\eta(4-\eta)}{(1-\eta)^4} w_{\nu-}^2\right] \nabla^2 \delta c_- = \frac{\kappa_D^2}{2} \left[1 + w_{s-}^2 + \frac{2\eta(4-\eta)}{(1-\eta)^4} w_{\nu-}^2\right] \delta c_- \tag{3.44}$$

Now, we can simplify this linearized expression by taking limits of κ_D, in relation to the characteristic length scale of the gradients in concentration, which is the ionic diameter d_- at high concentration. As a quick side note, the limit of $d_- \to 0$ gives the Debye-Huckel linearized form:

$$\nabla^2 \delta c_- = \kappa_D^2 \delta c_-, \tag{3.45}$$

so dilute electrolytes still have the Debye length as the characteristic decay length, as long as the filling fraction η in the electrolyte is near zero. If $\kappa_D d_- \ll 1$ and $\eta \neq 0$, then we get the following leading order differential equation for δc_-:

$$\left[1 + \frac{2\eta(4-\eta)}{(1-\eta)^4} w_{\nu-}^2\right] \nabla^2 \delta c_- = 0 \tag{3.46}$$

which is the same differential equation as for the filling fraction of the symmetric system, δp, in Equation 3.35, with an additional Laplacian operator. The more relevant limit to

concentrated ILs is when $\kappa_D d \to \infty$, which at leading order gives:

$$\left[1 + w_{s-}^2 + \frac{2\eta(4-\eta)}{(1-\eta)^4} w_{v-}^2\right] \delta c_- = 0 \tag{3.47}$$

For the purpose of simplicity, while still acknowledging the introduction of some error in the approximation, we can assume roughly that $w_{s-} \approx w_{v-}$. Next, at the filling fraction in the given parameter space, it is safely assumed that the term involving η dominates the differential equation at large filling fraction, such that the form of the equation can be approximated as:

$$\left[1 + \frac{2\eta(4-\eta)}{(1-\eta)^4} w_{v-}^2\right] \delta c_- = 0 \tag{3.48}$$

These simplifying assumptions ensure that Equation 3.48 matches the Equations 3.35 and 3.46. In the limit of large filling fraction and perfect asymmetry, the longest decaying mode governing the decay of the ionic concentration can be approximated by, κ_m, again with real and imaginary components:

$$\kappa_{1m} = \mathrm{Re}(\kappa_m) = \frac{\sqrt{40}}{d_-} \sqrt{-\frac{1}{2} + \frac{1}{2}\sqrt{1 + \frac{(1-\eta)^4}{2\eta(4-\eta)}}} \tag{3.49}$$

$$\kappa_{2m} = \mathrm{Im}(\kappa_m) = \pm\frac{\sqrt{40}}{d_-} \sqrt{\frac{1}{2} + \frac{1}{2}\sqrt{1 + \frac{(1-\eta)^4}{2\eta(4-\eta)}}}. \tag{3.50}$$

Here, the asymmetric system has one main decaying mode, owing to the coupling of oscillations in charge and number density.

Small degrees of asymmetry: One important question is whether there is a smooth transition between the symmetric behavior and the asymmetric behavior depending on the extent of asymmetry. The degree of coupling between the charge density and total number density can be determined via the linear response equations. As a starting point, we

consider the sum of the linear equations for the cation and anion, $\delta c_+ + \delta c_-$:

$$\delta c_+ + \delta c_- \approx c_0 e\beta(-w_{s+} + w_{s-}) * \phi - \frac{(v_+ w_{v+} + v_- w_{v-})c_0}{\hat{v}} \frac{2(4-\eta)}{(1-\eta)^4} * \sum_j v_j w_{vj} * \delta c_j \tag{3.51}$$

The coupling of the charge density decay with the number density decay is controlled by the term containing ϕ. From this term, we observe that the system is decoupled when $w_{s+} \approx w_{s-}$, or in terms of the approximate differential operators, $1 + d_+^2/24\nabla^2 \approx 1 + d_-^2/24\nabla^2$. From these relationships, we find that decoupling occurs when $d_+ \approx d_-$, for symmetric ion sizes. Approximately, the extent of asymmetry can be quantified using the difference in differential operators, $w_{s-} - w_{s+}$, assuming gradients on the order of the smallest length scale in the system, the smallest ion size (d_+ in this case). Therefore, the system will reproduce perfect asymmetric behavior when:

$$\frac{|\, d_-^2 - d_+^2 \,|}{d_+^2} \gg 1 \tag{3.52}$$

and will reproduce perfect symmetric behavior when:

$$\frac{|\, d_-^2 - d_+^2 \,|}{d_+^2} \ll 1. \tag{3.53}$$

Therefore, according to the linear response to small perturbations in the theory, systems with only slight asymmetry will behave similar to the symmetric system if they satisfy equation 3.53.

Summary of linear response results: In the linear response regime, we find that the charge density oscillations in the symmetric system are independent of the number density oscillations, as they are decoupled from each other. However, in the asymmetric system, in linear response, consistent with our explanation for the results of the simulations and the full integro-differential theory, we find that the period (as well as the decay length) of oscillations in both charge and number density is determined by the diameter of the larger ion, and so the two are coupled to each other.

For the asymmetric system, in the limit of large filling fraction and perfect asymmetry,

the longest decay mode in charge and number density can be approximately described by the definitions of κ_{1m} and κ_{2m} as derived above in equations 3.49 and 3.50. Therefore, for the asymmetric system, this mode dominates the value of the disjoining pressure at all surface charges. The decay of oscillations in this high packing fraction limit is independent of the background permittivity and ionic charge.

For the symmetric system, as mentioned above, the ordering in charge and number density are decoupled. For this case, the number density decays with modes described by κ_{1m} and κ_{2m} in equations 3.37 and 3.38 since these formulas are generally applicable for the decay in number density in a dense fluid at a hard wall. In contrast, the charge density decays as given by the definitions for κ_{1c} and κ_{2c} in the highly concentrated limit by equations 3.39 and 3.40. For the symmetric system at low surface charge, the decay of charge is unimportant in the interfacial structure, so the decay in the number density (and filling fraction), κ_m, will dominate in determining the pressure profile. Alternatively, at high surface charge, the mode governing the decay of charge, κ_c, will dominate. One could expect similar trends for ions that are only approximately symmetric in size, with only a small degree of asymmetry. Therefore, as $v_- \to v_+$, there is a transition between the perfectly asymmetric and the perfectly symmetric behaviors, as analyzed in the linear response behavior above.

We demonstrate our important findings for both the symmetric and asymmetric systems in Figure 3-8, where the approximations corresponding to equation 3.23 with κ_m as given in equations 3.37 and 3.38 and κ_c as given in equations 3.39 and 3.40 are plotted, manually fitting the point of the first minimum of the simulation data with P_0 and z_0, but keeping all other analytical formulas above. The decay decrement, κ_m, governed by the filling fraction is plotted with the dashed-dot cyan lines (– - –), while the decay decrement, κ_c, governed by the decay in charge is plotted with the dashed magenta lines (– – –).

For the asymmetric system (panels a-c), as mentioned above, κ_m dominates at all surface charges. Therefore, in Figure 3-8, one can observe that the dashed-dot cyan lines (– - –) fitted to the first minimum compare almost perfectly at all surface charges to the pressure oscillations found in the simulations.

For the symmetric system, however, the decaying mode given by κ_m, plotted with the

dashed-dot cyan lines (– · –), only dominates at zero surface charge (panel e). In contrast, since the decay in pressure oscillations at high electrode charges such as $q_s = \pm 0.12$ C/m^2 is dominated by the decrement, κ_c, the plotted dashed magenta lines (– – –) in Figure 3-8, panels d and f, match better to the pressure oscillations found in the simulations at these high surface charges (one can see how the dashed-dot cyan line for κ_m is in offset and does not describe well the simulated pressure oscillations).

Seeing as how the approximated equations from linear response describe quite accurately the simulated pressure profiles, we can now compare and validate quantitatively the periodicities of the pressure oscillations displayed in Figure 3-8. In the simulations, the period of the first oscillation (distance from first to second minimum) in the asymmetric system for the surface charges of $q_s =$ -0.12, -0.06, 0, +0.06, and +0.12 C/m^2 are 0.59, 0.62, 0.57, 0.60, and 0.61 nm, respectively. This compares well to the result from the linearized formula for κ_m in equation 3.38, which predicts a period of 0.62 nm for the asymmetric system. This value is essentially the effective largest ionic diameter $d_i \approx 0.9\sigma_i$, where $\sigma_- = 0.7$ nm (our criterion that takes into account the overlap of ions in the simulations), showing numerically that the periodicity of oscillations in asymmetric systems at all surface charges is determined by the diameter of the larger ion. For the symmetric system, the simulated periods of the first oscillation for $q_s = 0$, ± 0.06, and ± 0.12 C/m^2 are 0.53, 0.58, and 0.66 nm, respectively. The periodicity values at low surface charges are given by κ_m in equation 3.38, which predicts a period of 0.52 nm (again, $d_i \approx 0.9\sigma_i$, where $\sigma_\pm = 0.58$ nm). At high surface charge densities, the periodicity values are given by κ_c in equation 3.40, which predicts a period of 0.68 nm, numerically showing the increase in periodicity with surface charge magnitude in this case.

We note that while in previous experimental measurements of surface forces in IL, the oscillation period has been described in terms of the ion pair diameter, [220, 221, 245, 246] the oscillation period in the simulations and the theory presented here, at the high concentration limit, more closely matches the diameter of the largest ion, in all cases, multiplied by the scalar prefactor that is close to 1. Even for the case of the symmetric system at high surface charge, where each period of oscillation corresponds to a layer of positive and a layer of negative charge, the pressure oscillation period is still close to an individual ion diameter.

The prefactor does not bring us to the sum of the two ion sizes; for the parameters in the simulations, the oscillation period is roughly the ion size multiplied by a prefactor of 1.3. These theoretical predictions, backed up by the simulated pressure profiles, highlight that the periodicity of structural forces in ILs may not have a direct one-to-one correspondence to the ionic size or the ion pair size. Nevertheless, the periodicity is still closely related to and is proportional to the ionic size. In particular, for strongly asymmetric systems, the larger ion diameter dominates the oscillation period.

3.3.5 Conclusions

All in all, the change in the oscillatory decay as a function of surface charge underlies a major difference between charge screening in concentrated asymmetric systems compared to concentrated symmetric ones. In asymmetric systems, the decay modes in charge and number density are coupled to each other, and therefore give the same decay mode. For the symmetric system, the two are decoupled. This essentially leads to differences in the microscopic ionic concentration profiles in nanoconfinement as a function of electrode charge magnitude and polarity, and ultimately to an observable difference in the disjoining pressure profile.

To summarize, the main novel scientific contribution of our work is our proposed continuum theory which describes well the density, charge distributions, and structural forces of ILs in nanoscale confinements and the effect of surface polarization on these quantities. Through application of our mathematical theory, we can relate the oscillation periodicity and decay of the molecular structuring in nanoconfinement to the physical properties of the IL, including the bulk ionic density, the ionic sizes, the temperature, and the background permittivity. While the MD simulations and theory profiles do not match perfectly, both approaches predict layered structures that lead to structural forces at small separation distances. Both simulations and theory also recover the main features of screening in asymmetric ILs, which are not present in symmetric ILs. Those include the variation of force amplitudes depending on the surface charge polarity, the 'preferential adsorption' of smaller ions at zero electrode charge, and the coupling of charge and number density

oscillations in systems of such high ionic concentration. Therefore, based on our findings, we conclude that the ionic size asymmetry is an important ingredient in describing ILs at the nanoscale.

3.4 Summary of Findings

In this chapter, I developed a thermodynamic model for ions as hard-sphere, charged shells, that was applied to understand the interfacial structure of concentrated electrolytes. While the theoretical predictions do not perfectly describe the MD simulation performed as a benchmark, they are consistent with the main qualitative features of the simulations. The theory predicts alternating layers of positive charge with period on the scale of an individual ionic diameter, the overscreening phenomenon. At high charge density, the theory describes layers of crowded ions of the same charge. A key output of the theory is the decay lengths in charge and number density, derived by truncating a gradient expansion of the full nonlocal theory. In these concentrated systems, as noted in previous studies for primitive model electrolytes, the decay length increases with increasing concentrations.

For asymmetric-sized, concentrated electrolytes and ionic liquids, the oscillations in number density and charge are highly coupled. In turn, the size-asymmetry influences the structural forces for electrolytes confined down to the molecular scale, as reproduced both in the theory and in MD simulations from our collaborators.

In the next chapter, I investigate the influence of confinement dimensionality on the screening within the electrical double layer. In general, I show that compared to the 2D confinement scenarios explored in this chapter, that 1D confinement leads to a stronger propensity towards electroneutrality breakdown. There, the interesting behavior will emerge in the low concentration limit instead of the high concentration limit. In Chapter 5, I will return to the delocalized shell model to study the orientational ordering of polar liquids at charged interfaces.

Chapter 4

Electroneutrality Breakdown in Nanopores

The following chapter is reproduced from my original theoretical paper that describes the properties of electroneutrality breakdown in nanopore arrays [36] with Dr. Amir Levy and Prof. Martin Bazant, with strong inspiration from ref. [30] that originally proposed the unique phenomenon of electroneutrality breakdown in 1D confinement.

4.1 Overview

The electrostatic screening of charge in one-dimensional confinement leads to long-range breakdown in electroneutrality within a nanopore. Through a series of continuum simulations, we demonstrate the principles of electroneutrality breakdown for electrolytes in one dimensional confinement. We show how interacting pores in a membrane can counteract the phenomenon of electroneutrality breakdown, eventually returning to electroneutrality. Emphasis is placed on applying simplifying formulas to reduce the multidimensional partial differential equations into a single ordinary differential equation for the electrostatic potential. Dielectric mismatch between the electrolyte and membrane, pore aspect ratio, and confinement dimensionality are studied independently, outlining the relevance of electroneutrality breakdown in nanoporous membranes for selective ion transport and separations.

4.2 Electroneutrality Breakdown in Nanopore Arrays

4.2.1 Introduction

The conduction of ions in nanochannels forms the basis of electrical signalling in biology [263–268] and of promising technologies in desalination [269,270], ionic separations [271, 272], and nanofluidic transistors [273–275]. As ions become confined to nanopores, they experience strong chemical and electrostatic interactions with the pore walls, leading to membrane selectivity based on charge or chemical interactions. Nanoporous membranes can even enter the regime where the double layers emanating from each charged surface begin to overlap, leading to strong electrokinetic coupling of fluid flow, electric field, and ionic fluxes [276–281]. Understanding the electrostatics of charges in confinement is crucial to determining the flux, selectivity, and driving force relationship for engineering applications [282, 283] and for understanding biological pore systems [51, 284–286].

The unique physics of ionic screening in one dimensional confinement leads to the phenomenon of electroneutrality breakdown, where the number of counter-charges within a pore does not perfectly counterbalance the number of fixed charges on the pore walls [30]. One dimensional (1D) confinement refers to confinement onto a line, for example, in a cylindrical nanopore connecting two reservoirs of fixed concentration. In essence, electroneutrality breakdown signifies that a fraction of the electric field must escape through the pore walls into the dielectric matrix constituting the membrane. The screening charge does not exist locally within the pore, but rather is distributed over the membrane surface in the reservoirs, outside of the membrane domain. Uniquely, in 1D confinement, the loss of electroneutrality can extend to macroscopic scales (beyond length $L = 10\ \mu$m), since for strong confinement $\kappa_D R \to 0$ the system only approaches electroneutrality as $\log(L/R) \to \infty$, where L is the length of a pore, R is its radius, and κ_D is the inverse Debye length. The long-range breakdown of local electroneutrality in 1D confinement is surprising, and many models of electrokinetic phenomena have assumed pore-wide electroneutrality, even in the limit of strong double layer overlap [277, 278, 287].

Here, we perform continuum simulations of 1D nanopores using COMSOL Multiphysics, to confirm the occurrence of electroneutrality breakdown. We show that the results

for the screening charge within an isolated 1D pore can be captured quantitatively with analytical formulas. Furthermore, we perform simulations of a periodic array of channels, a multipore membrane, with varying spacing between the channels. There, we find how the interactions of closely-spaced channels can lead to the return of electroneutrality in the system. In the limit of strongly interacting channels, the variations in potential in the axial direction dominate the distribution of ionic charges within the membrane. Effectively, when channels are too close to each other, the electric field lines cannot emanate through the membrane domain.

The continuum simulation results show the ensemble interactions of the channels with each other play a role in ionic conduction through nanochannels. In membrane applications, the interactions mean that the greatest ionic selectivity and per-channel-conductivity can be achieved when channels are close together for the regime of strong double layer overlap. Further, the results point to ensemble interactions between 1D-confined channels, and the importance of electric field spilling into the dielectric matrix when channels are isolated. The competition between channel interactions and electroneutrality breakdown ultimately affects the conductance and selectivity behavior of arrays of nanochannels in the low concentration limit.

4.2.2 Theoretical framework

Outline of equations

As explained in more detail in Appendix A of reference [36], the ionic flux and selectivity out of equilibrium can be assumed to be related to the solution of the Poisson-Boltzmann (PB) equation in equilibrium, assuming that both reservoirs on each side of the membrane have the same concentration of electrolyte and fluid flow is neglected [276, 277]. As emphasized in Fig. 4-1 , the simulation is composed of a square membrane domain, Ω_m, with side length ℓ, through which a cylindrical pore of radius R and length L connects two reservoirs of fixed concentration. The reservoirs and pore constitute the electrolyte domain, signified as Ω_w, where w is chosen to signify water.

As exhibited in Fig. 4-1 (a-d), the system of equations being solved in the electrolyte

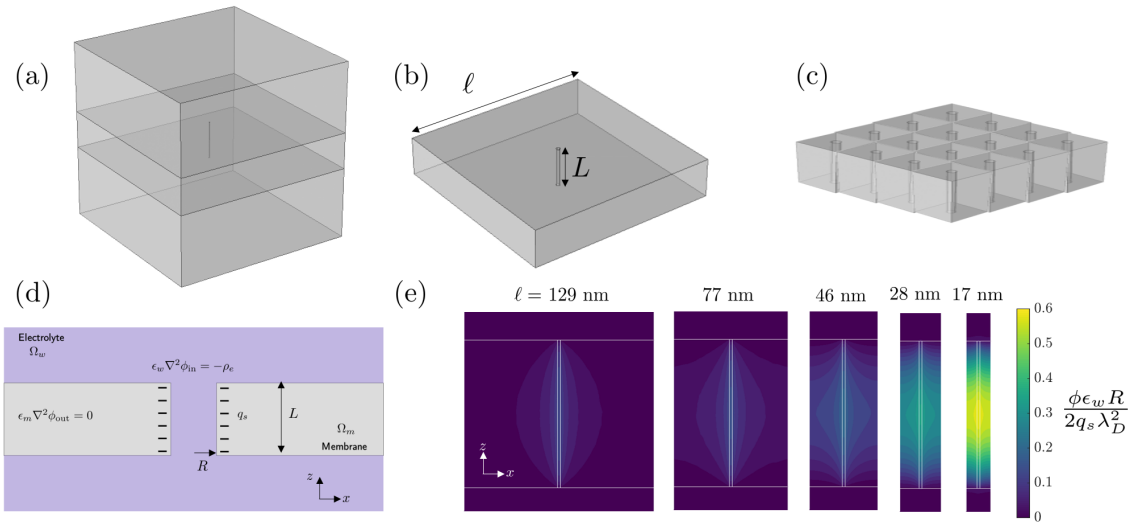

Figure 4-1: The simulation configuration in COMSOL (a) with the membrane, pore, and electrolyte (b) for an isolated pore that does not feel its periodic neighbors and (c) a periodic arrangement of pores on a square lattice. (d) A cross-section of the system through the center of the cylindrical pore is shown to describe the domains and equations applied in the simulations. (e) A sample of continuum simulation results showing the progress from non-interacting to interacting channels for small charge densities. For all channels, the channel radius is 1 nm and the length is 100 nm. The membrane dielectric constant is $\varepsilon_m = 10\varepsilon_0$ and the electrolyte dielectric constant is $\varepsilon_w = 80\varepsilon_0$. The salt concentration is 1 mM. In order from left to right, the spacing between the channel centers ℓ is 129 nm, 77 nm, 46 nm, 28 nm, and 17 nm. Also in order, the amount of charge within the pore versus on the channel walls, $|\, Q_{\text{in}}/Q_{\text{out}} \,|$ is: 12%,13%, 17%, 26%, and 43%. As the channels become closer together and more interacting, the system returns closer to electroneutrality, which is evidenced by the higher ϕ values within the pore.

domain Ω_w is:

$$\varepsilon_w \nabla^2 \phi = -\rho_e \tag{4.1}$$

with dielectric constant ε_w, electrostatic potential ϕ, and charge density ρ_e where the ionic concentrations are Boltzmann-distributed:

$$\rho_e = \sum_i z_i e c_{i,b} \exp\left(-\frac{z_i e \phi}{k_B T}\right), \tag{4.2}$$

where z_i are the ion valencies, e is the elementary charge, $c_{i,b}$ is the bulk reservoir concentration for ion i, k_B is the Boltzmann constant, and T is the absolute temperature. Here we neglect any packing [17], correlation [34], or charge regulation [288] effects in our model. We assume a 1:1 solution of salt with concentration c_0 in units of number density, such that the PB equation is reduced to:

$$\varepsilon_w \nabla^2 \phi = 2 e c_0 \sinh\left(\frac{e\phi}{k_B T}\right) \tag{4.3}$$

In the membrane domain, we solve the Laplace equation:

$$\varepsilon_m \nabla^2 \phi = 0 \tag{4.4}$$

assuming that the membrane is a perfect dielectric material with dielectric constant ε_m.

At the membrane/electrolyte domain interface, Maxwell's equation is enforced:

$$\hat{\mathbf{n}} \cdot [-\varepsilon_m \nabla \phi + \varepsilon_w \nabla \phi] \Big|_s = q_s \tag{4.5}$$

where $\hat{\mathbf{n}}$ is the unit normal pointing from the electrolyte to the membrane domain and q_s is the surface charge density. To isolate the electrostatic potential variations due to fixed charge on the channel walls, q_s is assumed to be zero on the membrane/electrolyte reservoir interfaces, but is nonzero at the pore walls.

At the lateral boundaries of each cell, symmetry conditions are applied; namely, the electric field at the boundary is zero $\hat{\mathrm{n}} \cdot \nabla \phi = 0$. The boundary conditions are identical to

assuming a periodic array of channels with regular spacing, consisting of unit cells identical to the simulation box, as illustrated in Fig. 4-1 (c). At the top and bottom boundaries of the simulation box, Dirichlet conditions are applied $\phi = 0$. A useful check to ensure that the simulation box is large enough is to ensure that all the integrated charges in the electrolyte domain are equal and opposite to the integrated amount of fixed charges on the pore walls. For this study, a reservoir height of 20 λ_D is sufficient to meet this criterion, where the Debye length, λ_D is given by:

$$\lambda_D = {\kappa_D}^{-1} = \sqrt{\frac{\varepsilon_w k_B T}{2e^2 c_0}} \tag{4.6}$$

Approximate formulas

While we compute the full results of the PB equation in 3D, we compare the results to mathematical simplified formulas. As outlined in more detail in Appendices B and C, we can reduce our partial differential equation system of the 3D PB and Laplace equations into ordinary differential equations with appropriate boundary conditions. For small potentials, we then linearize the equations and get simple analytical formulas for the number of ionic charges within the membrane. In order to quantify the extent of electroneutrality breakdown, we take the ratio for the integrated amount of charge within the pore and the integrated amount of charge on the pore walls: $\mid Q_{\text{in}}/Q_{\text{out}} \mid$. In the limit of electroneutrality, we get $\mid Q_{\text{in}}/Q_{\text{out}} \mid \rightarrow 1$, whereas in the limit of complete electroneutrality breakdown, we get $\mid Q_{\text{in}}/Q_{\text{out}} \mid \rightarrow 0$.

No end effects: Ignoring end effects, the inner potential can be solved for in terms of only the radial coordinate:

$$\frac{\varepsilon_w}{r}\frac{d}{dr}\left(r\frac{d\phi}{dr}\right) = 2ec_0 \sinh\left(\frac{e\phi}{k_B T}\right) \tag{4.7}$$

with boundary conditions given by:

$$\frac{d\phi}{dr}(r=R) = \frac{q_s}{\varepsilon_w} - \frac{\varepsilon_m}{\varepsilon_w}\frac{\phi(r=R)}{RM_{L/R}}, \quad \frac{d\phi}{dr}\left(r=\frac{\ell}{2}\right) = 0 \tag{4.8}$$

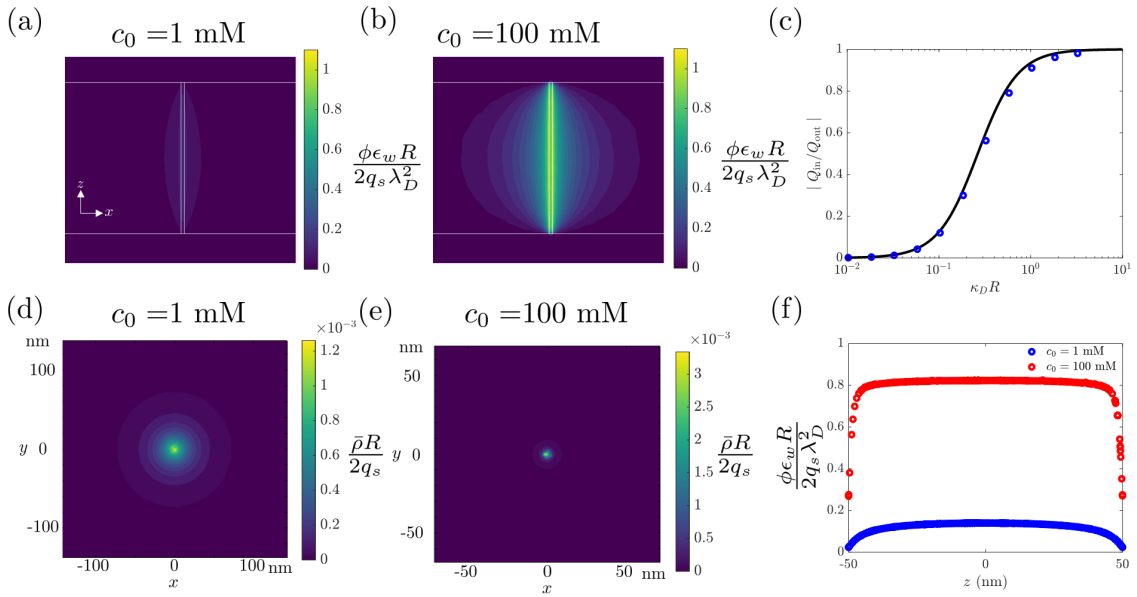

Figure 4-2: The results for an isolated pore with overlapping and non-overlapping double layers within the pore. (a) plot of the potential profile for overlapping double layers at $c_0 = 1$ mM ($\kappa_D R \approx 0.1$) (a) versus less overlapping double layers at $c_0 = 100$ mM ($\kappa_D R \approx 1$)(b). The same parameters are used as in Fig. 4-1 (e), except the center to center distance between pores is 500 nm such that the periodic channels are not interacting. For (a) 12% of the charge is contained within the pore, whereas for (b) 91% of the charge is contained within the pore.(c) The charge within the pore versus on the pore walls as a function of $\kappa_D R$ for the same channel in parts (a) and (b). Electroneutrality breakdown occurs in the region of strong double layer overlap $\kappa_D R \to 0$. For (c) the markers are the COMSOL simulations, whereas the line is the application of the approximate formula in equation 4.10. (d-e) The integrated ionic charge as a function of the lateral position for $c_0 = 1$ mM and 100 mM. The charge is distributed over a wide area $O(L)$ extending beyond the pore mouth when electroneutrality is broken (c_0=1 mM), but is more localized when electroneutrality is maintained (c_0=100 mM) . (e) Quantification of end effects for two different concentrations. The electrostatic potential is plotted as a function of the z coordinate, evaluated at the center axis of the channel. End effects are not significant for isolated channels.

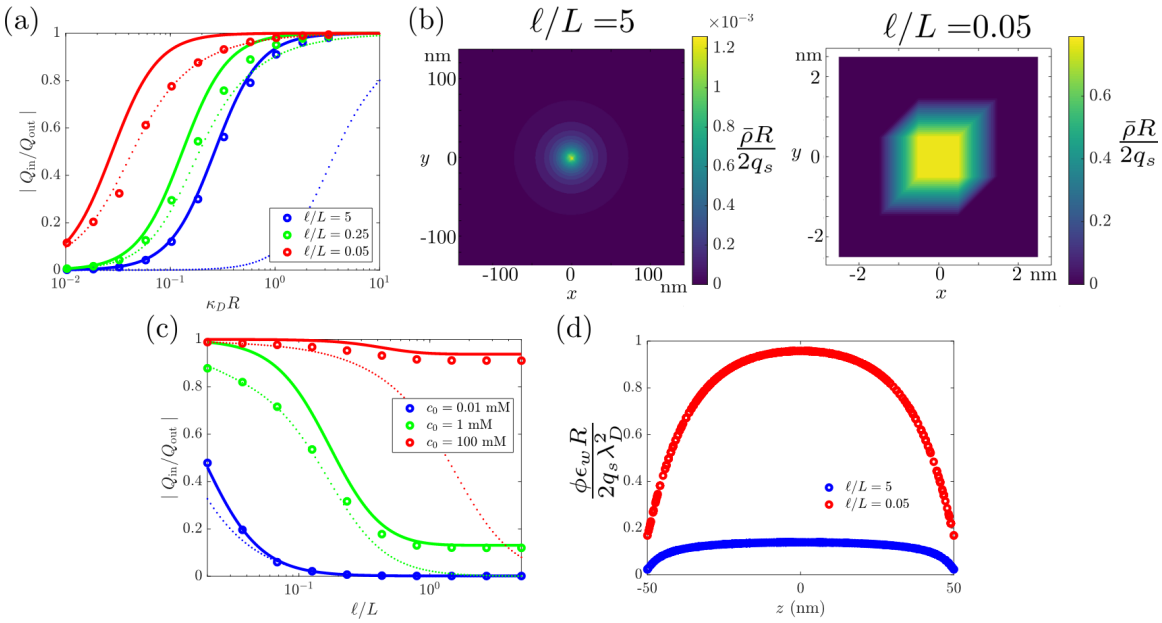

Figure 4-3: Extent of electroneutrality breakdown for channels of different center-to-center separation distances on a lattice. (a) $|\,Q_{\text{in}}/Q_{\text{out}}\,|$ versus $\kappa_D R$ for $\ell/L = 5$, $\ell/L = 1$, $\ell/L = 0.1$. (c) $|\,Q_{\text{in}}/Q_{\text{out}}\,|$ versus ℓ/L for $c_0 = 0.01, 1, 100$ mM for $\ell/L = 0.02$ to $\ell/L = 0.5$. For both (a) and (c), the markers are the COMSOL simulations, whereas the solid lines are the application of the approximate formula in equation 4.10 and the dotted lines are the application of the approximate formula in equation 4.14. (b) The integrated ionic charge as a function of the lateral position for $\ell/L = 5$ and 0.05, with $c_0 = 1$ mM. The charge is distributed over a wide area when channels are isolated, but is localized when the channels are closely spaced and strongly interacting. (d) Quantification of end effects for two different lattice spacings with $c_0 = 1$ mM. The electrostatic potential is plotted as a function of the z coordinate, evaluated at the center axis of the channel. End effects are significant when the channels are interacting.

where the constant $M_{L/R}$ is:

$$M_{L/R} = \log\left(\frac{2L}{\pi R}\right) - \gamma + \frac{\mathrm{K}_1(\frac{\pi\ell}{2L})}{\mathrm{I}_1(\frac{\pi\ell}{2L})}. \tag{4.9}$$

with $\gamma = 0.577$ signifying the Euler-Mascheroni constant. Here, we assume circular shape of a unit cell for analytical simplicity, and the derivation is presented in Appendix B of ref. [36]. Linearizing the equations and solving, we find the folllowing relationship for the amount of charge inside versus the amount of charge fixed on the pore walls:

$$\left|\frac{Q_{\text{in}}}{Q_{\text{out}}}\right| = \frac{1}{1 + \frac{\varepsilon_m}{\varepsilon_w}\frac{2}{\kappa_D{}^2 R^2 M_{L/R}}} \tag{4.10}$$

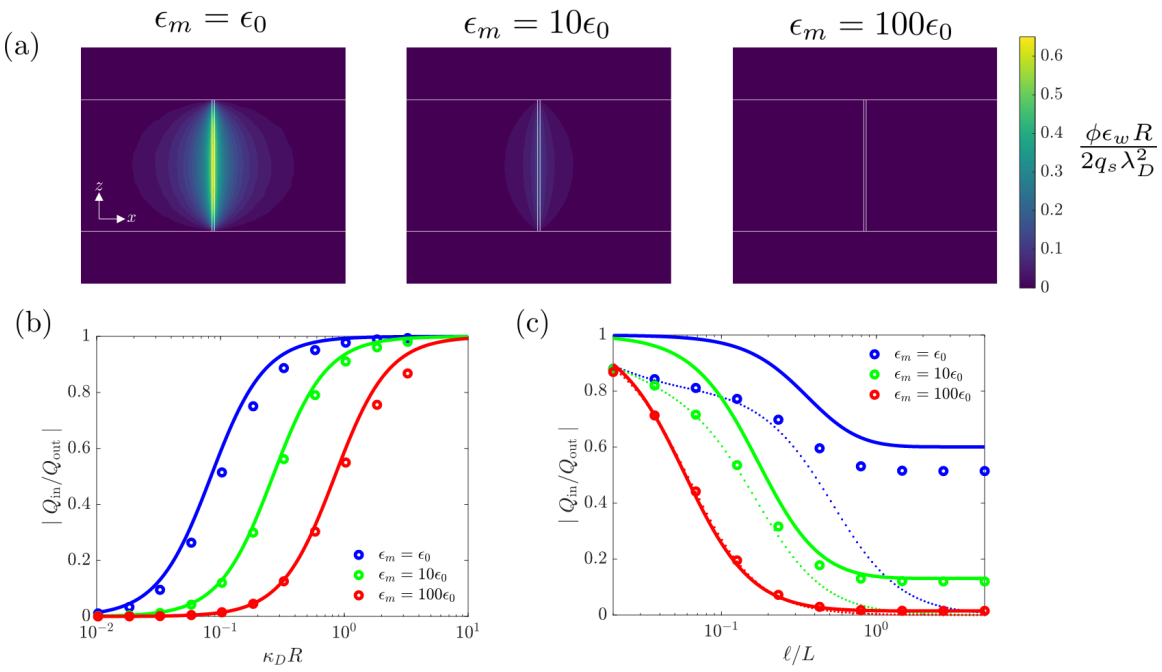

Figure 4-4: Role of dielectric mismatch on extent of electroneutrality breakdown. (a)Results for isolated pore with same properties as in Fig. 4-1 (e), but with $\varepsilon_m = \varepsilon_0$, $\varepsilon_m = 10\varepsilon_0$, and $\varepsilon_m = 100\varepsilon_0$. (b) $|\,Q_{\text{in}}/Q_{\text{out}}\,|$ versus $\kappa_D R$ for varying ε_m. (b) $|\,Q_{\text{in}}/Q_{\text{out}}\,|$ versus ℓ/L with $c_0 = 1$ mM for varying ε_m.For both (b) and (c), the markers are the COMSOL simulations, whereas the solid lines are the application of the approximate formula in equation 4.10 and the dotted lines are the application of the approximate formula in equation 4.14.

Looking at the form of the above equation, one recognizes that electroneutrality breakdown is promoted as $\kappa_D R \to 0$. Furthermore, the effect has a weak dependence on the

length of non-interacting nanopores, since the length appears logarithmically in $M_{L/R}$. However, the electrostatic interactions of the cylinders with each other can cause a return to electroneutrality as $\ell/L \to 0$. Furthermore, the amount of charge within the pore is strongly controlled by the dielectric constant of the membrane (and not necessarily the inner pore dielectric constant).

No radial variations: On the other hand, when channels become strongly interacting ($\ell/L \to 0$), the potential variations happen principally in the axial direction along the pore, governed by the dimensionless ratio λ_D/L. In order to capture the end effects of the channel, which become important on the scale of the Debye length, we write down a homogenized equation for the potential in linear response, which neglects radial variations in the potential by integrating over the lateral dimensions of a unit cell:

$$\bar{\varepsilon}\frac{d^2\phi}{dz^2} = -\frac{2q_s}{R} + 2ec_0 \sinh\left(\frac{\phi e}{k_B T}\right) \tag{4.11}$$

$$\bar{\varepsilon} = \varepsilon_w - \varepsilon_m + \varepsilon_m\left(\frac{\ell^2}{\pi R^2}\right) \tag{4.12}$$

The linear response boundary conditions are given by:

$$\frac{d\phi}{dz}(z=0,L) = \pm\frac{\varepsilon_w}{\bar{\varepsilon}}\frac{\ell^2}{\pi R^2}\frac{\phi(z=0,L)}{\lambda_D}. \tag{4.13}$$

Solving the set of equations, we get the following fraction of charge inside the pore.

$$\left|\frac{Q_{\text{in}}}{Q_{\text{out}}}\right| = \frac{1-(\gamma-p)\tanh(1/\gamma)}{1+p\tanh(1/\gamma)} \tag{4.14}$$

with constants

$$\gamma = 2\sqrt{\frac{\bar{\varepsilon}}{\varepsilon_w}}\frac{\lambda_D}{L}, \quad p = \sqrt{\frac{\bar{\varepsilon}}{\varepsilon_w}}\frac{\pi R^2}{\ell^2} \tag{4.15}$$

For strongly interacting channels, the electroneutrality condition is controlled by the ratio of λ_D/L. As $\lambda_D/L \to 0$, the system returns to overall electroneutrality within the pore.

Following the theoretical argument, a comprehensive set of numerical simulations is presented to validate the above formulas in their regime of validity, focusing on the linear

regime with small but finite surface charge, $q_s \to 0$. The standard conditions chosen for the simulations, unless otherwise stated, are a pore length of 100 nm, a pore radius of 1 nm, a membrane permittivity of $\varepsilon_m = 10\varepsilon_0$, an electrolyte permittivity of $\varepsilon_w = 80\varepsilon_0$. Finally, a comparison is also made to the nonlinear solution of the full 3D equations.

The results are presented with a number of dimensionless numbers, so a reader can easily interpret the plots. First, the dimensionless number $\kappa_D R$ indicates the extent of double layer overlap within the channel. $\kappa_D R \to 0$ indicates strong double layer overlap while $\kappa_D R \to \infty$ indicates thin double layers relative to the pore radius. ℓ/L is the ratio of the center to center spacing between channels to the length of the channels. In plotting, the potential is normalized by the charge per unit length of a cylinder:

$$\tilde{\phi} = \frac{\phi \varepsilon_w R}{2 q_s \lambda_D^2} \tag{4.16}$$

One can roughly interpret these graphs as $\tilde{\phi} \approx 1$ means local electroneutrality in a give cross section of the pore, and $\tilde{\phi} \approx 0$ as local electroneutrality within the pore. Further, the depth-integrated charge density is plotted as a function of lateral position, to illustrate the extent of screening charges at the membrane/reservoir interfaces:

$$\bar{\rho}_e(x,y) = \frac{\int \rho_e(x,y,z) dz}{L}. \tag{4.17}$$

4.2.3 Results and Discussion

First, Fig. 4-1 (e) summarizes the main trends seen in the simulations, where the potential is plotted as a function of position around the pore, as the spacing between pores is modified. When channels are isolated ($\ell = 129$ nm), the potential within the channel is fairly constant. The variations in the potential in the radial direction are dominant. For the parameters chosen ($\kappa_D R = 0.1$, $c_0 = 1$ mM), the amount of charge within the channel is only 12% of the charge on the pore walls. However, as the size of a unit cell is reduced ($\ell = 17$ nm) the variations in the potential become dominant in the axial direction, and edge effects become more pronounced. Furthermore, the potential does not vary significantly in the radial direction from the channel center axis. The close channel spacing also limits the

amount of field that can escape out of the pore, meaning that more charges are present within the channel, 43%.

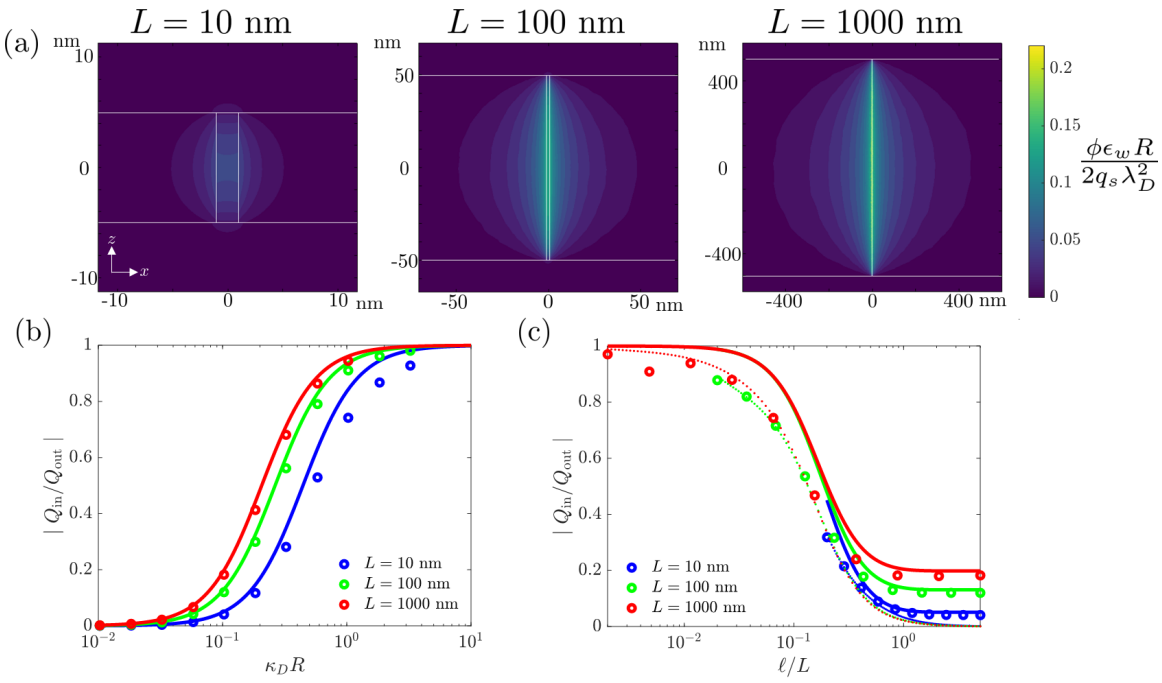

Figure 4-5: Role of aspect ratio on extent of electroneutrality breakdown. (a)Results for isolated pore with same properties as in Fig. 4-1 (e), but with $L = 10$ nm, $L = 100$ nm, and $L = 1000$ nm, also with $c_0 = 1$ mM. (b) $|\, Q_{\text{in}}/Q_{\text{out}} \,|$ versus $\kappa_D R$ for varying L, with $\ell/L = 5$. (b) $|\, Q_{\text{in}}/Q_{\text{out}} \,|$ versus ℓ/L with $c_0 = 1$ mM for varying L. For both (b) and (c), the markers are the COMSOL simulations, whereas the solid lines are the application of the approximate formula in equation 4.10 and the dotted lines are the application of the approximate formula in equation 4.14.

The trends in the potential profiles as a function of the salt concentration are shown in Fig. 4-2 . Fig. 4-2 (a) corresponds to $\kappa_D R = 0.1$ or c_0=1 mM, and 2(b) corresponds to $\kappa_D R = 1$ of $c_0 = 100$ mM, illustrating that electroneutrality is restored as the concentration is increased. The solid line in Fig. 4-2 (c) given by equation 4.10 coincides quite closely with the results of the continuum simulations for the isolated channels. For these cases, neglecting end effects is a reasonable approximation for determining the number of charges within the pore, which is confirmed via the plot of the potential as a function of position along the center axis of the pore in Fig. 4-2 (f). The 'plumes' of screening charge near the pore mouth are not immediately visible in the plots of the electrostatic potential, since the charges are far less concentrated outside of the pore. We can ascertain the extent of the screening at the membrane interfaces by analyzing the depth-integrated charge density.

In Fig. 4-2 (d-e), the depth-integrated charge density, $\bar{\rho}_e$, is plotted as a function of the x and y coordinate. When electroneutrality is broken within the pore, the screening charge is distributed over the membrane surface over a distance that is on the order of the channel length, L. However, if electroneutrality is maintained, the screening charge is localized within the channel, and does not extend very far beyond the pore mouth.

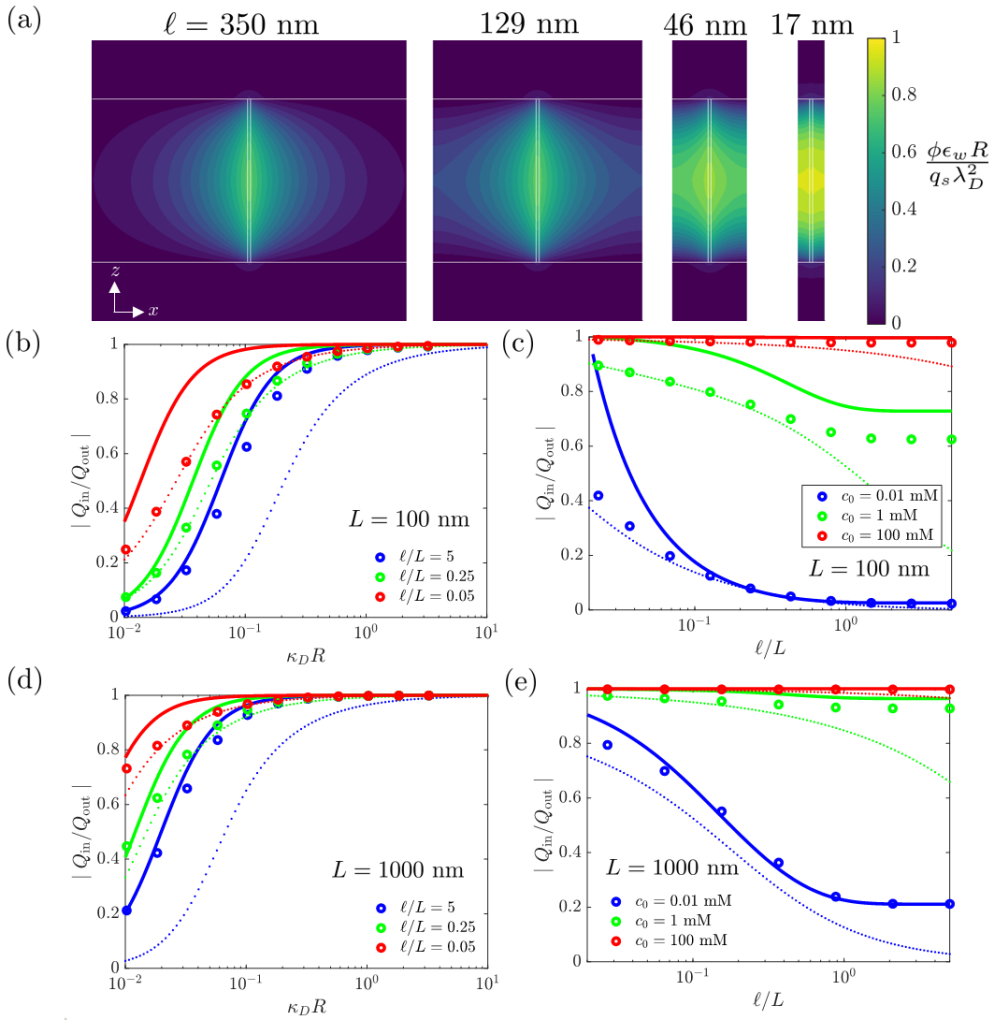

Figure 4-6: Role of dimensionality of confinement by inspecting a slit pore geometry. (a)Results for isolated pore with same properties as in Fig. 4-1 (e), but for a slit pore. (b) $|Q_{in}/Q_{out}|$ versus $\kappa_D R$ for varying ℓ/L. (c) $|Q_{in}/Q_{out}|$ versus ℓ/L for varying c_0. (d-e) The same as (b-c) but with $L = 1000$ nm. For (b), (c), (d), and (e), the markers are the COMSOL simulations, whereas the solid lines are the application of the approximate formula in equation 4.18 and the dotted lines are equation 4.14 with constants given by equations 4.20 and 4.21.

Next, we isolate the influence of channels interacting through the membrane domain, via modifying the ratio ℓ/L in Fig. 4-3. As channels are closer together, $\ell/L \to 0$, the

amount of charge within the channel is increased closer towards electroneutrality. We also see a clear difference between the predictions neglecting end effects (equation 4.10) in solid lines and the predictions neglecting radial variations (equation 4.14) in dotted lines. As $\ell/L \ll 1$, the predictions of the model neglecting radial variations become superior. However, when ℓ/L is 1 or greater, the predictions of the model that neglects end effects are superior. Such a result is expected, given the illustrative example in Fig. 4-1(e), where the importance of end effects are visible on the plot when channels are close together. For further confirmation, the magnitude of the electric field is plotted as a function of position for varying channel spacings in Fig. S2 in reference [36], exhibiting the importance of end effects for closely spaced channels. In Fig. 4-3(d), the potential plotted as a function of position on the center axis of the nanopore shows significant end effects for closely spaced channels (ℓ/L=0.05). Also, the closely spaced channels localize the screening charge near the pore mouth, as evidenced by the depth-averaged charge density in Fig. 4-3(b).

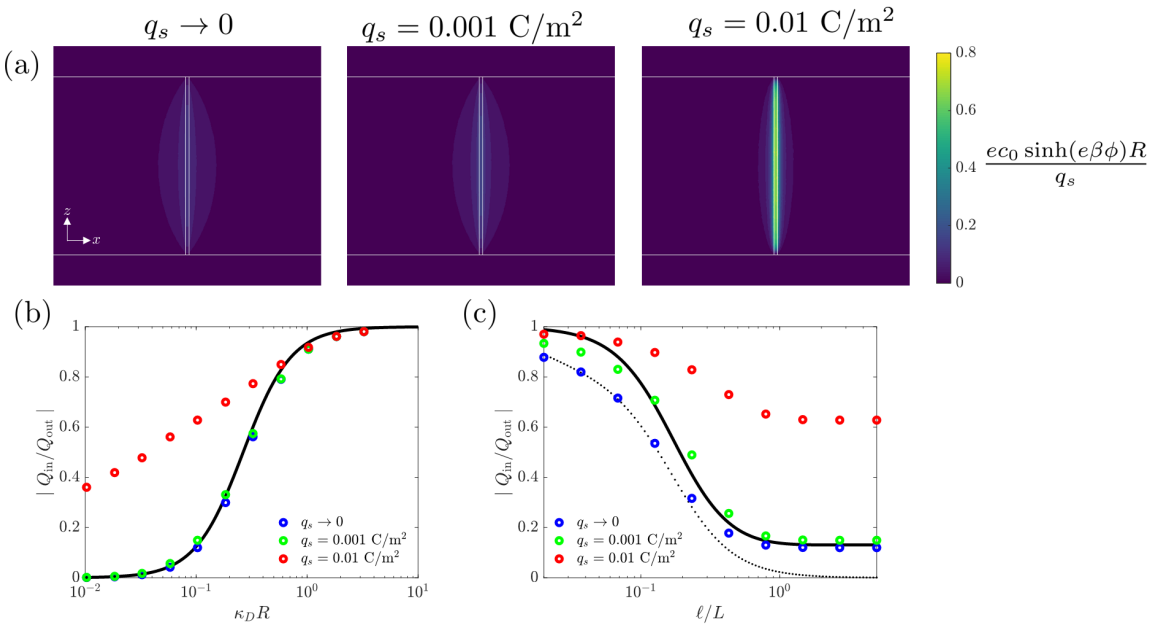

Figure 4-7: Role of nonlinearity on extent of electroneutrality breakdown. (a)Results for isolated pore with same properties as in Fig. 4-1 (e), but with $q_s \to 0$, $q_s = 0.001$ C/m^2, and $q_s = 0.01$ C/m^2 with $c_0 = 1$ mM. (b) $|\,Q_{in}/Q_{out}\,|$ versus $\kappa_D R$ for varying q_s. (b) $|\,Q_{in}/Q_{out}\,|$ versus ℓ/L with $c_0 = 1$ mM for varying q_s. For both (b) and (c), the markers are the COMSOL simulations, whereas the solid line is the application of the approximate formula in equation 4.10 and the dotted line is the application of the approximate formula in equation 4.14.

The interactions of channels has a profound impact on the selectivity of a multipore

dielectric membrane. The ensemble interactions can lead to a return to electroneutrality in strongly confined systems, leading to more charge selectivity and higher channel conductance. The extent of electrokinetic couplings are also maximized when the amount of ionic charge within the pore is higher [277, 289]. Such a design principle could be used to promote higher electrokinetic conversion efficiencies in "blue energy" harvesting of salinity gradients [290, 291].

Another important design parameter is the dielectric constant of the membrane matrix. In Figure 4, we examine the influence of the membrane dielectric constant on the extent of electroneutrality breakdown. As the membrane dielectric constant decreases, the system moves closer towards electroneutrality in the pore. Again, the predictions from equations 4.10 and 4.14 seem to describe the data quite well within their respective realms of validity.

A critical question remains to understand the influence of the aspect ratio on the extent of electroneutrality breakdown, the subject of Figure 5. Again observing equation 4.10, for an isolated channel, the electroneutrality is enforced as $\log(L/R) \to \infty$. Therefore, the electroneutrality breakdown is only weakly affected by the length of the channel. As shown in Figure 5(b), we see only small shifts in the extent of electroneutrality breakdown with increasing channel length, L. Furthermore, the channels exhibit similar behavior with varying channel spacing, ℓ. Such results arise from the exponentially long screening length in one dimensional confinement [30]. The weak dependence of the extent of electroneutrality on the aspect ratio is a hallmark of electroneutrality breakdown in 1D channels.

As a point of comparison, it is instructive to perform the same analysis for two dimensional confinement, or slit pore geometry. Here, we perform analogous continuum simulations to the 1D confinement case. In Figure 6, we have simulated a slit pore with width $2R$ and length L, with channel center to channel center distances of ℓ. We compare the simulation results to two analytical formulas, one where we have neglected end effects, and one where we have neglected normal variations in the potential to the pore walls (again termed "neglecting 'radial' variations"), similar to the analysis for 1D confinement, as outlined below.

The extent of electroneutrality breakdown in 2D confinement, **ignoring edge effects**,

is:

$$\left|\frac{Q_{\text{in}}}{Q_{\text{out}}}\right| = \frac{1}{1+\frac{\varepsilon_m}{\varepsilon_w}\frac{1}{\kappa_D{}^2R^2M_{L/R}}} \tag{4.18}$$

with modified constant $M_{L/R}$ given by:

$$M_{L/R} = \frac{L}{\pi R}\coth\left(\frac{\pi}{L}(\ell/2-R)\right) \tag{4.19}$$

Observing the form of the 2D $M_{L/R}$ in this scenario, it is apparent that electroneutrality is enforced as $L/R \to \infty$. This means that electroneutrality will be much more strongly upheld in 2D confinement compared to 1D confinement.

When ℓ/L becomes smaller, the potential variations in the axial direction of the 2D slit pore become dominant, similar to 1D confinement. The extent of electroneutrality breakdown **neglecting 'radial' variations** is given identically by equation 4.14, but with constants

$$\gamma = 2\sqrt{\frac{\bar{\varepsilon}}{\varepsilon_w}}\frac{\lambda_D}{L}, \quad p = \left(\frac{\bar{\varepsilon}}{\varepsilon_w}\frac{4R^2}{\ell^2}\right)^{1/2} \tag{4.20}$$

where

$$\bar{\varepsilon} = \varepsilon_w - \varepsilon_m + \varepsilon_m\left(\frac{\ell}{2R}\right). \tag{4.21}$$

The progression towards electroneutrality breakdown for 2D confinement is similar to 1D confinement when the channel spacing is close together.

In Fig. 4-6 (b-e), we see that the propensity towards electroneutrality is much stronger in 2D confinement than in 1D confinement. We find that, similar to 1D confinement, electroneutrality is promoted when channels are strongly interacting. We also find that the extent of electroneutrality breakdown is extremely sensitive the to the length of the channel domain, especially as compared to 1D confinement, as emphasized by comparing Fig. 4-6 (d-e) to Fig. 4-6 (b-c). Note that the normalization of the potential in Fig. 4-6 (a) is adjusted from the definition in equation 4.16 due to the difference in geometry.

So far, we have examined the linear regime with small but finite values of q_s. Evidently, the nonlinearity in the equations will affect the validity of our approximations in equations 4.10 and 4.14. In Fig. 4-7, we show that as the charge density is increased into the nonlinear regime, the system moves closer towards electroneutrality. The approximations we

derived earlier are insufficient to describe the extent of electroneutrality breakdown in the nonlinear limit. It is particularly difficult to derive analytical approximations in the nonlinear limit, so we do not explore such approximations here. Even so, for isolated channels, the electroneutrality breakdown emerges as a function of the ratio of the Gouy-Chapman length to the pore radius in this limit [30].

Finally, we preview the possible manifestations of electroneutrality breakdown that could be observed in experiments: single channel conductance and transference number, using the simplified formulas in equation 4.10 and equation 4.14. We assume a KCl solution with fixed and equal mobilites, equal to the bulk value of $D = D_+ = D_- = 2 \times 10^{-9}$ m^2/s. For an uncharged pore, the fraction of current carried by each ion would be 50%. However, in this case, we assume that the pore walls are negatively charged with a value of $q_s = -0.001$ C/m^2. Therefore, we approximate the anion and cation concentrations within the channel as:

$$c_+ = c_0 + \frac{2 \mid q_s \mid}{eR} \frac{\mid Q_{\text{in}} \mid}{\mid Q_{\text{out}} \mid}, \quad c_- = c_0 \tag{4.22}$$

We approximate the overall channel conductance as:

$$G = \frac{2\pi D R^2 e^2 c_0}{k_B T L} + \frac{2\pi D R e \mid q_s \mid}{k_B T L} \frac{\mid Q_{\text{in}} \mid}{\mid Q_{\text{out}} \mid} \tag{4.23}$$

which can be rendered dimensionless:

$$\tilde{G} = G / \left(\frac{2\pi D R^2 e^2 c_{\text{ref}}}{k_B T L} \right) = \frac{c_0}{c_{\text{ref}}} + \frac{\mid q_s \mid}{R e c_{\text{ref}}} \frac{\mid Q_{\text{in}} \mid}{\mid Q_{\text{out}} \mid} \tag{4.24}$$

where c_{ref} is arbitrarily chosen to be 1 mM. The corresponding cation transference number, or fraction of current carried by the cation, is:

$$t_+ = \left(c_0 + \frac{2 \mid q_s \mid}{eR} \frac{\mid Q_{\text{in}} \mid}{\mid Q_{\text{out}} \mid} \right) / \left(2c_0 + \frac{2 \mid q_s \mid}{eR} \frac{\mid Q_{\text{in}} \mid}{\mid Q_{\text{out}} \mid} \right). \tag{4.25}$$

The dimensionless conductance and cation transference number are shown in Fig. 4-8 , for a channel with the sample parameters: $L = 100$ nm, $R = 1$ nm, $\varepsilon_m = 10\varepsilon_0$, $\varepsilon_w = 80\varepsilon_0$, and $T = 300$ K. The plateau in conductance does not occur when electroneutrality breakdown

is present. The decrease in conductance at low concentration has been experimentally observed in Refs. [287] and [292], but the effects were ascribed to surface reactions and electrokinetic coupling, respectively. Here, the large resistance through the pore is expected at low concentration due to electroneutrality breakdown, since fewer counterions are present as charge carriers. As channels become closely spaced or strongly interacting, their behavior returns to the plateau behavior. The presence of electroneutrality breakdown does not rule out the previous explanations for deviations from the conductance plateau at low concentrations. However, the charge regulation reactions and electrokinetic effects might be less sensitive to the interactions of the pores. In addition to electroneutrality breakdown, experiments might also include resistances incurred from microchannel domains that connect to the nanopore. [293, 294] In terms of the transference number, electroneutrality breakdown at low concentrations leads to a cation transference number that does not saturate at $t_+ = 1$, again due to the reduction in screening counterions. Another practically significant quantity is the capacitance of a conducting nanotube embedded in a membrane dielectric medium, which is explored in the Supplemental Information. Electroneutrality breakdown can be used to increase the effective capacitance per unit pore area at low ionic concentrations. However, the capacitance per total membrane area and per total membrane volume do not benefit from electroneutrality breakdown, since the dense channel spacing reduces the effectiveness of electroneutrality breakdown.

Nanoconfined domains are most ubiquitous in biological membranes, where protein channels selectively conduct specific ions. The selectivity filter in ion channels are at the molecular scale, with a radii on the order of single angstroms [295]. In our model thus far, the radius of the channel signifies the accessible area for the *ion centers*, which becomes negligible in true molecular confinement, $R \to 0$. Therefore, we expect electroneutrality breakdown to be critical in describing the conduction of ions through protein channels. In the absence of an electroneutrality constraint, molecular separation in the selectivity filter would instead rely on specific chemical interactions or energy barriers to enter the pore [296]. Closely spaced channels on the order of the membrane thickness ~ 10 nm could interact electrostatically with each other, leading to ensemble gating and ion conduction events.

The electrokinetic coupling and electrokinetic conversion from salinity gradients or pressure gradients are most effective and efficient in the regime of strong double layer overlap. Electroneutrality breakdown can adversely impact the expected performance of such a process. A large density of channels is not only desired for higher flux membranes, but to eliminate the possibility of electroneutrality breakdown at low concentration.

In unstructured charged nanoporous media, such as porous rock or polymer membranes, a large network of charged pores are connected and interact strongly with each other. Applications include desalination, ionic separations, and oil recovery [297–302]. In an interconnected porous medium consisting of closely spaced pores, a similar homogenized model to equation 4.14 should be pursued [303]. If the medium length scale is large relative to the Debye length, then electroneutrality will be maintained.

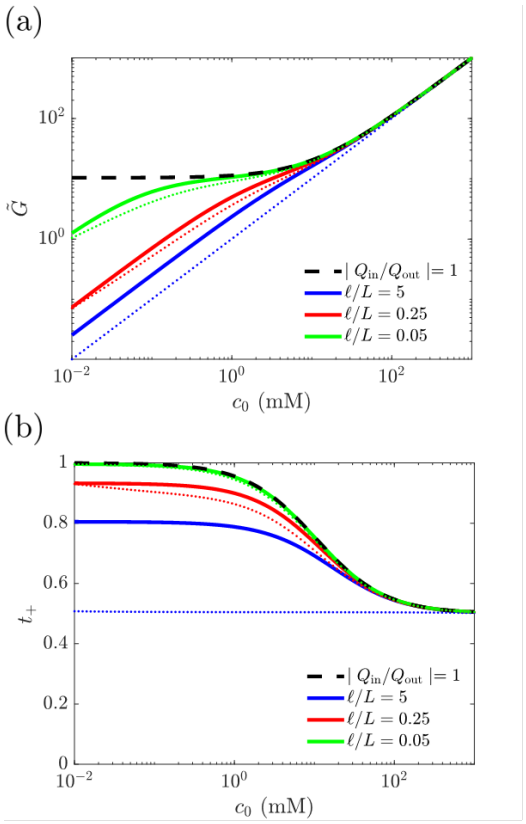

Figure 4-8: The dimensionless conductance (a) and cation transference number (b) through a negatively charged nanochannel for varying channel separation distances. The solid lines are the predictions using equation 4.10 and the dotted lines are the predictions using equation 4.14. The dotted lines are good predictors of the extent of electroneutrality breakdown at small ℓ/L, but fail at large ℓ/L, e.g. the blue dotted lines. The plateau in conductance at low concentration is only apparent when $|\, Q_{in}/Q_{out}\,| = 1$. As the ratio ℓ/L decreases, the system moves closer to electroneutrality. When electroneutrality is broken, the cation transference number does not saturate to 1 at low concentration.

With our emphasis on the physics of electroneutrality breakdown, we have neglected other chemical mechanisms, such as charge regulation [288, 304–306]. Charge regulation, or reactions to form or neutralize surface charge, is certainly occurring at the pore walls– after all, the origin of surface charge is a result of charge adsorption to the interface. Even if charge regulation is present, the effect of electroneutrality breakdown should still be important. In order to delineate from a chem-

ical mechanism, one convincing evidence of electric field escape from a channel would be to observe differences in measureable quantities as a function of the spacing between channels. Only measurements that determine single channel conductance, transference number, or capacitance, as a function of the density of channels in a membrane could distinguish the electroneutrality breakdown mechanism from other competing chemical mechanisms. Furthermore, in Single Digit Nanopores channels, we can expect energy barriers associated with ions' dehydration to enter the channel. Energy barriers in the pore domain can be easily added to the model explored here, by changing the effective chemical potential for ions within the pore [30]. Non-ideal effects [17] such as packing effects [307, 308] or electrostatic correlations [34, 58, 309],are also not considered in this work.

4.2.4 Conclusions

The electroneutrality breakdown phenomenon is studied with an extensive set of continuum simulations. The results are shown to agree with simplifying analytical formulas within their regime of validity. Furthermore, the practical influence of electroneutrality breakdown on channel conductance and selectivity is discussed.

The experimental validation of screening in lower dimensions presents multiple competing mechanisms which can obscure the presence of electroneutrality breakdown. Even so, the set of simulation results presented here can guide researchers to isolate electroneutrality breakdown for multipore systems. One can expect wide variations of properties as a function of channel number density per area when electric fields enter into the membrane domain. As channels are placed closer together, they interact more strongly, changing the transport properties.

4.3 Summary of Findings

In this chapter, I demonstrated the unique screening features of electrolytes in 1D confinement. The propensity towards electroneutrality breakdown is very strong in 1D, where the scaling of the effective screening length . As channels are placed closer together, the escaping electric fields begin to interact, shifting the system back towards electroneutral-

ity. The pore-pore interactions become significant when the lateral pore spacing becomes comparable to the pore length. The electric fields extending from the pore walls through the dielectric membrane imbue some nonlocality into the screening of the charge within a channel.

In summary, we found that the dielectric properties and geometry of the confining surfaces are extremely important in determining the screening structure in 1D confinement. In the next chapter, I will investigate the micrscopic ordering of polar solvent which can affect the dielectric properties of the liquid near interfaces, especially for systems under extreme confinement.

Chapter 5

Interfacial Ordering in Polar Liquids

The following chapter is reproduced from my published paper with Prof. Alexei Kornyshev and Prof. Martin Bazant on the orientational ordering of polar liquids at charged interfaces [35]. I also present preliminary results comparing the theory to the orientational ordering in simulations of various confined polar liquids done by Dr. Karina Pivnic.

5.1 Overview

The structure of polar liquids and electrolytic solutions, such as water and aqueous electrolytes, at interfaces underlies numerous phenomena in physics, chemistry, biology, and engineering. In this work, we develop a continuum dipolar shell theory that captures the essential features of dielectric screening by polar liquids at charged interfaces, including oscillations in charge and mass, starting from the molecular properties of the solvent. The theory predicts an anisotropic dielectric tensor of interfacial polar liquids previously studied in molecular dynamics simulations. We explore the effect of the interfacial polar liquid properties on the capacitance of the electrode/electrolyte interface and on hydration forces between two plane-parallel polarized surfaces. In the linear response approximation, we obtain simple formulas for the characteristic decay lengths of molecular and ionic profiles at the interface.

The interactions between colloidal particles are mediated by nanoconfined polar liquids. Therefore, the resulting hydration or solvation forces between the bounding particle

surfaces are greatly sensitive to the orientational structuring of the polar liquids near the surfaces. By using direct comparison to molecular dynamics simulations, we test the applicability of the dipolar shell theory for three different polar liquids. The three liquids (dichloromethane, acetonitrile, and water) possess very different shapes, sizes, and bulk dielectric constants. As we show, the agreement between the theoretically-predicted and simulated orientational ordering in the diverse set of confined polar liquids demonstrates the predictive power of our theory as well as some limitations.

5.2 Dipolar Shell Theory

5.2.1 Introduction

Polar liquids such as water are ubiquitous in all areas of science and engineering, including biological media, [310, 311] electrochemical interfaces, [16] colloids, [14, 312] synthetic membranes, [313, 314] and lubrication. [315, 316] At charged interfaces, the structure of polar liquids governs the screening of charge by ions in the electrical double layer. [317] The key and still not fully understood feature here is the interplay between the molecular structure of the solvent and the correlations in ionic subsystems. Theoretical models of interfacial polar liquids are therefore critical in the design and understanding of electrified interfaces.

Typically, the dielectric properties of interfacial polar liquids are lumped into two main regions of the electrical double layer: (i) the diffuse layer first described by Gouy and Chapman [318, 319] in which diffuse ionic charges screen the surface charge and (ii) the Stern layer composed exclusively of solvent molecules adjacent to the interface, [223] represented as layer of depressed dielectric constant and fixed thickness. [17] In the diffuse layer, the solvent dielectric constant is usually chosen as its bulk value, and the ions are treated as dilute point charges in the standard Poisson-Boltzmann form. While such a general approach describes numerous electrochemical measurements, the Gouy-Chapman-Stern (GCS) representation does not capture the microscopic details of the structuring of the fluid near the surface, [93, 320–322] nor the electric-field dependent response of the polar

solvent. [323, 324] One clear shortcoming of the GCS model is its failure to describe oscillatory profiles seen in hydration force measurements [32] and x-ray synchrotron-radiation assessed atomic distribution profiles. [325–327]

A plethora of modifications to the Poisson-Boltzmann theory have been proposed to include the correlated structure and crowding of ions at an interface, usually based on theories of inhomogeneous hard sphere fluids. [17, 99, 328] Applications of such theories to electrolytes usually ignore the solvent molecules by treating the fluid as a constant permittivity medium, ε, with hard-sphere ions, the so-called primitive model. [3, 33, 235] While such a model can describe the long-range behavior of dilute electrolytes, it does not capture the short-wavelength structuring of the solvent that affects electrostatic interactions between the ions at a nanometer scale.

In fact, simulations and indirect experimental evidence have demonstrated that the bulk dielectric response of water is nonlocal at short distances. Thus, the studied wave-number dependent static dielectric tensor of water has revealed singularities at short wavelengths, giving rise to the phenomenon of overscreening and alternating bound charges of the polar solvent in response to external perturbation. [329–332] At interfaces, molecular dynamics simulations of interfacial water have shown similar overscreening signatures with singularities in the normal component of the anisotropic static dielectric tensor. [31, 322, 333–336]

To incorporate the dipolar nature of the solvent, a mean-field dipolar Poisson-Boltzmann equation has been developed [324] and extended further in Refs. [67, 337–339]. These mean-field dipolar models have not yet captured the overscreening signatures of dipolar molecules at interfaces. Theoretical analysis including the overscreening phenomenon by polar liquids has mainly been limited to situations in which the nonlocal permittivity tensor can be included as an input [340–342] or through effective Landau-Ginzburg models. [331, 332] These approaches, while generally accurate in comparison to simulations and capable of capturing important features of hydration forces, are not derived from the molecular properties of the solvent and require assumptions to match the bulk screening to the interface.

On the other hand, sophisticated molecular theories including the reference interaction site model (RISM) can accurately predict the spatially-correlated structures of polar liquids

in the bulk and near interfaces. [343–352] Due to the complexity of the integral equations involved in solving these theories, some of the analytical tractability and physical transparency is lost in favor of model accuracy, compared to local dipolar theories. [324] The integral equation theories are therefore difficult to incorporate directly with standard continuum dielectric theory approaches.

Clearly, a physically-transparent continuum model that incorporates the dipolar, molecular nature of solvent molecules to capture the overscreening behavior at the interface would be useful for understanding the interfacial properties of solvents, solvent mixtures, and electrolytes of varying ionic composition, including at large applied voltages.

Here, we derive a modified Langevin-Poisson equation in which we include the nonlocal dielectric response of a polar liquid by employing a weighted-density functional, treating dipolar molecules as shells of charge. The model captures many of the properties of interfacial liquids, including the overscreening of surface charge by the dipolar solvent charges. Singularities in the normal component of the effective static dielectric permittivity at an interface emerge naturally from the theory. After analyzing pure polar liquids, we then include into the theory a finite ion concentration, thus unravelling the fine double layer structure at a charged interface. Further, we apply the theory to describe the hydration forces betweeen two charged surfaces. Finally, we derive a formula for the hydration length, λ_s, which depends only on the diameter of the solvent molecule, d, and the relative permittivity of the liquid, ε_r, where $\lambda_s = d\sqrt{(\varepsilon_r - 1)/6}$, governing the decay of the oscillations

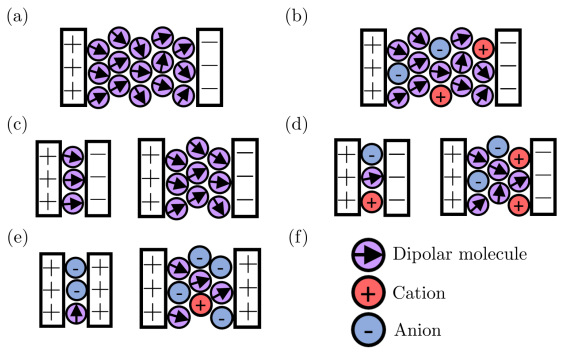

Figure 5-1: Schematic of various systems under consideration in the application of the dipolar shell theory. (a) A pure polar fluid between two oppositely charged surfaces of the same magnitude, obeying overall charge neutrality. (b) A 1:1 electrolyte in a polar solvent with ions of the same size as the dipolar molecules, again with surfaces of equal but opposite charge. (c) A confined pure polar fluid with varying extent of confinement between walls of equal but opposite charge with varying extent of confinement. (d) A 1:1 electrolyte confined between two walls of equal but opposite charge with varying extent of confinement. (e) A 1:1 electrolyte confined between two walls of the same charge with varying extent of confinement. (f) Dipolar molecule, cation, and anion symbols.

in charge ordering in the polar liquid from a surface. We will explain in the chapter the assumptions required to obtain the formula of such extraordinary simplicity, but taken for estimates, it seems to be consistent with existing molecular simulations [31,333,336,353,354].

In this work, we demonstrate the effects of bulk relative permittivity, surface charge density magnitude from linear to nonlinear response, extent of confinement between two surfaces, and ionic concentration on the interfacial properties of the polar liquid. As depicted in Fig. 5-1, the systems under consideration will include (a) a pure polar liquid between oppositely charged surfaces (b) an electrolyte between two oppositely charged surfaces (c) confined pure polar liquids between oppositely charged surfaces, and (d-e) confined electrolytes between oppositely charged surfaces and identically charged surfaces, respectively. From our theoretical analysis, we demonstrate the importance of the molecular properties of the polar liquid in hydration interactions and double layer capacitance of charged interfaces.

5.2.2 Theory

The theoretical approach presented here originates from the model for ionic liquids of ref. [7], to which we add dipolar molecules as hard spheres with dipolar shells of charge. The model treats the equilibrium properties of a concentrated system of dipolar shells in a manner similar to the Langevin-Poisson theories previously described for point dipoles. [324] For simplicity, we limit our analysis to the case of equally sized ions and dipolar molecules with radius, R. This system of ions and dipoles will be positioned between two flat surfaces. We assume that the dipoles and ions in this nanoslit are in equilibrium with a reservoir with fixed bulk concentrations of both ions and dipoles, within the grand canonical ensemble.

Density functional

The theoretical framework is based on a definition of the Helmholtz free energy functional of the system, and could be classified as a classical Density Functional Theory approach. The Helmholtz free energy, $\mathscr{F}$ can be split into three parts: an ideal part $\mathscr{F}^{\mathrm{id}}$, an excess

part accounting for excluded volume effects, $\mathscr{F}^{\text{ex}}$, and an electrostatic part, $\mathscr{F}^{\text{el}}$,

$$\mathscr{F} = \mathscr{F}^{\text{id}} + \mathscr{F}^{\text{ex}} + \mathscr{F}^{\text{el}}. \tag{5.1}$$

As a standard definition, the ideal part of the free energy density is given by:

$$\mathscr{F}^{\text{id}}[\{c_i(\mathbf{r})\}] = \sum_i k_B T \int d\mathbf{r}\, c_i(\mathbf{r}) \left[\ln(\Lambda_i^3 c_i(\mathbf{r})) - 1\right], \tag{5.2}$$

where k_B is the Boltzmann constant, T is the absolute temperature, c_i is the concentration of species i, and Λ_i is the de Broglie wavelength for species i. The ideal part of the chemical potential for species i, μ_i^{id}, relative to some reference bulk solution denoted as b, is thus:

$$\beta\mu_i^{\text{id}} = \beta\left(\frac{\delta\mathscr{F}^{\text{id}}}{\delta c_i} - \frac{\delta\mathscr{F}^{\text{id}}}{\delta c_i}\Big|_b\right) = \ln\left(\frac{c_i}{c_{i0}}\right), \tag{5.3}$$

where c_{i0} is the concentration in the bulk and β is the inverse thermal energy, $\beta^{-1} = k_B T$.

For the excess free energy density, we will assume that all species are approximately spherical and equal in size. Here, we adopt a weighted-density approximation from ref. [7] that was constructed to recover the Carnahan-Starling equation of state:

$$\mathscr{F}^{\text{ex}}[\bar{c}_i(\mathbf{r})] = \frac{k_B T}{v} \int d\mathbf{r} \left[\frac{1}{1-\bar{\eta}} - 3\bar{\eta} + \frac{1}{(1-\bar{\eta})^2}\right]. \tag{5.4}$$

Here, v is the volume of a molecule, $\eta = \sum_i v c_i$ is the local filling fraction, and $\eta_0 = \sum_i v c_{i0}$ is the bulk filling fraction. The bar notation denotes a convolution with the volumetric weighting function, $\bar{\eta} = w_v * \eta$, where $w_v(r) = \Theta(R - \mid r \mid)/v$, is a Heaviside step function that only turns on within the volume of the sphere, with R defined as the radius of the molecular sphere. The $*$ operator corresponds to a convolution integral, $f * g = \int d\mathbf{r}' f(\mathbf{r}') g(\mathbf{r} - \mathbf{r}')$. Therefore, the excluded volume interactions appear in a non-local fashion in the chemical potential, describing the filling within a molecular-sized neighborhood

of a point. The associated weighted excess chemical potential, $\bar{\mu}_i^{\text{ex}}$,is:

$$\begin{aligned}\beta\bar{\mu}_i^{\text{ex}} &= \beta\left(\frac{\delta\mathscr{F}^{\text{ex}}}{\delta c_i} - \frac{\delta\mathscr{F}^{\text{ex}}}{\delta c_i}\Big|_b\right) \\ &= w_v * \left(\frac{8\bar{\eta} - 9\bar{\eta}^2 + 3\bar{\eta}^3}{(1-\bar{\eta})^3} - \frac{8\eta_0 - 9\eta_0^2 + 3\eta_0^3}{(1-\eta_0)^3}\right).\end{aligned} \tag{5.5}$$

Derivation of electrostatic variables

The key development in the theory presented in this work is the electrostatic part of the free energy. Here, we spread the ionic charge and bound charges on dipoles over their surface, so that they act electrostatically as shells rather than points. The smeared shell charge appears in the mean-field Poisson equation for both the ions and the polar liquid molecules. The charged shell formulation here is directly based on the theory for concentrated ionic liquids presented in ref. [7]. The approach is preceded by similar theoretical models for electrolytes composed of ions with intramolecular charge distributions, [196, 200–204] as well as charged shell representation of the mean-spherical approximation. [52, 205, 206] The charged shell approximation is applicable not only to ions and dipoles with charge form factors in the shape of a spherical shell, but also for hard sphere ions and dipoles with point charges and point dipole moments at their centers in which the electrostatic potential can only develop beyond the ionic radius or dipolar molecule radius. The electrostatic part of the free energy, defined in terms of weighted densities, is therefore:

$$\mathscr{F}^{\text{el}}[\phi, \bar{\rho}_e, \bar{\mathbf{P}}] = \int d\mathbf{r}\Big\{-\frac{\varepsilon_0}{2}(\nabla\phi)^2 + \bar{\rho}_e\phi + \bar{\mathbf{P}}\cdot\nabla\phi\Big\}, \tag{5.6}$$

where ϕ is the electrostatic potential, ε_0 is the permittivity of free space, $\bar{\rho}_e = w_s * \rho_e$ is the weighted charge density, and $\bar{\mathbf{P}} = w_s * \mathbf{P}$ is the weighted polarization vector, originating from the weighted bound charge on the dipolar molecules, $\bar{\rho}_b = w_s * \rho_b = \nabla\cdot\bar{\mathbf{P}}$. Here, the convolution with the weighting function $w_s(r) = \delta(R - \mid r \mid)/(4\pi R^2)$ homogenizes the charge and polarization over a spherical shell.

Using the definition of the polarization vector, $\mathbf{P}$, as the concentration of dipoles, c_w, multiplied by their individual dipole moments, $\mathbf{p}$, we can next define the weighted polar-

ization vector, $\bar{\mathbf{P}}$:

$$\mathbf{P} = c_w \mathbf{p}, \quad \bar{\mathbf{P}} = w_s * (c_w \mathbf{p}), \tag{5.7}$$

for which there will be a distribution of dipole orientations that we will ultimately need to average over. The electrochemical potential of the dipole, μ_w can be found by taking the variational derivative of the free energy with respect to the dipole concentration:

$$\beta \mu_w = \ln\left(\frac{c_w}{c_{w0}}\right) + \beta \mathbf{p} \cdot \nabla \bar{\phi} + \beta \bar{\mu}_w^{\mathrm{ex}}. \tag{5.8}$$

Here, $\bar{\phi} = w_s * \phi$ is the weighted electrostatic potential, and $\bar{\mu}_w^{\mathrm{ex}} = w_v * \mu_w^{\mathrm{ex}}$ is the weighted excess chemical potential. Mathematically, the weighted electrostatic potential and weighted excess chemical potential emerge due to the minimization of the free energy with respect to the concentration variables, which are present in the free energy in terms of convolutions with weighting functions. Physically, these are a result of the delocalization of bound charge over the dipolar molecule surface and the nonlocal packing effects, respectively. This procedure embeds the finite size of dipolar molecules into the theory, which plays a key role in capturing the effects of layering and decoupling the packing periodicity from the longer range electrostatic correlations. Thus, although this approach should still be classified as a mean field theory, it makes an essential step towards accounting for molecular structure of the liquid. The dipole concentration at a given position is thus:

$$c_w = c_{w0} \exp\left(-\beta \mathbf{p} \cdot \nabla \bar{\phi} - \beta \bar{\mu}_w^{\mathrm{ex}}\right). \tag{5.9}$$

Therefore, the local dipole concentration depends on the angle, θ, between the dipole moment of the molecule and the weighted electric field, $\overline{\mathbf{E}} = w_s * \mathbf{E} = -\nabla \bar{\phi}$, where

$$\mathbf{p} \cdot \nabla \bar{\phi} = p_0 \mid \nabla \bar{\phi} \mid \cos\theta, \tag{5.10}$$

assuming a constant effective dipole moment magnitude, p_0. Averaging over the possible

orientations of the molecule gives:

$$\langle c_w \rangle = c_{w0} e^{-\beta \bar{\mu}_w^{\text{ex}}} \left\langle e^{-\beta p_0 |\nabla \bar{\phi}| \cos\theta} \right\rangle \tag{5.11}$$

for the dipole concentration and:

$$\langle \mathbf{P} \rangle = c_{w0} p_0 e^{-\beta \bar{\mu}_w^{\text{ex}}} \frac{\nabla \bar{\phi}}{|\nabla \bar{\phi}|} \left\langle \cos(\theta) e^{-\beta p_0 |\nabla \bar{\phi}| \cos\theta} \right\rangle \tag{5.12}$$

for the polarization vector, where $\langle\rangle$ denotes the average over θ. Averaging over the dipole orientations gives:

$$\begin{aligned} \left\langle e^{-\beta p_0 |\nabla \bar{\phi}| \cos\theta} \right\rangle &= \frac{1}{2} \int_0^{\pi} e^{-\beta p_0 |\nabla \bar{\phi}| \cos\theta} \sin\theta d\theta \\ &= \frac{\sinh\left(\beta p_0 \mid \nabla \bar{\phi} \mid\right)}{\beta p_0 \mid \nabla \bar{\phi} \mid} \end{aligned} \tag{5.13}$$

and

$$\begin{aligned} \left\langle \cos(\theta) e^{-\beta p_0 |\nabla \bar{\phi}| \cos\theta} \right\rangle &= \frac{1}{2} \int_0^{\pi} e^{-\beta p_0 |\nabla \bar{\phi}| \cos\theta} \cos\theta \sin\theta d\theta \\ &= -\frac{\sinh\left(\beta p_0 \mid \nabla \bar{\phi} \mid\right)}{\beta p_0 \mid \nabla \bar{\phi} \mid} \mathscr{L}\left(\beta p_0 \mid \nabla \bar{\phi} \mid\right) \end{aligned} \tag{5.14}$$

where $\mathscr{L}(x) = \coth(x) - 1/x$ is the Langevin function. Therefore, the dipole concentration can be written as:

$$\langle c_w \rangle = c_{w0} e^{-\beta \bar{\mu}_w^{\text{ex}}} \frac{\sinh\left(\beta p_0 \mid \nabla \bar{\phi} \mid\right)}{\beta p_0 \mid \nabla \bar{\phi} \mid}, \tag{5.15}$$

and the polarization density can be expressed as:

$$\langle \mathbf{P} \rangle = -p_0 \langle c_w \rangle \frac{\nabla \bar{\phi}}{|\nabla \bar{\phi}|} \mathscr{L}\left(\beta p_0 \mid \nabla \bar{\phi} \mid\right). \tag{5.16}$$

In turn, the weighted polarization vector is defined as:

$$\langle \bar{\mathbf{P}} \rangle = -w_s * \left[p_0 \langle c_w \rangle \frac{\nabla \bar{\phi}}{|\nabla \bar{\phi}|} \mathscr{L}\left(\beta p_0 \mid \nabla \bar{\phi} \mid\right) \right]. \tag{5.17}$$

Moving forward, we drop the bracket notation, such that $\mathbf{P}$ refers to $\langle \mathbf{P} \rangle$, $\bar{\mathbf{P}}$ refers to $\langle \bar{\mathbf{P}} \rangle$,

and c_w refers to $\langle c_w \rangle$.

Along with the description of the polarization vector, we must also describe the ionic charge when there is a non-zero electrolyte concentration. The ionic electrochemical potential is defined as:

$$\beta\mu_i = \ln\left(\frac{c_i}{c_{i0}}\right) + z_i e\beta\bar{\phi} + \beta\bar{\mu}_i^{\text{ex}}. \tag{5.18}$$

Therefore, the distributions of the ions are given by:

$$c_i = c_{i0}\exp\left(-\beta e\bar{\phi} - \beta\bar{\mu}_i^{\text{ex}}\right). \tag{5.19}$$

For a 1:1 solution of concentration c_0, the electrolyte charge density is therefore:

$$\rho_e = -2ec_0\sinh\left(\beta e\bar{\phi}\right)e^{-\beta\bar{\mu}_i^{\text{ex}}}, \tag{5.20}$$

and the weighted electrolyte charge density is $\bar{\rho}_e = w_s * \rho_e$.

The Poisson equation consistent with the free energy density in Eq. 5.6 is:

$$-\varepsilon_0\nabla^2\phi = -\nabla\cdot\bar{\mathbf{P}} + \bar{\rho}_e. \tag{5.21}$$

as shown in Appendix A of ref. [35]. The source of the electric field is therefore the delocalized shells of charge of the ions and bound charge on dipolar molecules, mathematically appearing as convolutions with the weighting function, w_s. Specifically, the overall charge density in the Poisson equation includes both the weighted bound charge density on the dipolar molecules, $\bar{\rho}_b = -\nabla\cdot\bar{\mathbf{P}}$, and the weighted ionic charge, $\bar{\rho}_e$.

Reducing to one dimension

In the 1D geometry between two flat plates, the weighting function formulas must be modified [55] to integrate over the y and z dimensions, since all variables depend only on x. Physically, the spherical shell of charge corresponding to w_s becomes equivalent to a line of charge with length $2R$ and uniform charge per length (the differential area of a sphere per differential in the axial coordinate). The spherical Heaviside weighting function, w_v,

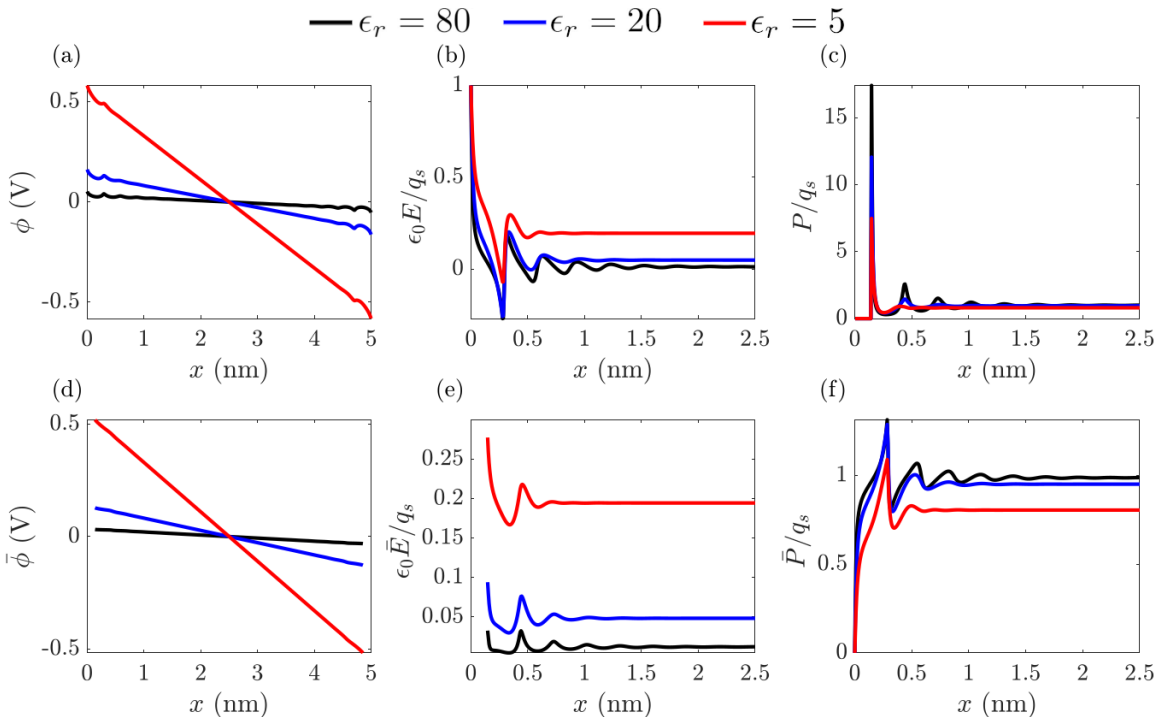

Figure 5-2: Electrostatic screening by pure polar liquids between two surfaces of opposite charge shown for different values of the bulk dielectric constant, comparing the weighted and nonweighted quantities. The curves are generated by solving Eq. 5.24 with $\bar{\rho}_e = 0$. Variables are plotted as functions of the normal coordinate, x, zooming into the profiles emerging from the left interface for b-c and e-f. The selected bulk dielectric permittivities, correspond to values of $p_0 = 4.86$ D for $\varepsilon_r = 80$, $p_0 = 2.38$ D for $\varepsilon_r = 20$, and $p_0 = 1.09$ D for $\varepsilon_r = 5$, keeping all other parameters constant ($T = 300$ K, $L = 5$ nm, $c_{w0} = 55$ M, $d = 0.285$ nm, and $q_s = 0.01$ C/m^2). (a) Electrostatic potential, ϕ, (b) electric field, $E = -\phi'$, (c) polarization density, P, (d) weighted electrostatic potential, $\bar{\phi}$, (e) weighted electric field, $\bar{E} = -\bar{\phi}'$, and (f) and weighted polarization density, $\bar{P}$. The local variables in a-c describe the “measured" local electrostatic response of the system, while the weighted potential and weighted electric field in d-e determine the electrochemical potential and orientation of dipoles. The weighted polarization vector in f corresponds to the polarization arising from the delocalized bound charge on the dipolar shells.

becomes a quadratic function, corresponding to the differential volume of a sphere per differential in the axial coordinate. Their modified forms are:

$$w_v(x-x') = \frac{\pi\left(R^2-(x-x')^2\right)}{v}\Theta\left(R-\mid x-x'\mid\right) \tag{5.22}$$

$$w_s(x-x') = \frac{1}{2R}\Theta\left(R-\mid x-x'\mid\right). \tag{5.23}$$

In 1D, the integro-differential equation for the electrostatic potential is:

$$0 = \varepsilon_0\frac{d^2\phi}{dx^2} - \frac{d\bar{P}}{dx} + \bar{\rho}_e \tag{5.24}$$

where

$$P = -p_0 c_{w0} e^{-\beta\bar{\mu}_w^{\mathrm{ex}}}\frac{\sinh\left(\beta p_0\bar{\phi}'\right)}{\beta p_0\bar{\phi}'}\mathscr{L}\left(\beta p_0\bar{\phi}'\right), \tag{5.25}$$

and $\bar{\phi}' = d\bar{\phi}/dx$ denotes a derivative with respect to x. In this geometry, the average orientation of the dipoles relative to the x-axis can be expressed as:

$$\langle\cos(\theta)\rangle = -\mathscr{L}\left(\beta p_0\bar{\phi}'\right). \tag{5.26}$$

We assume that the surface charge is uniformly distributed on bounding flat hard walls at $x = 0$ and $x = L$. For simplicity, here, the surface charge density is assumed not to have any finite size, so the boundary conditions reduce to:

$$\begin{aligned}\left(-\varepsilon_0\phi'\right)\Big|_{x=0} &= q_s\\ \left(-\varepsilon_0\phi'\right)\Big|_{x=L} &= \pm q_s\end{aligned} \tag{5.27}$$

where we have the surface charge density of magnitude q_s on each side. Depending on the scenario under investigation, the charge on each surface is either opposite in sign or the same in sign, as sketched in Fig. 5-1. If the charge at x=L is negative, we choose “+" in the second line of Eq. 5.27, and the opposite is true if the charge is positive. The local dipolar and ionic concentrations are zero in the regions $x < R$ and $x > L-R$ owing to the hard sphere repulsion with the flat bounding surfaces. To solve these equations, we discretized them using finite difference formulas.

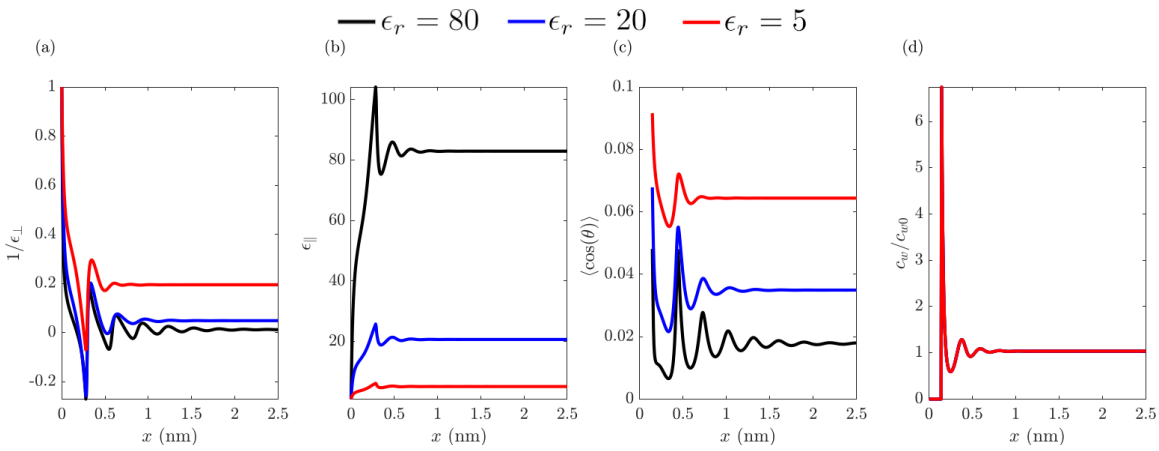

Figure 5-3: Dielectric tensor, average orientation, and density of pure polar fluids between two surfaces of opposite charge, generated for model polar liquids with different values of the bulk dielectric constant. The curves are generated by solving Eq. 5.24 with $\bar{\rho}_e = 0$. Variables are plotted as functions of the normal coordinate, x, zooming into the profiles emerging from the left interface. The results are plotted for three pure polar fluids, corresponding to $p_0 = 4.86$ D for $\varepsilon_r = 80$, $p_0 = 2.38$ D for $\varepsilon_r = 20$, and $p_0 = 1.09$ D for $\varepsilon_r = 5$, keeping all other parameters constant ($T = 300$ K, $L = 5$ nm, $c_{w0} = 55$ M, $d = 0.285$ nm, and $q_s = 0.01$ C/m^2). (a) Normal component of the dielectric tensor, $\varepsilon_\perp$, plotted in terms of its inverse. (b) Tangential component of the dielectric tensor, $\varepsilon_\parallel$. (c) Average orientation of dipolar molecules, $\langle\cos(\theta)\rangle$. (d) Density profile of dipolar molecules, c_w, normalized by the bulk value. In (d), the density profiles are closely overlapping each other, due to the low applied surface charge.

Extracting the effective local dielectric tensor

1. Normal component

   A fundamental calculation involves extracting the static dielectric profile from the predicted polarization vector. Here, we choose a permittivity definition that is consistent with the weighted Poisson equation. The self-consistent definition of the normal permittivity is given by:

$$\varepsilon_\perp = 1 - \frac{\bar{P}}{\varepsilon_0 \phi'} \tag{5.28}$$

   which represents the total displacement vector, $D = -\varepsilon_0\phi' + \bar{P}$, divided by the electric field, both extracted directly from our model. Note that while the electrochemical potential of the dipoles depends on the weighted electrostatic field, the displacement vector includes a contribution from the local electric field ($-\phi'$) and also the weighted polarization vector ($\bar{P}$). The modified Poisson equation can be written in

terms of the effective normal permittivity in the form:

$$\frac{d}{dx}\left(\varepsilon_0\varepsilon_\perp\frac{d\phi}{dx}\right)=-\bar{\rho}_e. \tag{5.29}$$

Here, the effective normal permittivity includes only the polarization of the solvent, and does not include the polarization from the ions. We will return to the nuances of the definition of the normal permittivity in the analysis of concentrated electrolytes.

2. Tangential component

While we assume no tangential component of the field in the solution of our model, we can also use the model to quantify the extent of tangential polarizability of the interfacial polar liquid in response to macroscopic electric fields tangential to the plane of the interface. If the tangential electric field is constant and weak relative to the normal electric field, then we can extract it as a small, constant perturbation upon the normal field. For example, we can assume a small perturbative component of the electric field in the y direction, E_y, that satisfies $\mid E_y \mid \ll \mid E_x \mid$. We can approximate the magnitude of the gradient of the weighted electrostatic potential as: $\mid \nabla\bar{\phi} \mid \approx \mid \bar{E}_x \mid = \mid \bar{\phi}' \mid$, where the prime notation still refers to derivatives in the x-direction, and $\bar{E}_x$ is the weighted electric field in the x-direction. If we apply such an assumption to the y-component of Eq. 5.17, the displacement vector in the y-direction is therefore:

$$\begin{aligned} D_y &= \varepsilon_0 E_y + \bar{P}_y \approx \varepsilon_0 E_y + w_s * \left[p_0 c_w \frac{\bar{E}_y}{\mid \bar{E}_x \mid} \mathscr{L}\left(\beta p_0 \mid \bar{E}_x \mid\right)\right] \\ &\approx \varepsilon_0 E_y + w_s * \left[p_0 c_w \frac{\bar{E}_y}{\bar{\phi}'} \mathscr{L}\left(\beta p_0 \bar{\phi}'\right)\right]. \end{aligned} \tag{5.30}$$

Next, we divide the tangential (y) component of the displacement vector by the tangential electric field (E_y). Since we assume the tangential electric field is constant due to the system's translational invariance in the $yz-$plane, it can be treated as a constant for the differentiation or convolution operations, so that $E_y \approx \bar{E}_y$. Through

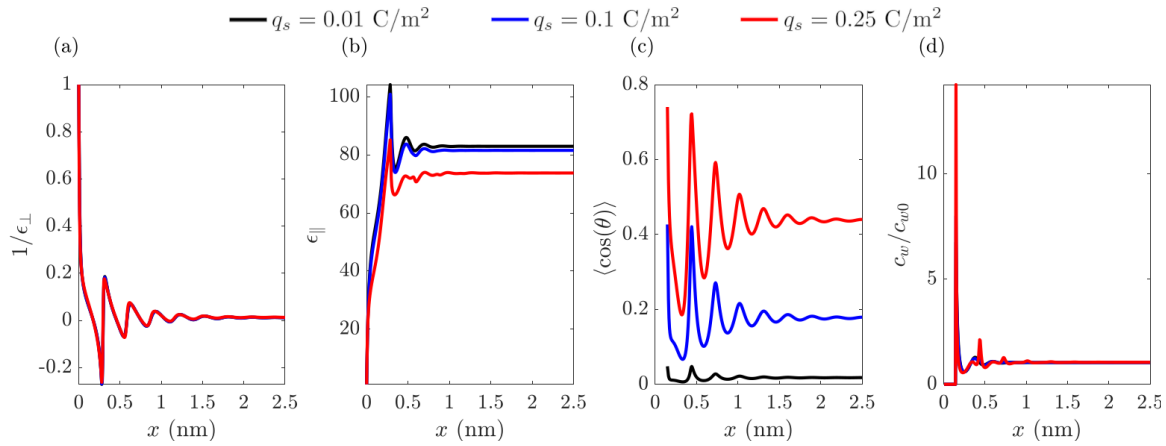

Figure 5-4: Dielectric tensor, average orientation, and density of pure polar fluids between two surfaces of opposite charge for varying surface charge density. The curves are generated by solving Eq. 5.24 with $\bar{\rho}_e = 0$. Variables are plotted as functions of the normal coordinate, x, zooming into the profiles emerging from the left interface. The results are plotted for varying surface charge density ($q_s = 0.01$ C/m^2, $q_s = 0.1$ C/m^2, and $q_s = 0.25$ C/m^2), keeping all other parameters constant ($T = 300$ K, $L = 5$ nm, $c_{w0} = 55$ M, $d = 0.285$ nm, and $p_0 = 4.86$ D). (a) Normal component of the dielectric tensor, $\varepsilon_\perp$, plotted in terms of its inverse. (b) Tangential component of the dielectric tensor, $\varepsilon_\parallel$. (c) Average orientation of dipolar molecules, $\langle\cos(\theta)\rangle$. (d) Density profile of dipolar molecules, c_w, normalized by the bulk value.

this process, the tangential permittivity, $\varepsilon_\parallel$, can be defined as:

$$\varepsilon_\parallel \approx 1 - w_s * \left(\frac{P}{\varepsilon_0 \bar{\phi}'}\right). \tag{5.31}$$

5.2.3 Results

The equations are solved between two surfaces with fixed charge densities of magnitude q_s and separation distance L. The baseline parameters correspond to the effective values for water: dipolar molecule concentration $c_{w0} = 55$ M (corresponding to ≈33 molecules per nm^3), temperature $T = 300$ K, and a diameter of $d = 0.285$ nm. While ε_r is the bulk dielectric constant far from the interface, the local static dielectric tensor can vary as a function of position. In the bulk, the relative permittivity as given by the dipolar model for small perturbations is given by: [324]

$$\varepsilon_r = 1 + \frac{\beta c_{w0} p_0^2}{3\varepsilon_0}. \tag{5.32}$$

For a dipolar concentration of $c_{w0} = 55$ M at $T = 300$ K, the bulk dielectric constant of $\varepsilon_r = 80$ requires an effective dipole moment of $p_0 = 4.86$ D. This effective value is significantly larger than the actual dipole moment of water, 1.8 D. The effective dipole moment accounts for correlations between the orientation of a single dipolar molecule and the orientation of its nearest neighbors, as accounted for in more sophisticated bulk dielectric theories. [337, 355–357] Here, we lump these effects into the effective dipole moment in our model, similar to previous dipolar Poisson-Boltzmann approaches. [67, 324] The default separation distance between the two charged surfaces is $L = 5$ nm, and the default surface charge density magnitude is $q_s = 0.01$ C/m^2.

With the inclusion of the polar fluid, the parameter space for the system under investigation is large. We therefore divide our results into five parts: (A) First, we present results for pure polar fluids between two opposite surfaces. We formally investigate how the interfacial electrostatic properties change with varying bulk dielectric constant, and also how nonlinear saturation of the dipole orientation arises at high surface charge. We also show the complicated layering of molecular orientation for dipolar fluids confined to the sub-nanometer scale. (B) Second, the interfacial electrostatic properties are investigated with a non-zero ionic concentration between oppositely charged surfaces. Here, the results are presented for varying ionic concentrations and for varying surface charge magnitudes. (C) Next, the theory is applied to understanding hydration interactions between two surfaces of (i) opposite charge with and without ions present and (ii) the same charge with a non-zero ionic concentration. (D) The double layer capacitance with ions present is then investigated, ensuring non-overlapping double layers with large separation distances between the surfaces. (E) Finally, the equations are linearized and cast into a differential form, which gives analytical decay lengths describing the layering of charge and mass at the interface.

Pure polar fluids: Interfacial dielectric structure

The system of a pure polar fluid is rare in practice, but it is a useful reference system to showcase the dipolar shell theory predictions. In order to maintain electroneutrality, the bounding surfaces must have equal but opposite charge density, since the pure polar fluid does not have any net charge. Within this system, we will highlight the influence of the

fluid bulk permittivity, ε_r, the strength of the electric field in the system that is set by the surface charge density on the boundaries, q_s, and the confinement extent of the fluid given by the surface separation distance, L.

To start, we investigate the effect of the effective dipole moment, p_0, on the resulting potential and electric field distribution. Since p_0, of course, determines the bulk macroscopic dielectric constant, ε_r, we may say that we will trace the effect of the latter on the local properties near the interface, although the variation ε_r is itself the result of variation of p_0. In order to study fluids of different bulk dielectric constants, we vary p_0 to take on the values $p_0 = 2.36$ D for $\varepsilon_r = 20$ and $p_0 = 1.09$ D for $\varepsilon_r = 5$, keeping all other variable constant.

In Fig. 5-2, the electrostatic potential, electric field, and polarization density are plotted along with their weighted counterparts for fluids of varying bulk permittivity, ε_r. For each fluid, the electrostatic potential, ϕ, oscillates near the surface, within the first nanometer. The potential difference across the nanoslit is greatest for the least polar fluid with $\varepsilon_r = 5$, since dielectric screening is the weakest for this system. The oscillations in the potential lead to sharp cusps and oscillations in the electric field, E, for all the fluids. The electric field even reverses signs at some points, corresponding to reversal in the local electric field direction, corresponding to *overscreening* of the surface charge. The oscillations and sign reversals in the electric field are stronger for the more polar fluids with higher ε_r. The local polarization density, P, has related signatures, where the local polarization density magnitude exceeds the imposed displacement field magnitude set by the surface charge density on the bounding walls. For the weighted variables, $\bar{\phi}$, $\bar{E}$, and $\bar{P}$, the weighting operation smooths out the oscillations compared to the local variables, but does not eliminate them.

The weighted electrostatic potential, $\bar{\phi}$, and weighted electric field, $\bar{E}$, determine the local electrostatic energy and orientation of the dipolar shells in the theory. The weighted polarization density, $\bar{P}$, contributes to the overall displacement field, $D = \varepsilon_0 E + \bar{P}$. Therefore, the overscreening of the surface charge occurs when $\bar{P}$ exceeds q_s, where the cumulative bound dipolar shell charge exceeds the surface charge density. All the fluids experience at least one overscreening peak in the weighted polarization profile. However, the oscillations decay more rapidly and the overscreening peaks are smaller for the lower bulk permittivity

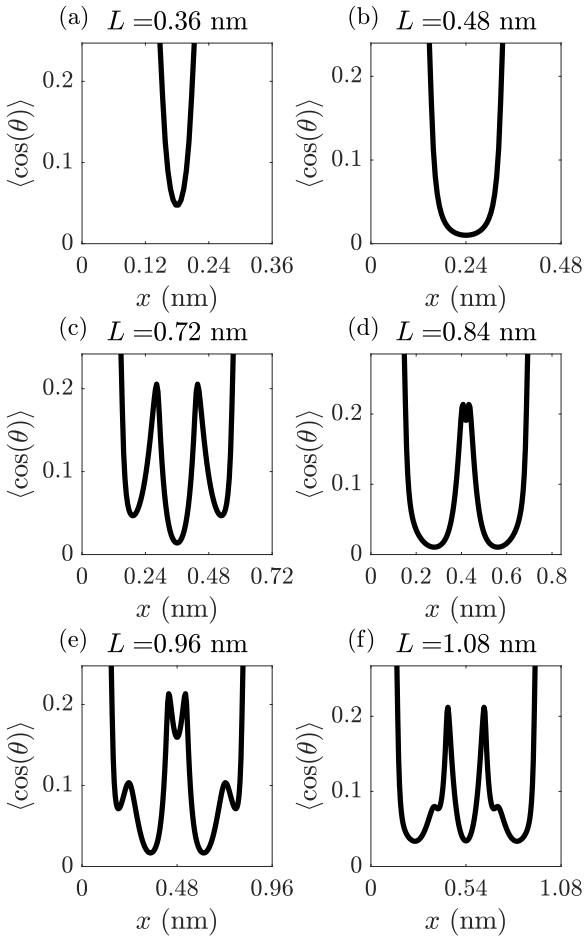

Figure 5-5: Orientation of molecules in a pure polar fluid between two oppositely charged surfaces as a function of the confinement distance between the surfaces. The curves are generated by solving Eq. 5.24 with $\bar{\rho}_e = 0$. The results are plotted for indicated separation distances between the two confining charged surfaces, L, keeping all other parameters constant ($T = 300$ K, $c_{w0} = 55$ M, $d = 0.285$ nm, $p_0 = 4.86$ D, $q_s = 0.05$ C/m^2).

liquids. From these profiles, we can deduce that the overscreening phenomenon is essential to describing the structuring of polar liquids with large bulk dielectric constant, and is microscopically sensitive to the effective dipole moment, p_0.

Next, we can use the electrostatic variables to determine the components of the dielectric tensor near the interface, as shown in Fig. 5-3, for fluids with different bulk dielectric constants. Due to the weighted polarization density overscreening the surface charge density, the normal component of the dielectric tensor has singularities. The tangential component, on the other hand, does not have the same overscreening structure since it is set by a long range tangential electric field, and the tangential component of the dielectric func-

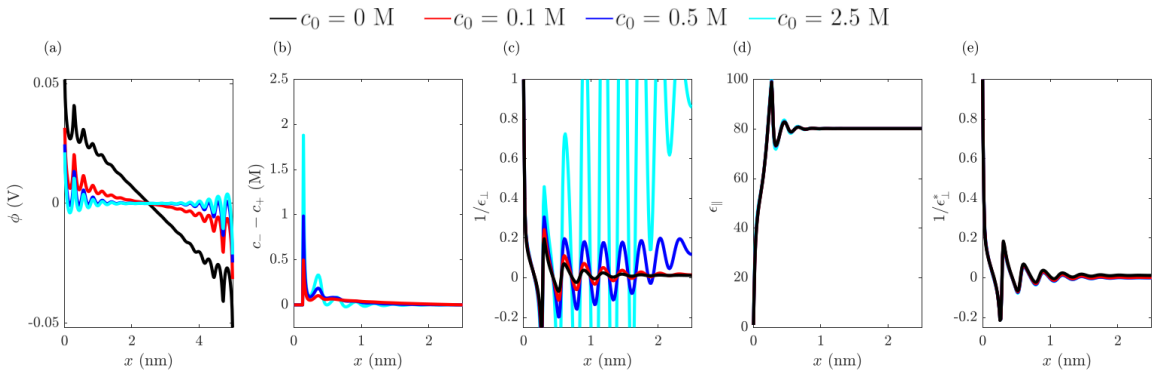

Figure 5-6: Electrolyte screening behavior between two surfaces of opposite charge for varying ionic concentration. The curves are generated by solving Eq. 5.24 with $\bar{\rho}_e \neq 0$. The ionic concentration is varied between $c_0 = 0$ M, $c_0 = 0.1$ M, $c_0 = 0.5$ M, and $c_0 = 2.5$ M, keeping all other parameters constant ($T = 300$ K, $L = 5$ nm, $c_{w0} = 55$ M, $d = 0.285$ nm, $q_s = 0.01$ C/m^2, and $p_0 = 4.86$ D). (a) Electrostatic potential, ϕ. (b) Local difference in ionic concentration, porportional to the local charge density. (c) Normal component of the dielectric tensor (effective–accounting only for the polarization of solvent), $\varepsilon_\perp$, plotted in terms of its inverse. (d) Tangential component of the dielectric tensor, $\varepsilon_\parallel$. (e) Normal component of the general dielectric tensor, $\varepsilon^*_\perp$ (accounting for the polarization of the solvent and ions).

tion varies closely with the local dipole concentration, c_w. The orientation of the dipoles, $\langle\cos(\theta)\rangle$, is actually higher for the fluid that is the least polar. This fact appears because the least polar fluid with $\varepsilon_r = 5$ corresponds to the weakest dielectric screening of the electric field. Even though large differences are observed in the dielectric profiles, at the low charge density of $q_s = 0.01$ C/m^2, the dipole concentration is not very strongly affected by electrostatics, as shown in Fig. 5-3(d). Instead, the dipole density is dominated by the packing effects embedded in $\bar{\mu}_i^{\text{ex}}$, which is independent of electrostatics at small potentials. The large contact value for the density is also governed by the nonlocal packing effects, similar to uncharged hard-sphere fluids. In turn, the excess chemical potential owing to packing plays a minor role in the overscreening structure in the normal component of the dielectric tensor. The overscreening signatures can therefore be attributed to the delocalization of the bound charge on dipoles over the dipole molecule surface. The remarkable anisotropic static dielectric tensor predicted by the dipolar shell theory here is similar to the reported Molecular Dynamics simulations of the dielectric properties of interfacial water. [31,322,336,353,354] The overscreening signatures also qualitatively match the results from simulations and a phenomenological electrostatic theory of confined liquids. [358]

Further, we explore what happens when a pure polar fluid with bulk dielectric constant

$\varepsilon_r = 80$ is subjected to a strong electric field at the boundaries, driving the system to non-linear response with experimentally feasible surface charge densities. Fig. 5-4 includes the normal dielectric permittivity, the tangential permittivity, the dipole orientation, and the dipole density as a function of distance from the left surface for different values of surface charge density. The overscreening structure and singularities in the normal dielectric constant are more or less unchanged as the surface charge increases. However, at the largest charge density, $q_s = 0.25$ C/m^2, the normal and tangential components of the permittivity saturate to a lower value. Even though the strong electric field leads to dielectric saturation and electrostriction (an increase in the local dipolar concentration near the interface), the saturation of the orientation of the dipoles due to the strong field intensity leads to a lower effective dielectric constant for the polar fluid in the nanoslit. Interestingly, the dipolar concentration profile at high charge density forms layers with sharp cusp-like peaks near the surface.

Finally, the behavior of the polar liquid model is studied as a function of the extent of confinement, as shown in Fig. 5-5. Here, the distance between the two surfaces, L, is varied between $L = 0.36$ nm to $L = 1.08$ nm. The layering in the orientation of dipole molecules relative to the normal axis, $\langle\cos(\theta)\rangle$, is complicated by the coherency of the layers of charge emanating from each surface. As the surface separation increases, the dipoles go from one layer, to two layers, to four layers, back to three layers, then three layers with smaller sublayers, then four layers. This means that single angstrom differences in separation can lead to constructive or destructive interference from opposing layers of dipoles, forming dipolar patterns with varying orientations, periodicity, and number of layers.

What changes in the presence of a strong electrolyte

Commonly, dissolved ions are present in polar fluids due to dissociation of electrolytes. In this section, we examine the screening of charge at interfaces for a polar fluid with nonzero ion concentration. Due to the nonzero ion concentration, the surface charges need not be equal nor do they need to be opposite, since any net charge of the two surfaces will be screened by ionic charges in the nanoslit. For the purposes of this section, however, to stay in line with the pure polar fluid case, we maintain equal but opposite surface charge density

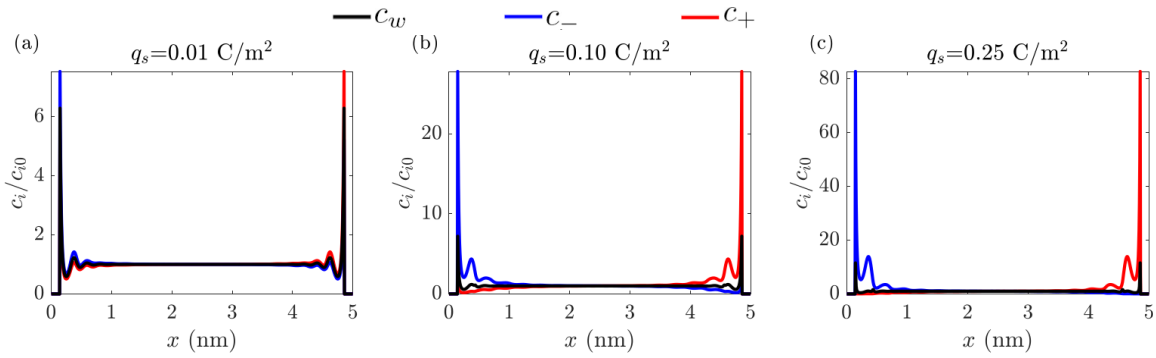

Figure 5-7: Electrolyte screening behavior between two surfaces of opposite charge for varying surface charge density. The curves are generated by solving Eq. 5.24 with $\bar{\rho}_e \neq 0$. The surface charge density is varied between $q_s = 0.01$ C/m^2,$q_s = 0.1$ C/m^2, and $q_s = 0.25$ C/m^2, keeping all other parameters constant ($T = 300$ K, $L = 5$ nm, $c_{w0} = 55$ M, $d = 0.285$ nm, $c_0 = 0.1$ M, and $p_0 = 4.86$ D). The cation (red), anion (blue), and dipolar molecule (black) profiles are plotted, normalized to their respective bulk values.

on the bounding walls of the nanoslit.

In Fig. 5-6, we highlight the main electrostatic properties for a 1:1 electrolyte of varying ionic concentration, c_0. Examining the potential, ϕ, in Fig. 5-6(a), the overscreening oscillations seem to only weakly depend on the ionic concentration. The difference in the local concentrations of anions and cations, $c_- - c_+$, includes oscillatory structures for all concentrations, owing to the dielectric overscreening. Further, at the highest concentration, the ions themselves also contribute to overscreening, where the local ionic charge density oscillates between negative and positive values. While the ionic concentration has a weak influence on the tangential dielectric permittivity, it strongly influences the normal component of the effective solvent dielectric permittivity. The nonzero ionic concentrations lead to longer range oscillations and more singularities in the normal component of the dielectric permittivity of the solvent, $\varepsilon_\perp$. For the highest concentration, the apparent normal dielectric permittivity appears to enter an exotic region $0 < \varepsilon_\perp < 1$, which is of course forbidden for the general dielectric constant $\varepsilon^*_\perp$, [359] but not for the effective dielectric constant, $\varepsilon_\perp$. Note that $\varepsilon_\perp$ is an effective quantity and the constraint of a forbidden band between 0 and 1, [359] does not apply to it. The general dielectric function, $\varepsilon^*_\perp$, includes both the polarization of the dipoles *and* the polarization from ions. For our geometry, it is

defined by:

$$\frac{d}{dx}\left(\varepsilon_{\perp}^{*}\frac{d\phi}{dx}\right)=0 \tag{5.33}$$

and is forbidden from the region $0<\varepsilon_{\perp}^{*}<1$ by the stability requirement. Here, we plot both $\varepsilon_{\perp}$ (Fig. 5-6(c)) that satisfies Eq. 5.29, and $\varepsilon_{\perp}^{*}$ (Fig. 5-6(a)) that satisfies Eq. 5.33. Therefore, the weighted ionic charge density acts as a source that allows for the effective solvent normal dielectric tensor component $\varepsilon_{\perp}$ to enter the region $0<\varepsilon_{\perp}<1$ when ionic overscreening occurs at high ionic concentration.

Next, the role of surface charge density on the accumulation of ions and dipolar molecules is investigated. Fig. 5-7 shows the anion, cation, and dipolar molecule density rescaled to their bulk values ($c_0 = 0.1$ M for the ions and $c_{w0} = 55$ M for the dipoles) as the surface charge density is varied from $q_s = 0.01$ C/m^2 to $q_s = 0.25$ C/m^2 . While the interfacial dipole concentration is increased at large electric field magnitudes, the counterion concentration increases much more rapidly with increasing surface charge density, relative to the bulk concentration. This is quite natural as electrostriction in dense polar liquids in the electric field of the electrical double layer is a much weaker effect than the compression of the double layer with increased voltage drop across it. Therefore, large surface potentials preferentially accumulate counterions instead of the dipolar molecules. But when the voltage drop is large, overcrowding of counterions can occur, where layers rich in counterions of the same sign form near each of the two surfaces, pushing out the dipolar molecules further from the surface. Clearly, this conclusion depends on the size of ions and of dipoles. In the case studied here, they are of the same size. But had this been different, for example, for a situation wheree the dipoles are much smaller than the ions, then the dipoles will be drawn into the double layer to screen the repulsions between the counterions.

Hydration forces

The layering of charged dipolar molecules confined between two interfaces causes an oscillatory hydration interaction. The hydration interaction is critical in colloidal stability, including describing forces experienced by charged biological proteins, lipid bilayers, or DNA at the nanometer scale. Here, we show that the dipolar shell theory can capture the

oscillatory hydration forces commonly observed in the measurements of the forces between smooth surfaces separated by liquid films.

To calculate the disjoining pressure, we can use the following definition for the electrostatic free energy:

$$\mathscr{F}^{\mathrm{el}}[\phi] = \int d\mathbf{r}\Big\{\frac{\varepsilon_0}{2}(\nabla\phi)^2\Big\}. \tag{5.34}$$

and the forms of $\mathscr{F}^{\mathrm{id}}$ and $\mathscr{F}^{\mathrm{ex}}$ in Eqs. 5.2 and 5.4 to compute the overall free energy as a function of the separation distance between two surfaces. In the calculation, we assume free exchange with a bulk reservoir at fixed concentration, the grand canonical ensemble. The grand potential can be written as:

$$\Omega = \mathscr{F} - \sum_i \int d\mathbf{r}\Big\{\mu_{ib}c_i\Big\} \tag{5.35}$$

where $\mu_{ib} = \delta\mathscr{F}/\delta c_i|_b$. The disjoining pressure can be calculated using the relation:

$$P = -\frac{d\,(\Omega/A)}{dL} \tag{5.36}$$

at constant temperature and reference chemical potential, where A is the area of the surfaces. [259–262] Here, we numerically compute the integrals that define Ω/A at various values of L, and numerically take the derivative to arrive at the pressure. Pressures are reported relative to the bulk reference value as $L \to \infty$, P_∞.

In Fig. 5-8, the disjoining pressure is plotted for (a) a pure polar fluid between two surfaces of opposite charge (b) a 0.1 M 1:1 electrolyte between two surfaces of opposite charge, and (c) a 0.1 M 1:1 electrolyte between two surfaces of the same charge. First we will discuss case (a) of the pure polar fluid. At zero surface charge density, the interactions are dominated by the packing effects captured in $\bar{\mu}_i^{\mathrm{ex}}$. At larger charge density, such as $q_s = 0.30$ C/m^2, the electrostatic contribution to the disjoining pressure dominates the interaction. While the initial few layers of the profile are jagged, the pressure profile gives way to regularly-shaped decaying oscillations at larger separation distances. For case (b), adding in an electrolyte at low concentration ($c_0 = 0.1$ M) relative to the dipole concentration (c_{w0}=55 M) does not significantly change the observed patterns in the short range

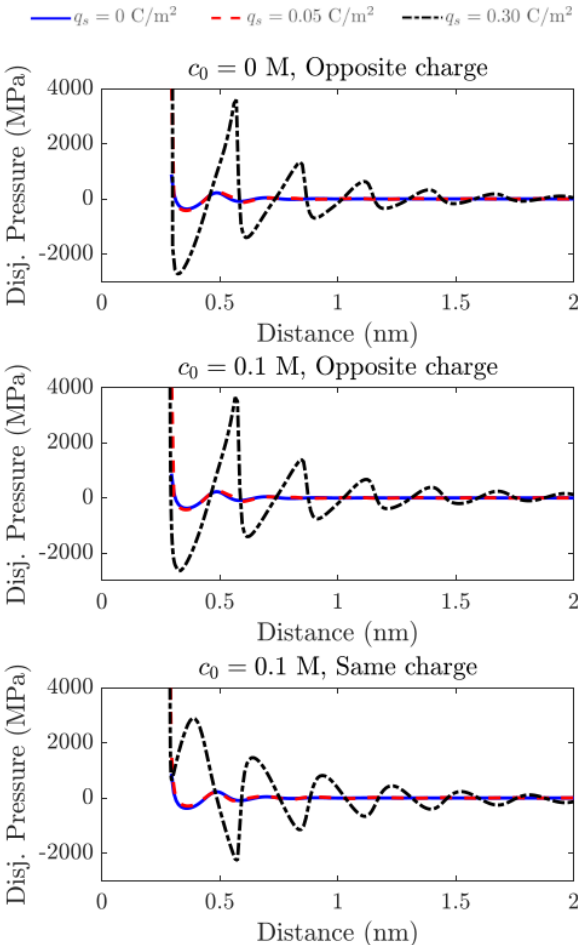

Figure 5-8: The disjoining pressure between two surfaces of varying separation distance plotted for different ionic concentrations and polarity of surface charges. Individual curves correspond to the indicated surface charge density, held constant for all separation distances. The ionic concentration, c_0, and the polarity of the surfaces are listed in the figure titles. The three lines in each plot correspond to values of the surface charge density from $q_s = 0$, 0.05, and 0.30 C/m^2.

hydration interaction at low or high surface charge density. However, if as shown in case (c), the charge on the two surfaces is of the same sign, then the oscillation pattern is shifted and the sharpness in the patterns is flipped. Even so, the general pattern for interactions between surfaces of the same charge and of opposite charge are relatively similar in their overall envelope and long-range decay. Such an angled pressure profile dependent on the surface charge polarity, while not immediately discernible in SFA experiments in the literature, could be detected with a carefully designed experiment, if it is in fact present. Furthermore, measurements with soft surfaces or surfaces that are rough might blur these predicted features

Model applied to double layer capacitance

In electrochemistry, one of the important measureable interfacial quantities is the double layer capacitance. In traditional theoretical approaches, the capacitance is composed of a constant Stern capacitance, C_s and a Gouy-Chapman diffuse layer capacitance C_D in series. The Stern capacitance is assumed to arise due to the layer of water hydrating the interface with depressed dielectric constant and fixed thickness. The diffuse layer capacitance accounts for the screening of the surface charge by the ionic charge distribution in the solution near the interface. The total differential capacitance of an electrode, C_T, is defined as:

$$C_T = \mid \frac{dq_s}{d\phi_s} \mid, \tag{5.37}$$

where ϕ_s is the surface potential. The total differential capacitance is therefore related to the Stern and Debye capacitance:

$$C_T = \left(C_D^{-1} + C_s^{-1}\right)^{-1}. \tag{5.38}$$

At small potential drops across the double layer for dilute solutions, the diffuse layer capacitance is approximatley equal to the Debye capacitance:

$$C_D = \frac{\varepsilon_r \varepsilon_0}{\lambda_D} \tag{5.39}$$

where λ_D is the Debye length,

$$\lambda_D = \sqrt{\frac{\varepsilon_r \varepsilon_0 k_B T}{2e^2 c_0}}. \tag{5.40}$$

In the dipolar shell theory, the equally-sized hard sphere assumption means that there is no layer of water near the surface. In the model, the water layering and ionic screening occur in a diffuse manner from the interface. Despite the overlap, the layering of water still leads to an *effective* Stern capacitance. [320]

In Fig. 5-9, we calculate the variation in the total double layer capacitance, effective Stern capacitance, and calculated Debye capacitance as the ionic concentration changes, all

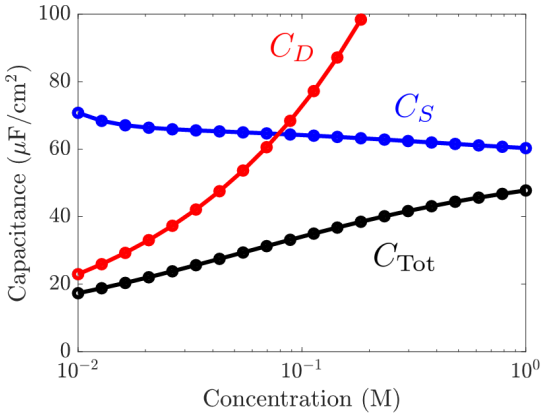

Figure 5-9: Effective capacitance at zero charge for an electrolyte as a function of ionic concentration. All other parameters are kept constant ($T = 300$ K, $L = 5$ nm, $c_{w0} = 55$ M, $d = 0.285$ nm, and $p_0 = 4.86$ D). The total capacitance is calculated numerically from an isolated (non-overlapping) double layer. The Debye capacitance is calculated as $C_D = \varepsilon_r\varepsilon_0/\lambda_D$, and the effective Stern capacitance is calculated assuming a series capacitance model to match the total capacitance from the dipolar shell theory.

calculated near the point of zero charge for non-overlapping double layers. While the theory does not contain a specific layer of water at an interface like the traditional Stern layer concept, it returns a nearly-constant effective Stern capacitance around 60 μF/cm^2. The general predictions of semi-phenomenological nonlocal electrostatic theory in ref. [320] is fully supported by this “molecular" level model. The details of the capacitance could be affected strongly by the size asymmetry of real polar liquids and ions. In other words, small water molecules would access the surface more easily than larger ions in the solution, in order to reduce the electrostatic repulsion between the counterions. Furthermore, the induced polarization of the solvent and ions can strongly affect the capacitance. [360]

Linearized form of equations

The system of equations outlined above are, generally, nonlinear integro-differential equations. While they can be solved in a straightforward manner numerically, they do not admit simple analytical solutions. Here, we show how the system of equations can be reduced to linear differential forms, where the oscillatory decay can be described analytically. While not valid for the first few layers of oscillations in charge and mass, the linearized forms of the theory are decent approximations for the long-range behavior of the polar fluid.

The linearized weighted Langevin-Poisson equation for the dipolar shell theory (combining linearized forms of Eqs. 5.17, 5.20, and 5.21) is:

$$\left[1+(\varepsilon_r-1)\hat{w}_s^2\right]\nabla^2\phi = \varepsilon_r\kappa_D^2\hat{w}_s^2\phi \tag{5.41}$$

where κ_D is the inverse Debye length and ϕ is written in its local form. For small perturbations, we can assume that the convolution with w_s acts as a differential operator, $\hat{w}_s \approx 1+\ell_s^2\nabla^2$, where $\ell_s = d/\sqrt{24}$. [7] The$\hat{}$symbol correpsonds to the differential form of the weighting function. In $1D$, if we assume $\phi = A\exp(\kappa x)$, we get the following characteristic equation for the decaying modes:

$$\kappa^2 + (1+\kappa^2\ell_s^2)^2\left[(\varepsilon_r-1)\kappa^2 - \varepsilon_r\kappa_D^2\right] = 0. \tag{5.42}$$

If there is no electrolyte present, $\kappa_D = 0$, then the solution for κ has a real and imaginary part as:

$$\begin{aligned} \mathrm{Re}(\kappa) &= 0, \quad \pm\frac{1}{\ell_s}\sqrt{-\frac{1}{2}+\frac{1}{2}\sqrt{\frac{\varepsilon_r}{\varepsilon_r-1}}} \\ \mathrm{Im}(\kappa) &= 0, \quad \pm\frac{1}{\ell_s}\sqrt{\frac{1}{2}+\frac{1}{2}\sqrt{\frac{\varepsilon_r}{\varepsilon_r-1}}}. \end{aligned} \tag{5.43}$$

In the limit of large $(\varepsilon_r - 1)$, we get:

$$\begin{aligned} \mathrm{Re}(\kappa) &= 0, \quad \pm\frac{1}{2\ell_s\sqrt{\varepsilon_r-1}} \\ \mathrm{Im}(\kappa) &= 0, \quad \pm\frac{1}{\ell_s}. \end{aligned} \tag{5.44}$$

This means that in the absence of ions, the effective hydration length governing decay of the oscillations scales as:

$$\lambda_s = d\sqrt{(\varepsilon_r-1)/6}, \tag{5.45}$$

and an oscillation wavelength of about one molecular diameter. For water, the effective hydration length turns out to be ≈ 1 nm at room temperature. The hydration length de-

scribes the decay of the alternating layers of bound charge emanating from a surface, and the magnitude of this decaying mode is determined by the magnitude of polarization at the surface.

Now, if we include salt, the expressions for the decaying modes become more complicated. In the limit of small but non-zero ion concentrations, $\kappa_D \to 0$ gives a longest decaying mode of of $\kappa = \kappa_D$, where the effective decay length is the Debye length, λ_D. In this limit, the hydration length can be thought to be independent of and additive to the long range Debye screening, as is commonly assumed in experimental measurements of surface forces. [340]

In the limit of large ionic concentrations and large $(\varepsilon_r - 1)$, another simplified formula can be attained for the slowest decaying mode:

$$\kappa \approx \frac{1}{2\sqrt{\varepsilon_r}\kappa_D \ell_s^2} \pm \frac{i}{\ell_s}. \tag{5.46}$$

This formula is valid when $\sqrt{\varepsilon_r}\kappa_D \ell_s \gg 1$, meaning that the molecule size is much larger than the Debye length in vacuum. The effective screening length becomes independent of the relative permittivity,

$$\lambda_s \approx \frac{2\ell_s^2\sqrt{\varepsilon_r}}{\lambda_D} = \frac{d^2\sqrt{\varepsilon_r}}{12\lambda_D} \tag{5.47}$$

since the dependence of ε_r cancels out, and the oscillations are on the order of one molecular diameter.

An additional source of oscillations is from the density variations owing to packing of molecules at a flat interface. Taking each set of species, we can assume small perturbations:

$$\begin{aligned} c_w &\approx c_{w0}\left(1 - \beta\bar{\mu}^{\mathrm{ex}}\right) \\ c_i &\approx c_{i_0}\left(1 - z_i e\beta\bar{\phi} - \beta\bar{\mu}^{\mathrm{ex}}\right). \end{aligned} \tag{5.48}$$

If we sum over all species assuming the same size of each molecule and thus identical excess chemical potential, we get an expression for the local filling fraction:

$$\eta - \eta_0 = -\eta_0\beta\bar{\mu}^{\mathrm{ex}} = -\frac{2\eta_0(4-\eta_0)}{(\eta_0-1)^4}\hat{w}_v^2(\eta - \eta_0) \tag{5.49}$$

where we have linearized the excess chemical potential. We can again assume small perturbations and treat w_v as an operator, $\hat{w}_v \approx 1 + \ell_v^2 \nabla^2$, where $\ell_v = d/\sqrt{40}$. The decay of the density for a symmetric fluid is independent of the decay of the electrostatic potential, and the characteristic equation, assuming $\eta - \eta_0 = A\exp(-\kappa_m x)$, is:

$$1 + \frac{2\eta_0(4-\eta_0)}{(\eta_0-1)^4}(1+\ell_v^2\kappa_m^2)^2 = 0. \tag{5.50}$$

Here, κ_m has real and imaginary parts:

$$\begin{aligned} \mathrm{Re}(\kappa_m) &= \frac{1}{\ell_v}\sqrt{-\frac{1}{2} + \frac{1}{2}\sqrt{1 + \frac{(1-\eta_0)^4}{2\eta_0(4-\eta_0)}}} \\ \mathrm{Im}(\kappa_m) &= \frac{1}{\ell_v}\sqrt{\frac{1}{2} + \frac{1}{2}\sqrt{1 + \frac{(1-\eta_0)^4}{2\eta_0(4-\eta_0)}}}. \end{aligned} \tag{5.51}$$

As $\eta_0 \to 0$, the oscillations decay rapidly over a small length scale $\lambda_m = \ell_v(8\eta_0)^{1/4}$. For dense solutions, as $\eta_0 \to 1$, the real and imaginary parts of the solution go to:

$$\begin{aligned} \mathrm{Re}(\kappa_m) &= \frac{(1-\eta_0)^2}{\sqrt{8}\ell_v\sqrt{\eta_0(4-\eta_0)}} \\ \mathrm{Im}(\kappa_m) &= \frac{1}{\ell_v}. \end{aligned} \tag{5.52}$$

In other words, the decay of mass oscillations with wavelength of the molecular diameter goes as:

$$\lambda_m \approx \sqrt{\frac{1}{5}}\frac{d\sqrt{\eta_0(4-\eta_0)}}{(1-\eta_0)^2}. \tag{5.53}$$

For water at room temperature, the decay length for mass oscillations is $\lambda_m \approx 0.4$ nm. Therefore, the mass density oscillations decay more rapidly (over a shorter length scale) than the oscillations in the potential. While the typical filling fraction for pure liquids is around $\eta_0 \approx 0.4$, an increase in the filling fraction corresponds to longer range oscillations in the liquid number density. The competition between mass and hydration length depends on the filling fraction of the fluid and the relative dielectric constant of the fluid, as well as

the magnitude of the surface charge density or surface potential. Even so, the oscillation wavelength for electrostatics and density variations remains comparable to the molecular or ionic diameter for each decay mode.

Thus, for highly charged surfaces, we expect to see oscillation patterns with the period of oscillations of the liquid molecule size and decay envelope of the order of 1 nm determined by the hydration length in Eq. 5.45, whereas for low charged or uncharged surfaces, the envelope will be much shorter based on Eq. 5.53. In experiments, people saw a variance of decay length of the force between neutral surfaces, [361] but this was explained by lateral inhomogeneity of the generally electroneutral charge distribution along the surface. [362] The oscillations themselves, get smeared by the smearing of the surfaces. Our model suggests that the interplay of charge ordering and packing effects will influence the observed decaying modes, as was demonstrated clearly by studying the hydration forces in Fig. 5-8 with varying surface charge magnitudes.

5.2.4 Conclusions

The dipolar shell theory describes layering in charge and mass for an interfacial polar fluid. In this work, we have demonstrated that the effective delocalized bound charge on the dipolar molecules underlies the overscreening phenomenon, with alternating layers of bound charge density on the dipoles.

The overscreening effect leads to significant anisotropy in the normal and tangential components of the permittivity. The normal component has singularities owing to the overscreening effect, while the tangential component scales more closely with the dipole concentration. The length scale governing the decay of oscillations from the interface is the *hydration length*, $\lambda_s = d\sqrt{(\varepsilon_r - 1)/6}$.

When ions are present, the ionic layering is influenced by the structuring of the polar fluid, and the ions also begin to contribute to the overscreening effect when they reach a sufficiently high concentration.

The theory could be extended further and applied to various other applications not mentioned in this work. Straightforward extensions of the theory could describe: (i) Varying

electrolyte composition with multivalent ions and mixtures of polar fluids, (ii) varying the geometry of the pore domain to cylindrical or spherical pores or using the theory to describe the double layer structure around cylindrical or spherical charged colloids, (iii) extending the analysis to non-uniform ion and water sizes, (iv) demonstrating the charging dynamics of the dipolar fluid orientation and layering, (v) showing the role of double layer and hydration oscillation overlap on the system capacitance, (vi) demonstrating the role of the dipolar fluid organization on the effective ζ-potential for electrokinetic measurements, and (vii) including the interfacial polar liquid structure in a formulation of interfacial electrochemical reactions.

Although the theory does capture the charge structuring at the interface, it still falls short of perfectly describing real polar liquids. For example, the theory does not reproduce the single-ion-level hydration. A more sophisticated approach may be necessary to keep track of the bound and free states of water that constitute the coordinated hydration shell of individual ions. Furthermore, the theory only indirectly captures the correlations between neighboring dipolar molecules, which requires an effective dipole moment that is larger than the true value for highly polar fluids.

The dipolar shell structure assumed in the theory is significantly simpler than typical charge distributions within polar molecules. For example, the higher-order multipole moments of water can strongly influence the interfacial polarization. [31, 363, 364] The model assumes a hard sphere repulsion, but real polar fluids will have softer repulsive interactions, as well as attractive dispersion interactions. Finally, we have neglected electronic degrees of freedom, always present in polar fluids, which contribute to the dielectric constant of the liquid independent of the fixed dipole orientations.

Despite the simplifications, the dipolar shell theory presents a powerful theoretical framework to investigate the interfacial properties of polar liquids. The system of integro-differential equations is readily soluble, especially in 1D geometries. The approximate, differential-form of the theory gives analytical formulas for quick computations and experimental comparisons.

5.3 Comparison to Molecular Dynamics Simulations of Confined Polar Liquids

5.3.1 Introduction

As discussed in detail in the previous section, the properties of interfacial polar liquids determine the electrochemical behavior of interfaces in a variety of applications.

Currently, there is not a unified understanding of charge ordering in polar liquids, especially as compared to our understanding of charge screening in dilute electrolytes. In dilute electrolytes, the charge at the interface generally decays over a well-known Debye length, which depends on the electrolyte valency and concentration, and governs the decay of interactions between charged surfaces in electrolyte solutions. For the solvent, typically, we assume constant dielectric properties, but this assumption breaks down near interfaces or in strong confinement. Numerous simulations [31, 322, 336, 353, 354, 358] and experiments [317, 325–327] have shown that there is structuring and charge layering due to the orientational ordering of polar liquids within ~ 1 nm of an interface. Although these polar liquid molecules possess no net charge, the local regions of positive and negative bound charge on the molecule form layers of positive and negative charge at the interface as the molecules are oriented by an applied electric field. This has strong implications for the the dielectric properties and thus the behaivor of the fluid under confinement between charged surfaces.

To capture such charge ordering in a continuum theoretical framework, one must resort to nonlocal dielectric theories that approximate the spatial correlations in the polarization of the solvent [192, 320, 331, 332, 340–342, 358]. The standard approach is to assume a wave-vector-dependent dielectric constant, $\varepsilon(k)$ or to construct a phenomenological Landau-Ginzburg free energy functional with higher-order terms in the polarization density, that returns the $\varepsilon(k)$ of a specific mathematical structure. These higher-order, differential theories rigorously capture the bulk dielectric properties especially for weak perturbations that do not violate the linear response or translational invariance assumptions. However, they necessitate the nonlocal polarization density as an input and require assumptions near

surfaces, where additional boundary conditions must be assigned. Therefore, while the $\varepsilon(k)$ approaches are routinely applied to interfacial electrostatics problems where the qualitative features are in agreement with simulations, their predictive power is expected to be limited near surfaces for a variety of liquids, especially at strong surface polarization.

In order to capture the orientational ordering with a molecular theory that is directly integrated into the mean-field equations at the interface while maintaining some analytical tractability, I proposed the dipolar shell theory in the previous section. The advantages of the dipolar shell theory are (i) we require no additional boundary conditions other than the intrinsic polarization of the surface (ii) it is derived directly from the (coarse-grained) microscopic properties of the polar liquid, (iii) in principle it is valid even in nonlinear response and (iv) the decaying modes in linear response can be easily approximated to give simple, closed-form expressions that describe the decay in solvent orientations (dielectric screening). Nevertheless, the charge and shape of the molecules in the dipolar shell theory are severely coarse-grained compared to real liquids. One significant disadvantage of the dipolar shell theory stems from the unphysical coarse-grained charge distribution. If one attempts to calculate the bulk dielectric function, $\varepsilon(k)$ within the theory, one arrives at something that poorly describes real liqiuds. This discrepancy is because the $\varepsilon(k)$ function becomes very sensitive to the actual interior molecular charge correlations at large k.

Evidently, the dipolar shell theory connects the orientational ordering structure to the properties of the liquid. [35] Principally, the properties that govern the charge ordering are the effective polar liquid molecular diameter, d and the bulk dielectric constant, ε_r. At linear response, we found that the nonlocal dielectric response gives decaying orientations of polar liquids over a hydration length, λ_h with oscillations on the order of a single molecular diameter. Since "hydration" refers to the solvation forces in water, the hydration length can more generally be described as a "solvation" length for polar liquids other than water.

Motivated by the simple relation that describes the decay in oscillations, in this work, we studied the orientational ordering of three polar liquids (dichloromethane, acetonitrile, and water) using classical molecular dynamics simulations between two oppositely charged surfaces at varying extents of confinement, performed by Dr. Karina Pivnic. Each liquid possesses different molecular size and dielectric constant, allowing us to test the theoretical

predictions for the liquid orientation.

The molecular simulations implemented in our study allow us to build a reference system that exposes the predictive power and also the limitations of the theoretical predictions of the dipolar shell theory compared to real molecular liquids. We can carefully control the molecular properties by inputting different molecule-specific force field parameters in the simulations and can set the boundary conditions of the confined fluids with charged bounding walls. We can also use our capability to calculate the structural/ solvation forces for the confined fluids to test the theoretical predictions for the molecular reference system.

We find that, for the three polar liquids, the dipolar shell theory can generally capture the orientational ordering near the interface, which follows the approximated decay length above. We also show that the orientational oscillations can overlap when the two confining surfaces are separated by nanometric or subnanometric distances, which are again predicted by the dipolar shell theory. Overall, the coarse-grained theory is not able to capture all features of the simulations, but gives good qualitative predictions for the behavior, and allows us to unify the orientational ordering under one theoretical framework that is based on the molecular properties of the liquids. In fact, the theory works well in capturing the structural features of the simulations of molecules of different shapes, partial charges, and force-field parameters, even though the theory coarse grains the molecules into effective hard spheres. Further, we show how the orientational ordering can impact the structural forces between two oppositely charged surfaces. We find that for very asymmetric shape, while the model can capture the ordering in orientation, it cannot capture the magnitude of the density variations in asymmetrically-shaped confined liquids, and therefore misses details of the structural forces at the closest separations.

5.3.2 Simulation Details

In Figure 5-10, we show the system being simulated. Here, polar liquids are simulated using coarse-grained, classical molecular dynamics. The dichloromethane molecule is simulated using OPLS-AA force field parameters, the acetonitrile is simulated using a coarse-grained model reported in [365], and the water molecules are represented using

the TIP3P model [366]. The bulk permittivity of each liquid is approximately $\varepsilon_r \approx 9$ for dichloromethane, $\varepsilon_r \approx 39$ for acetonitrile, and $\varepsilon_r \approx 100$ for TIP3P water. These liquids, due to their different sizes and bulk dielectric constants, allow us to sample various values of the effective hydration length.

Details of the simulation techniques are already reported elsewhere [35]. The details of the simulation set up differ slightly in the polar liquid, where the surfaces are of opposite charge, but the guiding principles are the same, so we do not report the details in this thesis.

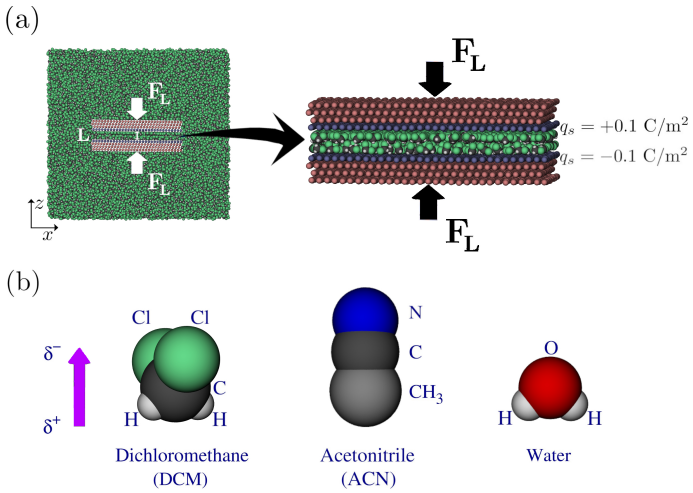

Figure 5-10: Simulation schematic. (a) The polar liquids are confined between two surfaces with separation distance L and with forces given by F_L. The surfaces are oppositely charged, and the polar liquid between them orients in response to this polarization. (b) The three molecules studied here, with dipole moment oriented upwards. The molecules are dichloromethane, acetonitrile, and water.

For comparison to theory, we directly apply the dipolar shell theory described in the previous section of this chapter. In order to reproduce the density and the bulk dielectric constants of the fluids, the density is chosen as: $c_d = 15.7$ M for dichloromethane, $c_d = 19.1$ M for acetonitrile, and $c_d = 55$ M for water, and the effective dipole moments as $p_0 = 2.91$ D for dichloromethane, $p_0 = 5.7$ D for acetonitrile, and $p_0 = 5.43$ D for TIP3P water. The effective spherical sizes of each molecule are an additional parameter, which for the purposes of this study, we choose: $d = 0.38$ nm for dichloromethane, $d = 0.424$ nm for acetonitrile, and $d = 0.285$ nm for TIP3P water.

Again, it should be noted that the coordinate system here is rotated compared to the previous section in this chapter such that the normal coordinate is now the z-coordinate instead of the x-coordinate, in order to be consistent with the orientation convention in the simulations.

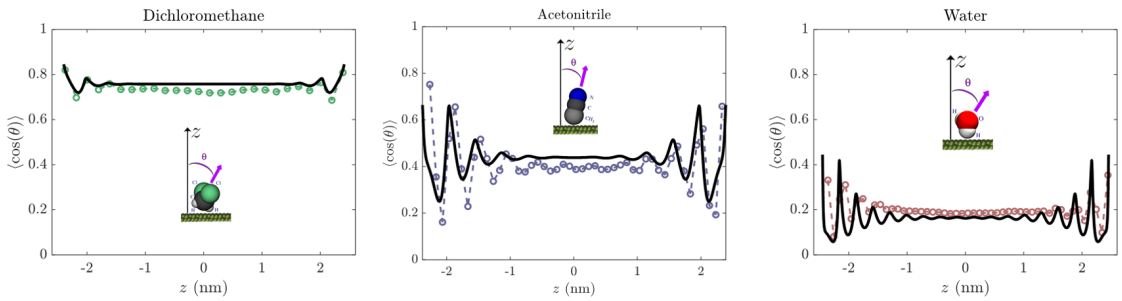

Figure 5-11: Liquid orientation comparison between simulation and theory for separations without solvation layering overlap. The simulation is shown with colored markers and dashed colored lines. The theory predictions are shown with black solid lines. The profiles of $\langle\cos(\theta)\rangle$ display decaying oscillations as a function of z until they reach a constant value in the center of the gap. The two surfaces have equal but opposite charge of $q_s = \pm 0.1$ C/m^2, and the separation distances of the two surfaces are around 5 nm for all the liquids.

5.3.3 Results

From a theoretical perspective, if we were to assume a constant dielectric constant, our system would turn into an ideal parallel plate capacitor, the electric field would be a constant, and the orientation of all dipoles would be constant between the two charged surfaces. However, as we can clearly see in Figure 5-11, the simulation predictions for each liquid returns oscillations in the orientations of the liquids near the interface. These orientational oscillations correspond to the charge layering near the interface which is not captured in standard dielectric theories. Nevertheless, the orientational ordering is closely captured by the dipolar shell theory.

At these separation distances, the oscillations decay to a constant in the center of the gap. Clearly, the oscillation decay closely mirrors the prediction of the solvation length for each polar liquid from the dipolar shell theory. The least polar fluid, dichloromethane, has a predicted decay length of $\lambda \approx 0.44$ nm, while acetonitrile has a decay length of $\lambda \approx 1$ nm and TIP3P water has a decay length of 1.2 nm. These decay length are qualitatively similar to what is observed in the simulations. In the simulations, slight asymmetries occur, presumably due to the the asymmetric size and/or charge distributions in the molecules.

Interestingly, the maximum in the orientation profiles occurs at the point of contact, which is equivalently the maximum of the density profiles in the theory. For this same system of a pure polar liquid between oppositely charged plates, a local dipolar theory

would predict that the maximum in the liquid density would correspond to the opposite prediction, to a *minimumum* in the orientation profile. Therefore, the delocalized dipolar shell theory is essential in capturing these features even qualitatively.

As two surfaces are confined, the orientational ordering of the polar liquids emanating surfaces can constructively or destructively interfere with each other. As shown in Figure 5-12, the extent of confinement can strongly influence the orientational ordering of the polar liquid. Again, the dipolar shell theory can capture the layered structures even at massive confinement. This includes regions where the argument of the Langevin function is quite large and nonlinear, nonlocal dielectric response of the liquid is activated. Clearly, there are some discrepancies between the simulation and the theory. For dichloromehtane, the oscillations are stronger in the simulation than they appear in the theory. On the other hand, for water, the oscillations appear to be too strong. Even so, the theory consistently predicts the main features observed in the simulations for the orientational ordering even for these

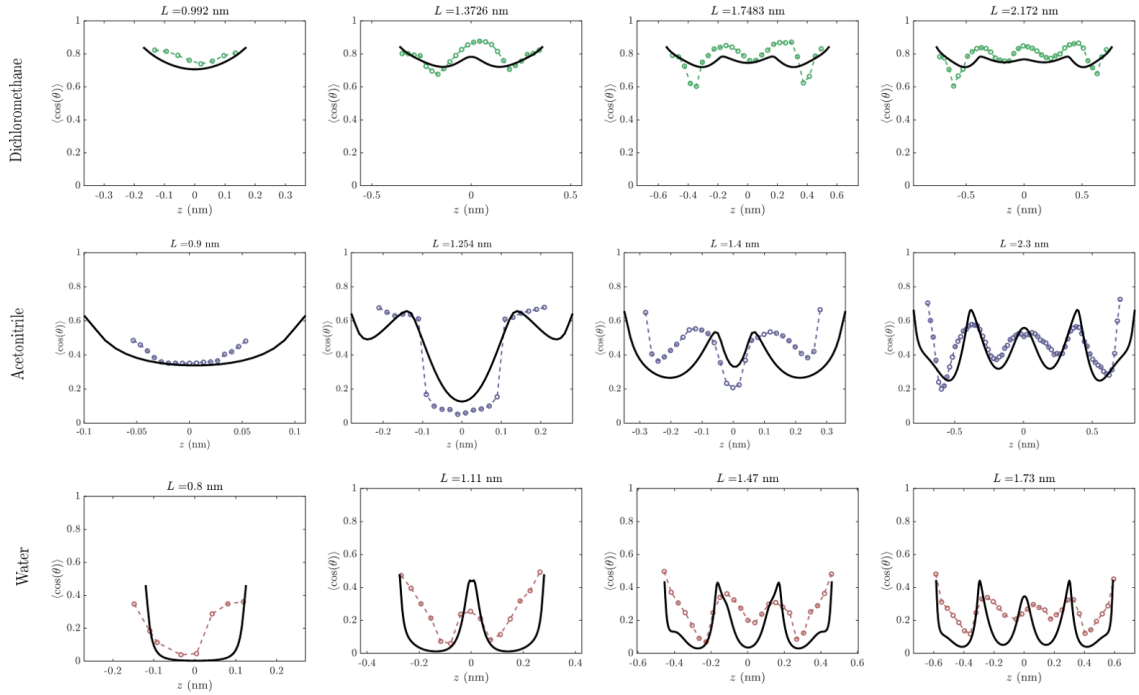

Figure 5-12: Confined liquid orientation comparison between simulation and theory for separations with solvation layering overlap. The simulation is shown with colored markers and dashed colored lines. The theory predictions are shown with black solid lines. The profiles of $\langle\cos(\theta)\rangle$ include oscillatory structures that emanate from each surface and overlap when the surfaces are confined. The two surfaces have equal but opposite charge of $q_s = \pm 0.1$ C/m^2, and the separation distance of the two surfaces, L, varies based on the title of each subplot.

liquids under extreme confinement.

Finally, in Figure 5-13, we present a comparison of the predicted disjoining pressure profiles between two oppositely charged surfaces for varying surface separations in the three liquids. We find that the theory generally under-predicts the magnitude of the oscillatory structural forces at small separations for the molecules with more asymmetric shape: dichloromethane and acetonitrile. This discrepancy appears to occur despite the strong agreement in the orientation profiles for both of these liquids. On the other hand, the theoretical predictions of the surface forces for the TIP3P water are reasonably closely matched to the simulations, even for the smallest separation distances. We suspect that the discrepancy between the disjoining pressures predictions of simulation and theory is mainly due to the theory's inaccuracies in predicting the density of solvent molecules of non-spherical shape.

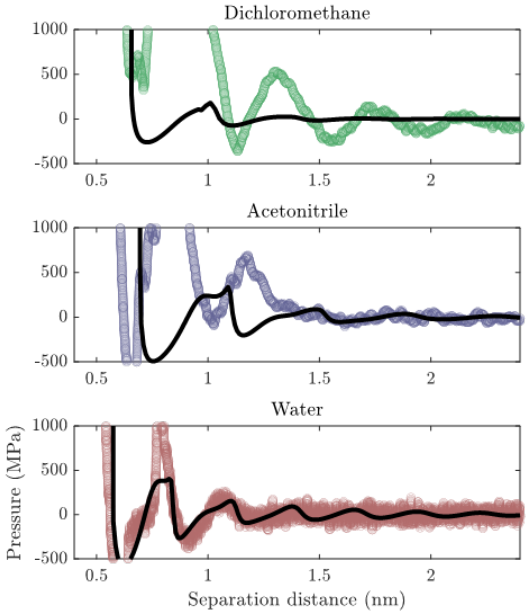

Figure 5-13: Disjoining pressure predictions for polar liquids between two oppositely charged surfaces as a function of surface separation distance. The colored markers now correspond to the pressure calculated from the MD simulations, while the black lines correspond to the theoretical prediction.

While not comprehensively shown in these preliminary results, and as will be shown more extensively in the completed study, the theory has some notable shortcomings compared to the MD simulation. The most prominent deficiency of the dipolar shell theory is the large discrepancies in the density profiles of the liquids compared to the simulations, especially in strong confinement. Primarily, these density discrepancies occur due to the fact that the dipolar shell theory represents the molecules of complicated shape and "soft" interaction potentials as effective hard spheres. Clearly, this hard sphere assumption is responsible for the poor performance of the theory to reproduce the structural forces at close separations for acetonitrile and dichloromethane.

5.3.4 Conclusions

The preliminary results presented here validate the predictions of the dipolar shell theory for pure polar liquids. We generally find that the orientation profiles in the simulations behave in a way that is consistent with the theory for liquids of different size and bulk dielectric constant. Although the theory is able to capture the orientations, it appears as though the theory cannot capture the structural forces for very asymmetrically sized molecules at the smallest separation distances. A more involved theoretical approach would be necessary to describe the orientation-dependent packing of the molecules when they have complicated shapes.

5.4 Summary of Findings

In this chapter, I found that the structuring of polar liquids such as water has a non-arbitrary influence on the electrostatic potenial profile near a charged interface. The bulk dielectric constant and the ion size determines the decay of alternating bound charges from a charged surface. The effective static dielectric tensor at the interface has surprising behavior, including singularities in the normal component and a stark anisotropy in the tangential component.

By comparison to MD simulations of three different polar liquids conducted by our collaborator, Dr. Karina Pivnic, we validate the predictions of the dipolar shell theory for a pure polar fluid confined between two oppositely charged surfaces. By testing molecules of different size, shape, and dipole moment, we find the limitations of the theoretical predictions, and yet also can point to some predictive accuracy of the theory.

In order to make the model even more realistic, one would need to include the preferential orientation of the solvent molecules and the solvent size asymmetry with the ions. The water structuring may have important consequences for electrokinetic transport and electrochemical reactions, phenomena that we have not specifically studied in this thesis.

Chapter 6

Conclusions

6.1 Thesis Summary

The electrical double layer exhibits rich behavior due to the underlying structures of ions and solvent at charged surfaces. Due to their simplicity, the standard approaches for modeling the EDL based on the GCS theory remain powerful tools to interpret the behavior of electrochemical interfaces involving electrolyte solutions. However, in many notable and practically-relevant situations, the GCS theory fails to capture the key physics, limiting its predictive power.

In my thesis, I have presented work to include more microscopic physics of discrete ions and solvent at isolated surfaces and in confinement between surfaces or in pores. In Chapter 2, I investigated the role of electrostatic correlations in determing the thermodynamic properties of electrolytes containing multivalent ions. To that end, I refined the BSK theory, which represents the correlation effects in a higher order nonlocal permittivity. I found that using the BSK theory with proper constraints and parameterization, we could describe the unique properties of systems with strong electrostatic correlations, including like-charge attraction. In Chapter 3, I turned to modeling the structures of ultra-concentrated electrolytes including ionic liquids. I found that a charged shell representation using a weighted-density functional could reproduce the layered structrues at charged interfaces including overscreening and crowding. For asymmetrically sized electrolytes, the oscillations of the number density and the charge density become highly coupled, with resulting implications

on the structural forces of ionic liquids between two charged surfaces. In Chapter 4, I investigated the role of confinement dimensionality on the electrolyte screening structures. I found that 1D confinement led to macroscopic-scale effective screening lengths that promote electroneutrality breakdown. I showed that the electric field leakage from the pore walls leads to pore-pore interactions that can influence the screening structures and push the system back towards electroneutrality. Finally, in Chapter 5, I implement a dipolar shell theory that captures the interfacial charge layering of polar liquids. The theory predicts an anisotropic interfacial static dielectric tensor with singularities in the normal component, corresponding to the overscreening or layering of charge. Each of these microscopic mechanisms could play a central role in determining colloidal interactions, transport properties, or the electrochemical response of interfacial electrolytes.

6.2 Future Work

While the mathematical modeling of the electrical double layer has a long history, many unanswered questions remain. For example, while the shortcomings of standard continuum approaches are often recognized, the ramifications of these nonidealities in practical situations are poorly understood. The reexamination, reinvention, and application of mathematical models for interfacial phenomena in electrolytes can uncover new insights and reveal knowledge gaps in the literature. The body of work presented in this thesis contributes to our understanding of the electrical double layer, yet also opens up some interesting research directions for the future.

The future work can take on a variety of forms: model development, model approximation, and model application. In model development, additional ingredients and analysis can be incorporated into the mathematical framework describing the double layer structure and dynamics. In any modified theory, it is preferable to start from a thermodynamic description of the free energy of the system in order to calculate self-consistent thermodynamic quantities such as the disjoining pressure. For model approximation, the full theories are reduced down to extract simple scaling relationships between system properties and measurable outputs. While the approximations can reduce the predictive power of a given the-

oretical approach, simple formulas are extremely valuable in interpreting and comparing to experiments. In model application, the models incorporating the microscopic physics of ionic structuring at charged interfaces can be applied to numerous problems in colloid science, especially when experimental measurements cannot be captured by standard GCS approaches or require unrealistic parameterization. For the purposes of this thesis, I will focus on future opportunities for model development and briefly discuss the possibilities for model approximation and application.

To capture electrostatic correlations in multivalent electrolytes in Chapter 2, I applied the BSK theory. While the BSK theory was shown to work incredibly well for dilute electrolytes near charged plates, questions remain about the application of the theory to concentrated or crowded electrolytes. The scaling relationship for the correlation length could change as a function of the local ionic concentrations or surface charge geometry, and molecular layering can occur that is not explicitly accounted for in the theory. It may be possible to incorporate the additional structuring by inlcuding higher order terms in the BSK free energy or integrating the BSK theory into other nonlocal approaches including the charged shell representation presented in Chapter 3.

The charged shell theories applied in Chapter 3 exhibited many of the same features as simulated concentrated electrolytes and ionic liquids. Nevertheless, the theory routinely underpredicts the extent of ordering at the interface, which might arise from additional bulk correlations not accounted for in the mean-field theory. The double layer structure in this limit may be sensitive to the ionic associations and ionic aggregation, especially when a gelation transition occurs at high concentration. Additionally, future work could incorporate more detailed descriptions of the electrolyte structures near interfaces, such as including image charge interactions or building models that apply to molecules of arbitrary shape and size.

In the analysis of electroneutrality breakdown in Chapter 4, we applied standard mean-field formulations in different confinement dimensionalities, and showed that 1D confinement led to unique screening behavior. In the dilute systems explored in this work, we typically assumed that we could safely time-average and work with smoothed out concentration variables. However, in many cases in nanopore systems, the occupancy of the pore

for given species is low, meaning that stochastic fluctuations in the ionic density can be important in determining the transport characteristics, including the local fields, forces, and flows through a channel. Furthermore, the analysis of electroneutrality breakdown neglects electrostatic correlations and solvent structuring within the pores. The structural features of the solvent in 1D confinement may yield a transition from overscreening/oscillations in the normal direction to overscreening in the axial direction along the channel. Such a transition may be connected to the electric field escape through the boundaries of the pore domain that reduces the extent of dielectric screening within the pore.

In Chapter 5, the dipolar shell theory predicted the main features of solvent orientations and the dielectric properties near charged surfaces. Clearly, the coarse-grained model does not capture all the details of solvent packing near surfaces, especially when solvent molecules are packed in an orientation-dependent manner in nanoconfined films. The model could also be extended to systems with mixtures of polar liquids and ions of different sizes, which will clearly influence and possibly enhance/disrupt the oscillatory structures. The dipolar structure cannot capture the true charge distributions in liquids, and more detailed charge form-factors or higher order moments of the charge distribution may need to be considered. Furthermore, polar liquids often have preferred orientations near surfaces , and this preferential orienation can lead to non-zero solvent charge layering even when the surface charge is zero, an effect currently not captured by the model.

While many of these models explored in this thesis assume smeared out, smooth surface charges, additional structure can emerge from patterning of the surface charges or surface roughness. Therefore, models that try to incorporate the 3D structuring of the double layer may be required.

Moreover, the models presented in this thesis are focused on the equilibrium structure of the electrical double layer. In order to extend the thermodynamic models to nonequlibrium, dynamic systems, additional assumptions must be made about the relationship between the thermodynamic forces in the system and the ionic and solvent fluxes/flows, including the coupling between transport of the different species.

As more complexity is built into the models, they become more difficult to analyze, solve, and apply to problems. Therefore, additional attention must be paid to develop

approximate, coarse-grained approaches that, while incorporating microscopic physics of electrolytes, facilitate more straightforward applications.

In any new theory, the far-field decay lengths could be similarly derived using techniques presented in this thesis in Chapters 3 and 5. Gradient expansions of nonlocal theories, while offering greater simplicity in deriving analytical solutions and numerical implementations, require additional boundary conditions which may be sought using techniques presented in this Chapter 2.

In the end, even for models of extreme complexity, it is useful to extract simple characteristic length scales that link physical properties of the system to the interfacial electrolyte behavior. In doing so, we arrive at simple mathematical relationships that characterize the complex, microscopic features of the electrical double layer.

Beyond model development and approximation, significant opportunities exist in incorporating the more sophisticated electrical double layer theories into multiscale models to understand processes in electrochemistry, biophysics, and electrokinetics. For example, the solvent structuring near interfaces could have a strong impact on electrochemical reactions, especially when the double layers are driven out of equilibrium.

Although the electrical double layer exists at the nanometer scale, it has an enormous impact on colloidal physics. Therefore, fresh modeling approaches will yield greater insight and predictive power to describe colloidal systems.

Bibliography

[1] AG Moreira and RR Netz. Simulations of counterions at charged plates. *The European Physical Journal E*, 8(1):33–58, may 2002.

[2] Juan Pablo Mallarino, Gabriel Tellez, and Emmanuel Trizac. Counterion density profile around charged cylinders: the strong-coupling needle limit. *J. Phys. Chem. B*, 117(42):12702–12716, 2013.

[3] Mónika Valiskó, Tamás Kristóf, Dirk Gillespie, and Dezső Boda. A systematic monte carlo simulation study of the primitive model planar electrical double layer over an extended range of concentrations, electrode charges, cation diameters and valences. *AIP Adv.*, 8(2):025320, 2018.

[4] Matthew A. Brown, Guilherme Volpe Bossa, and Sylvio May. Emergence of a Stern Layer from the Incorporation of Hydration Interactions into the Gouy–Chapman Model of the Electrical Double Layer. *Langmuir*, 31(42):11477–11483, oct 2015.

[5] Cédric Plassard, Eric Lesniewska, Isabelle Pochard, and André Nonat. Nanoscale experimental investigation of particle interactions at the origin of the cohesion of cement. *Langmuir*, 21(16):7263–70, aug 2005.

[6] A. A. Kornyshev. Double-layer in ionic liquids: Paradigm change? *J. Phys. Chem. B*, 111:5545–5557, 2007.

[7] J. Pedro de Souza, Zachary A. H. Goodwin, Michael McEldrew, Alexei A. Kornyshev, and Martin Z. Bazant. Interfacial layering in the electric double layer of ionic liquids. *Phys. Rev. Lett.*, 125:116001, Sep 2020.

[8] Todd M Squires. Particles in electric fields. *Fluids, Colloids and Soft Materials: An Introduction to Soft Matter Physics*, pages 59–79, 2016.

[9] J-L Liu and Bob Eisenberg. Correlated ions in a calcium channel model: a poisson–fermi theory. *J. Phys. Chem. B*, 117(40):12051–12058, 2013.

[10] Håkan Wennerström, Eloy Vallina Estrada, Jens Danielsson, and Mikael Oliveberg. Colloidal stability of the living cell. *Proceedings of the National Academy of Sciences*, 117(19):10113–10121, 2020.

[11] Till Briskot, Tobias Hahn, Thiemo Huuk, and Jürgen Hubbuch. Adsorption of colloidal proteins in ion-exchange chromatography under consideration of charge regulation. *Journal of Chromatography A*, 1611:460608, 2020.

[12] Xiao-Lin Wang, Toshinori Tsuru, Shin-ichi Nakao, and Shoji Kimura. Electrolyte transport through nanofiltration membranes by the space-charge model and the comparison with teorell-meyer-sievers model. *Journal of membrane science*, 103(1-2):117–133, 1995.

[13] Maxim V Fedorov and Alexei A Kornyshev. Ionic liquids at electrified interfaces. *Chemical reviews*, 114(5):2978–3036, 2014.

[14] Jacob N Israelachvili. *Intermolecular and surface forces*. Academic press, 2011.

[15] Johannes Lyklema. Fundamentals of interface and colloid science. volume ii: Solid-liquid interfaces. 1995.

[16] Allen J Bard, Larry R Faulkner, et al. Fundamentals and applications. *Electrochemical methods*, 2(482):580–632, 2001.

[17] Martin Z Bazant, Mustafa Sabri Kilic, Brian D Storey, and Armand Ajdari. Towards an understanding of induced-charge electrokinetics at large applied voltages in concentrated solutions. *Adv. Colloid Interface Sci.*, 152(1-2):48–88, 2009.

[18] J Ross Macdonald and Carl A Barlow Jr. Theory of double-layer differential capacitance in electrolytes. *The Journal of Chemical Physics*, 36(11):3062–3080, 1962.

[19] Á V Delgado, F González-Caballero, RJ Hunter, LK Koopal, and J Lyklema. Measurement and interpretation of electrokinetic phenomena. *Journal of colloid and interface science*, 309(2):194–224, 2007.

[20] Jacob N Israelachvili and Gayle E Adams. Measurement of forces between two mica surfaces in aqueous electrolyte solutions in the range 0–100 nm. *Journal of the Chemical Society, Faraday Transactions 1: Physical Chemistry in Condensed Phases*, 74:975–1001, 1978.

[21] Jacob Israelachvili and Håkan Wennerström. Role of hydration and water structure in biological and colloidal interactions. *Nature*, 379(6562):219–225, 1996.

[22] RJ-M Pellenq, JM Caillol, and A Delville. Electrostatic attraction between two charged surfaces: A (n, v, t) monte carlo simulation. *J. Phys. Chem. B*, 101(42):8584–8594, 1997.

[23] Rahul Prasanna Misra, J Pedro de Souza, Daniel Blankschtein, and Martin Z Bazant. Theory of surface forces in multivalent electrolytes. *Langmuir*, 35(35):11550–11565, 2019.

[24] B Derjaguin and L Landau. Theory of the stability of strongly charged lyophobic sols and of the adhesion of strongly charged particles in solutions of electrolytes. *Progress in Surface Science*, 43(1-4):30–59, may 1993.

[25] C. E. Marshall. "Theory of the stability of lyophobic colloids." E. J. W. Verwey and J. T. G. Overbeek, with the collaboration of K. van Ness. Elsevier, New York-Amsterdam, 1948, 216 pp. *Journal of Polymer Science*, 4(3):413–414, jun 1949.

[26] Gregor Trefalt, Sven Holger Behrens, and Michal Borkovec. Charge regulation in the electrical double layer: ion adsorption and surface interactions. *Langmuir*, 32(2):380–400, 2015.

[27] Erich Hückel. Zur theorie der elektrolyte. *Ergebnisse der exakten Naturwissenschaften*, pages 199–276, 1924.

[28] Amir Levy, Michael McEldrew, and Martin Z Bazant. Spin-glass charge ordering in ionic liquids. *Phys. Rev. Mat.*, 3(5):055606, 2019.

[29] Michael McEldrew, Zachary A. H. Goodwin, Sheng Bi, Martin Z. Bazant, and Alexei A. Kornyshev. Theory of ion aggregation and gelation in super-concentrated electrolytes. *The Journal of Chemical Physics*, 152(23):234506, 2020.

[30] Amir Levy, J Pedro de Souza, and Martin Z Bazant. Breakdown of electroneutrality in nanopores. *Journal of Colloid and Interface Science*, 2020.

[31] Douwe Jan Bonthuis, Stephan Gekle, and Roland R Netz. Profile of the static permittivity tensor of water at interfaces: Consequences for capacitance, hydration interaction and ion adsorption. *Langmuir*, 28(20):7679–7694, 2012.

[32] Jacob N Israelachvili and Richard M Pashley. Molecular layering of water at surfaces and origin of repulsive hydration forces. *Nature*, 306(5940):249–250, 1983.

[33] J Pedro de Souza and Martin Z Bazant. Continuum theory of electrostatic correlations at charged surfaces. *The Journal of Physical Chemistry C*, 124(21):11414–11421, 2020.

[34] Martin Z. Bazant, Brian D. Storey, and Alexei A. Kornyshev. Double layer in ionic liquids: overscreening versus crowding. *Phys. Rev. Lett.*, 106(4):046102, jan 2011.

[35] J. Pedro de Souza, Alexei A. Kornyshev, and Martin Z. Bazant. Polar liquids at charged interfaces: A dipolar shell theory. *The Journal of Chemical Physics*, 156(24):244705, 2022.

[36] J Pedro de Souza, Amir Levy, and Martin Z Bazant. Electroneutrality breakdown in nanopore arrays. *Physical Review E*, 104(4):044803, 2021.

[37] Mohamed T Ghoneim, Atieh Sadraei, Pedro de Souza, Grace C Moore, Martin Z Bazant, and Canan Dagdeviren. A protocol to characterize ph sensing materials and systems. *Small Methods*, 3(2):1800265, 2019.

[38] Aymar CL de Lichtervelde, J Pedro de Souza, and Martin Z Bazant. Heat of nervous conduction: A thermodynamic framework. *Physical Review E*, 101(2):022406, 2020.

[39] J Pedro de Souza, Chun-Man Chow, Rohit Karnik, and Martin Z Bazant. Nonlinear ion transport mediated by induced charge in ultrathin nanoporous membranes. *Physical Review E*, 104(4):044802, 2021.

[40] Zachary AH Goodwin, Michael McEldrew, J Pedro de Souza, Martin Z Bazant, and Alexei A Kornyshev. Gelation, clustering and crowding in the electrical double layer of ionic liquids. *arXiv preprint arXiv:2204.11123*, 2022.

[41] Jake W Polster, Fikret Aydin, J Pedro de Souza, Martin Z Bazant, Tuan Anh Pham, and Zuzanna S Siwy. Rectified and salt concentration dependent wetting of hydrophobic nanopores. *Journal of the American Chemical Society*, 2022.

[42] Yan Levin and Y Levin. Electrostatic correlations: from plasma to biology. *Rep. Prog. Phys*, 65(02):1577–1632, 2002.

[43] A Yu Grosberg, TT Nguyen, and BI Shklovskii. Colloquium: the physics of charge inversion in chemical and biological systems. *Rev. Mod. Phys.*, 74(2):329, 2002.

[44] Christopher W Outhwaite and Lutful B Bhuiyan. An improved modified poisson–boltzmann equation in electric-double-layer theory. *J. Chem. Soc., Faraday Trans. 2: Mol. and Chem. Phys.*, 79(5):707–718, 1983.

[45] Douglas Henderson and Lesser Blum. Some exact results and the application of the mean spherical approximation to charged hard spheres near a charged hard wall. *J. Chem. Phys.*, 69(12):5441–5449, 1978.

[46] Douglas Henderson, Lesser Blum, and William R Smith. Application of the hypernetted chain approximation to the electric double layer at a charged planar interface. *Chem. Phys. Lett.*, 63(2):381–383, 1979.

[47] Marcelo Lozada-Cassou, Rafael Saavedra-Barrera, and Douglas Henderson. The application of the hypernetted chain approximation to the electrical double layer: Comparison with monte carlo results for symmetric salts. *J. Chem. Phys.*, 77(10):5150–5156, 1982.

[48] Roland Kjellander, Torbjörn Åkesson, Bo Jönsson, and Stjepan Marčelja. Double layer interactions in mono-and divalent electrolytes: A comparison of the anisotropic hnc theory and monte carlo simulations. *J. Chem. Phys.*, 97(2):1424–1431, 1992.

[49] Adelina Voukadinova, Mónika Valiskó, and Dirk Gillespie. Assessing the accuracy of three classical density functional theories of the electrical double layer. *Phys. Rev. E*, 98(1):012116, 2018.

[50] E Kierlik and ML Rosinberg. Density-functional theory for inhomogeneous fluids: adsorption of binary mixtures. *Phys. Rev. A*, 44(8):5025, 1991.

[51] Dirk Gillespie, Wolfgang Nonner, and Robert S Eisenberg. Coupling poisson–nernst–planck and density functional theory to calculate ion flux. *J. Phys. Condens. Matter*, 14(46):12129, 2002.

[52] Roland Roth and Dirk Gillespie. Shells of charge: a density functional theory for charged hard spheres. *J. Phys. Condens. Matter*, 28(24):244006, 2016.

[53] Yaakov Rosenfeld. Free energy model for inhomogeneous fluid mixtures: Yukawa-charged hard spheres, general interactions, and plasmas. *J. Chem. Phys.*, 98(10):8126–8148, 1993.

[54] Yaakov Rosenfeld. Free-energy model for the inhomogeneous hard-sphere fluid mixture and density-functional theory of freezing. *Phys. Rev. Lett.*, 63(9):980, 1989.

[55] Roland Roth. Fundamental measure theory for hard-sphere mixtures: a review. *J. Phys. Condens. Matter*, 22(6):063102, 2010.

[56] Christian D Santangelo. Computing counterion densities at intermediate coupling. *Phys. Rev. E*, 73(4):041512, 2006.

[57] M. M. Hatlo and L. Lue. Electrostatic interactions of charged bodies from the weak- to the strong-coupling regime. *Europhys. Lett.*, 89(2):25002, jan 2010.

[58] Brian D Storey and Martin Z Bazant. Effects of electrostatic correlations on electrokinetic phenomena. *Phys. Rev. E*, 86(5):056303, nov 2012.

[59] Robert F Stout and Aditya S Khair. A continuum approach to predicting electrophoretic mobility reversals. *J. Fluid Mech.*, 752:R1, aug 2014.

[60] Chao Wang, Jie Bao, Wenxiao Pan, and Xin Sun. Modeling electrokinetics in ionic liquids. *Electrophoresis*, 38(13-14):1693–1705, jul 2017.

[61] Hui Zhao. Diffuse-charge dynamics of ionic liquids in electrochemical systems. *Phys. Rev. E*, 84(5):051504, 2011.

[62] Xikai Jiang, Jingsong Huang, Hui Zhao, Bobby G Sumpter, and Rui Qiao. Dynamics of electrical double layer formation in room-temperature ionic liquids under constant-current charging conditions. *J. Phys. Condens. Matter*, 26(28):284109, jul 2014.

[63] Alpha A. Lee, Svyatoslav Kondrat, Dominic Vella, and Alain Goriely. Dynamics of ion transport in ionic liquids. *Phys. Rev. Lett.*, 115(10):106101, Sep 2015.

[64] Pedro HR Alijó, Frederico W Tavares, Evaristo C Biscaia Jr, and Argimiro R Secchi. Effects of electrostatic correlations on ion dynamics in alternating current voltages. *Electrochim. Acta*, 152:84–92, 2015.

[65] Elaheh Alidoosti and Hui Zhao. On the impact of electrostatic correlations on the double-layer polarization of a spherical particle in an alternating current field. *Langmuir*, 34(19):5592–5599, 2018.

[66] DW Lee, DJ Im, and IS Kang. Electric double layer at the interface of ionic liquid–dielectric liquid under electric field. *Langmuir*, 29(6):1875–1884, feb 2013.

[67] Michael McEldrew, Zachary AH Goodwin, Alexei A Kornyshev, and Martin Z Bazant. Theory of the double layer in water-in-salt electrolytes. *J. Phys. Chem. Lett.*, 9(19):5840–5846, oct 2018.

[68] Ahmed Shalabi, Lindsey Daniels, Matthew Scott, and ZL Mišković. Differential capacitance of ionic liquid interface with graphene: The effects of correlation and finite size of ions. *Electrochim. Acta*, 319:423–434, 2019.

[69] Dexuan Xie and Yi Jiang. Nonlocal poisson-fermi double-layer models: Effects of nonuniform ion sizes on double-layer structure. *Phys. Rev. E*, 97(5):052610, 2018.

[70] Yu Dong Yang, Gi Jong Moon, Jung Min Oh, and In Seok Kang. Discrete and continuum analyses of confinement effects of an ionic liquid on the edl structure and the pressure acting on the wall. *J. Phys. Chem. C*, 123(4):2516–2525, 2019.

[71] Xikai Jiang, Ying Liu, and Rui Qiao. Current rectification for transport of room-temperature ionic liquids through conical nanopores. *J. Phys. Chem. C*, 120(8):4629–4637, mar 2016.

[72] Gi Jong Moon, Myung Mo Ahn, and In Seok Kang. Osmotic pressure of ionic liquids in an electric double layer: Prediction based on a continuum model. *Phys. Rev. E*, 92(6):063020, 2015.

[73] Mirella S Santos, Evaristo C Biscaia Jr, and Frederico W Tavares. Effect of electrostatic correlations on micelle formation. *Colloids and Surfaces A: Physicochemical and Engineering Aspects*, 533:169–178, nov 2017.

[74] Jinn-Liang Liu and Bob Eisenberg. Poisson–fermi model of single ion activities in aqueous solutions. *Chem. Phys. Lett.*, 637:1–6, 2015.

[75] Sven Schlumpberger and Martin Z Bazant. Simple theory of ionic activity in concentrated electrolytes. *arXiv preprint arXiv:1709.03106*, 2017.

[76] Jinn-Liang Liu and Bob Eisenberg. Poisson-fermi modeling of ion activities in aqueous single and mixed electrolyte solutions at variable temperature. *J. Chem. Phys.*, 148(5):054501, 2018.

[77] Issei Nakamura. Effects of dielectric inhomogeneity and electrostatic correlation on the solvation energy of ions in liquids. *J. Phys. Chem. B*, 122(22):6064–6071, 2018.

[78] Jinn-Liang Liu and Chin-Lung Li. A generalized debye-hückel theory of electrolyte solutions. *AIP Adv.*, 9(1):015214, 2019.

[79] Jun Huang. Confinement induced dilution: Electrostatic screening length anomaly in concentrated electrolytes in confined space. *J. Phys. Chem. C*, 122(6):3428–3433, 2018.

[80] Jinn-Liang Liu. Numerical methods for the poisson–fermi equation in electrolytes. *J. Comput. Phys.*, 247:88–99, 2013.

[81] Jinn-Liang Liu and Bob Eisenberg. Poisson-nernst-planck-fermi theory for modeling biological ion channels. *J. Chem. Phys.*, 141(22):12B640_1, dec 2014.

[82] Jinn-Liang Liu and Bob Eisenberg. Analytical models of calcium binding in a calcium channel. *J. Chem. Phys.*, 141(7):075102, aug 2014.

[83] Jinn-Liang Liu and Bob Eisenberg. Numerical methods for a poisson-nernst-planck-fermi model of biological ion channels. *Phys. Rev. E*, 92(1):012711, jul 2015.

[84] Martin Z Bazant. Theory of chemical kinetics and charge transfer based on nonequilibrium thermodynamics. *Acc. Chem. Res.*, 46(5):1144–1160, 2013.

[85] AP dos Santos, A Diehl, and Y Levin. Electrostatic correlations in colloidal suspensions: Density profiles and effective charges beyond the Poisson–Boltzmann theory. *J. Chem. Phys.*, 2009.

[86] Ankur Gupta and Howard A Stone. Electrical double layers: Effects of asymmetry in electrolyte valence on steric effects, dielectric decrement, and ion–ion correlations. *Langmuir*, 34(40):11971–11985, 2018.

[87] Herbert H Woodson and James R Melcher. Electromechanical dynamics. 1968.

[88] M Alawneh and D Henderson. Monte carlo simulation of the double layer at an electrode including the effect of a dielectric boundary. *Molecular Simulation*, 33(6):541–547, 2007.

[89] Douglas Henderson, Lesser Blum, and Joel L Lebowitz. An exact formula for the contact value of the density profile of a system of charged hard spheres near a charged wall. *J. Electroanal. Chem. Interf. Electrochem.*, 102(3):315–319, 1979.

[90] Yoram Burak, David Andelman, and Henri Orland. Test-charge theory for the electric double layer. *Phys. Rev. E*, 70(1):016102, 2004.

[91] Steven L Carnie and Derek YC Chan. Ionic adsorption from a primitive model electrolyte—nonlinear treatment. *J. Chem. Phys.*, 75(7):3485–3494, 1981.

[92] AA Kornyshev, AI Rubinshtein, and MA Vorotyntsev. Model nonlocal electrostatics. i. *J. Phys. C*, 11(15):3307, 1978.

[93] AA Kornyshev. Nonlocal screening of ions in a structurized polar liquid—new aspects of solvent description in electrolyte theory. *Electrochim. Acta*, 26(1):1–20, 1981.

[94] Ivan Palaia, Martin Trulsson, Ladislav Šamaj, and Emmanuel Trizac. A correlation-hole approach to the electric double layer with counter-ions only. *Molecular Physics*, 116(21-22):3134–3146, 2018.

[95] Ladislav Šamaj, Martin Trulsson, and Emmanuel Trizac. Strong-coupling theory of counterions between symmetrically charged walls: from crystal to fluid phases. *Soft Matter*, 14(20):4040–4052, 2018.

[96] Ali Naji and Roland R Netz. Counterions at charged cylinders: criticality and universality beyond mean-field theory. *Phys. Rev. Lett.*, 95(18):185703, 2005.

[97] Gerald S Manning. Limiting laws and counterion condensation in polyelectrolyte solutions I. Colligative properties. *J. Chem. Phys.*, 51(3), 1969.

[98] Minryeong Cha, Juyeon Yi, and Yong Woon Kim. Hidden criticality of counterion condensation near a charged cylinder. *Sci. Rep.*, 7(1):10551, 2017.

[99] Dirk Gillespie. A review of steric interactions of ions: Why some theories succeed and others fail to account for ion size. *Microfluidics and Nanofluidics*, 18(5-6):717–738, 2015.

[100] Zachary AH Goodwin, Guang Feng, and Alexei A Kornyshev. Mean-field theory of electrical double layer in ionic liquids with account of short-range correlations. *Electrochim. Acta*, 225:190–197, 2017.

[101] André G Moreira and Roland R Netz. Counterions at charge-modulated substrates. *Europhys. Lett.*, 57(6):911, 2002.

[102] Alexander M Smith, Alpha A Lee, and Susan Perkin. The electrostatic screening length in concentrated electrolytes increases with concentration. *J. Phys. Chem. Lett.*, 7(12):2157–2163, 2016.

[103] Frieder Mugele, Bijoyendra Bera, Andrea Cavalli, Igor Siretanu, Armando Maestro, Michel Duits, Martien Cohen-Stuart, Dirk Van Den Ende, Isabella Stocker, and Ian Collins. Ion adsorption-induced wetting transition in oil-water-mineral systems. *Sci. Rep.*, 5:10519, 2015.

[104] Jacob N Israelachvili. *Intermolecular and surface forces*. Academic Press, 2015.

[105] M. Olvera de la Cruz, L Belloni, M Delsanti, J P Dalbiez, O Spalla, and M Drifford. Precipitation of highly charged polyelectrolyte solutions in the presence of multivalent salts. *The Journal of Chemical Physics*, 103(13):5781–5791, oct 1995.

[106] Eric Raspaud, M. Olvera de la Cruz, J-L Sikorav, and Francoise Livolant. Precipitation of DNA by Polyamines: A Polyelectrolyte Behavior. *Biophysical Journal*, 74(1):381–393, jan 1998.

[107] Francisco J Solis and Monica Olvera de la Cruz. Collapse of flexible polyelectrolytes in multivalent salt solutions. *The Journal of Chemical Physics*, 112(4):2030–2035, jan 2000.

[108] Alexei A Kornyshev, Dominic J Lee, Sergey Leikin, and Aaron Wynveen. Structure and interactions of biological helices. *Reviews of Modern Physics*, 79(3):943–996, aug 2007.

[109] Paul Dubin, J Bock, Richie Davis, Donald N Schulz, and Curt Thies. *Macromolecular complexes in chemistry and biology*. Springer Science & Business Media, 2012.

[110] Drew McCormack, Steven L Carnie, and Derek Y.C. Chan. Calculations of Electric Double-Layer Force and Interaction Free Energy between Dissimilar Surfaces. *Journal of Colloid and Interface Science*, 169(1):177–196, jan 1995.

[111] S J Miklavic, D Y C Chan, L R White, and T W Healy. Double Layer Forces between Heterogeneous Charged Surfaces. *The Journal of Physical Chemistry*, 98(36):9022–9032, sep 1994.

[112] Rahul Prasanna Misra, Siddhartha Das, and Sushanta K. Mitra. Electric double layer force between charged surfaces: Effect of solvent polarization. *J. Chem. Phys.*, 138(11):114703, mar 2013.

[113] BV Derjaguin. Theory of the stability of strongly charged lyophobic sols and the adhesion of strongly charged particles in solutions of electrolytes. *Acta Physicochim. USSR*, 14:633–662, 1941.

[114] B V Derjaguin, A S Titijevskaia, I I Abricossova, and A D Malkina. Investigations of the forces of interaction of surfaces in different media and their application to the problem of colloid stability. *Discussions of the Faraday Society*, 18:24, 1954.

[115] J Lyklema and Karol J Mysels. A Study of Double Layer Repulsion and van der Waals Attraction in Soap Films. *Journal of the American Chemical Society*, 87(12):2539–2546, jun 1965.

[116] R.M Pashley. Hydration forces between mica surfaces in aqueous electrolyte solutions. *Journal of Colloid and Interface Science*, 80(1):153–162, mar 1981.

[117] R.M Pashley. DLVO and hydration forces between mica surfaces in Li+, Na+, K+, and Cs+ electrolyte solutions: A correlation of double-layer and hydration forces with surface cation exchange properties. *Journal of Colloid and Interface Science*, 83(2):531–546, oct 1981.

[118] R. M. Pashley, P. M. McGuiggan, B. W. Ninham, J. Brady, and D. F. Evans. Direct measurements of surface forces between bilayers of double-chained quaternary ammonium acetate and bromide surfactants. *The Journal of Physical Chemistry*, 90(8):1637–1642, apr 1986.

[119] Christopher P Smith, Mayumi Maeda, Ljiljana Atanasoska, Henry S White, and D J McClure. Ultrathin platinum films on mica and the measurement of forces at the platinum/water interface. *The Journal of Physical Chemistry*, 92(1):199–205, jan 1988.

[120] R G Horn, D R Clarke, and M T Clarkson. Direct measurement of surface forces between sapphire crystals in aqueous solutions. *Journal of Materials Research*, 3(03):413–416, jun 1988.

[121] R.G. Horn, D.T. Smith, and W Haller. Surface forces and viscosity of water measured between silica sheets. *Chemical Physics Letters*, 162(4-5):404–408, oct 1989.

[122] William A Ducker, Tim J Senden, and Richard M Pashley. Direct measurement of colloidal forces using an atomic force microscope. *Nature*, 353(6341):239–241, sep 1991.

[123] William A Ducker, Tim J Senden, and Richard M Pashley. Measurement of forces in liquids using a force microscope. *Langmuir*, 8(7):1831–1836, jul 1992.

[124] Laurence Meagher. Direct measurement of forces between silica surfaces in aqueous CaCl2 solutions using an atomic force microscope. *Journal of Colloid and Interface Science*, 152(1):293–295, aug 1992.

[125] Gene Vigil, Zhenghe Xu, Suzi Steinberg, and Jacob Israelachvili. Interactions of Silica Surfaces. *Journal of Colloid and Interface Science*, 165(2):367–385, jul 1994.

[126] Ian Larson, Calum J Drummond, Derek Y C Chan, and Franz Grieser. Direct force measurements between titanium dioxide surfaces. *Journal of the American Chemical Society*, 115(25):11885–11890, dec 1993.

[127] Nir Kampf, Dan Ben-Yaakov, David Andelman, S. A. Safran, and Jacob Klein. Direct Measurement of Sub-Debye-Length Attraction between Oppositely Charged Surfaces. *Phys. Rev. Lett.*, 103(11):118304, sep 2009.

[128] Roland Kjellander, Stjepan Marčelja, and J P Quirk. Attractive double-layer interactions between calcium clay particles. *Journal of Colloid and Interface Science*, 126(1):194–211, 1988.

[129] R Kjellander, S Marčelja, R M Pashley, and J P Quirk. Double-layer ion correlation forces restrict calcium-clay swelling. *The Journal of Physical Chemistry*, 92(23):6489–6492, nov 1988.

[130] R Kjellander, S Marčelja, R M Pashley, and J P Quirk. A theoretical and experimental study of forces between charged mica surfaces in aqueous CaCl 2 solutions. *The Journal of Chemical Physics*, 92(7):4399–4407, apr 1990.

[131] P Kékicheff, Stjepan Marcúelja, T J Senden, and V E Shubin. Charge reversal seen in electrical double layer interaction of surfaces immersed in 2:1 calcium electrolyte. *The Journal of Chemical Physics*, 99(8):6098–6113, oct 1993.

[132] Ohad Zohar, Ilya Leizerson, and Uri Sivan. Short Range Attraction between Two Similarly Charged Silica Surfaces. *Physical Review Letters*, 96(17):177802, may 2006.

[133] K. Besteman, M. A. G. Zevenbergen, H. A. Heering, and S. G. Lemay. Direct Observation of Charge Inversion by Multivalent Ions as a Universal Electrostatic Phenomenon. *Phys. Rev. Lett.*, 93(17):170802, oct 2004.

[134] K. Besteman, M. A. G. Zevenbergen, and S. G. Lemay. Charge inversion by multivalent ions: Dependence on dielectric constant and surface-charge density. *Phys. Rev. E*, 72(6):061501, dec 2005.

[135] Roland Kjellander, Torbj?rn ?kesson, Bo J?nsson, and Stjepan Mar?elja. Double layer interactions in mono? and divalent electrolytes: A comparison of the anisotropic HNC theory and Monte Carlo simulations. *J. Chem. Phys.*, 97(2):1424–1431, jul 1992.

[136] Lars Guldbrand, Bo Jönsson, Håkan Wennerström, and Per Linse. Electrical double layer forces. A Monte Carlo study. *The Journal of Chemical Physics*, 80(5):2221–2228, mar 1984.

[137] Alexei I. Abrikosov, Björn Stenqvist, and Mikael Lund. Steering patchy particles using multivalent electrolytes. *Soft Matter*, 13(26):4591–4597, 2017.

[138] † Bo Jönsson, *, ‡ A. Nonat, ‡ C. Labbez, , § B. Cabane, and H. Wennerström‖. Controlling the Cohesion of Cement Paste. *Langmuir*, 21(20):9211–9221, sep 2005.

[139] Victor A Bloomfield. Condensation of DNA by multivalent cations: Considerations on mechanism. *Biopolymers*, 31(13):1471–1481, nov 1991.

[140] Peter A Kralchevsky and Vesselin N Paunov. Contribution of ionic correlations to excess free energy and disjoining pressure of thin liquid films 1. electric double layer inside the film. *Colloids and surfaces*, 64(3-4):245–264, jul 1992.

[141] V.I Perel and B.I Shklovskii. Screening of a macroion by multivalent ions: a new boundary condition for the Poisson–Boltzmann equation and charge inversion. *Physica A: Statistical Mechanics and its Applications*, 274(3-4):446–453, dec 1999.

[142] G. N. Patey. The interaction of two spherical colloidal particles in electrolyte solution. An application of the hypernetted-chain approximation. *The Journal of Chemical Physics*, 72(10):5763–5771, may 1980.

[143] Matej Kanduč, Mohsen Moazzami-Gudarzi, Valentina Valmacco, Rudolf Podgornik, and Gregor Trefalt. Interactions between charged particles with bathing multivalent counterions: experiments vs. dressed ion theory. *Physical Chemistry Chemical Physics*, 19(15):10069–10080, 2017.

[144] Matej Kanduč, Ali Naji, Jan Forsman, and Rudolf Podgornik. Dressed counterions: Strong electrostatic coupling in the presence of salt. *The Journal of Chemical Physics*, 132(12):124701, mar 2010.

[145] Jinn-Liang Liu and Bob Eisenberg. Correlated Ions in a Calcium Channel Model: A Poisson–Fermi Theory. *The Journal of Physical Chemistry B*, 117(40):12051–12058, oct 2013.

[146] Jinn-Liang Liu and Bob Eisenberg. Analytical models of calcium binding in a calcium channel. *The Journal of Chemical Physics*, 141(7):075102, aug 2014.

[147] J Pedro de Souza and Martin Z Bazant. Continuum theory of electrostatic correlations at charged surfaces. *arXiv preprint arXiv:1902.05493*, 2019.

[148] Martin Z. Bazant, Mustafa Sabri Kilic, Brian D. Storey, and Armand Ajdari. Towards an understanding of induced-charge electrokinetics at large applied voltages in concentrated solutions. *Adv. Colloid Interface Sci.*, 152(1):48–88, nov 2009.

[149] Otto Stern. The theory of the electrolytic double-layer. *Zeitschrift fuer Elektrochemie und Angewandte Physikalische Chemie*, 1924.

[150] Klemen Bohinc, Ahis Shrestha, Milan Brumen, and Sylvio May. Poisson-Helmholtz-Boltzmann model of the electric double layer: Analysis of monovalent ionic mixtures. *Physical Review E*, 85(3):031130, mar 2012.

[151] Jacob N. Israelachvili and Richard M. Pashley. Molecular layering of water at surfaces and origin of repulsive hydration forces. *Nature*, 306(5940):249–250, nov 1983.

[152] D.M. LeNeveu and R.P. Rand. Measurement and modification of forces between lecithin bilayers. *Biophysical Journal*, 18(2):209–230, may 1977.

[153] Sven H. Behrens and David G. Grier. The charge of glass and silica surfaces. *The Journal of Chemical Physics*, 115(14):6716–6721, oct 2001.

[154] Derek Y.C Chan, Richard M Pashley, and Lee R White. A simple algorithm for the calculation of the electrostatic repulsion between identical charged surfaces in electrolyte. *Journal of Colloid and Interface Science*, 77(1):283–285, sep 1980.

[155] Tomer Markovich, David Andelman, and Rudi Podgornik. Charge regulation: A generalized boundary condition? *EPL (Europhysics Letters)*, 113(2):26004, jan 2016.

[156] Gregor Trefalt, Sven Holger Behrens, and Michal Borkovec. Charge Regulation in the Electrical Double Layer: Ion Adsorption and Surface Interactions. *Langmuir*, 32(2):380–400, jan 2016.

[157] André Nonat. The structure and stoichiometry of CSH. *Cement and Concrete Research*, 34(9):1521–1528, 2004.

[158] Biljana Uzelac, Valentina Valmacco, and Gregor Trefalt. Interactions between silica particles in the presence of multivalent coions. *Soft Matter*, 13(34):5741–5748, 2017.

[159] Yaohua Li, Martin Girard, Meng Shen, Jaime Andres Millan, and Monica Olvera de la Cruz. Strong attractions and repulsions mediated by monovalent salts. *Proceedings of the National Academy of Sciences*, 114(45):11838–11843, nov 2017.

[160] Y. Marcus. Ionic radii in aqueous solutions. *Journal of Solution Chemistry*, 12(4):271–275, apr 1983.

[161] Harold D Ackler, Roger H French, and Yet-Ming Chiang. Comparisons of hamaker constants for ceramic systems with intervening vacuum or water: From force laws and physical properties. *Journal of Colloid and Interface Science*, 179(2):460–469, 1996.

[162] Matan Dishon, Ohad Zohar, and Uri Sivan. From repulsion to attraction and back to repulsion: the effect of nacl, kcl, and cscl on the force between silica surfaces in aqueous solution. *Langmuir*, 25(5):2831–2836, 2009.

[163] Ram M Adar, Tomer Markovich, and David Andelman. Bjerrum pairs in ionic solutions: A poisson-boltzmann approach. *The Journal of chemical physics*, 146(19):194904, 2017.

[164] Daniel Martin-Jimenez, Enrique Chacon, Pedro Tarazona, and Ricardo Garcia. Atomically resolved three-dimensional structures of electrolyte aqueous solutions near a solid surface. *Nature communications*, 7:12164, 2016.

[165] Jianzhong Wu, Tao Jiang, De En Jiang, Zhehui Jin, and Douglas Henderson. A classical density functional theory for interfacial layering of ionic liquids. *Soft Matter*, 2011.

[166] J Pedro de Souza, Karina Pivnic, Martin Z Bazant, Michael Urbakh, and Alexei A Kornyshev. Structural forces in ionic liquids: The role of ionic size asymmetry. *The Journal of Physical Chemistry B*, 126(6):1242–1253, 2022.

[167] M. V. Fedorov and A. A. Kornyshev. Ionic liquids at electrified interfaces. *Chem. Rev.*, 114:2978–3036, 2014.

[168] John G Kirkwood. Statistical mechanics of liquid solutions. *Chem. Rev.*, 19(3):275–307, 1936.

[169] Luis M. Varela, Mannuel Garcia, and Victor Mosquera. Exact mean-field theory of ionic solutions: non-debye screening. *Phys. Rep.*, 382:1–111, 2003.

[170] GN Patey. The interaction of two spherical colloidal particles in electrolyte solution. an application of the hypernetted-chain approximation. *J. Chem. Phys.*, 72(10):5763–5771, 1980.

[171] Phil Attard. Asymptotic analysis of primitive model electrolytes and the electrical double layer. *Phys. Rev. E*, 48(5):3604, 1993.

[172] Roland Kjellander and D John Mitchell. An exact but linear and poisson—boltzmann-like theory for electrolytes and colloid dispersions in the primitive model. *Chem. Phys. Lett.*, 200(1-2):76–82, 1992.

[173] R. Kjellander. Focus article: Oscillatory and long-range monotonic exponential decays of electrostatic interactions in ionic liquids and other electrolytes: The significance of dielectric permittivity and renormalized charges. *J. Chem. Phys.*, 148:193701, 2018.

[174] R. J. F. Leote de Carvalho and R. Evans. The decay of correlations in ionic fluids. *Mol. Phys.*, 83:619–654, 1994.

[175] B. Rotenberg, O. Bernard, and J.-P. Hansen. Underscreening in ionic liquids: A first principles analysis. *J. Phys. Condens. Matter*, 30:054005, 2018.

[176] Johannes Lischner and T. A. Arias. Kohn-sham-like approach toward a classical density-functional theory of inhomogeneous polar molecular liquids: An application to liquid hydrogen chloride. *Phys. Rev. Lett.*, 101:216401, 2008.

[177] Ke Ma, Jan Forsman, and Clifford E. Woodward. Influence of ion pairing in ionic liquids on electrical double layer structures and surface force using classical density functional approach. *J. Chem. Phys.*, 142:174704, 2015.

[178] J. Reszko-Zygmunt, S. Sokołowski, D. Henderson, and D. Boda. Temperature dependence of the double layer capacitance for the restricted primitive model of an electrolyte solution from a density functional approach. *J. Chem. Phys.*, 112:084504, 2005.

[179] L. B. Bhuiyan, S. Lamperski, J. Wu, and D. Henderson. Monte carlo simulation for the double layer structure of an ionic liquid using a dimer model: A comparison with the density functional theory. *J. Phys. Chem. B*, 116:10364–10370, 2012.

[180] N. Gavish, D. Elad, and A. Yochelis. From solvent-free to dilute electrolytes: Essential components for a continuum theory. *J. Phys. Chem. Lett.*, 9:36, 2018.

[181] Jianzhong Wu, Tao Jiang, De-en Jiang, Zhehui Jin, and Douglas Henderson. A classical density functional theory for interfacial layering of ionic liquids. *Soft Matter*, 7(23):11222–11231, 2011.

[182] Douglas Henderson, Stanisław Lamperski, Zhehui Jin, and Jianzhong Wu. Density functional study of the electric double layer formed by a high density electrolyte. *J. Phys. Chem. B*, 115(44):12911–12914, 2011.

[183] Ke Ma, Cheng Lian, Clifford E Woodward, and Boyu Qin. Classical density functional theory reveals coexisting short-range structural decay and long-range force decay in ionic liquids. *Chem. Phys. Lett.*, 739:137001, 2020.

[184] A. Ciach. Simple theory for oscillatory charge profile in ionic liquids near a charged wall. *J. Mol. Liq.*, 270:138, 2018.

[185] Roland Kjellander and D John Mitchell. Dressed-ion theory for electrolyte solutions: A debye–hückel-like reformulation of the exact theory for the primitive model. *J. Chem. Phys.*, 101(1):603–626, 1994.

[186] T. Welton. Room-temperature ionic liquids. solvents for synthesis and catalysis. *Chem. Rev.*, 99:2071–2083, 1999.

[187] Jason P. Hallet and Tom Welton. Room-temperature ionic liquids: Solvents for synthesis and catalysis. 2. *Chem. Rev.*, 111:3508–3576, 2011.

[188] Svyatoslav Kondrat and Alexei A. Kornyshev. Pressing a spring: what does it take to maximize the energy storage in nanoporous supercapacitors? *Nanoscale Horiz.*, 1:45–52, 2016.

[189] S. Perkin. Ionic liquids in confined geometries. *Phys. Chem. Chem. Phys.*, 14:5052–5062, 2012.

[190] M. V. Fedorov and A. A. Kornyshev. Towards understanding the structure and capacitance of electrical double layer in ionic liquids. *Electrochim. Acta*, 53:6835–6840, 2008.

[191] M. V. Fedorov, N. Georgi, and A. A. Kornyshev. Double layer in ionic liquids: The nature of the camel shape of capacitance. *Electrochem commun*, 12:296–299, 2010.

[192] M. Z. Bazant, B. D. Storey, and A. A. Kornyshev. Double layer in ionic liquids: Overscreening versus crowding. *Phys. Rev. Lett.*, 109:046102, 2011.

[193] Kathleen Kirchner, Tom Kirchner, V Ivaništšev, and Maxim V Fedorov. Electrical double layer in ionic liquids: Structural transitions from multilayer to monolayer structure at the interface. *Electrochimica Acta*, 110:762–771, 2013.

[194] M. S. Kilic, M. Z. Bazant, and A. Ajdari. Steric effects in the dynamics of electrolytes at large applied voltages. i. double-layer charging. *Phys. Rev. E*, 75:021502, 2007.

[195] J Pedro de Souza and Martin Z Bazant. Continuum theory of electrostatic correlations at charged surfaces. *The Journal of Physical Chemistry C*, 124(21):11414–11421, 2020.

[196] Ram M Adar, Samuel A Safran, Haim Diamant, and David Andelman. Screening length for finite-size ions in concentrated electrolytes. *Physical Review E*, 100(4):042615, 2019.

[197] Yael Avni, Ram M Adar, and David Andelman. Charge oscillations in ionic liquids: A microscopic cluster model. *Physical Review E*, 101(1):010601, 2020.

[198] Pedro Tarazona. Free-energy density functional for hard spheres. *Phys. Rev. A*, 31(4):2672, 1985.

[199] NW Ashcroft. Electron-ion pseudopotentials in metals. *Physics Letters*, 23(1):48–50, 1966.

[200] Derek Frydel and Yan Levin. The double-layer of penetrable ions: An alternative route to charge reversal. *The Journal of chemical physics*, 138(17):174901, 2013.

[201] Zhen-Gang Wang. Fluctuation in electrolyte solutions: The self energy. *Physical Review E*, 81(2):021501, 2010.

[202] Sylvio May, Aleš Iglic, Jurij Rešcic, Stefano Maset, and Klemen Bohinc. Bridging like-charged macroions through long divalent rodlike ions. *The Journal of Physical Chemistry B*, 112(6):1685–1692, 2008.

[203] Derek Frydel. Mean-field electrostatics beyond the point-charge description. *arXiv preprint arXiv:1411.7577*, 2014.

[204] Derek Frydel. The double-layer structure of overscreened surfaces by smeared-out ions. *The Journal of chemical physics*, 145(18):184703, 2016.

[205] L Blum and Yaakov Rosenfeld. Relation between the free energy and the direct correlation function in the mean spherical approximation. *Journal of statistical physics*, 63(5):1177–1190, 1991.

[206] Jian Jiang and Dirk Gillespie. Revisiting the charged shell model: A density functional theory for electrolytes. *Journal of Chemical Theory and Computation*, 2021.

[207] Martin Z. Bazant, Mustafa Sabri Kilic, Brian D. Storey, and Armand Ajdari. Towards an understanding of induced-charge electrokinetics at large applied voltages in concentrated solutions. *Adv. Colloid Interface Sci.*, 152:48–88, 2009.

[208] Ju Swift and Pierre C Hohenberg. Hydrodynamic fluctuations at the convective instability. *Physical Review A*, 15(1):319, 1977.

[209] KR Elder and Martin Grant. Modeling elastic and plastic deformations in nonequilibrium processing using phase field crystals. *Physical Review E*, 70(5):051605, 2004.

[210] A. A. Lee, C. Perez-Martinez, A. M. Smith, and S. Perkin. Underscreening in concentrated electrolytes. *Faraday Discuss.*, page DOI: 10.1039/c6fd00250a, 2017.

[211] A. M. Smith, A. A. Lee, and S. Perkin. The electrostatic screening length in concentrated electrolytes increases with concentration. *J. Phys. Chem. Lett.*, 7:2157–2163, 2016.

[212] Zachary A. H. Goodwin, Guang Feng, and Alexei A. Kornyshev. Mean-field theory of electrical double layer in ionic liquids with account of short-range correlations. *Electrochim. Acta*, 225:190–196, 2017.

[213] Hao-Kun Li, J Pedro de Souza, Ze Zhang, Joel Martis, Kyle Sendgikoski, John Cumings, Martin Z Bazant, and Arun Majumdar. Imaging arrangements of discrete ions at liquid–solid interfaces. *Nano Letters*, 20(11):7927–7932, 2020.

[214] Ingo Krossing, John M Slattery, Corinne Daguenet, Paul J Dyson, Alla Oleinikova, and Hermann Weingärtner. Why are ionic liquids liquid? a simple explanation based on lattice and solvation energies. *Journal of the American Chemical Society*, 128(41):13427–13434, 2006.

[215] Jason P Hallett and Tom Welton. Room-temperature ionic liquids: solvents for synthesis and catalysis. 2. *Chemical reviews*, 111(5):3508–3576, 2011.

[216] Manuel Palacio and Bharat Bhushan. A review of ionic liquids for green molecular lubrication in nanotechnology. *Tribology Letters*, 40(2):247–268, 2010.

[217] Hua Li, Ross J Wood, Mark W Rutland, and Rob Atkin. An ionic liquid lubricant enables superlubricity to be "switched on" in situ using an electrical potential. *Chemical Communications*, 50(33):4368–4370, 2014.

[218] Karina Pivnic, Fernando Bresme, Alexei A Kornyshev, and Michael Urbakh. Electrotunable friction in diluted room temperature ionic liquids: Implications for nanotribology. *ACS Applied Nano Materials*, 3(11):10708–10719, 2020.

[219] Rob Atkin and Gregory G Warr. Structure in confined room-temperature ionic liquids. *The Journal of Physical Chemistry C*, 111(13):5162–5168, 2007.

[220] Susan Perkin. Ionic liquids in confined geometries. *Physical Chemistry Chemical Physics*, 14(15):5052–5062, 2012.

[221] Günther Krämer, Florian Hausen, and Roland Bennewitz. Dynamic shear force microscopy of confined liquids at a gold electrode. *Faraday discussions*, 199:299–309, 2017.

[222] Karina Pivnic, Fernando Bresme, Alexei A Kornyshev, and Michael Urbakh. Structural forces in mixtures of ionic liquids with organic solvents. *Langmuir*, 35(47):15410–15420, 2019.

[223] Otto Stern. Zur theorie der elektrolytischen doppelschicht. *Zeitschrift für Elektrochemie und angewandte physikalische Chemie*, 30(21-22):508–516, 1924.

[224] JJ Bikerman. Structure and capacity of electrical double layer. *The London, Edinburgh, and Dublin Philosophical Magazine and Journal of Science*, 33(220):384–397, 1942.

[225] V Freise. Zur theorie der diffusen doppelschicht. *Zeitschrift für Elektrochemie, Berichte der Bunsengesellschaft für physikalische Chemie*, 56(8):822–827, 1952.

[226] Maxim V Fedorov and Alexei A Kornyshev. Ionic liquid near a charged wall: Structure and capacitance of electrical double layer. *The Journal of Physical Chemistry B*, 112(38):11868–11872, 2008.

[227] Zachary A. H. Goodwin, J. Pedro de Souza, Martin Z. Bazant, and Alexei A. Kornyshev. *Mean-Field Theory of the Electrical Double Layer in Ionic Liquids*, pages 1–13. Springer Singapore, Singapore, 2021.

[228] De-en Jiang and Jianzhong Wu. Microscopic insights into the electrochemical behavior of nonaqueous electrolytes in electric double-layer capacitors. *The journal of physical chemistry letters*, 4(8):1260–1267, 2013.

[229] Y. Han, S. Huang, and T. Yan. A mean-field theory on the differential capacitance of asymmetric ionic liquid electrolytes. *J. Phys.: Condens. Matter*, 26:284103, 2014.

[230] Ekaterina Gongadze and Aleš Iglič. Asymmetric size of ions and orientational ordering of water dipoles in electric double layer model-an analytical mean-field approach. *Electrochimica Acta*, 178:541–545, 2015.

[231] A. C. Maggs and R. Podgornik. General theory of asymmetric steric interactions in electrostatic double layers. *Soft Mater*, 12:1219–1229, 2016.

[232] M. Popović and A. Šiber. Lattice-gas poisson-boltzmann approach for sterically asymmetric electrolytes. *Phys. Rev. E*, 88:022302, 2013.

[233] Li Yin, Yike Huang, Houxian Chen, and Tianying Yan. A mean-field theory on the differential capacitance of asymmetric ionic liquid electrolytes. ii. accounts of ionic interactions. *Physical Chemistry Chemical Physics*, 20(26):17606–17614, 2018.

[234] De-en Jiang, Dong Meng, and Jianzhong Wu. Density functional theory for differential capacitance of planar electric double layers in ionic liquids. *Chemical Physics Letters*, 504(4-6):153–158, 2011.

[235] P Cats, R Evans, A Härtel, and R van Roij. Primitive model electrolytes in the near and far field: Decay lengths from dft and simulations. *The Journal of Chemical Physics*, 154(12):124504, 2021.

[236] Dirk Gillespie, Wolfgang Nonner, and Robert S Eisenberg. Density functional theory of charged, hard-sphere fluids. *Physical Review E*, 68(3):031503, 2003.

[237] Andreas Härtel. Structure of electric double layers in capacitive systems and to what extent (classical) density functional theory describes it. *Journal of Physics: Condensed Matter*, 29(42):423002, 2017.

[238] Steven L Carnie, Derek YC Chan, D John Mitchell, and Barry W Ninham. The structure of electrolytes at charged surfaces: the primitive model. *The Journal of Chemical Physics*, 74(2):1472–1478, 1981.

[239] Jonathan Ennis, Roland Kjellander, and D John Mitchell. Dressed ion theory for bulk symmetric electrolytes in the restricted primitive model. *The Journal of chemical physics*, 102(2):975–991, 1995.

[240] RJF Leote de Carvalho and R Evans. The decay of correlations in ionic fluids. *Molecular Physics*, 83(4):619–654, 1994.

[241] G Iván Guerrero-García, Enrique González-Tovar, Marcelo Lozada-Cassou, and F de J. Guevara-Rodríguez. The electrical double layer for a fully asymmetric electrolyte around a spherical colloid: An integral equation study. *The Journal of chemical physics*, 123(3):034703, 2005.

[242] Hans Greberg and Roland Kjellander. Charge inversion in electric double layers and effects of different sizes for counterions and coions. *The Journal of chemical physics*, 108(7):2940–2953, 1998.

[243] Jacob N Israelachvili. *Intermolecular and surface forces*. Academic press, 2015.

[244] Kazuhide Ueno, Motohiro Kasuya, Masayoshi Watanabe, Masashi Mizukami, and Kazue Kurihara. Resonance shear measurement of nanoconfined ionic liquids. *Physical Chemistry Chemical Physics*, 12(16):4066–4071, 2010.

[245] Robert Hayes, Natalia Borisenko, Matthew K Tam, Patrick C Howlett, Frank Endres, and Rob Atkin. Double layer structure of ionic liquids at the au (111) electrode interface: an atomic force microscopy investigation. *The Journal of Physical Chemistry C*, 115(14):6855–6863, 2011.

[246] Alexander M Smith, Susan Perkin, et al. Switching the structural force in ionic liquid-solvent mixtures by varying composition. *Physical review letters*, 118(9):096002, 2017.

[247] Matthew A. Gebbie, Alexander M. Smith, Howard A. Dobbs, Alpha A. Lee, Gregory G. Warr, Xavier Banquy, Markus Valtiner, Mark W. Rutland, Jacob N. Israelachvili, Susan Perkin, and Rob Atkin. Long range electrostatic forces in ionic liquids. *Chem. Commun.*, 53:1214–1224, 2017.

[248] OY Fajardo, F Bresme, AA Kornyshev, and M Urbakh. Electrotunable lubricity with ionic liquid nanoscale films. *Scientific reports*, 5(1):1–7, 2015.

[249] Oscar Y Fajardo, Fernando Bresme, Alexei A Kornyshev, and Michael Urbakh. Electrotunable friction with ionic liquid lubricants: how important is the molecular structure of the ions? *The journal of physical chemistry letters*, 6(20):3998–4004, 2015.

[250] Céline Merlet, Clarisse Péan, Benjamin Rotenberg, Paul A Madden, Patrice Simon, and Mathieu Salanne. Simulating supercapacitors: Can we model electrodes as constant charge surfaces? *The journal of physical chemistry letters*, 4(2):264–268, 2013.

[251] Justin B Haskins and John W Lawson. Evaluation of molecular dynamics simulation methods for ionic liquid electric double layers. *The Journal of chemical physics*, 144(18):184707, 2016.

[252] Samuel Ntim and Marialore Sulpizi. Role of image charges in ionic liquid confined between metallic interfaces. *Physical Chemistry Chemical Physics*, 22(19):10786–10791, 2020.

[253] S Kondrat, Nikolaj Georgi, Maxim V Fedorov, and Alexei A Kornyshev. A superionic state in nano-porous double-layer capacitors: insights from monte carlo simulations. *Physical Chemistry Chemical Physics*, 13(23):11359–11366, 2011.

[254] Silvia Di Lecce, Alexei A Kornyshev, Michael Urbakh, and Fernando Bresme. Structural effects in nanotribology of nanoscale films of ionic liquids confined between metallic surfaces. *Physical Chemistry Chemical Physics*, 23(38):22174–22183, 2021.

[255] Brian Giera, Neil Henson, Edward M Kober, M Scott Shell, and Todd M Squires. Electric double-layer structure in primitive model electrolytes: comparing molecular dynamics with local-density approximations. *Langmuir*, 31(11):3553–3562, 2015.

[256] John P Valleau and L Kenneth Cohen. Primitive model electrolytes. i. grand canonical monte carlo computations. *The Journal of chemical physics*, 72(11):5935–5941, 1980.

[257] Jian Jiang, Dapeng Cao, Douglas Henderson, and Jianzhong Wu. Revisiting density functionals for the primitive model of electric double layers. *The Journal of chemical physics*, 140(4):044714, 2014.

[258] Norman F Carnahan and Kenneth E Starling. Equation of state for nonattracting rigid spheres. *The Journal of chemical physics*, 51(2):635–636, 1969.

[259] David Andelman. Introduction to electrostatics in soft and biological matter. *Soft condensed matter physics in molecular and cell biology*, 6, 2006.

[260] Peter I Ravikovitch and Alexander V Neimark. Density functional theory model of adsorption deformation. *Langmuir*, 22(26):10864–10868, 2006.

[261] Peter I Ravikovitch and Alexander V Neimark. Density functional theory model of adsorption on amorphous and microporous silica materials. *Langmuir*, 22(26):11171–11179, 2006.

[262] JR Henderson. Statistical mechanics of the disjoining pressure of a planar film. *Physical Review E*, 72(5):051602, 2005.

[263] Bertil Hille et al. *Ion channels of excitable membranes*, volume 507. Sinauer Sunderland, MA, 2001.

[264] RS Eisenberg. Computing the field in proteins and channels. *Journal of Membrane Biology*, 150(1):1–25, 1996.

[265] Declan A Doyle, Joao Morais Cabral, Richard A Pfuetzner, Anling Kuo, Jacqueline M Gulbis, Steven L Cohen, Brian T Chait, and Roderick MacKinnon. The structure of the potassium channel: molecular basis of k+ conduction and selectivity. *science*, 280(5360):69–77, 1998.

[266] William A Catterall. From ionic currents to molecular mechanisms: the structure and function of voltage-gated sodium channels. *Neuron*, 26(1):13–25, 2000.

[267] Bert Sakmann. *Single-channel recording*. Springer Science & Business Media, 2013.

[268] Christopher Maffeo, Swati Bhattacharya, Jejoong Yoo, David Wells, and Aleksei Aksimentiev. Modeling and Simulation of Ion Channels. *Chemical Reviews*, 112(12):6250–6284, dec 2012.

[269] Mark A Shannon, Paul W Bohn, Menachem Elimelech, John G Georgiadis, Benito J Marinas, and Anne M Mayes. Science and technology for water purification in the coming decades. In *Nanoscience and technology: a collection of reviews from nature Journals*, pages 337–346. World Scientific, 2010.

[270] PS Goh, AF Ismail, and Nidal Hilal. Nano-enabled membranes technology: sustainable and revolutionary solutions for membrane desalination? *Desalination*, 380:100–104, 2016.

[271] Jun Lu, Huacheng Zhang, Jue Hou, Xingya Li, Xiaoyi Hu, Yaoxin Hu, Christopher D Easton, Qinye Li, Chenghua Sun, Aaron W Thornton, et al. Efficient metal ion sieving in rectifying subnanochannels enabled by metal–organic frameworks. *Nature Materials*, pages 1–8, 2020.

[272] Zhongwu Li, Yuhao Li, Yun-Chiao Yao, Fikret Aydin, Cheng Zhan, Yunfei Chen, Menachem Elimelech, Tuan Anh Pham, and Aleksandr Noy. Strong differential monovalent anion selectivity in narrow diameter carbon nanotube porins. *ACS nano*, 14(5):6269–6275, 2020.

[273] Rohit Karnik, Chuanhua Duan, Kenneth Castelino, Hirofumi Daiguji, and Arun Majumdar. Rectification of ionic current in a nanofluidic diode. *Nano letters*, 7(3):547–551, 2007.

[274] Rohit Karnik, Rong Fan, Min Yue, Deyu Li, Peidong Yang, and Arun Majumdar. Electrostatic control of ions and molecules in nanofluidic transistors. *Nano letters*, 5(5):943–948, 2005.

[275] Hirofumi Daiguji. Ion transport in nanofluidic channels. *Chemical Society Reviews*, 39(3):901–911, 2010.

[276] Richard J Gross and JF Osterle. Membrane transport characteristics of ultrafine capillaries. *The Journal of chemical physics*, 49(1):228–234, 1968.

[277] PB Peters, R Van Roij, Martin Z Bazant, and PM Biesheuvel. Analysis of electrolyte transport through charged nanopores. *Physical review E*, 93(5):053108, 2016.

[278] PM Biesheuvel and MZ Bazant. Analysis of ionic conductance of carbon nanotubes. *Physical Review E*, 94(5):050601, 2016.

[279] Shima Alizadeh and Ali Mani. Multiscale model for electrokinetic transport in networks of pores, part i: model derivation. *Langmuir*, 33(25):6205–6219, 2017.

[280] R Qiao and Narayana R Aluru. Scaling of electrokinetic transport in nanometer channels. *Langmuir*, 21(19):8972–8977, 2005.

[281] R Qiao and Narayana R Aluru. Surface-charge-induced asymmetric electrokinetic transport in confined silicon nanochannels. *Applied Physics Letters*, 86(14):143105, 2005.

[282] Menachem Elimelech and William A Phillip. The future of seawater desalination: energy, technology, and the environment. *science*, 333(6043):712–717, 2011.

[283] Samuel Faucher, Narayana Aluru, Martin Z Bazant, Daniel Blankschtein, Alexandra H Brozena, John Cumings, J Pedro de Souza, Menachem Elimelech, Razi Epsztein, John T Fourkas, et al. Critical knowledge gaps in mass transport through single-digit nanopores: A review and perspective. *The Journal of Physical Chemistry C*, 123(35):21309–21326, 2019.

[284] Daniel Branton, David W. Deamer, Andre Marziali, Hagan Bayley, Steven A. Benner, Thomas Butler, Massimiliano Di Ventra, Slaven Garaj, Andrew Hibbs, Xiaohua Huang, Stevan B. Jovanovich, Predrag S. Krstic, Stuart Lindsay, Xinsheng Sean Ling, Carlos H. Mastrangelo, Amit Meller, John S. Oliver, Yuriy V. Pershin, J. Michael Ramsey, Robert Riehn, Gautam V. Soni, Vincent Tabard-Cossa, Meni Wanunu, Matthew Wiggin, and Jeffery A. Schloss. The potential and challenges of nanopore sequencing. *Nature biotechnology*, 26(10):1146–1153, Oct 2008. 18846088[pmid].

[285] Farzin Haque, Jinghong Li, Hai-Chen Wu, Xing-Jie Liang, and Peixuan Guo. Solid-state and biological nanopore for real-time sensing of single chemical and sequencing of dna. *Nano Today*, 8(1):56–74, 2013.

[286] Duan Chen, James Lear, and Bob Eisenberg. Permeation through an open channel: Poisson-nernst-planck theory of a synthetic ionic channel. *Biophysical Journal*, 72(1):97–116, 1997.

[287] Eleonora Secchi, Antoine Niguès, Laetitia Jubin, Alessandro Siria, and Lydéric Bocquet. Scaling behavior for ionic transport and its fluctuations in individual carbon nanotubes. *Physical review letters*, 116(15):154501, 2016.

[288] Gregor Trefalt, Sven Holger Behrens, and Michal Borkovec. Charge regulation in the electrical double layer: ion adsorption and surface interactions. *Langmuir*, 32(2):380–400, 2016.

[289] Frank H. J. van der Heyden, Derek Stein, Koen Besteman, Serge G. Lemay, and Cees Dekker. Charge Inversion at High Ionic Strength Studied by Streaming Currents. *Phys. Rev. Lett.*, 96(22):224502, jun 2006.

[290] Jan W. Post, Joost Veerman, Hubertus V.M. Hamelers, Gerrit J.W. Euverink, Sybrand J. Metz, Kitty Nymeijer, and Cees J.N. Buisman. Salinity-gradient power: Evaluation of pressure-retarded osmosis and reverse electrodialysis. *Journal of Membrane Science*, 288(1):218–230, 2007.

[291] Yuhui He, Zhuo Huang, Bowei Chen, Makusu Tsutsui, Xiang Shui Miao, and Masateru Taniguchi. Electrokinetic analysis of energy harvest from natural salt gradients in nanochannels. *Scientific Reports*, 7(1):13156, 2017.

[292] Yun-Chiao Yao, Amir Taqieddin, Mohammad A Alibakhshi, Meni Wanunu, Narayana R Aluru, and Aleksandr Noy. Strong electroosmotic coupling dominates ion conductance of 1.5 nm diameter carbon nanotube porins. *ACS nano*, 13(11):12851–12859, 2019.

[293] Yoav Green, Ran Eshel, Sinwook Park, and Gilad Yossifon. Interplay between nanochannel and microchannel resistances. *Nano letters*, 16(4):2744–2748, 2016.

[294] Yoav Green, Shahar Shloush, and Gilad Yossifon. Effect of geometry on concentration polarization in realistic heterogeneous permselective systems. *Physical Review E*, 89(4):043015, 2014.

[295] Attila Malasics, Dirk Gillespie, Wolfgang Nonner, Douglas Henderson, Bob Eisenberg, and Dezső Boda. Protein structure and ionic selectivity in calcium channels: Selectivity filter size, not shape, matters. *Biochimica et Biophysica Acta (BBA)-Biomembranes*, 1788(12):2471–2480, 2009.

[296] Razi Epsztein, Evyatar Shaulsky, Mohan Qin, and Menachem Elimelech. Activation behavior for ion permeation in ion-exchange membranes: Role of ion dehydration in selective transport. *Journal of Membrane Science*, 580:316–326, 2019.

[297] E. Victoria Dydek and Martin Z. Bazant. Nonlinear Dynamics of Ion Concentration Polarization in Porous Media: The Leaky Membrane Model. apr 2013.

[298] Daosheng Deng, Wassim Aouad, William A Braff, Sven Schlumpberger, Matthew E Suss, and Martin Z Bazant. Water purification by shock electrodialysis: Deionization, filtration, separation, and disinfection. *Desalination*, 357:77–83, 2015.

[299] Sven Schlumpberger, Nancy B Lu, Matthew E Suss, and Martin Z Bazant. Scalable and continuous water deionization by shock electrodialysis. *Environmental Science & Technology Letters*, 2(12):367–372, 2015.

[300] Mohammad A Alkhadra, Kameron M Conforti, Tao Gao, Huanhuan Tian, and Martin Z Bazant. Continuous separation of radionuclides from contaminated water by shock electrodialysis. *Environmental Science & Technology*, 54(1):527–536, 2019.

[301] Kameron M Conforti and Martin Z Bazant. Continuous ion-selective separations by shock electrodialysis. *AIChE Journal*, 66(1):e16751, 2020.

[302] Mohammad A Alkhadra, Tao Gao, Kameron M Conforti, Huanhuan Tian, and Martin Z Bazant. Small-scale desalination of seawater by shock electrodialysis. *Desalination*, 476:114219, 2020.

[303] Markus Schmuck and Martin Z Bazant. Homogenization of the poisson–nernst–planck equations for ion transport in charged porous media. *SIAM Journal on Applied Mathematics*, 75(3):1369–1401, 2015.

[304] Sven H Behrens and David G Grier. The charge of glass and silica surfaces. *The Journal of Chemical Physics*, 115(14):6716–6721, 2001.

[305] Chih-Yuan Lin, Elif Turker Acar, Jake W Polster, Kabin Lin, Jyh-Ping Hsu, and Zuzanna S Siwy. Modulation of charge density and charge polarity of nanopore wall by salt gradient and voltage. *ACS nano*, 13(9):9868–9879, 2019.

[306] Chih-Yuan Lin, Pei-Hsuan Wong, Pei-Hsin Wang, Zuzanna S Siwy, and Li-Hsien Yeh. Electrodiffusioosmosis-induced negative differential resistance in ph-regulated mesopores containing purely monovalent solutions. *ACS Applied Materials & Interfaces*, 2019.

[307] Mustafa Sabri Kilic, Martin Z Bazant, and Armand Ajdari. Steric effects in the dynamics of electrolytes at large applied voltages. i. double-layer charging. *Phys. Rev. E*, 75(2):021502, 2007.

[308] Alexei A. Kornyshev, Dominic J. Lee, Sergey Leikin, and Aaron Wynveen. Structure and interactions of biological helices. *Rev. Mod. Phys.*, 79(3):943–996, aug 2007.

[309] J Pedro de Souza and Martin Z Bazant. Continuum theory of electrostatic correlations at charged surfaces. *The Journal of Physical Chemistry C*, 124(21):11414–11421, 2020.

[310] Martin Chaplin. Do we underestimate the importance of water in cell biology? *Nature Reviews Molecular Cell Biology*, 7(11):861–866, 2006.

[311] Philip Ball. Water as an active constituent in cell biology. *Chemical reviews*, 108(1):74–108, 2008.

[312] J Lyklema. Fundamentals of interface and colloid science, volume ii, solid-liquid interfaces, 1995.

[313] Geoffrey M Geise, Donald R Paul, and Benny D Freeman. Fundamental water and salt transport properties of polymeric materials. *Progress in Polymer Science*, 39(1):1–42, 2014.

[314] Sophie Marbach and Lydéric Bocquet. Osmosis, from molecular insights to large-scale applications. *Chemical Society Reviews*, 48(11):3102–3144, 2019.

[315] F Bowden and D Tabor. The friction and lubrication of solids, new york: Oxford univ, 1950.

[316] Bharat Bhushan, Jacob N Israelachvili, and Uzi Landman. Nanotribology: friction, wear and lubrication at the atomic scale. *Nature*, 374(6523):607–616, 1995.

[317] Olle Bjorneholm, Martin H Hansen, Andrew Hodgson, Li-Min Liu, David T Limmer, Angelos Michaelides, Philipp Pedevilla, Jan Rossmeisl, Huaze Shen, Gabriele Tocci, et al. Water at interfaces. *Chemical reviews*, 116(13):7698–7726, 2016.

[318] M Gouy. Sur la constitution de la charge électrique à la surface d'un électrolyte. *J. Phys. Theor. Appl.*, 9(1):457–468, 1910.

[319] David Leonard Chapman. Li. a contribution to the theory of electrocapillarity. *The London, Edinburgh, and Dublin philosophical magazine and journal of science*, 25(148):475–481, 1913.

[320] AA Kornyshev, W Schmickler, and MA Vorotyntsev. Nonlocal electrostatic approach to the problem of a double layer at a metal-electrolyte interface. *Physical Review B*, 25(8):5244, 1982.

[321] AA Kornyshev and MA Vorotyntsev. Nonlocal electrostatic approach to the double layer and adsorption at the electrode-electrolyte interface. *Surface Science*, 101(1-3):23–48, 1980.

[322] Douwe Jan Bonthuis and Roland R Netz. Beyond the continuum: How molecular solvent structure affects electrostatics and hydrodynamics at solid–electrolyte interfaces. *The Journal of Physical Chemistry B*, 117(39):11397–11413, 2013.

[323] David C Grahame. Effects of dielectric saturation upon the diffuse double layer and the free energy of hydration of ions. *The Journal of Chemical Physics*, 18(7):903–909, 1950.

[324] Ariel Abrashkin, David Andelman, and Henri Orland. Dipolar poisson-boltzmann equation: ions and dipoles close to charge interfaces. *Physical review letters*, 99(7):077801, 2007.

[325] Paul Fenter and Neil C Sturchio. Mineral–water interfacial structures revealed by synchrotron x-ray scattering. *Progress in Surface Science*, 77(5-8):171–258, 2004.

[326] L Cheng, P Fenter, KL Nagy, ML Schlegel, and NC Sturchio. Molecular-scale density oscillations in water adjacent to a mica surface. *Physical review letters*, 87(15):156103, 2001.

[327] Jeffrey G Catalano. Weak interfacial water ordering on isostructural hematite and corundum (0 0 1) surfaces. *Geochimica et Cosmochimica Acta*, 75(8):2062–2071, 2011.

[328] Derek Frydel and Yan Levin. A close look into the excluded volume effects within a double layer. *The Journal of chemical physics*, 137(16):164703, 2012.

[329] Philippe A Bopp, Alexei A Kornyshev, and Godehard Sutmann. Frequency and wave-vector dependent dielectric function of water: Collective modes and relaxation spectra. *The Journal of chemical physics*, 109(5):1939–1958, 1998.

[330] Philippe A Bopp, Alexei A Kornyshev, and Godehard Sutmann. Static nonlocal dielectric function of liquid water. *Physical review letters*, 76(8):1280, 1996.

[331] Alexei A Kornyshev and Godehard Sutmann. Nonlocal dielectric saturation in liquid water. *Physical review letters*, 79(18):3435, 1997.

[332] Alexei A Kornyshev and Godehard Sutmann. The shape of the nonlocal dielectric function of polar liquids and the implications for thermodynamic properties of electrolytes: A comparative study. *The Journal of chemical physics*, 104(4):1524–1544, 1996.

[333] Douwe Jan Bonthuis, Stephan Gekle, and Roland R Netz. Dielectric profile of interfacial water and its effect on double-layer capacitance. *Physical review letters*, 107(16):166102, 2011.

[334] Alexander Schlaich, Ernst W Knapp, and Roland R Netz. Water dielectric effects in planar confinement. *Physical review letters*, 117(4):048001, 2016.

[335] Philip Loche, Cihan Ayaz, Alexander Schlaich, Douwe Jan Bonthuis, and Roland R Netz. Breakdown of linear dielectric theory for the interaction between hydrated ions and graphene. *The journal of physical chemistry letters*, 9(22):6463–6468, 2018.

[336] Sergi Ruiz-Barragan, Daniel Muñoz-Santiburcio, Saskia Körning, and Dominik Marx. Quantifying anisotropic dielectric response properties of nanoconfined water within graphene slit pores. *Physical Chemistry Chemical Physics*, 22(19):10833–10837, 2020.

[337] Amir Levy, David Andelman, and Henri Orland. Dielectric constant of ionic solutions: A field-theory approach. *Physical review letters*, 108(22):227801, 2012.

[338] Aleš Iglič, Ekaterina Gongadze, and Klemen Bohinc. Excluded volume effect and orientational ordering near charged surface in solution of ions and langevin dipoles. *Bioelectrochemistry*, 79(2):223–227, 2010.

[339] Rahul Prasanna Misra, Siddhartha Das, and Sushanta K Mitra. Electric double layer force between charged surfaces: Effect of solvent polarization. *The Journal of chemical physics*, 138(11):114703, 2013.

[340] Alexei A Kornyshev. Non-local dielectric response of a polar solvent and debye screening in ionic solution. *Journal of the Chemical Society, Faraday Transactions 2: Molecular and Chemical Physics*, 79(5):651–661, 1983.

[341] ML Belaya, MV Feigel'Man, and VG Levadny. Hydration forces as a result of non-local water polarizability. *Chemical physics letters*, 126(3-4):361–364, 1986.

[342] Amir Levy, Martin Bazant, and Alexei Kornyshev. Ionic activity in concentrated electrolytes: Solvent structure effect revisited. *Chemical Physics Letters*, 738:136915, 2020.

[343] David Chandler and Hans C Andersen. Optimized cluster expansions for classical fluids. ii. theory of molecular liquids. *The Journal of Chemical Physics*, 57(5):1930–1937, 1972.

[344] Fumio Hirata, B Montgomery Pettitt, and Peter J Rossky. Application of an extended rism equation to dipolar and quadrupolar fluids. *The Journal of Chemical Physics*, 77(1):509–520, 1982.

[345] B Montgomery Pettitt and Peter J Rossky. Integral equation predictions of liquid state structure for waterlike intermolecular potentials. *The Journal of Chemical Physics*, 77(3):1451–1457, 1982.

[346] Mitsunori Ikeguchi and Junta Doi. Direct numerical solution of the ornstein–zernike integral equation and spatial distribution of water around hydrophobic molecules. *The Journal of chemical physics*, 103(12):5011–5017, 1995.

[347] Leo Lue and Daniel Blankschtein. Application of integral equation theories to predict the structure, thermodynamics, and phase behavior of water. *The Journal of chemical physics*, 102(13):5427–5437, 1995.

[348] Dmitrii Beglov and Benoît Roux. An integral equation to describe the solvation of polar molecules in liquid water. *The journal of physical chemistry B*, 101(39):7821–7826, 1997.

[349] Andrij Trokhymchuk, Douglas Henderson, and Darsh T Wasan. A molecular theory of the hydration force in an electrolyte solution. *Journal of colloid and interface science*, 210(2):320–331, 1999.

[350] Qishi Du, Dmitrii Beglov, and Benoît Roux. Solvation free energy of polar and nonpolar molecules in water: An extended interaction site integral equation theory in three dimensions. *The Journal of Physical Chemistry B*, 104(4):796–805, 2000.

[351] Maxim V Fedorov and Alexei A Kornyshev. Unravelling the solvent response to neutral and charged solutes. *Molecular Physics*, 105(1):1–16, 2007.

[352] Jianzhong Wu and Zhidong Li. Density-functional theory for complex fluids. *Annu. Rev. Phys. Chem.*, 58:85–112, 2007.

[353] Jean-François Olivieri, James T Hynes, and Damien Laage. Confined water's dielectric constant reduction is due to the surrounding low dielectric media and not to interfacial molecular ordering. *The Journal of Physical Chemistry Letters*, 12(17):4319–4326, 2021.

[354] Florian Deißenbeck, Christoph Freysoldt, Mira Todorova, Joerg Neugebauer, and Stefan Wippermann. Dielectric properties of nanoconfined water: A canonical thermopotentiostat approach. *Physical Review Letters*, 126(13):136803, 2021.

[355] F Booth. The dielectric constant of water and the saturation effect. *The Journal of Chemical Physics*, 19(4):391–394, 1951.

[356] John G Kirkwood. The dielectric polarization of polar liquids. *The Journal of Chemical Physics*, 7(10):911–919, 1939.

[357] Ekaterina Gongadze, Ursula van Rienen, Veronika Kralj-Iglič, and Aleš Iglič. Spatial variation of permittivity of an electrolyte solution in contact with a charged metal surface: a mini review. *Computer methods in biomechanics and biomedical engineering*, 16(5):463–480, 2013.

[358] Geoffrey Monet, Fernando Bresme, Alexei Kornyshev, and Hélène Berthoumieux. The nonlocal dielectric response of water in nanoconfinement. *arXiv preprint arXiv:2102.09309*, 2021.

[359] OV Dolgov, DA Kirzhnits, and EG Maksimov. On an admissible sign of the static dielectric function of matter. *Reviews of Modern Physics*, 53(1):81, 1981.

[360] Marius M Hatlo, RHHG Van Roij, and Leo Lue. The electric double layer at high surface potentials: The influence of excess ion polarizability. *EPL (Europhysics Letters)*, 97(2):28010, 2012.

[361] Sergey Leikin, V Adrian Parsegian, Donald C Rau, and R Peter Rand. Hydration forces. *Annual review of physical chemistry*, 44(1):369–395, 1993.

[362] S Leikin and AA Kornyshev. Theory of hydration forces. nonlocal electrostatic interaction of neutral surfaces. *The Journal of chemical physics*, 92(11):6890–6898, 1990.

[363] Ekaterina Gongadze, Aljaž Velikonja, Tomaž Slivnik, Veronika Kralj-Iglič, and Aleš Iglič. The quadrupole moment of water molecules and the permittivity of water near a charged surface. *Electrochimica Acta*, 109:656–662, 2013.

[364] Radomir I Slavchov and Tzanko I Ivanov. Quadrupole terms in the maxwell equations: Born energy, partial molar volume, and entropy of ions. *The Journal of chemical physics*, 140(7):074503, 2014.

[365] Duncan MF Edwards, Paul A Madden, and Ian R McDonald. A computer simulation study of the dielectric properties of a model of methyl cyanide: I. the rigid dipole case. *Molecular physics*, 51(5):1141–1161, 1984.

[366] Pekka Mark and Lennart Nilsson. Structure and dynamics of the tip3p, spc, and spc/e water models at 298 k. *The Journal of Physical Chemistry A*, 105(43):9954–9960, 2001.